Modeling the Active Sites of Non-Heme Diiron Metalloproteins with Sterically Hindered Carboxylates and Syn *N*-Donor Ligands

by

Simone Friedle

Diplom-Chemikerin, University of Karlsruhe, Germany, 2004

SUBMITTED TO THE DEPARTMENT OF CHEMISTRY
IN PARTIAL FULFILLMENT OF THE REQUIREMENTS
FOR THE DEGREE OF

DOCTOR OF PHILOSOPHY IN INORGANIC CHEMISTRY
AT THE
MASSACHUSETTS INSTITUTE OF TECHNOLOGY

ARCHIVES

September 2009

Signature of
Author:_____

Department of Chemistry
July 20, 2009

Certified
By:_____

Stephen J. Lippard
Arthur Amos Noyes Professor of Chemistry
Thesis Supervisor

Accepted
By:_____

Robert W. Field
Haslam and Dewey Professor of Chemistry
Chairman, Department Committee on Graduate Studies

This doctoral thesis has been examined by a committee of the Department of Chemistry as follows:

Christopher C. Cummins
Professor of Chemistry
Committee Chairperson

Stephen J. Lippard
Arthur Amos Noyes Professor of Chemistry
Thesis Supervisor

Richard R. Schrock
Frederick G. Keyes Professor of Chemistry

Modeling the Active Sites of Non-Heme Diiron Metalloproteins with Sterically Hindered Carboxylates and Syn *N*-Donor Ligands

by
Simone Friedle

Submitted to the Department of Chemistry on July 20, 2009 in partial fulfillment of the requirements for the Degree of Doctor of Philosophy in Inorganic Chemistry

Abstract

Chapter 1. Different Synthetic Approaches to Modeling the Active Sites of Carboxylate-Bridged Non-Heme Diiron Enzymes

Carboxylate-bridged non-heme diiron enzymes activate dioxygen to perform a variety of biological functions. Synthetic model compounds have been prepared to gain insight into the intricacies of dioxygen activation in these enzymes. In this introductory chapter, the challenges and advances of different diiron systems with terphenyl and dendrimer-appended carboxylates, nitrogen-rich, and syn *N*-donor ligands are highlighted.

Chapter 2. 9-Triptycenecarboxylate-Bridged Diiron(II) Complexes: Capture of the Paddlewheel Geometric Isomer

The synthesis and characterization of diiron(II) complexes supported by 9-triptycenecarboxylate ligands ($^{-}O_2CTrp$) is described. The interlocking nature of the triptycenecarboxylates facilitates formation of quadruply bridged diiron(II) complexes of the type $[Fe_2(\mu\text{-}O_2CTrp)_4(L)_2]$ (L = THF, pyridine or imidazole derivative) with a paddlewheel geometry. A systematic lengthening of the Fe–Fe distance occurs with the increase in steric bulk of the neutral donor L, resulting in

values of up to 3 Å without disassembly of the paddlewheel structure. Reactions with an excess of water do not lead to decomposition of the diiron(II) core, indicating that these quadruply bridged complexes are exceptionally stable. The red-colored complexes $[Fe_2(\mu\text{-}O_2CTrp)_4(4\text{-}AcPy)_2]$ (**10**) and $[Fe_2(\mu\text{-}O_2CTrp)_4(4\text{-}CNPy)_2]$ (**11**) exhibit solvent-dependent thermochromism in coordinating solvents that was studied by variable temperature UV-vis spectroscopy. Reaction of $[Fe_2(\mu\text{-}O_2CTrp)_4(THF)_2]$ with *N,N,N',N'*-tetramethylethylenediamine (TMEDA), tetra-*n*-butyl ammonium thiocyanate, or excess 2-methylimidazole resulted in the formation of mononuclear complexes $[Fe(O_2CTrp)_2(TMEDA)]$ (**13**), $(^nBu_4N)_2[Fe(O_2CTrp)_2(SCN)_2]$ (**14**), and $[Fe(O_2CTrp)_2(2\text{-}MeIm)_2]$ (**15**) having an O_4/N_2 coordination sphere composition.

Chapter 3. Synthesis, Characterization, and Oxygenation Studies of Carboxylate-Bridged Diiron(II) Complexes with Aromatic Substrates Tethered to Pyridine Ligands and the Formation of a Unique Trinuclear Complex

In this study, diiron(II) complexes were synthesized as small molecule mimics of the reduced active sites in the hydroxylase components of bacterial multicomponent monooxygenases (BMMs). Tethered aromatic substrates were introduced in the form of 2-phenoxypyridines, incorporating hydroxy and methoxy functionalities into windmill-type diiron(II) compounds $[Fe_2(\mu\text{-}O_2CAr^R)_2(O_2CAr^R)_2(L)_2]$ (**1–4**), where $^-O_2CAr^R$ is a sterically encumbering carboxylate, 2,6-di(4-fluorophenyl)- or 2,6-di(*p*-tolyl)benzoate (R = 4-FPh or Tol, respectively). The inability of **1–4** to hydroxylate the aromatic substrates was ascertained. Upon reaction with dioxygen, compounds **2** and **3** (L = 2-(*m*-MeOPhO)Py, 2-(*p*-MeOPhO)Py, respectively) decompose by a known bimolecular pathway to form mixed-valent diiron(II,III) species at low temperature. Use of 2-(pyridin-2-yloxy)phenol as the ligand L resulted in a doubly bridged diiron complex (**4**) and

an unprecedented phenoxide-bridged triiron(II) complex (**5**) under slightly modified reaction conditions.

Chapter 4. Modeling the Syn-Disposition of Nitrogen Donors in Non-Heme Diiron Enzymes. Synthesis, Characterization and Hydrogen Peroxide Reactivity of Diiron(III) Complexes with the Syn *N*-Donor Ligand H_2BPG_2DEV

In order to model the syn disposition of histidine residues in carboxylate-bridged non-heme diiron enzymes, we prepared a new dinucleating ligand, H_2BPG_2DEV, that provides this geometric feature. The ligand incorporates biologically relevant carboxylate functionalities, which have not been explored as extensively as nitrogen-only analogs. Three novel oxo-bridged diiron(III) complexes $[Fe_2(\mu\text{-}O)(H_2O)_2(BPG_2DEV)](ClO_4)_2$ (**6**), $[Fe_2(\mu\text{-}O)(\mu\text{-}O_2CAr^{iPrO})(BPG_2DEV)](ClO_4)$ (**7**), and $[Fe_2(\mu\text{-}O)(\mu\text{-}CO_3)(BPG_2DEV)]$ (**8**) were prepared. Single crystal X-ray structural characterization confirms that two pyridines are bound syn with respect to the Fe–Fe vector in these compounds. The carbonato-bridged complex **8** forms quantitatively from **6** in a rapid reaction with gaseous CO_2 in organic solvents. A common maroon-colored intermediate (λ_{max} = 490 nm; ε = 1500 M^{-1} cm^{-1}) forms in reactions of **6**, **7**, or **8** with H_2O_2 and NEt_3 in CH_3CN/H_2O solutions. Mass spectrometric analyses of this species, formed using ^{18}O-labeled H_2O_2, indicate the presence of a peroxide ligand bound to the oxo-bridged diiron(III) center. The Mössbauer spectrum at 90 K of the EPR-silent intermediate exhibits a quadrupole doublet with δ = 0.58 mm/s and ΔE_Q = 0.58 mm/s. The isomer shift is typical for a peroxodiiron(III) species, but the quadrupole splitting parameter is unusually small compared to related complexes. These Mössbauer parameters are comparable to those observed for a peroxo intermediate formed in the reaction of reduced toluene/*o*-xylene monooxygenase hydroxylase (ToMOH) with dioxygen. Resonance Raman studies reveal an unusually low-energy O–O stretching mode in the peroxo intermediate that is consistent with a short diiron

distance. Although peroxodiiron(III) intermediates generated from **6**, **7**, and **8** are poor O-atom transfer catalysts, they display highly efficient catalase activity, with turnover numbers up to 10,000. In contrast to hydrogen peroxide reactions of diiron(III) complexes that lack a dinucleating ligand, the intermediates generated here could be reformed in significant quantities after a second addition of H_2O_2, as observed spectroscopically and by mass spectrometry.

Appendix 1. Supporting Tables and Figures for Chapter 2

Appendix 2. Supporting Information for Chapter 4

Appendix 3. Synthesis of Triptycene Carboxylate-Bridged Dimetallic Complexes with First Row Transition Metals

The synthesis and structural characterization of dimetallic complexes of the type $[M_2(\mu\text{-}O_2CTrp)_4(THF)_2]$ (M = Mn, Co, Ni, Cu, Zn) supported by triptycene-carboxylate ligands ($^{-}O_2CTrp$) is described.

Appendix 4. Synthesis and Structure of a Molecular Ferrous Wheel, $[Fe(O_2CH)(O_2CAr^{iPrO})(1,4\text{-dioxane})]_6$

The structural characterization of a novel, hexanuclear iron(II) compound with the carboxylate $Ar^{iPrO}CO_2^-$ is described.

Thesis Supervisor: Stephen J. Lippard
Title: Arthur Amos Noyes Professor of Chemistry

To my parents and Trillium

Acknowledgements

I am delighted to express my gratitude and appreciation to several people, without whose encouragement and support this thesis would not have been possible.

First and foremost, I want to thank my advisor, Steve Lippard, for giving me the opportunity to work in his lab and for the confidence he showed in me over the years. I am grateful to have had the opportunity to work in a well-equipped and diverse lab and I am proud to have been part of it. I also thank my thesis chair Professor Kit Cummins for helpful discussions throughout the years and Professor Richard R. Schrock for serving on my thesis committee.

I am grateful to have had wonderful coworkers in the original diiron subgroup. When I joined this group, I shared a hood with Emily Carson, who helped me settle down in the lab. I thank her for her excellent mentoring and patience in answering my questions during preparation for orals and thesis writing via email or phone after she had graduated. Jeremy Kodanko was my desk neighbor and I enjoyed his humor and advice in organic chemistry. Rayane Moreira and YooJin Kim provided a fun working atmosphere in our subgroup. I appreciate the friendship and guidance offered by labmates Erwin Reisner and Todd Harrop in the synthetic subgroup, which was founded in my second year. Erwin arrived with a fresh perspective and Lebensfreude unlike anyone's I have ever known. I enjoyed working with Min Zhao and her daughter Jia Jia's visits to the lab. Mentoring a talented undergraduate, Kyrstin Fornace, who worked with me for two years, was an enjoyable and invaluable experience. Loi Do and Zachary Tonzetich, who joined the subgroup more recently, always had time for discussions and I thank them for helping me with any kind of problem I had. I enjoyed conversations with Rachel Behan, Woon Ju Song, and Christy Tinberg, members of the BMM subgroup, and thank them for their insights in diiron metalloprotein chemistry.

Significant portions of my thesis work would not have been possible with the help from students and post-docs from our lab and outside collaborators. When I first joined the lab, Datong Song trained me in crystallographic methods. I want to thank him and especially Peter Müller from whose lectures, book, and personal interactions I learned a substantial amount about the discipline. Sebastian Stoian, an expert in Mössbauer and EPR spectroscopy, was always exceptionally helpful and I learned a great deal about these techniques from him. I am grateful to Takahiro Hayashi from Pierre Moënne-Loccoz' lab for his enthusiastic collaboration on my Raman samples. Wanhua Ye from Tufts University always had time for a chat while she helped me measuring my mass spectra. I appreciate Liz Nolan's help with our Raman collaboration during my first year as well as her friendship over the years. Mi Hee Lim always was a cheerful and insightful discussion partner when I had questions about diiron chemistry.

My fellow class- and labmates, Katie Lovejoy, Erik Dill, and Brian Wong have all become good friends of mine during our time at MIT. Katie, thanks for changing your flight to be around for my thesis defense! To my classmates Alex Fox and Becky Nicodemus: thanks for the fun nights out enjoying music! My German labmates Matthias Ober and Nora Graf relieved my homesickness. I especially appreciate the friendships with Nora, Daniela Buccella, and Shanta Dhar and enjoyed our regular lunch and coffee breaks, as well as tasty Indian and Turkish food prepared by Shanta and Nora. I enjoyed Xiao-an Zhang's interest and enthusiasm in scientific discussions, as well as having him as a friend and lab partner. I know I shall miss all of them and many others, including Wee Han Ang, Elisa Tomat, Semi Park, Guangyu Zhu, Juliana Fedoce Lopes, Youngmin You, and Caroline Saouma when I leave MIT.

I also appreciate the help offered by the DCIF staff, especially Jeff Simpson and Li Li. I would always find spare parts and help in Ed Udas' shop and Scott Wade was always available when I needed something urgently. I thank Rich Girardi and Susan Brighton their kindness and assistance in sorting out all kinds of problems.

Thanks to Manfred Persohn, my mentor during my apprenticeship at the Forschungszentrum Karlsruhe who initially sparked my interest in chemistry and to my high school teacher Dr. Karl-Claudius Kniehl for encouraging me to study chemistry. I appreciate Professor Hansgeorg Schnöckel supporting my decision to go abroad to do my diploma thesis research, and I thank Professor Dick Holm at Harvard for giving me the opportunity to do research in his lab during this time. Furthermore, I also would like to thank Professors Wolfgang Höll and Leverett Zompa for their support during the time I spent in their labs.

A special thanks to several friends outside of MIT: To Briony, Harriet, and Scott for the great times, fun and laughter we shared. To Barbara and Michael Levine for letting me relax at their house and always caring for me. To Debbie for opening an enriching new chapter in my life and to Evelyn, Marianne, Laura, and Debi: I am glad I met you and that we had such a great time practicing yoga together. Thanks to my family in Germany and in the U.S. and all my friends overseas for keeping in touch even when I had little time. I want to especially thank Bettina Bechlars that she was always there for me, no matter how far away.

Finally, I want to thank my parents for their limitless love and especially for their motivation when I went through stressful times. I appreciate that they have always supported me and given me the freedom to make my own decisions. My partner Trillium Levine is an incredible source of strength for me, and words cannot express how grateful I am for his love and support. I know I can always lean on him. I wouldn't have gotten to this point without him by my side.

Table of Contents

List of Tables

Chapter 2

Chapter 3

Chapter 4

Appendix 1

List of Charts

List of Schemes

Chapter 1

Chapter 2

Chapter 3

Chapter 4

List of Figures

Chapter 1

Chapter 2

Chapter 3

Appendix 2

Chapter 1

Synthetic Strategies to Modeling the Active Sites of Carboxylate-Bridged Non-Heme Diiron Enzymes

I. Carboxylate-Bridged Non-Heme Diiron Enzymes – Structural and Functional Similarities.

Iron plays an important role in the chemistry of life.[1,2] The versatile functionality of iron-containing enzymes can be attributed to the Lewis acidity and redox properties of this element. Carboxylate-bridged non-heme diiron proteins are involved in dioxygen binding and/or activation.[3-7] Well-studied members of this protein family have various roles in biology, such as generation of an essential tyrosyl radical in the ribonucleotide reductase subunit R2 (RNR-R2),[8-11] fatty acid desaturation in Δ^9 stearoyl-acyl carrier protein desaturase (Δ^9D),[12,13] iron storage in ferritins (Ft),[3,14,15] and hydrocarbon oxidation in the hydroxylase components of bacterial multicomponent monooxygenases (BMMs).[16,17] Hydroxylase proteins belonging to the BMM family are soluble methane monooxygenase (sMMOH),[18-20] toluene/*o*-xylene monooxygenase (ToMOH),[21] and phenol hydroxylase (PHH).[22] The diiron active sites, which are each embedded in a four-helix bundle of protein α-helices, bear a common structural motif. Each diiron center is coordinated by four carboxylates from glutamate and/or aspartate residues and two imidazoles from histidine side chains that are bound in a syn disposition with respect to the diiron vector. The reduced and oxidized diiron sites of sMMOH and RNR-R2 are depicted in Figure 1.1. For both of these enzymes, a carboxylate shift of the bridging glutamate residue is observed upon interconversion between the two oxidation states. It is evident that subtle differences between these active sites, such as the coordination number of each iron atom, the carboxylate binding mode, and additional ligation

by water or hydroxide, as well as energetic and structural contributions from the surrounding protein environment, play important roles in the functional versatility of these enzymes.

The most recently recognized members of this family of enzymes contain carboxylate-bridged diiron sites with more than two histidine residues. One of them is *myo*-inositol oxygenase, which catalyzes the ring-opening glycol cleavage of *myo*-inositol by a radical new pathway for dioxygen activation at a non-heme diiron cluster.[23] The other enzyme is a flavo-diiron protein, which is reported to function as a dioxygen- and/or nitric oxide-scavenging reductase.[24]

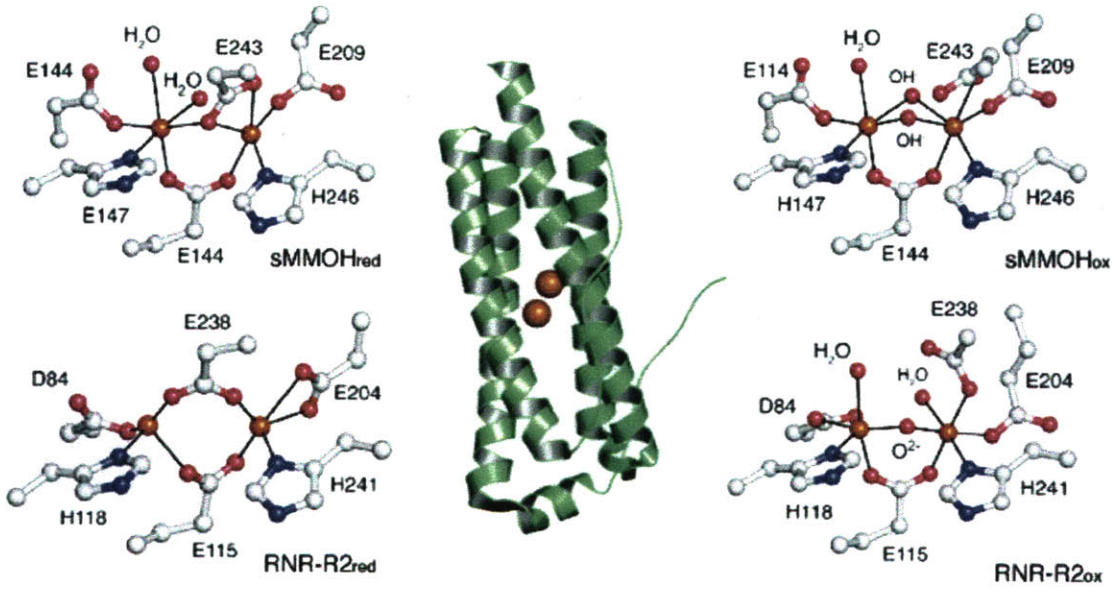

Figure 1.1. Carboxylate-bridged non-heme diiron enzyme active sites of sMMOH and RNR–R2 in their oxidized (ox) and reduced (red) forms. A schematic view of the four-helix bundle is displayed in the center.

The general pathway of dioxygen activation in carboxylate-bridged non-heme diiron enzymes is illustrated in Scheme 1.1. Dioxygen activation is initiated by reduction of the diiron(III) resting state by two electrons originating from either

NADH or NADPH to form a reactive diiron(II) species. Upon reaction with dioxygen, peroxodiiron(III) species with common spectroscopic features are observed. Some characteristic signatures include a peroxo ligand-to-iron(III) charge transfer (LMCT) band centered between 650 to 725 nm and Mössbauer parameters of $\delta = 0.62–0.68$ mm/s and $\Delta E_Q > 1.0$ mm/s.[20] Mechanistic hypotheses logically imply that the formation of a superoxodiiron(II,III) species precedes generation of the peroxodiiron(III) complex, since superoxo species are observed in heme proteins[25] and synthetic iron porphyrin complexes.[26] Experimental evidence for such species, however, has not been observed.

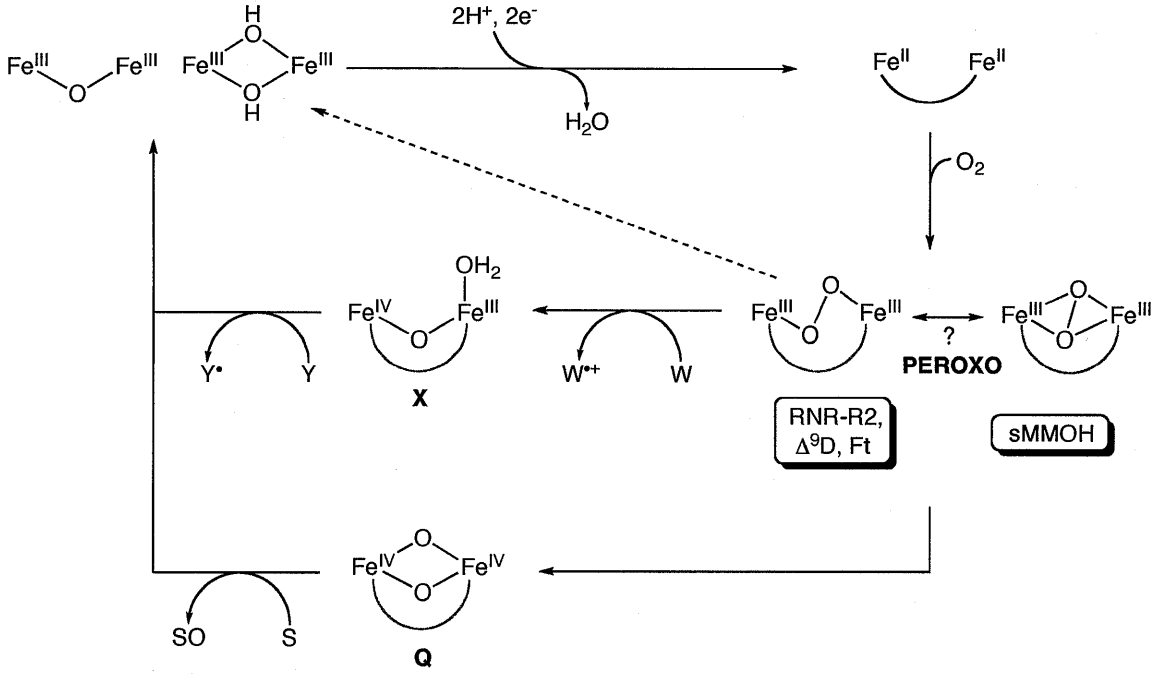

Scheme 1.1. Dioxygen activation at carboxylate-bridged non-heme diiron centers. Abbreviations: Y = tyrosine; W = tryptophan; S = substrate.

Spectroscopic studies of peroxo intermediates of ferritin,[27-29] RNR-R2[30,31] and Δ^9D[32,33] suggest a *cis*-μ-1,2-peroxo binding mode (Chart 1.1), but studies of the

peroxo intermediate in sMMOH (H_{peroxo})[34-36] have not been conclusive. Based on UV-vis, resonance Raman, and Mössbauer spectroscopic data of a structurally characterized synthetic peroxodiiron(III) complex, a μ-1,2-peroxo binding mode in H_{peroxo} seems to be a reasonable assignment.[37] Theoretical studies of this intermediate, however, propose a μ-η^2:η^2-peroxo butterfly structure, which could explain its competence for hydrocarbon oxidation.[38] In contrast to these peroxo species, the oxygenated intermediate in ToMOH, which catalyzes the oxidation of aromatics like toluene and phenol, has distinctive Mössbauer parameters and lacks an observable UV-vis absorption band.[39,40] This intermediate was tentatively assigned as a peroxodiiron(III) species having a different coordination mode and/or protonation state. It has also been demonstrated that an oxygenated intermediate formed by PHH has nearly identical spectroscopic features, implying a structure related to that of ToMOH.[41]

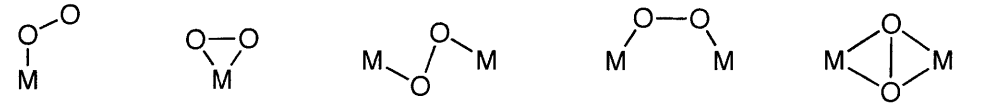

η^1-superoxo η^2-superoxo *trans*-μ-1,2-peroxo *cis*-μ-1,2-peroxo μ-η^2:η^2-peroxo

Chart 1.1. Common metal–dioxygen adduct structures.

Following O–O bond cleavage of the peroxo moiety, high-valent iron species, such as the mixed-valent (μ-oxo)diiron(III,IV) intermediate X in RNR-R2[42,43] and the methane-oxidizing di(μ-oxo)diiron(IV) intermediate Q in sMMOH[20,44] are formed.[45,46] Intermediate X catalyzes the one-electron oxidation of aromatic amino residues, whereas intermediate Q can oxidize methane and various other substrates. Despite extensive studies on sMMOH, two important

goals remain. The first is to determine the geometric structures of H_{peroxo} and Q, which to date have not been established with certainty. The second is to understand factors that govern the formation of spectroscopically different oxygenated intermediates in ToMOH and PHH.

II. Synthetic Modeling Chemistry.

The purpose of modeling the active site of carboxylate-bridged non-heme diiron enzymes is not only to achieve an understanding of their functions and how they relate to one another, but also to develop new biomimetic iron catalysts for synthetic applications.[47] The construction of functional and structural small molecule protein mimics encompasses ligand design and synthesis, coordination chemistry, and catalysis.[2,48-52] One disadvantage of small molecule model complexes is that they cannot mimic the environmental effects that are imposed by the surrounding protein. Instead they offer a glimpse at the intrinsic properties of the active site, without any secondary influence from the protein environment. Attempts to more closely imitate the protein scaffold have relied on different strategies, such as the use of sterically demanding groups,[49,53] dendrimer ligands,[54] or artificial proteins.[55] Different approaches to model the enzyme active site have been pursued. One method focuses on the synthesis of carboxylate-rich diiron complexes - a challenging task due to their tendency to form mono- or polyiron species.[56] The introduction of sterically hindered carboxylate ligands afforded discrete diiron species and this approach was consequently expanded to include carboxylate-functionalized dendrimers to provide a more protective

sheath. A second method has been the use of nitrogen-rich chelating ligands, which facilitate the formation of high-valent diiron intermediates. A third approach utilizes dinucleating alkoxide- and phenoxide-bridged ligands to stabilize the diiron core and prevent dissociation. Finally, a fourth strategy is the incorporation of ligands that mimic the syn orientation of the histidine residues in non-heme diiron enzymes. Examples of these ligand systems and the oxidation chemistry of the resulting diiron complexes are outlined in this introductory chapter.

A. Carboxylate-Rich Coordination Environments

(i) Diiron Model Complexes with Sterically-Hindered Carboxylate Ligands

Sterically-hindered ligands facilitate the synthesis of discrete diiron(II) complexes with a stoichiometry identical to that in non-heme diiron enzymes, with four carboxylates and two neutral donors (L).[7,49,57-59] Examples of these carboxylate ligands are shown in Chart 1.2. The hydrophobic shield that is provided by the backbone mimics the protein environment that encapsulates the enzyme active site and dramatically influences the geometry and hence the dioxygen reactivity of the resulting diiron(II) complexes.

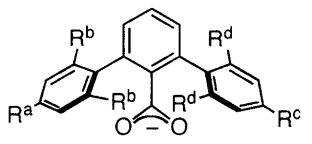

R^a, R^c = CH_3; R^b, R^d = H: $Ar^{Tol}CO_2^-$
R^a, R^c = F; R^b, R^d = H: $Ar^{4\text{-}FPh}CO_2^-$
R^a, R^b, R^c, R^d = CH_3: $Ar^{Mes}CO_2^-$
R^b = CH_3; R^a, R^c, R^d = H: $Ar^{Ph,Xyl}CO_2^-$

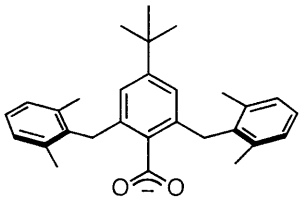

$dxlCO_2^-$

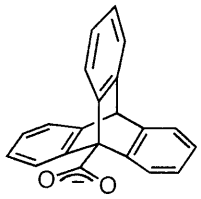

$TrpCO_2^-$

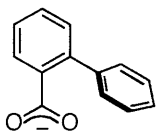

$biphCO_2^-$

Chart 1.2.

The *m*-terphenyl-based carboxylates, 2,6-di(*p*-tolyl)benzoate ($Ar^{Tol}CO_2^-$) and 2,6-di(4-fluorophenyl)benzoate ($Ar^{4\text{-}FPh}CO_2^-$), afford neutral diiron(II) complexes having the general formula $[Fe_2(O_2CR)_4(L)_2]$. An equilibrium between doubly- and quadruply-bridged species was found by variable-temperature solution ^{19}F NMR spectroscopic studies and X-ray crystallography (Chart 1.3).[60] The Fe–Fe distances vary between 3.8 and 4.4 Å in doubly bridged diiron complexes and are reduced to ca. 2.8 Å in quadruply bridged diiron complexes. Several triply bridged diiron species with the general formula $[Fe_2(\mu\text{-}O_2CR)_3(O_2CR)(L)]$ and Fe–Fe distances of 3.2–3.4 Å were also characterized, suggesting possible intermediates in this equilibrium.[60-62] One remarkable observation is the conversion from a paddlewheel to a windmill species induced by the binding of two water molecules.[63,64] The introduction of electron-poor donor ligands, such as 4-cyano- and 4-acetylpyridine facilitated the synthesis of colored diiron(II) complexes by shifting the ligand-to-metal charge-transfer (LMCT) band into the visible region of the absorption spectrum.[65] With these compounds, it was possible to study the effect of water on the oxygenation rate by stopped-flow spectroscopy; the rate of oxygenation increases by a factor of 10 in the presence of water when compared to the reactivity of the anhydrous analog.[65,66] Differences in the rate of oxygenation due to carboxylate shifts is a significant discovery that has important implications for understanding the mechanism of dioxygen activation at non-heme diiron sites. The ability of diiron complexes with tolyl- and 4-fluorophenyl-substituted *m*-terphenyl carboxylates to provide carboxylate shifts is extraordinary and can be attributed to the rotational

flexibility of these substituents as compared to those with mesityl-substituents (vide infra), which are less accommodating.

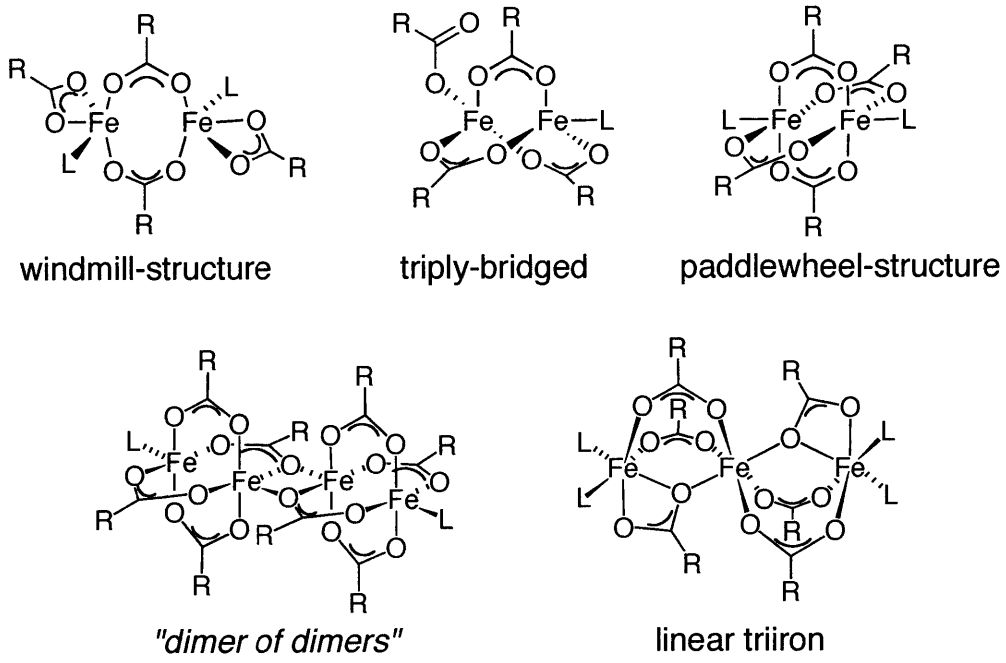

Chart 1.3. Oligonuclear structural motifs in carboxylate-rich diiron(II) complexes containing a $\{Fe_n(O_2CR)_{2n}\}$ core.

The 2,6-dimesitylbenzoate ligand ($Ar^{Mes}CO_2^-$) facilitates the formation of a diiron windmill compound, $[Fe_2(\mu\text{-}O_2CAr^{Mes})_2(O_2CAr^{Mes})_2(MeCN)_2]$, that can dissociate into mononuclear species upon addition of various pyridine donors.[59] The less sterically demanding, asymmetric *m*-terphenyl carboxylate ligand $Ar^{Ph,Xyl}CO_2^-$ was introduced with the intention of synthesizing doubly bridged diiron(II) complexes with short Fe–Fe distances.[62] As predicted, the M–M distances shortened to 3.36 Å (vide supra). In combination with 2,6-di(*p*-tolyl)benzoate ligands ($Ar^{Tol}CO_2^-$), the first diiron complexes with mixed carboxylates were synthesized, with a general formula $[Fe_2(\mu\text{-}$

$O_2CAr^{Tol})_2(O_2CAr^{Ph,Xyl})_2(MeCN)_2]$, in which the bridging 2,6-di-(*p*-tolyl)benzoate prevents a shortening of the Fe–Fe distances.

The benzyl-substituted benzoate ligand $dxlCO_2^-$ was designed to ease steric crowding around the dimetal center and provide more structural flexibility. Diiron paddlewheel complexes, however, were exclusively observed in the solid state.[67] The same trend is observed for the recently introduced triptycene carboxylate ligand ($TrpCO_2^-$).[68] Here, the stability of the paddlewheel diiron(II) complexes was tested by adding either sterically hindered neutral donors or excess water, but neither a carboxylate shift nor dissociation of the dinuclear core was observed. Instead, a systematic lengthening of the Fe–Fe distance up to values of 3.007(2) Å, the longest so far reported for diiron paddlewheel compounds, resulted in proportion to the steric bulkiness of the neutral donor ligand. X-ray structural analysis reveals an interlocking geometry for the triptycene units, which stabilizes the diiron core. Studies with the less bulky biphenyl carboxylate ($biphCO_2^-$) facilitated the synthesis of iron clusters of higher nuclearity.[69] Here, linear triiron(II) and tetrairon(II) (*"dimer of dimers"*) assemblies were observed, which could be converted into paddlewheel complexes by addition of strong *N*-donors, such as pyridine and 1-methylimidazole.[69] The tetranuclear complex revealed an unprecedentedly strong association between the two diiron units through the anti lone pairs of the bridging oxygen atoms of the carboxylates. The introduction of sterically encumbering or dinucleating neutral donors to any of these carboxylate-bridged clusters generally results in the formation of mononuclear complexes.[68-73]

Diiron(II) complexes of the type $[Fe_2(O_2CAr^{Tol})_4(L)_2]$ (L = 4-^{t}BuPy and Py, for example) formed a deep green solution with dioxygen at –78 °C in non-coordinating solvents (CH_2Cl_2, toluene).[57,74] Detailed analyses of the oxygenated product confirmed the presence of an equal mixture of the quadruply bridged diiron(II,III)[75] and a diiron(III,IV)[76] species. The proposed reaction pathway of formation is outlined in Scheme 1.2. Initially, a peroxodiiron(III) species forms in the reaction of the diiron(II) complex with dioxygen, which may convert to a high-valent diiron(IV) species. The latter acts as one-electron oxidant towards the diiron(II) starting material, which leads to the formation of a 1:1 mixture of the two mixed-valent species. The diiron(III,IV) species effects the oxidation of phenol substrates: this process closely resembles the mechanism in RNR-R2, in which the diiron(III,IV) intermediate X oxidizes a neighboring tyrosine residue.[42]

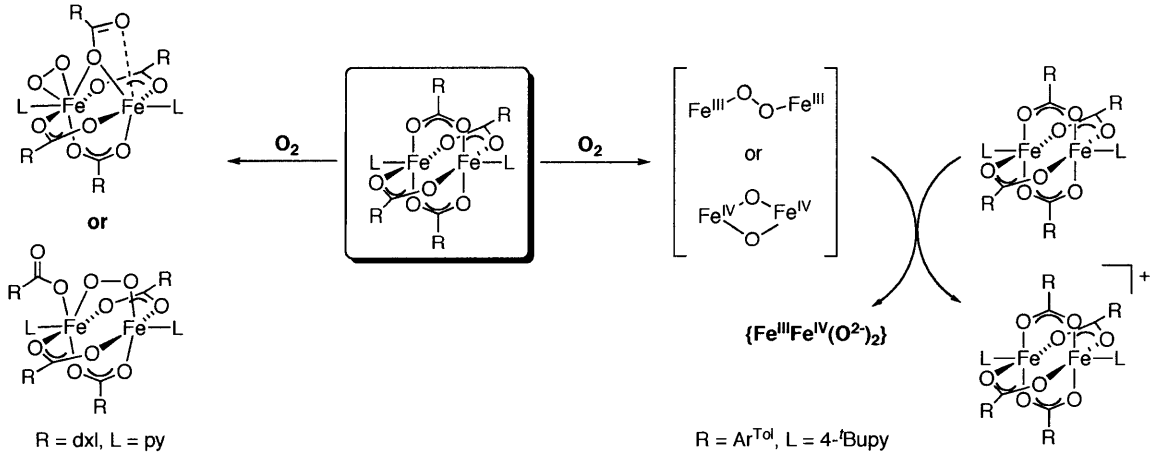

Scheme 1.2.

Oxygenation reactions with $[Fe_2(\mu\text{-}O_2CAr^{Mes})_2(O_2CAr^{Mes})_2(MeCN)_2]$ at low temperatures yielded a purple-colored intermediate, which was spectroscopically

assigned as a symmetric peroxo-bridged species.[58] The quadruply bridged diiron(II) complex with $dxlCO_2^-$, $[Fe_2(\mu\text{-}O_2Cdxl)_4(py)_2]$, reacted with dioxygen to generate an asymmetrically bound peroxo species. Two possible structures were suggested by spectroscopic analysis (Scheme 1.2).[67]

Tethered Substrates

Generally, the ability of an oxygenated diiron species to transfer an O–atom is determined by examining its reaction toward external substrates.[4,77,78] This reaction has not yet been achieved with carboxylate-rich diiron complexes, possibly due to restricted access of the substrate due to steric encumberance by the ligands and quenching of the reactive species by an intramolecular electron-transfer (ET) pathway. In order to circumvent this problem, the potential substrate was tethered to ancillary neutral donor ligands. The diiron(II) complex $[Fe_2(\mu\text{-}O_2CAr^{Tol})_2(O_2CAr^{Tol})_2(N,N\text{-}Bn_2en)_2]$ incorporates *N*,*N*-dibenzylethylenediamine, which upon reaction with dioxygen undergoes intramolecular benzylic oxidation, followed by oxidative *N*-dealkylation to afford benzaldehyde (Scheme 1.3).[71,79] A detailed investigation of the mechanism of this reaction, including Hammett analysis and kinetic isotope effects, suggests that it proceeds by a one-electron oxidation of the amine nitrogen atom, followed by an α-H atom abstraction and subsequent oxygen rebound.[80,81] This study was extended to include benzyl- and ethyl- substituted pyridines and anilines,[82,83] and *N*-donors where the benzylic position was substituted with a sulfide or phosphine functionality.[61,62] The extent of substrate oxidation depends considerably on the proximity of the substrate to

the diiron center. Either no or very little oxidation was observed when the substrate moiety was installed in the meta or para position of the pyridine ligand.[84] The tethering of aromatic substrates did not lead to any oxidation, most likely due to restricted access to the diiron center.[85]

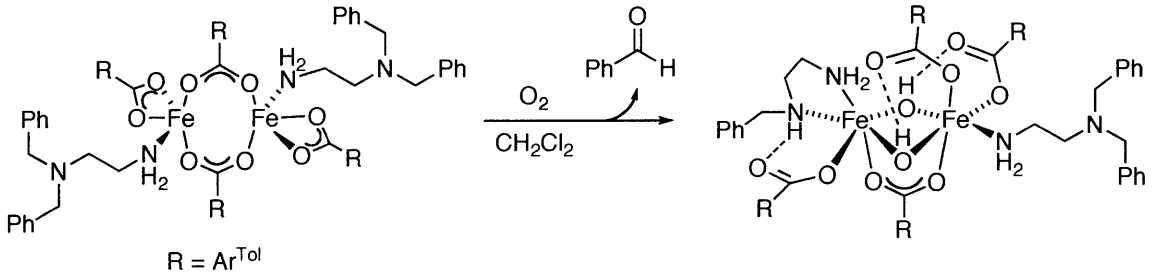

Scheme 1.3.

(ii) Dendrimer Encapsulation of the Diiron Active Site

Significant advances have been made in the synthesis of catalytically active dendrimer complexes as biomimetic analogs of enzymes.[54] Dendrimers have highly branched and organized three-dimensional structures that facilitate the encapsulation of reactive metallocenters. Similar to the protein scaffold in a metalloenzyme, the dendritic shielding creates a distinct microenvironment around the active core, which protects it from unwanted side reactions and controls its reactivity. Dendritically functionalized ligands have been explored extensively to model heme enzymes[86-89] and were recently applied towards understanding non-heme diiron systems. The first dendrimer-derived mimic of a non-heme diiron enzyme contained a triazacyclononane ligand bearing poly(benzylether) dendritic substituents (L_3TACN).[90] The resulting mononuclear iron(II) starting material reacted upon oxygenation to form an oxo-bridged

diiron(III) complex, assigned as $[Fe_2(\mu\text{-}O)(\mu\text{-}OAc)_2(L_3TACN)_2]^{2+}$. Photoirradiation of this complex led to 2-electron reduction and subsequent oxidation to the diiron(III) complex in the presence of dioxygen. In order to prevent deleterious intermolecular ET reactions as observed in compounds with *m*-terphenyl carboxylate ligands (vide supra) and restrict access of solvent molecules to the active site, the basic structure of these ligands was extended with third-generation dendritic poly(benzylether) units.[66] The dendrimer-appended carboxylate, [G-3]-CO_2^-, facilitated the synthesis of doubly bridged diiron(II) complexes with a general formula $[Fe_2(\mu\text{-}O_2C\text{-}[G3])_2(O_2C\text{-}[G3])_2(4\text{-}RPy)_2]$ (R = cyano, pyrrolidino). The hydrophobic shield diminished gas permeability, which resulted in a 300-fold decrease in reaction rate compared with those of the unsubstituted *m*-terphenyl carboxylate-based complexes (Scheme 1.4).[65]

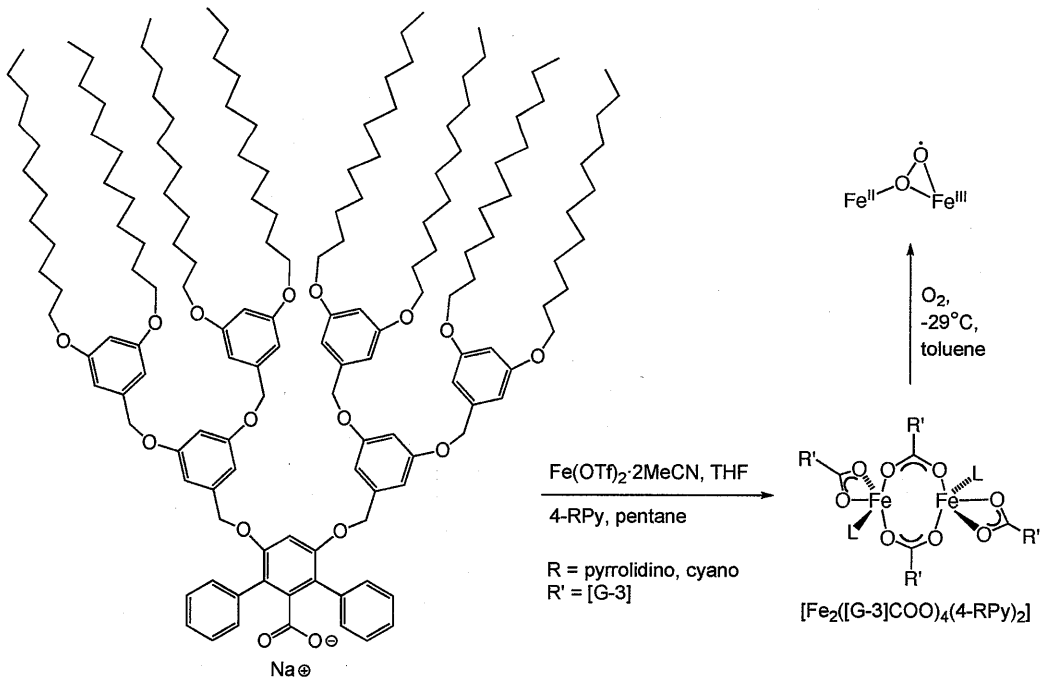

Scheme 1.4.

Unlike the parent compounds, the dendrimer complexes allow the stabilization of a new intermediate upon oxygenation. Mössbauer, UV-vis, EPR, and X-ray absorption spectroscopic studies suggest the formation of a superoxodiiron(II,III) species. This intermediate was stable at temperatures below –5 °C, which can be accounted for by the protective shell of the dendrimer. Preliminary studies also revealed the oxidation of external substrates by this oxygenated product.

B. Nitrogen-Rich Ligand Systems

(i) Ligands Based on Tris(picolyl)amine

Although they do not resemble the coordination environment in carboxylate-bridged non-heme diiron enzymes, a successful strategy to model the active site of these enzymes is based on the use of chelating nitrogen-rich capping ligands. These molecules facilitate the assembly of diiron(II) and diiron(III) complexes with oxo, hydroxo, and carboxylato bridging ligands.

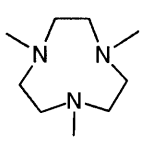

Me_3tacn

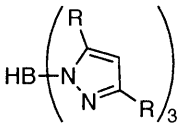

R = H: $HBpz_3$
R = ^{i}Pr: $HB(3,5\text{-}^iPr_2pz)_3$

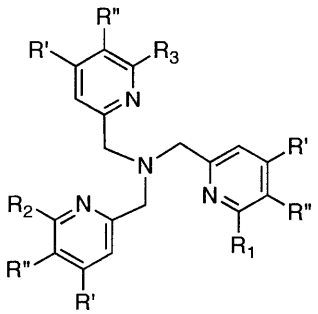

R, R', R" = H: TPA
R, R" = H; R = CH_3: 6-Me_3-TPA
R, R' = H; R" = CH_3: 5-Me_3-TPA
R, R' = H; R" = C_2H_5: 5-Et_3-TPA
R, R", R_1, R_2 = H; R_3 = CH_3: 6-Me-TPA
R = R' = CH_3; R" = OCH_3

Chart 1.4.

The first synthetic complexes to mimic the reduced state of hemerythrin (Hr) were prepared with triazacyclononane ligands (Chart 1.4).[91] The tris(pyrazolyl)borate framework supported peroxodiiron(III) complexes.[49,53]

Noteworthy is the versatile biomimetic chemistry observed with ligands derived from tris(picolyl)amine (TPA), which have afforded several high-valent diiron core structures relevant to the metalloenzymes of interest.[92] The ligands L = TPA; 5-Me_3-TPA; 5-Et_3-TPA facilitate the formation of diiron(III) complexes of the type $[Fe_2(\mu\text{-}O)(OH)(H_2O)L_2]^{3+}$, which react with hydrogen peroxide at –40 °C to form a deep green species. Spectroscopic, mass spectral[93,94] and X-ray crystallographic[95] analyses implied a mixed-valent di(μ-oxo)diiron(III,IV) species $[Fe^{III}Fe^{IV}(\mu\text{-}O)_2L_2]^{3+}$, with an overall S = 3/2 ground state. In contrast, application of the derivative 6-Me-TPA led to the formation of a diiron(III,IV) intermediate with a unique geometric and electronic structure. Spectroscopic and reactivity studies revealed properties that resemble those of the key biological intermediate, compound X in RNR-R2.[5,42] Here the high spin iron atoms are antiferromagnetically coupled to form an S = 1/2 ground state and one of the oxo groups is bound terminally (Scheme 1.5.A).[96,97] Reactions of the diiron(II) and diiron(III) complexes with the slightly modified ligand 6-Me_3-TPA with dioxyen and hydrogen peroxide, respectively, afforded a (μ-oxo)(μ-peroxo)diiron(III) intermediate as a precursor to this high-valent intermediate.[98,99] Lowering the reaction temperature from –60 to –80 °C in this oxygenation reaction gave rise to end-on bound η^1-superoxo diiron(II,III) and η^1-hydroperoxo diiron(III,III) species, as revealed by resonance Raman spectroscopy.[100] These intermediates are the

precursor states to the (μ-oxo)(μ-peroxo)diiron(III) species (Scheme 1.5.A). In contrast to the peroxo species, which is inert toward 2,4-di-*tert*-butylphenol (DTBP), the superoxo species readily performs a one-electron oxidation on this substrate, suggesting that metal-superoxo species may play an unprecedented role as oxidants in metalloenzymes. Recently, a more electron-donating ligand, tris(4-methoxy-3,5-dimethylpyridyl-2-methyl)amine, was prepared and, for the first time, a diiron(IV) complex with a $[Fe^{IV}_2(\mu\text{-}O)_2]$ core structure, proposed for intermediate Q in sMMOH, was obtained.[101] This species was generated by bulk electrolysis of the di(μ-oxo)diiron(III,IV) precursor $[Fe^{III}Fe^{IV}(\mu\text{-}O)_2L_2]^{3+}$ and characterized by resonance Raman and Mössbauer spectroscopy and extended X-ray absorption fine structure (EXAFS) analysis. In a subsequent study, this diiron(IV) complex was chemically synthesized from a diiron(III) precursor and stoichiometric amounts of hydrogen peroxide and perchloric acid (Scheme 1.5.B).[102] Here, a new diiron(IV) species, with distinct Mössbauer parameters for each iron atom, was observed as a precursor to the di(μ-oxo)diiron(IV) species. EXAFS studies and DFT geometry optimizations suggested a diiron site with a single terminal oxo ligand. It must be noted that, despite their similarity to the proposed structure of intermediate Q in sMMOH, these complexes have a nitrogen-rich ligand set and do not incorporate any carboxylate ligands, which results in low-spin diiron compounds. Therefore, the UV-vis and Mössbauer spectroscopic properties differ significantly from those in the enzyme and the oxidative strength towards substrates is greatly diminished.

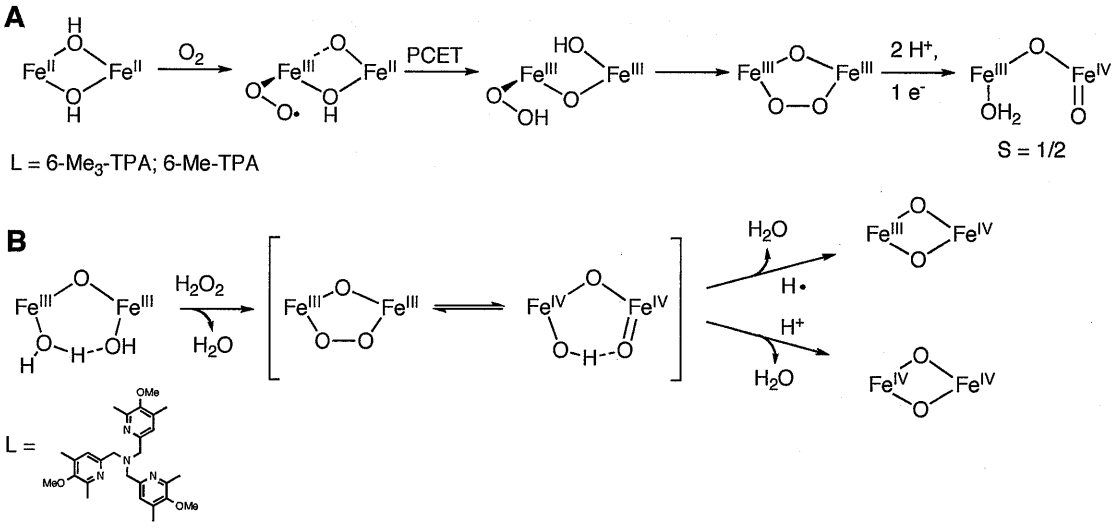

Scheme 1.5.

(ii) Dinucleating Ligands With Alkoxide and Phenoxide Bridges

In order to form kinetically stable diiron complexes, polypyridyl-, polyimidazolyl-, and polybenzimidazolyl-based ligands with a bridging alkoxide or phenoxide group were designed (Chart 1.5).[53,103] These systems chelate two metal centers with Fe–Fe distances of ca. 3.5 Å and have one or two carboxylates bridging the diiron center, as found in the enzyme active sites. Substitution on the pyridine and imidazole units facilitates formation of a cavity that encapsulates the diiron center and prevents the bimolecular decay of oxygenated intermediates. Some of the corresponding diiron(II) complexes exhibit reversible binding of dioxygen to form peroxodiiron(III) species, which were characterized spectroscopically. In the pyridyl series, the peroxide stability increases with increasing donor strength of the pyridine and bridging carboxylate.[104] The stability of two peroxodiiron(III) complexes with benzimidazole- (*N*-Et-HPTB)[105] and imidazole-substituted (HPh-BIMP)[106] ligands

allowed their low temperature crystallization and structural determination. These structures revealed a *cis*-μ-1,2-peroxo coordination mode, buried deep in the cavity. The decomposition of $[Fe_2(\mu\text{-}O_2)(\mu\text{-}O_2CPh)(N\text{-Et-HPTB})]^{2+}$ with an irreversibly bound peroxide has been studied in detail and found to undergo a bimolecular pathway.[107,108] These findings accentuate the importance of a ligand design that protects reactive oxygenated diiron species from this type of decomposition reaction.

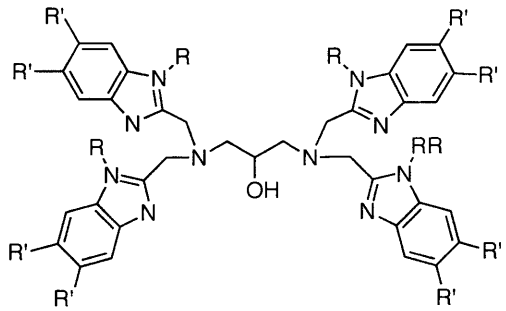

R, R' = H: HPTB
R = EtOH; R' = H: H-EtOH-HPTB
R = H; R' = CH_3: Me_2HPTB
R = Et; R' = H: *N*-Et-HPTB

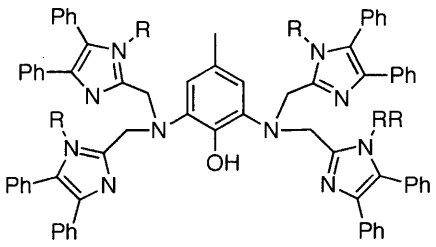

HPh-BIMP

Chart 1.5.

C. Syn *N*-Donor Ligands

Despite the large number of model complexes, a structural feature that none of the previous ligand motifs can rigidly enforce is the syn disposition of the nitrogen donors with respect to the diiron vector present in all carboxylate-bridged non-heme diiron enzymes. Its significance is still unclear, but it is likely that nature did not choose this stereochemistry arbitrarily and that it plays an essential role in dioxygen activation. Recent DFT studies on the intermediate Q of sMMOH suggest that a stereoelectronic effect is born from this configuration

that helps to control the reactivity of this key intermediate.[44] For this reason, we designed and synthesized dinucleating ligands that enforce the desired coordination mode. A requirement of the ligand is that the linker must fix the *N*-donor groups at the correct distance and orientation yet be sufficiently flexible to accommodate different Fe–Fe distances. In addition, the resulting metal complexes should have a carboxylate-rich coordination environment and withstand bimolecular decomposition or oligomerization. To address these challenges, we prepared a series of ligands with a 1,2-diethynylbenzene linker connecting two heterocycles such as pyridines, quinolines, and imidazoles. The facile functionalization of the pyridine substituent allowed the synthesis of a series of ligands with the 1,2-bis(pyridin-3-ylethynyl)benzene moiety.[109,110] This type of ligand has proved to be a useful template for preparing dimetallic complexes with a syn *N*-donor configuration. Interesting structural features were noted upon inspection of dimetallic compounds with this ligand scaffold. The complexes revealed M–M distances that range from 2.54 to 5.17 Å (Figure 1.2), suggesting that this seemingly rigid linker is flexible enough to accommodate changes in the Fe–Fe distance upon reaction with dioxygen.[111-113] Additionally, the diethynylbenzene backbone provides a pocket in which a bridging oxo-group can be accommodated, as may occur in intermediate Q of sMMOH. Finally, functionalization of the pyridine moiety can provide additional protection from bimolecular decomposition, formation of polymers, or *head-to-head* ligand dimerization as observed with PIC_2DET (Figure 1.2, **5**).

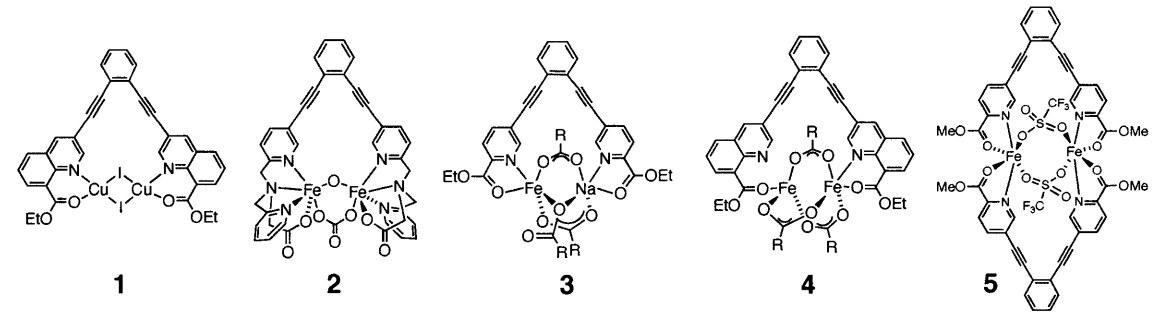

Figure 1.2. Structures of complexes $[Cu_2(Et_2BCQEB^{Et})(\mu\text{-}I)_2]$ (**1**), $[Fe_2(\mu\text{-}O)(\mu\text{-}CO_3)BPG_2DEV]$ (**2**), $[NaFe(PIC_2DET)(O_2CTrp)_3]$ (**3**), $[Fe_2(Et_2BCQEB^{Et})(\mu\text{-}O_2CAr^{Tol})_3]^+$ (**4**), $[Fe_2(\mu\text{-}OTf)_2(PIC_2DET)_2]^{2+}$ (**5**), and comparison of the M–M distances in these compounds.

The structures of several diiron complexes were recently characterized by X-ray crystallography as the first to display syn coordination of two *N*-donors (Figure 1.2). The quinoline-based ligand Et_2BCQEB^{Et} (1,2-bis(3-ethynyl-8-carboxylatequinoline)benzene ethyl ester), afforded a diiron(II) complex, $[Fe_2(Et_2BCQEB^{Et})(\mu\text{-}O_2CAr^{Tol})_3]^+$ (**4**), with three bridging carboxylates.[111] Furthermore, another carboxylate-rich, but heterodinuclear complex, $[NaFe(PIC_2DET)(\mu\text{-}O_2CTrp)_3]$ (**3**), was isolated.[113] The recently introduced H_2BPG_2DEV ligand affords three oxo-bridged diiron(III) complexes, $[Fe_2(\mu\text{-}O)(H_2O)_2BPG_2DEV](ClO_4)_2$, $[Fe_2(\mu\text{-}O)(\mu\text{-}O_2CAr^{iPrO})BPG_2DEV](ClO_4)$, and $[Fe_2(\mu\text{-}O)(\mu\text{-}CO_3)BPG_2DEV]$ (**2**), which form peroxodiiron(III) species upon reaction with hydrogen peroxide.[114] The spectroscopic properties of these intermediates differ significantly from those of related (μ-oxo)(μ-peroxo)diiron(III) species, which may be a result of the rigid scaffold that restrains the diiron distance to shorter values. Finding a correlation between the properties of the peroxo moiety and the Fe–Fe

distances is important for understanding the chemistry of oxygenated intermediates in the enzymes.

III. Conclusions and Perspective

The different types of ligand systems outlined in this chapter highlight the progress that has been made in modeling the active sites of carboxylate-bridged non-heme diiron centers and the challenges that remain. Terphenyl-based carboxylate ligands allow the synthesis of diiron complexes that have the adequate flexibility to perform bio-inspired reactions, but cannot sufficiently stabilize high-valent species. Compounds with dendrimer-appended terphenyl carboxylates protect the diiron core in such a way that allows the isolation of novel oxygenated diiron species. Nitrogen-rich ligand systems have the advantage to stabilize high-valent diiron species, but the iron atoms are in a low-spin rather than a high-spin state, which results in less reactive oxygenated species and non-biomimetic spectral properties. Syn *N*-donor ligands enable incorporation of a more carboxylate-rich system that more accurately resembles the geometry and stoichiometry of the enzyme active sites. This last strategy may allow access of the structural and functional features of dioxygen-activating non-heme diiron enzymes.

Progress towards the goal of understanding the chemistry occurring at the active site of carboxylate-bridged non-heme diiron enzymes by developing structural, functional and spectroscopic models is outlined in this dissertation. Based on previous work on diiron complexes with *m*-terphenyl carboxylate

ligands, the coordination chemistry of the sterically encumbering triptycene carboxylate was explored, as described in Chapter 2. Chapter 3 explores the synthesis and dioxygen reactivity of carboxylate-rich diiron(II) complexes containing phenoxypyridine ligands, which were designed as functional models for aromatic hydroxylation in bacterial multicomponent monoxygenases. The synthesis and characterization of three diiron(III) compounds with a novel syn *N*-donor ligand is described in Chapter 4. This dinucleating ligand system stabilizes a peroxodiiron(III) species having spectroscopic properties relevant to those in peroxo intermediates in non-heme diiron enzymes.

Acknowledgement. Work in our laboratory presented here has been supported over the years by grants from the National Science Foundation and the National Institutes of Health.

References

(1) Holm, R. H.; Kennepohl, P.; Solomon, E. I. *Chem. Rev.* **1996**, *96*, 2239-2314.

(2) Lippard, S. J.; Berg, J. M. *Principles of Bioinorganic Chemistry*; University Science Books: Mill Valley, CA, 1994.

(3) Kurtz, D. M., Jr. *J. Biol. Inorg. Chem.* **1997**, *2*, 159-167.

(4) Feig, A. L.; Lippard, S. J. *Chem. Rev.* **1994**, *94*, 759-805.

(5) Wallar, B. J.; Lipscomb, J. D. *Chem. Rev.* **1996**, *96*, 2625-2657.

(6) Que, L., Jr. *J. Chem. Soc., Dalton Trans.* **1997**, 3933-3940.

(7) Lee, D.; Lippard, S. J. In *Comprehensive Coordination Chemistry II*; McCleverty, J., Meyer, T. J., Eds.; Oxford, U.K., 2003; Vol. 8, pp 309-342.

(8) Jordan, A.; Reichard, P. *Annu. Rev. Biochem.* **1998**, *67*, 71.

(9) Logan, D. T.; Su, X. D.; Åberg, A.; Regnström, K.; Hajdu, J.; Eklund, H.; Nordlund, P. *Structure* **1996**, *4*, 1053-1064.

(10) Stubbe, J. *Curr. Opin. Chem. Biol.* **2003**, *7*, 183-188.

(11) Stubbe, J.; Nocera, D. G.; Yee, C. S.; Chang, M. C. Y. *Chem. Rev.* **2003**, *103*, 2167-2201.

(12) Lindqvist, Y.; Huang, W.; Schneider, G.; Shanklin, J. *EMBO J.* **1996**, *15*, 4081-4092.

(13) Shanklin, J.; Guy, J. E.; Mishra, G.; Lindqvist, Y. *J. Biol. Chem.* **2009**, *284*, 18559-18563.

(14) Harrison, P. M.; Arosio, P. *Biochim. Biophys. Acta* **1996**, *1275*, 161-203.

(15) Hintze, K. J.; Theil, E. C. *Cell. Mol. Life Sci.* **2006**, *63*, 591-600.

(16) Sazinsky, M. H.; Lippard, S. J. *Acc. Chem. Res.* **2006**, *39*, 558-566.

(17) Murray, L. J.; Lippard, S. J. *Acc. Chem. Res.* **2007**, *40*, 466-474.

(18) Rosenzweig, A. C.; Frederick, C. A.; Lippard, S. J.; Nordlund, P. *Nature* **1993**, *366*, 537-543.

(19) Elango, N.; Radhakrishnan, R.; Froland, W. A.; Wallar, B. J.; Earhart, C. A.; Lipscomb, J. D.; Ohlendorf, D. H. *Protein Sci.* **1997**, *6*, 556-568.

(20) Merkx, M.; Kopp, D. A.; Sazinsky, M. H.; Blazyk, J. L.; Müller, J.; Lippard, S. J. *Angew. Chem., Int. Ed.* **2001**, *40*, 2782-2807.

(21) Sazinsky, M. H.; Bard, J.; Di Donato, A.; Lippard, S. J. *J. Biol. Chem.* **2004**, *279*, 30600-30610.

(22) Sazinsky, M. H.; Dunten, P. W.; McCormick, M. S.; Di Donato, A.; Lippard, S. J. *Biochemistry* **2006**, *45*, 15392-15404.

(23) Bollinger, J. M., Jr.; Diao, Y.; Matthews, M. L.; Xing, G.; Krebs, C. *Dalton Trans.* **2009**, 905-914 and references therein.

(24) Kurtz, D. M., Jr. *Dalton Trans.* **2007**, 4115-4121 and references therein.

(25) Schlichting, I.; Berendzen, J.; Chu, K.; Stock, A. M.; Maves, S. A.; Benson, D. E.; Sweet, R. M.; Ringe, D.; Petsko, G. A.; Sligar, S. G. *Science* **2000**, *287*, 1615-1622.

(26) Momenteau, M.; Reed, C. A. *Chem. Rev.* **1994**, *94*, 659-698.

(27) Hwang, J.; Krebs, C.; Huynh, B. H.; Edmondson, D. E.; Theil, E. C.; Penner-Hahn, J. E. *Science* **2000**, *287*, 122-125.

(28) Pereira, A. S.; Small, W.; Krebs, C.; Tavares, P.; Edmondson, D. E.; Theil, E. C.; Huynh, B. H. *Biochemistry* **1998**, *37*, 9871-9876.

(29) Moënne-Loccoz, P.; Krebs, C.; Herlihy, K.; Edmondson, D. E.; Theil, E. C.; Huynh, B. H.; Loehr, T. M. *Biochemistry* **1999**, *38*, 5290-5295.

(30) Moënne-Loccoz, P.; Baldwin, J.; Ley, B. A.; Loehr, T. M.; Bollinger, J. M. *Biochemistry* **1998**, *37*, 14659-14663.

(31) Bollinger, J. M., Jr.; Krebs, C.; Vicol, A.; Chen, S.; Ley, B. A.; Edmonson, D. E.; Huynh, B. H. *J. Am. Chem. Soc.* **1998**, *120*, 1094-1095.

(32) Broadwater, J. A.; Ai, J.; Loehr, T. M.; Sanders-Loehr, J.; Fox, B. G. *Biochemistry* **1998**, *37*, 14664-14671.

(33) Broadwater, J. A.; Achim, C.; Münck, E.; Fox, B. G. *Biochemistry* **1999**, *38*, 12197-12204.

(34) Liu, K. E.; Valentine, A. M.; Wang, D.; Huynh, B. H.; Edmondson, D. E.; Salifoglou, A.; Lippard, S. J. *J. Am Chem. Soc.* **1995**, *117*, 10174-10185.

(35) Liu, K. E.; Valentine, A. M.; Qiu, D.; Edmondson, D. E.; Appelman, E. H.; Spiro, T. G.; Lippard, S. J. *J. Am. Chem. Soc.* **1995**, *117*, 4997-4998; 11134.

(36) Valentine, A. M.; Stahl, S. S.; Lippard, S. J. *J. Am. Chem. Soc.* **1999**, *121*, 3876-3887.

(37) Kim, K.; Lippard, S. J. *J. Am. Chem. Soc.* **1996**, *118*, 4914-4915.

(38) Rinaldo, D.; Philipp, D. M.; Lippard, S. J.; Friesner, R. A. *J. Am. Chem. Soc.* **2007**, *129*, 3135-3147.

(39) Murray, L. J.; García-Serres, R.; Naik, S.; Huynh, B. H.; Lippard, S. J. *J. Am. Chem. Soc.* **2006**, *128*, 7458-7459.

(40) Murray, L. J.; Naik, S. G.; Ortillo, D. O.; García-Serres, R.; Lee, J. K.; Huynh, B. H.; Lippard, S. J. *J. Am. Chem. Soc.* **2007**, *129*, 14500-14510.

(41) Izzo, V.; Tinberg, C. E.; García-Serres, R.; Naik, S.; Huynh, B. H.; Lippard, S. J. Unpublished results.

(42) Stubbe, J.; van der Donk, W. A. *Chem. Rev.* **1998**, *98*, 705-762.

(43) Riggs-Gelasco, P. J.; Shu, L.; Chen, S.; Burdi, D.; Huynh, B. H.; Que, L., Jr.; Stubbe, J. *J. Am. Chem. Soc.* **1998**, *120*, 849-860.

(44) Baik, M.-H.; Gherman, B. F.; Friesner, R. A.; Lippard, S. J. *J. Am. Chem. Soc.* **2002**, *124*, 14608-14615.

(45) Bollinger, J. M., Jr.; Krebs, C. *J. Inorg. Biochem.* **2006**, *100*, 586-605.

(46) Kovaleva, E. G.; Neibergall, M. B.; Chakrabarty, S.; Lipscomb, J. D. *Acc. Chem. Res.* **2007**, *40*, 475-483.

(47) Arakawa, H.; Aresta, M.; Armor, J. N.; Barteau, M. A.; Beckman, E. J.; Bell, A. T.; Bercaw, J. E.; Creutz, C.; Dinjus, E.; Dixon, D. A.; Domen, K.; DuBois, D. L.; Eckert, J.; Fujita, E.; Gibson, D. H.; Goddard, W. A.; Goodman, D. W.; Keller, J.; Kubas, G. J.; Kung, H. H.; Lyons, J. E.; Manzer, L. E.; Marks, T. J.; Morokuma, K.; Nicholas, K. M.; Periana, R.; Que, L., Jr.; Rostrup-Nielson, J.; Sachtler, W. M. H.; Schmidt, L. D.; Sen, A.; Somorjai, G. A.; Stair, P. C.; Stults, B. R.; Tumas, W. *Chem. Rev.* **2001**, *101*, 953-996.

(48) Ibers, J. A.; Holm, R. H. *Science* **1980**, *209*, 223-235.

(49) Tshuva, E. Y.; Lippard, S. J. *Chem. Rev.* **2004**, *104*, 987-1012.

(50) Fontecave, M.; Ménage, S.; Duboc-Toia, C. *Coord. Chem. Rev.* **1998**, *178-180*, 1555-1572.

(51) Lippard, S. J. *Nature* **2002**, *416*, 587.

(52) Kryatov, S. V.; Rybak-Akimova, E. V.; Schindler, S. *Chem. Rev.* **2005**, *105*, 2175-2226.

(53) Du Bois, J.; Mizoguchi, T. J.; Lippard, S. J. *Coord. Chem. Rev.* **2000**, *200-202*, 443-485.

(54) Hecht, S.; Fréchet, J. M. J. *Angew. Chem., Int. Ed.* **2001**, *40*, 74-91.

(55) Calhoun, J. R.; Nastri , F.; Maglio, O.; Pavone, V.; Lombardi, A.; DeGrado, W. F. *Peptide Sci.* **2005**, *80*, 264-278.

(56) Lippard, S. J. *Angew. Chem., Int. Ed.* **1988**, *27*, 344-361.

(57) Lee, D. W.; Lippard, S. J. *J. Am. Chem. Soc.* **1998**, *120*, 12153-12154.

(58) Hagadorn, J. R.; Que, L., Jr.; Tolman, W. B. *J. Am. Chem. Soc.* **1998**, *120*, 13531-13532.

(59) Tolman, W. B.; Que, L., Jr. *J. Chem. Soc., Dalton Trans.* **2002**, *5*, 653-660.

(60) Lee, D.; Lippard, S. J. *Inorg. Chem.* **2002**, *41*, 2704-2719.

(61) Carson, E. C.; Lippard, S. J. *Inorg. Chem.* **2006**, *45*, 837-848.

(62) Reisner, E.; Abikoff, T. C.; Lippard, S. J. *Inorg. Chem.* **2007**, *46*, 10229-10240.

(63) Yoon, S.; Lippard, S. J. *J. Am Chem. Soc.* **2004**, *126*, 16692-16693.

(64) Yoon, S.; Kelly, A. E.; Lippard, S. J. *Polyhedron* **2004**, *23*, 2805-2812.

(65) Yoon, S.; Lippard, S. J. *J. Am Chem. Soc.* **2005**, *127*, 8386-8397.

(66) Zhao, M.; Song, D.; Lippard, S. J. *Inorg. Chem.* **2006**, *45*, 6323-6330.

(67) Chavez, F. A.; Ho, R. Y. N.; Pink, M.; Young, V. G., Jr.; Kryatov, S. V.; Rybak-Akimova, E. V.; Andres, H.; Münck, E.; Que, L., Jr.; Tolman, W. B. *Angew. Chem., Int. Ed.* **2002**, *41*, 149-152.

(68) Friedle, S.; Kodanko, J. J.; Fornace, K. L.; Lippard, S. J. *J. Mol. Struct.* **2008**, *890*, 317-327.

(69) Reisner, E.; Telser, J.; Lippard, S. J. *Inorg. Chem.* **2007**, *46*, 10754-10770.

(70) Lee, D.; DuBois, J. L.; Pierce, B.; Hedman, B.; Hodgson, K. O.; Hendrich, M. P.; Lippard, S. J. *Inorg. Chem.* **2002**, *41*, 3172-3182.

(71) Lee, D.; Lippard, S. J. *J. Am. Chem. Soc.* **2001**, *123*, 4611-4612.

(72) Friese, S. J.; Kucera, B. E.; Que, L., Jr.; Tolman, W. B. *Inorg. Chem.* **2006**, *45*, 8003-8005.

(73) Hagadorn, J. R.; Que, L., Jr.; Tolman, W. B. *Inorg. Chem.* **2000**, *39*, 6086-6090.

(74) Lee, D.; Du Bois, J.; Petasis, D.; Hendrich, M. P.; Krebs, C.; Huynh, B. H.; Lippard, S. J. *J. Am. Chem. Soc.* **1999**, *121*, 9893-9894.

(75) Lee, D.; Krebs, C.; Huynh, B. H.; Hendrich, M. P.; Lippard, S. J. *J. Am. Chem. Soc.* **2000**, *122*, 5000-5001.

(76) Lee, D.; Pierce, B.; Krebs, C.; Hendrich, M. P.; Huynh, B. H.; Lippard, S. J. *J. Am. Chem. Soc.* **2002**, *124*, 3993-4007.

(77) Costas, M.; Chen, K.; Que, L., Jr. *Coord. Chem. Rev.* **2000**, *200-202*, 517-544.

(78) Que, L., Jr.; Tolman, W. B. *Nature* **2008**, *455*, 333-340.

(79) Lee, D.; Lippard, S. J. *Inorg. Chem.* **2002**, *41*, 827-837.

(80) Yoon, S.; Lippard, S. J. *Inorg. Chem.* **2003**, *42*, 8606-8608.

(81) Yoon, S.; Lippard, S. J. *Inorg. Chem.* **2006**, *45*, 5438-5446.

(82) Carson, E. C.; Lippard, S. J. *Inorg. Chem.* **2006**, *45*, 828-836.

(83) Carson, E. C.; Lippard, S. J. *J. Inorg. Biochem.* **2006**, *100*, 1109-1117.

(84) Carson, E. C.; Lippard, S. J. *J. Am. Chem. Soc.* **2004**, *126*, 3412-3413.

(85) Friedle, S.; Lippard, S. J. Unpublished results.

(86) Jiang, D.-L.; Aida, T. *Chem. Commun.* **1996**, 1523-1524.

(87) Jiang, D.-L.; Aida, T. *J. Macromol. Sci., Pure Appl. Chem.* **1997**, *A34*, 2047-2055.

(88) Collman, J. P.; Fu, L.; Zingg, A.; Diederich, F. *Chem. Commun.* **1997**, 193-194.

(89) Zingg, A.; Felber, B.; Gramlich, V.; Fu, L.; Collman, J. P.; Diederich, F. *Helv. Chim. Acta* **2002**, *85*, 333-351.

(90) Enomoto, M.; Aida, T. *J. Am. Chem. Soc.* **2002**, *124*, 6099-6108.

(91) Hartman, J. A. R.; Rardin, R. L.; Chaudhuri, P.; Pohl, K.; Wieghardt, K.; Nuber, B.; Weiss, J.; Papaefthymiou, G. C.; Frankel, R. B.; Lippard, S. J. *J. Am. Chem. Soc.* **1987**, *109*, 7387-7396.

(92) Que, L., Jr.; Tolman, W. B. *Angew. Chem., Int. Ed.* **2002**, *41*, 1114-1137.

(93) Leising, R. A.; Brennan, B. A.; Que, L., Jr.; Fox, B. G.; Münck, E. *J. Am. Chem. Soc.* **1991**, *113*, 3988-3990.

(94) Dong, Y.; Fujii, H.; Hendrich, M. P.; Leising, R. A.; Pan, G.; Randall, C. R.; Wilkinson, E. C.; Zang, Y.; Que, L., Jr. *J. Am. Chem. Soc.* **1995**, *117*, 2778-2792.

(95) Hsu, H.-F.; Dong, Y.; Shu, L.; Young, V. G.; Que, L., Jr. *J. Am. Chem. Soc.* **1999**, *121*, 5230-5237.

(96) Dong, Y.; Que, L. J.; Kauffmann, K.; Münck, E. *J. Am. Chem. Soc.* **1995**, *117*, 11377-11378.

(97) Zheng, H.; Yoo, S. J.; Münck, E.; Que, L., Jr. *J. Am. Chem. Soc.* **2000**, *122*, 3789-3790.

(98) MacMurdo, V. L.; Zheng, H.; Que, L., Jr. *Inorg. Chem.* **2000**, *39*, 2254-2255.

(99) Dong, Y.; Zang, Y.; Shu, L.; Wilkinson, E. C.; Que, L., Jr.; Kauffmann, K.; Münck, E. *J. Am. Chem. Soc.* **1997**, *119*, 12683-12684.

(100) Shan, X.; Que, L., Jr. *Proc. Natl. Acad. Sci. U.S.A.* **2005**, *102*, 5340-5345.

(101) Xue, G.; Wang, D.; De Hont, R.; Fiedler, A. T.; Shan, X.; Münck, E.; Que, L., Jr. *Proc. Natl. Acad. Sci. U.S.A.* **2007**, *104*, 20713-20718.

(102) Xue, G.; Fiedler, A. T.; Martinho, M.; Münck, E.; Que, L., Jr. *Proc. Natl. Acad. Sci. U.S.A.* **2008**, *105*, 20615-20620.

(103) Suzuki, M. *Pure Appl. Chem.* **1998**, *70*, 955-960.

(104) Hayashi, Y.; Kayatani, T.; Sugimoto, H.; Suzuki, M.; Inomata, K.; Uehara, A.; Mizutani, Y.; Kitagawa, T.; Maeda, Y. *J. Am. Chem. Soc.* **1995**, *117*, 11220-11229.

(105) Dong, Y.; Yan, S.; Young, J. V. G.; Que, L., Jr. *Angew. Chem., Int. Ed.* **1996**, *35*, 618-620.

(106) Ookubo, T.; Sugimoto, H.; Nagayama, T.; Masuda, H.; Sato, T.; Tanaka, K.; Maeda, Y.; Ōkawa, H.; Hayashi, Y.; Uehara, A.; Suzuki, M. *J. Am. Chem. Soc.* **1996**, *118*, 701-702.

(107) Feig, A. L.; Becker, M.; Schindler, S.; van Eldik, R.; Lippard, S. J. *Inorg. Chem.* **1996**, *35*, 2590-2601.

(108) Feig, A. L.; Lippard, S. J. *J. Am. Chem. Soc.* **1994**, *116*, 8410-8411.

(109) Kodanko, J. J.; Morys, A. J.; Lippard, S. J. *Org. Lett.* **2005**, *7*, 4585-8.

(110) Reisner, E.; Lippard, S. J. *Eur. J. Org. Chem.* **2008**, *2008*, 156-163.

(111) Kuzelka, J.; Farrell, J. R.; Lippard, S. J. *Inorg. Chem.* **2003**, *42*, 8652-8662.

(112) Kodanko, J. J.; Lippard, S. J. *Inorg. Chim. Acta* **2008**, *361*, 894-900.

(113) Kodanko, J. J.; Xu, D.; Song, D. T.; Lippard, S. J. *J. Am. Chem. Soc.* **2005**, *127*, 16004-16005.

(114) Friedle, S. In *Doctoral Dissertation in Inorganic Chemistry* Massachusetts Institute of Technology: Cambridge, MA, 2009; Chapter 4.

Chapter 2

Triptycenecarboxylate-Bridged Diiron(II) Complexes: Capture of the Paddlewheel Geometric Isomer

This work was previously published: Friedle, S.; Kodanko, J. J.; Fornace, K. L.; Lippard, S. J. *J. Mol. Struct.* **2008**, *890*, 317-327.

Introduction

Dinuclear metal complexes bridged by four carboxylate ligands, such as occurs in the classic paddlewheel "copper acetate" core,[1-3] comprise an extensive class of compounds. More than 1600 structures of this type have been reported.[4] Tetracarboxylate-bridged diiron(II) complexes are relatively rare species, however, with only 25 crystallographically characterized structures reported in the literature to date.[5-8] This small number is not surprising, considering that Fe(II) carboxylate complexes are rather kinetically labile and have a strong tendency to form species of higher nuclearity.[9,10]

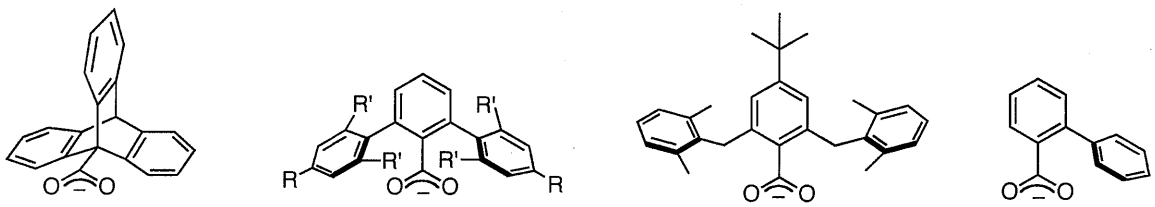

Chart 2.1

Tetracarboxylate-bridged diiron(II) complexes with sterically encumbered carboxylate ligands have been prepared in order to model enzyme active sites, examples of which are displayed in Chart 2.1. The Fe(II) coordination chemistry of these carboxylates has been investigated with the aim of synthesizing model complexes for the active sites of such carboxylate-bridged diiron metalloproteins[11-14] as soluble methane monooxygenase (sMMOH),[15,16] ribonucleotide reductase (RNR-R2),[17-19] stearoyl-acyl carrier protein (ACP) Δ^9-desaturase (Δ^9D),[20,21] and toluene monooxygenase (ToMOH).[22,23] The active

sites of these enzymes share the following structural features: two iron atoms coordinated by four carboxylates from either glutamate and/or aspartate and two *N*-donor ligands from histidines. However, they differ in the carboxylate coordination mode, metal ion coordination number, and the presence of additional ligands, such as water or hydroxide ion.

The steric requirements of these sterically demanding carboxylate ligands determine the geometry of the resulting diiron(II) compounds and significantly influence their reactivity. Discrete diiron(II) tetracarboxylate compounds, which have the same ligand stoichiometry as the enzymes, can be obtained from an Fe(II) source and an *m*-terphenyl-derived carboxylate $^{-}O_2CAr^{R}$ (R = Tol, 4-FPh, Mes) or the dixylyl-substituted benzoates $^{-}O_2Cdxl$ in an efficient self-assembly process.[24] Despite the similarity of the carboxylate ligand structures, the resulting diiron(II) complexes differ in their solid-state geometries, forming either doubly (windmill) or quadruply (paddlewheel) bridged species. Moreover, the physical properties and reactivities of these complexes vary. The compounds with $^{-}O_2CAr^{R}$ (R = Tol, 4-FPh) undergo dynamic carboxylate shifts between the windmill and paddlewheel forms in solution (Scheme 2.1),[25] whereas those with $^{-}O_2CAr^{Mes}$ are trapped in the doubly bridged windmill conformation.[26] The former ligand also facilitates formation of triply bridged diiron(II) complexes with bulkier neutral ligands.[25] The Fe–Fe distances range between 2.7 and 4.3 Å for the doubly, triply, and quadruply bridged species. The selective addition of stoichiometric amounts of water affects the stereochemistry of dinuclear complexes and also yields doubly bridged complexes with two additional bridging

water molecules.[27-29] The carboxylate ligand $^{-}O_2$Cdxl facilitates formation of paddlewheel diiron(II) complexes, which can undergo carboxylate shifts in reactions with dioxygen to form stable diiron(III) peroxo intermediates, revealing a flexibility of the paddlewheel core.[8] The sterically less hindered biphenylcarboxylate ligand ($^{-}O_2$Cbiph), which is asymmetric, preferentially forms tetranuclear iron(II) complexes. These oligomers, however, can disassemble when *N*-donors are added to form either linear trinuclear iron(II) or paddlewheel diiron(II) species.[30] Scheme 2.1 summarizes the structural conformations and transformations that these iron-carboxylate compounds can undergo.

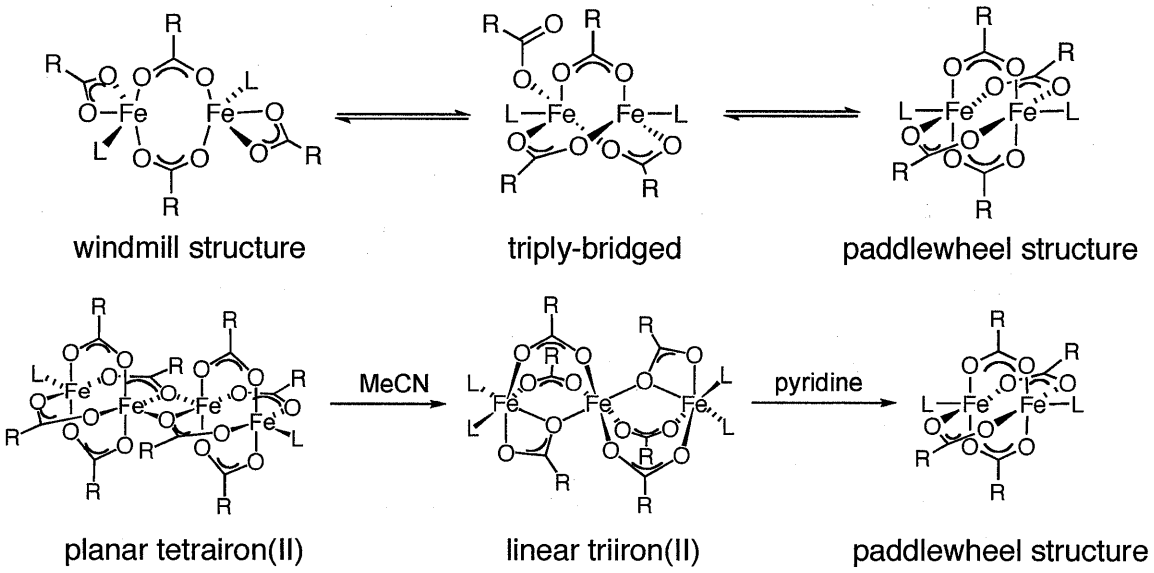

Scheme 2.1.

In this chapter, the synthesis and characterization of quadruply bridged diiron(II) complexes with the general formula $[Fe_2(\mu\text{-}O_2CTrp)_4(L)_2]$, bearing four bridging 9-triptycenecarboxylates ($^{-}O_2$CTrp) and two terminal neutral donor ligands (L), is described. These complexes are noteworthy for their stability with

respect to disassembly or rearrangement of the diiron(II) paddlewheel core. Introduction of pyridine ligands with electron-withdrawing groups, such as 4-cyano- or 4-acetylpyridine, results in compounds with red-shifted absorption bands that facilitate the study of solvent-dependent thermochromism in coordinating solvents. The disassembly of paddlewheel complexes into mononuclear species by addition of sterically demanding or chelating neutral or anionic donor ligands is also described.

Experimental Section

General Procedures and Methods. Tetrahydrofuran (THF), diethyl ether (Et_2O), pentane, toluene, and dichloromethane (CH_2Cl_2) were saturated with nitrogen and purified by passage through activated alumina columns under an argon atmosphere. Anhydrous 1,2-dichloroethane (DCE), 1,2-dimethoxyethane (DME), and chlorobenzene were purchased from Aldrich. The 9-triptycenecarboxylate (HO_2CTrp) was prepared by a modification of literature procedures[31,32] and the corresponding sodium salt was synthesized by allowing the acid to react with a stoichiometric amount of NaOH in MeOH. $Fe(OTf)_2 \cdot 2MeCN$ was prepared by a reported method.[33] The synthesis of 1-Et-2-^{i}PrIm has been reported previously,[34] but a different synthetic route was followed here. All other reagents were obtained from commercial sources and used as received unless otherwise noted. Air-sensitive manipulations were performed by using Schlenk techniques or under a nitrogen atmosphere in an MBraun glovebox.

Physical Measurements. ^{1}H NMR spectra were recorded on a Varian 300 spectrometer in the Massachusetts Institute of Technology Department of Chemistry Instrument Facility (MIT DCIF). Chemical shifts were referenced to the residual solvent peaks. All spectra were recorded at ambient probe temperature. FT-IR spectra were measured on a Thermo Nicolet Avatar 360 spectrometer with OMNIC software. UV-vis spectra were obtained on a Hewlett-Packard 8453 diode-array spectrophotometer under anaerobic conditions. The temperature was controlled with an Oxford ITC 601 cryostat during variable temperature UV-vis studies. Melting points were acquired on an electrothermal Mel-Temp melting point apparatus. When a compound was prepared by two methods, the composition of the material synthesized by the alternative method was confirmed by a unit cell determination of crystalline material and by IR spectroscopy. Mössbauer spectra were obtained on an MS1 spectrometer (WEB Research Co.) with a ^{57}Co source in a Rh matrix maintained at room temperature. Solid samples of **1**, **8**, **9**, and **13** were prepared by suspending ca. 25 μmol of pulverized crystalline material in Apiezon N grease and loading the suspension into a nylon sample holder. All data were collected at 4.2 K and the isomer shift (δ) values are reported with respect to natural iron foil that was used for velocity calibration at room temperature. The spectra were fit to Gaussian lines by using the WMOSS plot and fit program.[35]

1-Ethyl-2-isopropyl-imidazole (1-Et-2-^{i}PrIm). To a suspension of NaH (0.350 g, 14.5 mmol) in 30 mL of dry THF under an argon atmosphere was added 2-isopropylimidazole (1.50 g, 13.6 mmol) in small portions. The resulting

reaction mixture was allowed to stir for 30 min. Ethyl iodide (1.16 mL, 14.5 mmol) was added dropwise to the pale yellow suspension over a period of 5 min and stirred for another hour. After removal of the solvent, water and CH_2Cl_2 (each 50 mL) were added. The organic phase was separated, washed with water (2 x 20 mL), and the combined organic layers were dried with Na_2SO_4. The crude material was purified on alumina using EtOAc/CH_2Cl_2 (2:1) to yield 1-Et-2-^{i}PrIm as pale yellow oil. Yield: 1.15 g (61%). ^{1}H NMR (300 MHz, $CDCl_3$) δ: 6.96 (s, 1H), 6.81 (s, 1H), 3.91 (q, 2H), 2.99 (m, 1H), 1.34 (m, 9H). FT-IR (cm^{-1}, film on NaCl): 3103 (w), 2972 (s), 2931 (m), 2870 (m), 1519 (w), 1491 (s), 1441 (m), 1381 (m), 1361 (w), 1332 (w), 1273 (s), 1185 (w), 1155 (m), 1088 (w), 1070 (m), 1054 (w), 962 (w), 923 (w), 749 (w), 719 (m). ESI-MS (*m/z*, MeOH/DCM): Calcd. for $C_8H_{15}N_2$ $[M+H]^+$: 139.1 Found: 139.0.

1-Propyl-2-isopropyl-imidazole (1-Pr-2-^{i}PrIm). This compound was prepared by a procedure analogous to that for 1-ethyl-2-isopropyl-imidazole, except that *n*-propyl iodide was added instead of ethyl iodide. The product was purified on alumina (EtOAc/$CHCl_3$, 1:1) to yield 1-Pr-2-^{i}PrIm as a colorless oil. Yield: 1.15 g (56%). ^{1}H NMR (300 MHz, $CDCl_3$) δ: 6.88 (s, 1H), 6.72 (s, 1H), 3.75 (t, 2H), 2.93 (m, 1H), 1.70 (m, 2H), 1.26 (m, 6H), 0.88 (t, 3H). FT-IR (cm^{-1}, film on NaCl): 3106 (w), 2968 (s), 2933 (m), 2877 (m), 1517 (w), 1490 (m), 1467 (m), 1440 (m), 1383 (w), 1359 (w), 1329 (w), 1275 (m), 1156 (w), 1133 (w), 1096 (w), 1071 (m), 926 (w), 798 (w), 748 (w), 722 (m). ESI-MS (*m/z*, MeOH/DCM): Calcd. for $C_9H_{17}N_2$ $[M+H]^+$: 153.1 Found: 153.0.

1-Propyl-2-phenyl-imidazole (1-Pr-2-PhIm). This compound was prepared by a procedure analogous to that for 1-ethyl-2-isopropyl-imidazole, except that *n*-propyl iodide was added instead of ethyl iodide. Purification on alumina (EtOAc/$CHCl_3$, 1:1) yielded 1-propyl-2-phenyl-imidazole as a yellow oil. ^1H NMR (300 MHz, $CDCl_3$) δ: 7.57 (m, 2H), 7.44 (m, 3H), 7.14 (s, 1H), 7.03 (s, 1H), 3.97 (t, 2H), 1.78 (m, 2H), 0.89 (t, 3H). FT-IR (cm^{-1}, film on NaCl): 3103 (m), 3063 (m), 2965 (s), 2934 (m), 2876 (m), 1605 (w), 1498 (m), 1474 (s), 1418 (s), 1384 (m), 1350 (w), 1272 (s), 1139 (m), 1101 (w), 1074 (m), 1018 (w), 917 (m), 801 (w), 773 (s), 744 (m), 700 (s), 680 (w). ESI-MS (*m/z*, MeOH/DCM): Calcd. for $C_{12}H_{15}N_2$ $[M+H]^+$: 187.1 Found: 187.0.

$[Fe_2(\mu\text{-}O_2CTrp)_4(THF)_2]$ (1a). Method A. A portion of NaO_2CTrp (845 mg, 2.64 mmol) in THF (20 mL) was added to a solution of $[Fe(H_2O)_6](BF_4)_2$ (446 mg, 1.32 mmol) in THF (30 mL) and the reaction mixture was stirred for 1 d in the presence of molecular sieves (4 Å). The suspension was filtered and the solvent removed to yield a dark pink microcrystalline solid. The crude material was recrystallized from CH_2Cl_2/THF/pentane to yield colorless blocks of **1a** and pink-brown crystals of the side-product **1b**, both suitable for X-ray crystallographic analysis. Yield: 517 mg (54%). **Method B.** A solution of NaO_2CTrp (50 mg, 156 μmol) in THF (5 mL) was added dropwise to a rapidly stirred THF solution (5 mL) of $Fe(OTf)_2{\cdot}2MeCN$ (33 mg, 76 μmol). The resulting pale yellow solution was stirred overnight. The solvent was removed and the product extracted with CH_2Cl_2 (2 x 5 mL) to yield 26 mg of crude material, which was recrystallized by diffusing pentane into a solution of CH_2Cl_2 that had been layered with THF to

yield colorless crystals (8 mg, 14%) suitable for X-ray crystallography. FT-IR (cm^{-1}, KBr): 3059 (w), 3036 (w), 3015 (w), 2957 (w), 2891 (w), 1612 (s), 1459 (s), 1446 (s), 1408 (s), 1314 (m), 1292 (m), 1178 (m), 1031 (m), 943 (m), 928 (m), 873 (m), 786 (m), 763 (m), 748 (s), 722 (m), 687 (m), 648 (m), 626 (s), 609 (m). Anal. Calcd. for **1a**·0.75CH_2Cl_2 ($C_{92.75}H_{69.5}Cl_{1.5}O_{10}Fe_2$): C, 73.83 ; H, 4.61. Found: C, 73.48; H, 4.41. Mp: 240 °C (dec).

[Fe_2(μ-O_2CTrp)$_4$(py)$_2$] (2) A solution of **1** (55 mg, 38 μmol) in chlorobenzene (8 mL) was treated with pyridine (py) (10 μL, 116 μmol) under vigorous stirring. Pale yellow rods of **2** formed after 5 d by introduction of Et_2O into this solution. Block-shaped crystals of **2** suitable for X-ray crystallography were obtained by vapor diffusion of Et_2O into a solution of **2** in DME. Yield: 40 mg (72%). FT-IR (cm^{-1}, KBr): 3059 (w), 2955 (w), 2856 (w), 1618 (s), 1486 (w), 1458 (m), 1447 (s), 1408 (s), 1292 (m), 1218 (w), 1179 (w), 1111 (w), 1083 (w), 1068 (w), 1018 (w), 947 (w), 873 (w), 846 (w), 785 (m), 746 (s), 722 (m), 699 (m), 688 (w), 658 (w), 648 (w), 625 (s), 479 (w), 457 (m), 417 (w). Mp: 235 °C (dec).

[Fe_2(μ-O_2CTrp)$_4$(1-MeIm)$_2$] (3). 1-Methylimidazole (1-MeIm) (14 mg, 220 μmol) was added to a solution of **1** (100 mg, 69 μmol) in toluene (4 mL) and stirred for 1.5 h. The colorless microcrystalline precipitate was isolated by filtration and washed with Et_2O. Colorless block crystals suitable for X-ray crystallography were obtained by vapor diffusion of Et_2O into a solution of **3** in DME. Yield: 67 mg (67%). FT-IR (cm^{-1}, KBr): 3129 (w), 3058 (w), 2956 (w), 1620 (s), 1535 (m), 1458 (m), 1446 (s), 1407 (s), 1287 (m), 1234 (w), 1178 (w), 1142

(w), 1110 (m), 1089 (m), 1032 (w), 947 (w), 873 (w), 786 (w), 749 (s), 721 (m), 688 (w), 658 (w), 648 (w), 625 (s), 610 (w), 481 (w), 464 (w). Mp: 235 °C (dec).

[$Fe_2(\mu\text{-}O_2CTrp)_4(2\text{-MeIm})_2$] (4). This compound was prepared from **1** (100 mg, 69 μmol) and 2-methylimidazole (2-MeIm) (14 mg, 220 μmol) by a procedure analogous to that used for synthesizing **3**. The colorless microcrystalline precipitate of **4** was recrystallized in hot DME followed by vapor diffusion of Et_2O to yield colorless crystals suitable for X-ray crystallography. Yield: 86 mg, (86%). FT-IR (cm^{-1}, KBr): 3383, 3190, 3059, 2957, 1598, 1485, 1458, 1445, 1402, 1287, 1177, 1155, 1128, 1109, 1033, 1016, 874, 806, 786, 750, 722, 688, 646, 625, 610, 482. Mp: 240 °C (dec).

[$Fe_2(\mu\text{-}O_2CTrp)_4(2\text{-}^{i}PrIm)_2$] (5). This compound was prepared from **1** (200 mg, 138 μmol) and 2-isopropylimidazole (2-^{i}PrIm) (34 mg, 440 μmol) by a procedure analogous to that used to obtain **3**. The colorless microcrystalline precipitate of **5** was recrystallized in hot DME followed by vapor diffusion of Et_2O to yield colorless block crystals suitable for X-ray crystallography. Yield: 120 mg (46%). FT-IR (cm^{-1}, KBr): 3403 (w), 3247 (w), 3058 (w), 2955 (w), 2926 (w), 2875 (w), 2818 (w), 1623 (s), 1562 (m), 1458 (s), 1446 (s), 1405 (s), 1291 (m), 1178 (w), 1132 (w), 1092 (m), 1062 (w), 1032 (w), 872 (w), 848 (w), 785 (m), 750 (s), 721 (m), 687 (w), 647 (m), 625 (s), 610 (m), 481 (m), 457 (m). Anal. Calcd. for **5**·1.5$C_4H_{10}O_2$, $C_{102}H_{87}N_4O_{11}Fe_2$: C, 73.96; H, 5.29; N, 3.38. Found: C, 73.81; H, 5.05; N, 3.56. Mp: 225 °C (dec).

[$Fe_2(\mu\text{-}O_2CTrp)_4(2\text{-PhIm})_2$] (6). This compound was prepared from **1** (100 mg, 69 μmol) and 2-phenylimidazole (2-PhIm) (22 mg, 220 μmol) by a procedure

analogous to that used for synthesizing **3**. The colorless microcrystalline precipitate of **6** was recrystallized in hot DME followed by vapor diffusion of Et_2O to yield colorless crystals suitable for X-ray crystallography. Yield: 75 mg (68%). FT-IR (cm^{-1}, KBr): 3136 (w), 3059 (w), 3007 (w), 2954 (w), 2827 (w), 1623 (s), 1458 (s), 1446 (s), 1404 (s), 1290 (m), 1176 (w), 1107 (m), 1086 (m), 1031 (m), 873 (w), 783 (m), 763 (m), 749 (m), 723 (w), 648 (w), 627 (s), 475 (w), 442 (w). Mp: 255 °C (dec).

$[Fe_2(\mu\text{-}O_2CTrp)_4(1\text{-}Et\text{-}2\text{-}^{i}Prlm)_2]$ (7). To a solution of **1** (40 mg, 27 μmol) in DCE (2 mL) was added a solution of 1-Et-2-^{i}PrIm (7.7 mg, 56 μmol) in CH_2Cl_2 (1 mL) and the resulting yellow solution was stirred overnight. After removal of the solvent the residue was recrystallized by vapor diffusion of Et_2O into a solution of chlorobenzene (2 mL) to yield colorless blocks of **7**. FT-IR (cm^{-1}, KBr): 3058 (w), 3031 (w), 3013 (w), 2967 (w), 2868 (w), 1624 (s), 1574 (m), 1477 (m), 1458 (m), 1446 (s), 1404 (s), 1286 (m), 1270 (m), 1177 (w), 1131 (w), 1084 (m), 1031 (m), 869 (w), 783 (m), 746 (s), 722 (m), 683 (m), 647 (w), 626 (s), 607 (w), 490 (w), 480 (w), 467 (w).

$[Fe_2(\mu\text{-}O_2CTrp)_4(1\text{-}Pr\text{-}2\text{-}^{i}Prlm)_2]$ (8) A chlorobenzene (1 mL) solution of **1** (48.4 mg, 33.5 μmol) was combined with a chlorobenzene (1 mL) solution of 1-Pr-2-^{i}PrIm (10 mg, 67 μmol) and the reaction mixture was stirred for 10 min. The resulting deep orange-yellow solution was filtered and subjected to vapor diffusion of pentane to yield colorless blocks of **8** (34 mg, 54%). FT-IR (cm^{-1}, KBr): 3058 (w), 2967 (w), 1622 (s), 1582 (m), 1477 (m), 1457 (m), 1445 (s), 1021 (s), 1290 (m), 1266 (w), 1177 (w), 1157 (w), 1132 (w), 1082 (m), 1032 (m), 1021

(m), 948 (w), 927 (w), 907 (w), 872 (w), 785 (m), 762 (m), 745 (s), 722 (m), 702 (m), 687 (m), 648 (m), 626 (s), 609 (w), 489 (w), 468 (w), 446 (w). Anal. Calcd. for **8**·4C_6H_5Cl, $C_{126}H_{104}Fe_2N_4O_8Cl_4$: C, 73.62; H, 5.10; N, 2.73. Found: C, 73.55; H, 4.92; N, 2.92.

[Fe_2(μ-O_2CTrp)$_4$(1-Pr-2-PhIm)$_2$] (9). A portion of 1-Pr-2-PhIm (30 mg, 160 μmol) was added to a DCE (3 mL) solution of **1** (116 mg, 80 μmol) to form a yellow solution, which was stirred for 10 min. Colorless blocks of **9** (84 mg, 63%), suitable for X-ray crystallography, were obtained by vapor diffusion of pentane into the filtered solution. FT-IR (cm^{-1}, KBr): 3057 (w), 2955 (w), 1624 (s), 1476 (m), 1458 (m), 1446 (s), 1404 (s), 1315 (w), 1285 (w), 1268 (w), 1213 (w), 1177 (w) 1146 (w), 1077 (w), 1033 (w), 1014 (w), 947 (w), 925 (w), 874 (w), 802 (w), 785 (m), 764 (m), 747 (m), 703 (m), 688 (w), 657 (w), 648 (m), 626 (s), 609 (w), 481 (w), 454 (w).

[Fe_2(μ-O_2CTrp)$_4$(4-AcPy)$_2$] (10). Bright red-orange crystals of **10**, suitable for X-ray crystallography, were isolated by vapor diffusion of pentane into a reaction mixture of **1** (60.0 mg, 42.1 μmol) and 4-acetylpyridine (4-AcPy) (10.4 mg, 91.2 μmol) in CH_2Cl_2 (2.5 mL). Yield: 24 mg (37%). FT-IR (cm^{-1}, KBr): 3058 (w), 3015 (w), 2953 (w), 2869 (w), 1701 (m, $\nu_{C=O(acetyl)}$), 1631 (s), 1614 (s), 1557 (m), 1458 (s), 1446 (s), 1407 (s), 1361 (m), 1291 (m), 1264 (m), 1175 (w), 1061 (w), 1033 (w), 1018 (w), 928 (w), 872 (w), 822 (w), 784 (w), 751 (s), 721 (m), 648 (w), 626 (s), 595 (w). UV–vis (CH_2Cl_2) (λ_{max}, nm (ε, M^{-1} cm^{-1})): 450 (1050). Mp: 320 °C (dec).

[$Fe_2(\mu\text{-}O_2CTrp)_4(4\text{-}CNPy)_2$] (11). Method A. Intensely red-orange colored crystals of **11**, suitable for X-ray crystallography, were isolated by vapor diffusion of pentane into a reaction mixture of **1** (80.0 mg, 55.4 μmol) and 4-cyanopyridine (4-CNPy) (11.5 mg, 111 μmol) in CH_2Cl_2 (6 mL). Yield: 49 mg (58%). **Method B.** To a rapidly stirred THF solution (5 mL) of $Fe(OTf)_2 \cdot 2MeCN$ (33 mg, 78 μmol) and NaO_2CTrp (50 mg, 156 μmol) was added dropwise a solution of 4-CNPy (8.1 mg, 78 μmol) in THF (5 mL). The resulting suspension was stirred overnight. The solvent was removed and the product was extracted with CH_2Cl_2 (2 x 3 mL), filtered, and recrystallized from CH_2Cl_2/pentane to yield red-orange colored crystals of **11**. Yield: 34 mg (57%). FT-IR (cm^{-1}, KBr): 3057 (w), 3016 (w), 2954 (w), 2870 (w), 2234 (s, $\nu_{C\equiv N}$), 2070 (w), 1611 (s), 1487 (w), 1458 (m), 1446 (m), 1407 (w), 1291 (m), 1261 (w), 1215 (w), 1178 (w), 1156 (w), 1065 (w), 1031 (w), 1017 (w), 944 (w), 926 (w), 872 (w), 829 (w), 786 (m), 763 (m), 749 (s), 721 (m), 688 (w), 648 (w), 626 (s), 609 (w), 600 (w). UV–vis (CH_2Cl_2) (λ_{max}, nm (ε, M^{-1} cm^{-1})): 475 (1230). Anal. Calcd. for **11**$\cdot 0.75CH_2Cl_2$, $C_{96.75}H_{61.5}N_4O_8Cl_{1.5}Fe_2$: C, 73.88; H, 3.94; N, 3.56. Found: C, 74.15; H, 4.47; N, 3.36. Mp: 315 °C (dec). The presence of residual CH_2Cl_2 was confirmed by ^1H NMR spectroscopy of **11** in $CDCl_3$.

[$Fe_2(\mu\text{-}O_2CTrp)_4(4\text{-}PPy)_2$] (12). Yellow crystals of **12**, suitable for X-ray crystallography, were isolated by vapor diffusion of Et_2O into a reaction mixture of **1** (40 mg, 28 μmol) and 4-pyrrolidinopyridine (4-PPy) (8.2 mg, 56 μmol) in CH_2Cl_2 (2.5 mL). Yield: 24 mg (54%). FT-IR (cm^{-1}, KBr): 3058 (w), 2955 (w), 2858 (w), 1719 (w), 1609 (s), 1532 (m), 1482 (w), 1458 (m), 1446 (m), 1408 (s),

1349 (w), 1316 (w), 1290 (w), 1226 (m), 1178 (w), 1156 (w), 1105 (w), 1033 (w), 1015 (m), 948 (w), 926 (w), 873 (w), 809 (w), 786 (w), 749 (m), 722 (m), 688 (w), 658 (w), 647 (w), 626 (m), 609 (w), 526 (w).

[Fe(O_2CTrp)$_2$(TMEDA)] (13). Method A. A CH_2Cl_2 solution (2 mL) of **1** (60 mg, 42 μmol) was allowed to react with *N,N,N',N'*-tetramethylethylenediamine (TMEDA) (7.5 mg, 84 μmol) for 10 min under stirring. Vapor diffusion of pentane into the pale yellow colored solution afforded colorless blocks of **13**. Yield: 36 mg (57%). **Method B.** To a rapidly stirred THF solution (5 mL) of Fe(OTf)$_2$·2MeCN (34 mg, 78 μmol) and NaO_2CTrp (50 mg, 156 μmol) was added dropwise a solution of TMEDA (9.5 mg, 82 μmol) in THF (5 mL) and the resulting suspension was stirred overnight. The solvent was removed and the product was extracted into CH_2Cl_2 (3 x 3 mL) and recrystallized from CH_2Cl_2/pentane to yield colorless crystals of **13**. Yield: 34 mg (57%). FT-IR (cm^{-1}, KBr): 3060 (w), 3003 (w), 2951 (w), 2848 (w), 2797 (w), 1566 (s), 1459 (s), 1445 (s), 1417 (s), 1400 (s), 1286 (m), 1263 (m), 1176 (m), 1029 (m), 950 (m), 875 (m), 797 (m), 764 (s), 732 (m), 688 (m), 645 (m), 625 (s), 608 (w). Anal. Calcd. for **13**·CH_2Cl_2, $C_{49}H_{44}N_2O_4Cl_2Fe$: C, 69.11; H, 5.21; N, 3.29. Found: C, 68.50; H, 5.18; N, 3.34. Mp: 250 °C (dec).

(^{n}Bu$_4$N)$_2$[Fe(O_2CTrp)$_2$(NCS)$_2$] (14). Colorless block crystals of **14**, suitable for X-ray crystallography, were obtained by vapor diffusion of Et_2O into a filtered, pale yellow reaction mixture of **1** (50 mg, 35 μmol) and tetrabutylammonium thiocyanate (^{n}Bu$_4$N)SCN (38.2 mg, 142 μmol) in CH_2Cl_2 (3 mL) that had been stirred for five min. Yield: 48 mg (55%). FT-IR (cm^{-1}, KBr): 3065 (w), 3014 (w), 2957 (s), 2932 (m), 2873 (m), 2078 (vs, $\nu_{C\equiv N}$), 1584 (s), 1573 (m), 1479 (m),

1458 (m), 1446 (m), 1408 (m), 1379 (m), 1287 (w), 1177 (w), 1152 (w), 1030 (w), 874 (w), 800 (m), 768 (m), 750 (m), 725 (w), 688 (w), 645 (w), 626 (m). Anal. Calcd. for **14**, $C_{76}H_{98}N_4FeO_4S_2$: C, 72.93; H, 7.89; N, 4.48. Found: C, 72.74; H, 7.73; N, 4.48. Mp: 210 °C (dec).

[Fe(O$_2$CTrp)$_2$(2-MeIm)$_2$] (15). Colorless block crystals of **15** (ca. 32 mg), suitable for X-ray crystallography, were obtained from Et_2O vapor diffusion into a reaction mixture of **1** (40 mg, 28 μmol) containing 6.0 equiv of (2-MeIm) (13.6 mg, 166 μmol) in a solution of DME (3 mL).

X-ray Crystallographic Studies. Single crystals were coated with Paratone-N oil, mounted at room temperature on the tips of glass fibers or nylon loops (Oxford magnetic mounting system), and cooled under a stream of cold N_2 maintained by a KRYO-FLEX low-temperature apparatus. Intensity data were collected on a Bruker APEX CCD diffractometer with graphite-monochromated Mo Kα radiation (λ = 0.71073 Å) controlled by a Pentium-based PC running the SMART software package.[36] A total of 2800 frames were acquired for each measurement. The structures were solved by difference Fourier or Patterson methods and refined on F^2 by using the SHELXTL-97 software included in the SHELXTL software package.[37,38] Empirical absorption corrections were applied with SADABS[39] and the structures were checked for higher symmetry with PLATON.[40] All non-hydrogen atoms were refined anisotropically. In general, hydrogen atoms were assigned idealized positions and given thermal parameters equivalent to either 1.5 (methyl hydrogen atoms) or 1.2 (all other hydrogen atoms) times the thermal parameter of the atom to which they were attached.

Crystal data, data collection parameters, and structure refinement details for all compounds are provided in Table A1.1. Bond distances and angles of **2–15** are displayed in Table A1.2, and ORTEP diagrams of the molecular structures of **2–12** are shown in Figures A1.1–A1.11 in Appendix 1.

Complex **1a** crystallizes with seven CH_2Cl_2 molecules per asymmetric unit. The structure of **2** has one DME molecule in the asymmetric unit that is not disordered and a second one that shares a position with an Et_2O molecule. Furthermore, one phenyl ring of a triptycene ligand is disordered and distributed at occupancies of 0.62 and 0.38. Compound **3** crystallizes with two DME molecules in the crystal lattice. Disordered molecules of DME and Et_2O were identified in the crystal lattice of **4**. The methyl group of one DME molecule was distributed over two positions with occupancies of 0.60 and 0.40, and the methoxy group of a second DME molecule was distributed with occupancies of 0.73 and 0.27 and refined. An Et_2O and a DME molecule share one position, with the latter being disordered over two positions. Compound **5** contains disordered DME and Et_2O molecules as well. The oxygen atom of one DME molecule is disordered over two positions with a ratio of 66:34. Another molecule of DME shares one position with an Et_2O molecule in a 56:44 ratio. An Et_2O molecule is present that lies on a center of symmetry and was refined at full occupancy, with the two ethyl groups equally distributed over two positions. An Et_2O molecule is present in the structure of **6**. In addition, an Et_2O and a DME molecule share one position at 0.52 and 0.48 occupancies, respectively. As in the structure of **4**, an Et_2O and a DME molecule share one position with the latter distributed over two

positions. The structures of **7** and **8** each have four chlorobenzene solvent molecules in the lattice. In **7**, one is disordered over two positions and was anisotropically refined at 0.91 and 0.09 occupancy. The structure of **9** contains two molecules of DCE, one being distributed over four positions and refined. Compound **10** has two CH_2Cl_2 molecules in the asymmetric unit, one of which was distributed over two positions with occupancies at 0.62 and 0.38 and refined. Compound **11** contains four CH_2Cl_2 molecules. Two of these have occupancy of 1.0 and are disordered over two positions. The other two have occupancy of 0.25 and are also disordered over two positions. The crystal lattice of **12** contains one molecule of CH_2Cl_2 at full occupancy. Another molecule of CH_2Cl_2 shares one position with a molecule of pentane and is additionally distributed over two positions. The mononuclear complex **13** has one molecule of CH_2Cl_2 in the asymmetric unit. No solvent molecules were located in the crystal structure of **14**. In the crystal structure of **15**, one Et_2O molecule has its ethyl groups disordered over two positions with occupancies of 0.65 and 0.35 and the oxygen atom at full occupancy. Compounds **5**, **7–9**, and **12–15** contain small fractions of brominated $^{-}O_2CTrp$, which cocrystallized with the unbrominated material. This impurity fraction was modeled in these structures.

Reactions with Water. In a typical experiment, a CH_2Cl_2 solution of **1** (20 mg, 14 μmol) was prepared and two equiv of the *N*-donor were added, followed by the addition of a deoxygenated solution of H_2O in THF. The reaction mixture was stirred vigorously, filtered, and subjected either to pentane or Et_2O vapor

diffusion. X-ray quality crystals were taken directly from the reaction vessel for analysis.

A. Reaction of **7** with H_2O. The general protocol described above was followed. Here, 13 equiv of water (1.08 mL, 0.18 mmol, 0.17 M) were added. After stirring for 5 min, the filtered reaction mixture was subjected to pentane vapor diffusion. A small amount of colorless crystals of **7**, suitable for X-ray crystallography, were recovered.

B. Reaction of **12** with H_2O. The general protocol above was followed. To a solution of **1** (20 mg, 14 μmol) in CH_2Cl_2 (1.5 mL) was added 4-PPy (4.1 mg, 28 μmol) and the resulting yellow solution was allowed to react for 5 min. Then, either 70 or 350 equiv of water in THF solution (0.49 mL, 0.98 mmol, 2.0 M or 2.44 mL, 4.65 mmol, 2.0 M) were added, and the resulting solutions were stirred for either 5 min (70 equiv) or 2.5 h (350 equiv), before being subjected to vapor diffusion of Et_2O. Pale yellow blocks with unit cell parameters identical to those of **12** were recovered in both cases.

Results and Discussion

Ligand Synthesis and Metalation; Preparation and Structural Characterization of $[Fe_2(\mu\text{-}O_2CTrp)_4(THF)_2]$ (1a). The sodium salt of the triptycenecarboxylic acid (HO_2CTrp) was prepared in three steps by modification of literature procedures. A summary of the synthetic steps is provided in Scheme 2.2.[31,32] 9-Bromotriptycene was obtained by a Diels-Alder reaction between 9-bromoanthracene and the benzyne intermediates, generated from the unstable

diazonium salt prepared from anthranilic acid. Treatment of this product with a lithiating agent led to the formation of 9-triptycyllithium, which was carbonated and subsequently protonated to form HO_2CTrp. Initially, this crude product was purified by recrystallization in 1,4-dioxane/petroleum ether and then treated with NaOH to obtain the metal salt NaO_2CTrp. This salt was employed in anion metathesis reactions with $[Fe(H_2O)_6](BF_4)_2$ or $Fe(OTf)_2 \cdot 2MeCN$ in anhydrous THF to synthesize the starting material **1** and the resultant iron(II) complexes. The carboxylate salt did not show any impurities when analyzed by ^1H NMR spectroscopy. Impurities derived from the 9-bromo-10-triptycenecarboxylic acid, however, were observed in crystal structures of the resulting iron complexes. This brominated ligand impurity could be eliminated by purification of HO_2CTrp on silica gel using ethyl acetate/hexanes (1:1) as eluent. Some of the crystal structures reported herein were determined for material synthesized with NaO_2CTrp containing fractions of the brominated side product (up to 6%), which cocrystallized as observed in the corresponding X-ray structures of the diiron compounds. Because the bromine atom is not located near the iron coordination site, it had no effect on the coordination geometry.

Reaction of $[Fe(H_2O)_6](BF_4)_2$ with two equivalents of NaO_2CTrp in anhydrous THF afforded the crude starting material **1**. Molecular sieves were present in this reaction mixture in order to keep it anhydrous. Recrystallization of the dark pink powder led to colorless crystals of the paddlewheel complex **1a** and larger, pink-brown block crystals of a side-product **1b**. The ratio of these two species was estimated to be approximately 7:1 by visual inspection. Compounds

1a and **1b**, which have an identical iron-to-carboxylate ratio, form in 54% yield based on **1a** and were employed in further reactions with *N*-donor ligands. For simplicity, the mixture of **1a** and **1b** is hereafter defined as starting material **1** and all yields are based on **1a**. An alternative route (B) for the synthesis of pure **1a** was established, in which $Fe(OTf)_2 \cdot 2MeCN$ was used a in metathesis reaction with the sodium salt of the carboxylate. This route yielded pure **1a** in smaller yields, however, so the starting material prepared by the former method (A) was employed in further reactions.

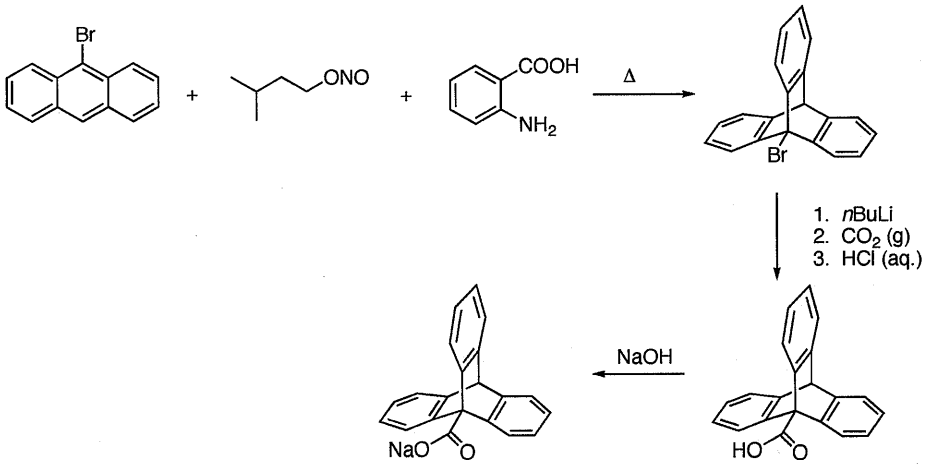

Scheme 2.2.

The colorless complex **1a** exhibits the well-known paddlewheel structure with two iron atoms bridged by four carboxylates. The crystal structure of **1a** is displayed in Figure 2.1 and selected bond angles and distances are depicted in Table 2.1. The two Fe(II) atoms are separated by 2.7307(8) Å and bridged by four carboxylate ligands, which are related by a pseudo-C_4 axis along the Fe–Fe vector. The structure of this paddlewheel complex is analogous to those of the diiron(II) compounds $[Fe_2(\mu\text{-}O_2CR)_4(THF)_2]$, where R = $Ar^{4\text{-}FPh}$ and dxl (Chart

2.1), which have very similar Fe–Fe distances of 2.7277(7) Å and 2.735 Å, respectively.[8,25] In all cases, the coordination sphere around the iron atoms is square pyramidal with the THF donor in the axial position.

During the synthesis of the paddlewheel complex $[Fe_2(\mu\text{-}O_2CTrp)_4(THF)_2]$ from $[Fe(H_2O)_6](BF_4)_2$ and two equivalents of NaO_2CTrp, pale pink-brown blocks of **1b** formed as a side-product. X-ray crystallographic analysis exhibited a neutral, trinuclear Fe(II) complex. A triply bridging fluoride ion is located in the center of a nearly equilateral triangle formed by the three iron atoms and is raised only slightly above this plane (ca. 0.14 Å). Two pairs of iron atoms are linked by two bridging carboxylates, whereas the other iron pair is only singly bridged by another carboxylate. The coordination spheres at these two iron atoms are completed by a sixth carboxylate ligand that is protonated and is therefore only bound in a monodentate fashion. Unfortunately, the quality of the data set was not to sufficient to provide a reliable assignment for the occupancy of this carboxylic acid ligand nor the remaining ligands for this coordination site and, therefore, detailed crystallographic information is not provided here. The proposed chemical structure of **1b** is displayed as Figure A1.12 (Appendix 1).

This type of $[Fe_3(\mu\text{-}F)]$ core has been observed before, but only in pentanuclear complexes in which two equivalent $[Fe_3(\mu\text{-}F)]$ triangles share a common vertex.[41] As in the synthesis of these complexes, the fluoride ion in **1b** apparently originates from the BF_4^- anion of the starting material. It is well-known that fluoride ions are released from BF_4^- in the presence of strong bases; in this

case hydroxide ions are present in the reaction mixture, derived from water molecules that are present in the iron starting material.[42]

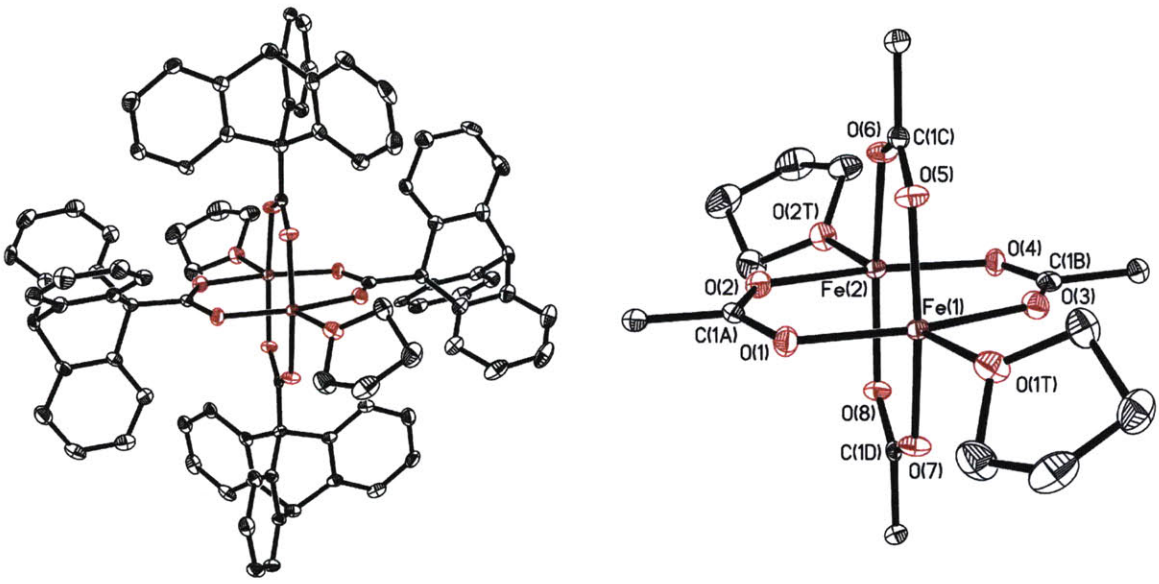

Figure 2.1. ORTEP diagrams of $[Fe_2(\mu\text{-}O_2CTrp)_4(THF)_2]$ (**1a**) showing 50% probability thermal ellipsoids for all non-hydrogen atoms. Left: The complete molecule. Right: The molecule omitting triptycene units.

Table 2.1. Selected Bond Lengths (Å) and Angles (deg) for **1a**.

Fe(1)–Fe(2)	2.7307(8)	Fe(1)–O(1)–C(1A)	119.1(3)
Fe(1)–O(1T)	2.083(3)	Fe(1)–O(3)–C(1B)	132.7(3)
Fe(1)–O(2T)	2.069(3)	Fe(1)–O(5)–C(1C)	126.7(3)
Fe(1)–O(1)	2.043(3)	Fe(1)–O(7)–C(1D)	122.8(2)
Fe(1)–O(3)	2.110(3)	Fe(2)–O(2)–C(1A)	131.3(3)
Fe(1)–O(5)	2.060(3)	Fe(2)–O(4)–C(1B)	117.3(3)
Fe(1)–O(7)	2.039(3)	Fe(2)–O(6)–C(1C)	122.8(3)
Fe(2)–O(2)	2.090(3)	Fe(2)–O(8)–C(1D)	127.6(2)
Fe(2)–O(4)	2.057(3)		
Fe(2)–O(6)	2.054(3)		
Fe(2)–O(8)	2.069(3)		

Numbers in parentheses are estimated standard deviations of the last significant figure.
Atoms are labeled as indicated in Figure 2.1.

Further evidence for **1b** only containing ferrous iron is provided by Mössbauer spectroscopy of the starting material **1**. Its Mössbauer spectrum, acquired at 4.2 K at zero field is displayed in Figure A1.13 (Appendix 1) and consists of a somewhat broader quadrupole doublet (δ = 1.33(2) mm/s, ΔE_Q = 2.64(2) mm/s and Γ = 0.54 mm/s). These values are characteristic for high spin Fe(II) in an oxygen-rich coordination environment and are in agreement with the proposed structure for **1b**.[29] The Mössbauer spectra of **8** and **9** that were acquired under the same conditions, exhibit nearly identical parameters (δ = 1.16(2) mm/s, ΔE_Q = 2.77(2) mm/s and Γ = 0.33 mm/s for **8** and δ = 1.16(2) mm/s, ΔE_Q = 2.69(2) mm/s and Γ = 0.39 mm/s for **9**) which are characteristic for high-spin iron sites in an N/O environment.[29] The corresponding spectra are shown in Appendix 1 in Figures A1.14 and A1.15.

Synthesis and Structural Characterization of Quadruply Bridged Diiron(II) Complexes [$Fe_2(\mu$-O_2CTrp)$_4$(L)$_2$], 2–12. Compounds **2–12** having the general formula [$Fe_2(\mu$-O_2CTrp)$_4$(L)$_2$] were prepared from **1** by displacement of the weakly bound THF molecules upon addition of two equiv of *N*-donor ligand (L) in modest to excellent yields (37%–86%). Scheme 2.3 summarizes the reactions and the corresponding products. The synthetic procedures for these paddlewheel complexes differ depending on the solubilities of the products. Compounds **3–6** are quite insoluble and a strategy to prepare them was to precipitate the microcrystalline product from a reaction mixture in toluene, which could then be recrystallized from boiling 1,2-dimethoxyethane followed by Et_2O vapor diffusion to obtain X-ray quality crystals. In addition, 2-PhIm and 2-^{i}PrIm

were alkylated in the N1-position (R' = propyl, ethyl) to enhance the solubility of the corresponding diiron complexes. This reaction involved deprotonation of the imidazole followed by nucleophilic substitution with an alkyl iodide. The resulting compounds **7–9** as well as those with pyridine ligands, **2**, **10–12**, had improved solubility, and X-ray quality crystals could be isolated by vapor diffusion of either Et_2O or pentane into the corresponding reaction mixtures. Paddlewheel diiron(II) compounds that are soluble in CH_2Cl_2 can be prepared in a one-pot reaction between $Fe(OTf)_2{\cdot}2MeCN$, NaO_2CTrp, and the *N*-donor in a 1:2:1 ratio. This alternative method was utilized for the synthesis of **11**, as well as for that of **1a**, vide supra.

The crystal structures of **2–12** are shown in Figures A1.1–A1.11 and selected bond distances and angles are displayed in Table A1.2 (Appendix 1). Crystal data and data collection parameters are presented in Table A1.1. All the paddlewheel complexes have structures with parameters comparable to those of compound **1a**, the only difference being the neutral donor ligand L. In all compounds except **11**, two five-coordinate iron centers are related by a crystallographic inversion center, requiring the iron atoms and four oxygen atoms from two of the bridging carboxylates to be positioned in a common plane. One *N*-donor ligand is bound axially to each of the iron atoms, which have square-pyramidal coordination geometry. Compound **11** crystallizes in a tetragonal space group with one molecule in the asymmetric unit and has analogous metrical parameters to those of the other paddlewheel complexes.

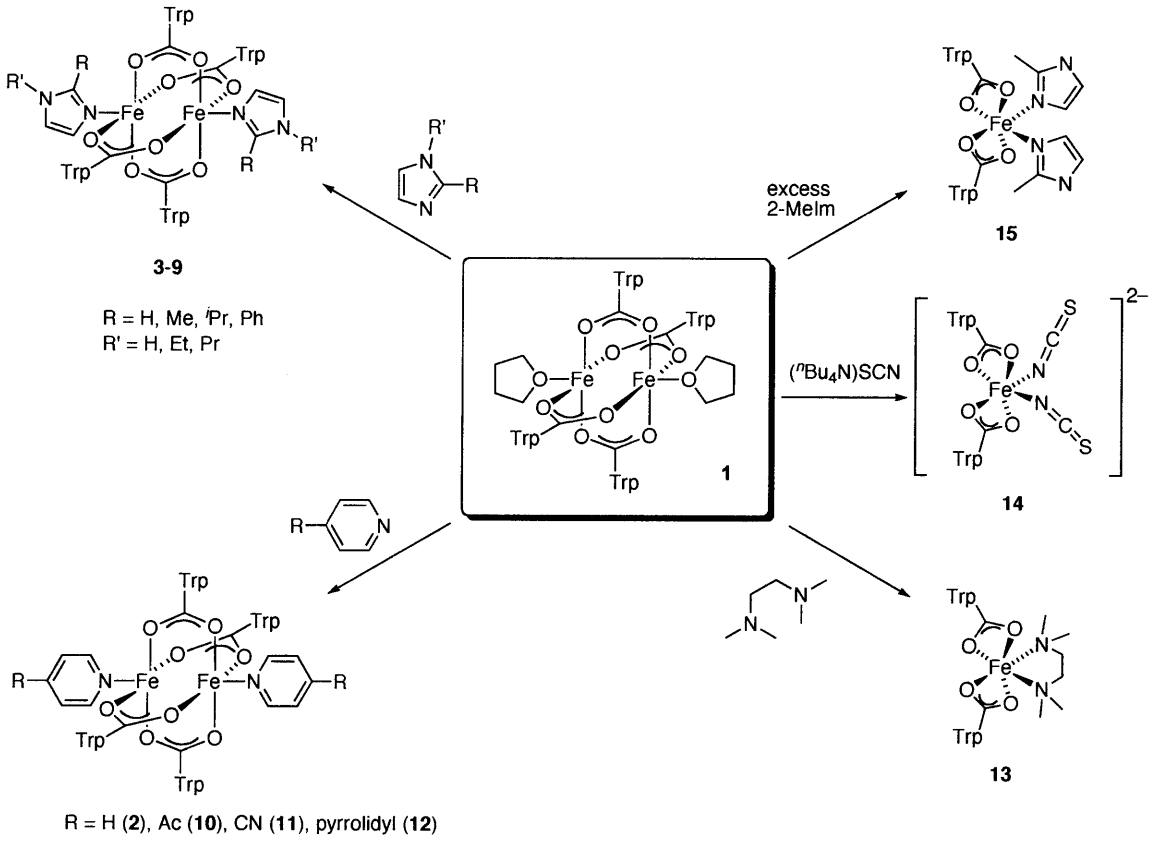

Scheme 2.3

The Fe–Fe distances in **1a**, **2–12** range from 2.7307(8) to 3.007(2) Å. The smallest distance occurs in the paddlewheel complex with L = THF followed by those with pyridine donor ligands, which have distances between 2.7718(14) and 2.8694(15) Å. In the series of paddlewheel complexes with imidazole-derived ligands the Fe–Fe distances increase significantly, from 2.8603(8) to 3.007(2) Å, with increasing bulkiness of the substituent R on the C2-position of the heterocycle (R = H < Me < ^{i}Pr < Ph). Compared to this 0.15 Å increase in Fe–Fe distance for the imidazole-substituted paddlewheel complexes, those in the series of pyridine-substituted compounds vary less, by ca. 0.10 Å. This difference can be explained by the fact that the residues R in the imidazole ligands sterically

interact with the neighboring triptycenecarboxylates, causing them to be pushed away from the Fe-center and the average Fe–O–C angle to increase. The para-substituents on the pyridine derivatives are directed away from the steric bulk of the triptycenecarboxylates and have no significant steric influence on the diiron distance.

A summary of Fe–Fe, Fe–L, and average Fe–O distances, and average Fe–O–C angles of **1a**, **2–12** is presented in Table 2.2. It reveals the aforementioned Fe–O–C angle variation (125.0°–128.3°) that reflects the increasing bulkiness of the *N*-donor, but no major change in $Fe–O_{avg}$ bond lengths. This difference is to be expected because angle deformations require less energy than lengthening or shortening of bonds.[43] Figure 2.2 illustrates the linear relationship between Fe–Fe distances and Fe–O–C angles in **1a**, **2–12**, revealing a systematic trend. These results stand in contrast to those obtained for a series of diiron(II) paddlewheel complexes with *m*-terphenylcarboxylate ligands of the type $[Fe_2(\mu\text{-}O_2CAr^{4\text{-}FPh})_4(L)_2]$, where L = THF, 1-MeIm, py and ^{t}BuPy.[25] Here, the Fe–Fe distances for all the compounds with *N*-donor ligands are essentially the same (2.8247–2.8249 Å) and the Fe–O–C angles span a narrow range (123.86°–124.89°); only the THF complex has smaller distances and angles. These dinuclear complexes disassemble to form a mononuclear species when the steric bulk on the *N*-donor increases (L = 1-benzylimidazole, 1-methylbenzimidazole).[44] These observations reveal that the triptycene-carboxylate imparts a significantly greater stability to the dinuclear core than other sterically hindered carboxylates.

Table 2.2. Comparison of Fe–Fe and Fe–L Distances (Å) and the Average Fe–O–C Angles (deg) in Complexes of the Type $[Fe_2(\mu\text{-}O_2CTrp)_4(L)_2]$.

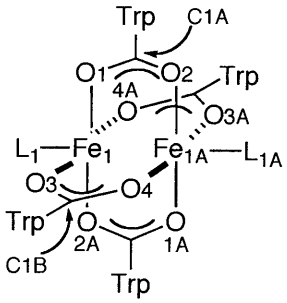

Ligand (L)	Fe–Fe	Fe–O–C_{avg}	Fe–L	Fe–O_{avg}
THF (**1a**)	2.7307(8)	125.0	2.076(3)[a]	2.065
4-CNPy (**11**)	2.772(2)	125.5	2.086(3)	2.054
4-PPy (**12**)	2.821(2)	126.3	2.083(3)	2.077
Py (**2**)	2.8460(6)	126.5	2.1184(19)	2.076
4-AcPy (**10**)	2.8692(15)	126.6	2.126(4)	2.067
1-MeIm (**3**)	2.8604(8)	126.8	2.080(3)	2.077
2-MeIm(**4**)	2.9033(9)	126.8	2.0837(19)	2.075
1-Pr-2-^{i}PrIm(**8**)	2.906(1)	126.9	2.088(2)	2.087
2-^{i}PrIm (**5**)	2.912(1)	127.2	2.084(2)	2.080
1-Et-2-^{i}PrIm (**7**)	2.9215(10)	127.1	2.094(2)	2.077
1-Pr-2-PhIm(**9**)	2.9639(11)	128.3	2.109(3)	2.079
2-PhIm(**6**)	3.007(2)	128.3	2.133(2)	2.089

Numbers in parentheses are estimated standard deviations of the last significant figure.
[a] Average value.

The Fe–Fe distances of 2.9036(9) Å to 3.007(2) Å observed for **4**–**9** are about 0.14 Å longer than the largest one previously reported, for the quadruply-bridged diiron(II) complex $[Fe_2(\mu\text{-}O_2Cdxl)_4(1\text{-MeIm})_2]$ (2.864 Å).[8] The Fe–Fe distance range that can be accommodated in these paddlewheel complexes is significant, 0.27 Å, compared to other dimetallic complexes with different carboxylates in which the distances between the metals usually fall into a narrow range.

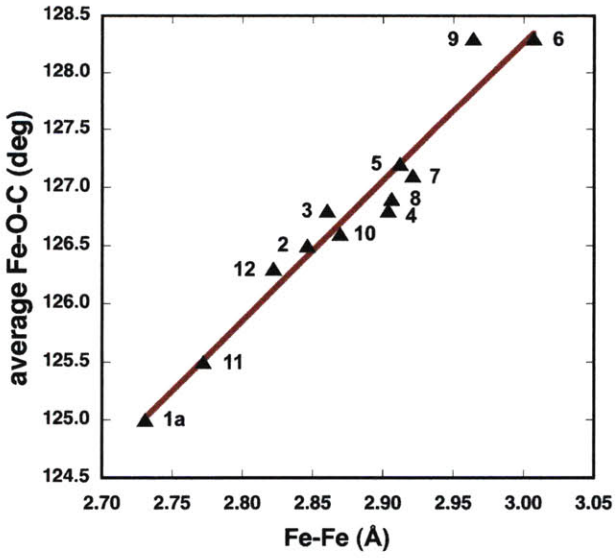

Figure 2.2. Correlation between Fe–Fe distances (Å) and the average Fe–O–C angles in complexes of the type $[Fe_2(\mu\text{-}O_2CTrp)_4(L)_2]$ **2–12**.

Stability of the Diiron Paddlewheel Core. As pointed out above, despite an increase in steric bulk of the neutral donor L, the paddlewheel core stays intact and undergoes neither a carboxylate shift nor disassembly into mononuclear species. In order to investigate further the stability of these diiron paddlewheels, the complexes were allowed to react with water and checked for decomposition of the core or carboxylate shifts. The influence of water on the conformational stability was previously discovered for *m*-terphenylcarboxylate diiron(II) complexes.[27-29,45] Here, addition of ~17 equiv of water to the diiron compound resulted in coordination of one water molecule to each iron center, converting it from a quadruply to a doubly bridging diiron carboxylate complex, as portrayed in Scheme 2.4.

Compounds **7** and **12** were chosen for water reactivity studies because of their good solubility in CH_2Cl_2. Solutions of water in anhydrous THF were added

to CH_2Cl_2 solutions of the diiron complexes in an excess of 13 to 350 equiv. The reaction mixtures were stirred for either five min or 2.5 h before being set up for crystallization by vapor diffusion. In all cases, even where a large excess of water had been added and the reaction time was extended to 2.5 h, the resulting crystalline products maintained their structural integrity. This behavior is remarkable, considering that a hexaaquairon(II) cation forms in the case of *m*-terphenylcarboxylate diiron(II) compounds with the addition of only 35 equiv of water to the dinuclear starting material.[28]

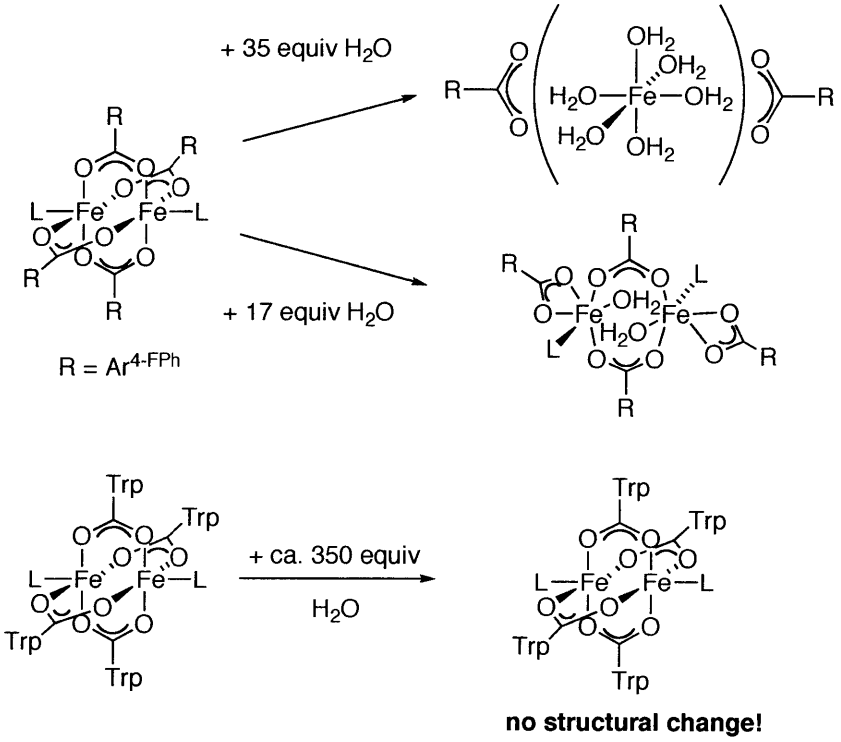

Scheme 2.4.

From these studies it can be concluded that the triptycene-bridged diiron(II) core has unprecedented conformational stability, which can be

attributed to interligand steric interactions between the triptycene units. These are locked together in a tongue-in-groove fashion, whereby one phenyl group is embedded between two phenyl rings of the neighboring triptycenecarboxylate, preventing them from undergoing carboxylate shifts. Two space-filling diagrams of compound **1a** are displayed in Figure 2.3 to illustrate this interaction.

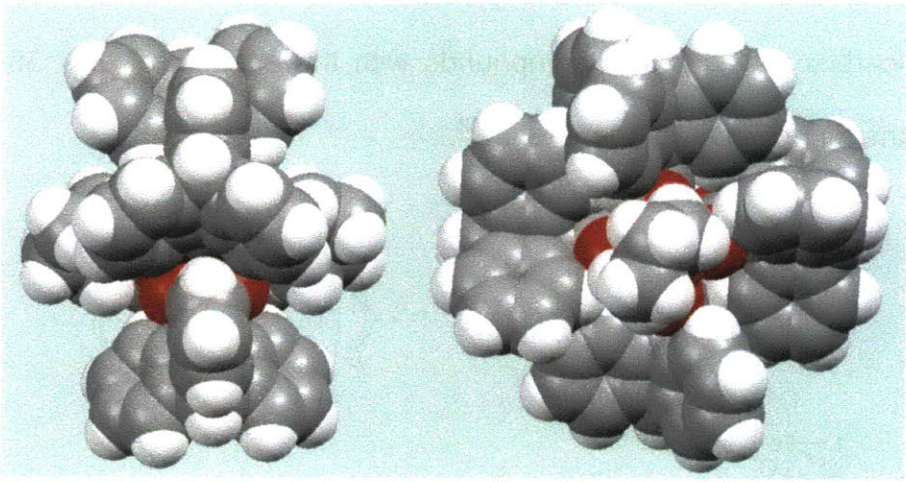

Figure 2.3. Space-filling diagram of $[Fe_2(\mu\text{-}O_2CTrp)_4(THF)_2]$ (**1a**). Left: View showing the Fe–Fe vector. Right: View along the Fe–Fe vector.

Electronic Spectroscopy and Equilibria in Coordinating Solvents. High-spin iron(II) complexes with a carboxylate-rich environment are typically colorless, making it difficult to apply UV-vis spectroscopic methods to investigate their chemical reactivity. For this reason, pyridine ligands with electron-withdrawing substituents, such as 4-cyano- (4-CNPy) and 4-acetylpyridine (4-AcPy), were introduced into triptycenecarboxylate-rich diiron(II) complexes, which resulted in the intensely colored complexes $[Fe_2(\mu\text{-}O_2CTrp)_4(4\text{-AcPy})_2]$ (**10**) and $[Fe_2(\mu\text{-}O_2CTrp)_4(4\text{-CNPy})_2]$ (**11**). In **10** and **11**, absorptions occur in the visible region at λ_{max} = 450 nm (ε_M = 1050 M^{-1} cm^{-1}) and λ_{max} = 475 nm (ε_M =

1230 M^{-1} cm^{-1}) in CH_2Cl_2 solutions, respectively. This approach was applied recently in our group for *m*-terphenyl-derived carboxylate diiron(II) compounds. Investigation by resonance Raman and electronic absorption spectroscopy confirmed that the colors originate from a charge-transfer transition from the ferrous iron to a π^* orbital of the pyridine ligand (MLCT).[29,45] Solutions of these diiron(II) complexes absorb in CH_2Cl_2 at somewhat longer wavelengths than the present diiron(II) compounds with $^{-}O_2CTrp$ ligands. For example, the complex $[Fe_2(\mu\text{-}O_2CAr^{Tol})_4(4\text{-}CNPy)_2]$ has an absorption maximum at λ_{max} = 510 nm (ε_M = 2200 M^{-1} cm^{-1}), but that of a compound having the more electron-withdrawing carboxylate ligands, $[Fe_2(\mu\text{-}O_2CAr^{4\text{-}FPh})_4(4\text{-}CNPy)_2]$ (ε_M = 2300 M^{-1} cm^{-1}), is blue-shifted to λ_{max} = 480 nm. This observation is consistent with the assignment of the electronic transition as a MLCT. The triptycenecarboxylate-bridged diiron(II) complex **11** absorbs at a wavelength similar to that of the diiron complex with the more electron-withdrawing terphenylcarboxylate ligands, which leads to the conclusion that the electron-donating capability of the $^{-}O_2CTrp$ is about the same as that of $^{-}O_2CAr^{4\text{-}FPh}$. The absorbance maximum of **10**, which has the neutral donor 4-AcPy, is blue-shifted by comparison to that of **11**. This trend is consistent with the hypsochromic shift in absorbance maximum when L is changed from 4-CNPy to 4-AcPy in the complex $[Fe_2(\mu\text{-}O_2CAr^{Tol})_4(L)_2]$.

When compounds **10** and **11** are dissolved in a coordinating solvent, such as THF, the color disappears, only to reappear when the solutions are cooled to low temperatures. This solvent-dependent thermochromism was investigated for **11** by variable-temperature UV-vis-spectroscopy, monitoring the absorbance

change over a temperature range from 193 to 293 K. The equilibrium between **11** and the colorless species can be described by eq 1.

$$[Fe_2(\mu\text{–}O_2CTrp)_4(4\text{-}CNPy)_2] + 2\ THF \rightleftharpoons [Fe_2(\mu\text{–}O_2CTrp)_4(THF)_2] + 2\ (4\text{-}CNPy) \quad (1)$$

A mathematical analysis that fits the data to a model represented by eq 1, which presumes constant extinction coefficients over the complete temperature range, has been described recently for a similar system.[29] The change in absorbance spectra and a least-squares fit are displayed in Figure 2.4. The thermodynamic parameters derived from this experiment are ΔH = 18.5(2) kJ mol^{-1} and ΔS = –16.3(10) J mol^{-1} K^{-1}, which are very similar to those determined from an analogous study of the windmill complex $[Fe_2(\mu\text{-}O_2CAr^{Tol})_2(O_2CAr^{Tol})_2(4\text{-}CNPy)_2]$, ΔH = 19.0(6) kJ mol^{-1}, ΔS = –16.2(16) J mol^{-1} K^{-1}.[29]

Considering that the geometric structure of the latter is quite different from that of paddlewheel complex **11**, this result may seem somewhat surprising. However, it was previously determined that these terphenylcarboxylate complexes undergo dynamic carboxylate-shifts from doubly to quadruply bridged structures in a process that does not require much energy. The thermodynamic parameters for exchange of 4-CNPy by THF solvent are therefore mainly determined by the relative strengths of the THF–Fe and (4-CNPy)–Fe bonds and by solvation energies. Preliminary kinetic measurements of a reaction between **11** with excess pyridine suggest that the diiron(II) paddlewheel core stays intact in solution during ligand substitution of 4-CNPy by pyridine.

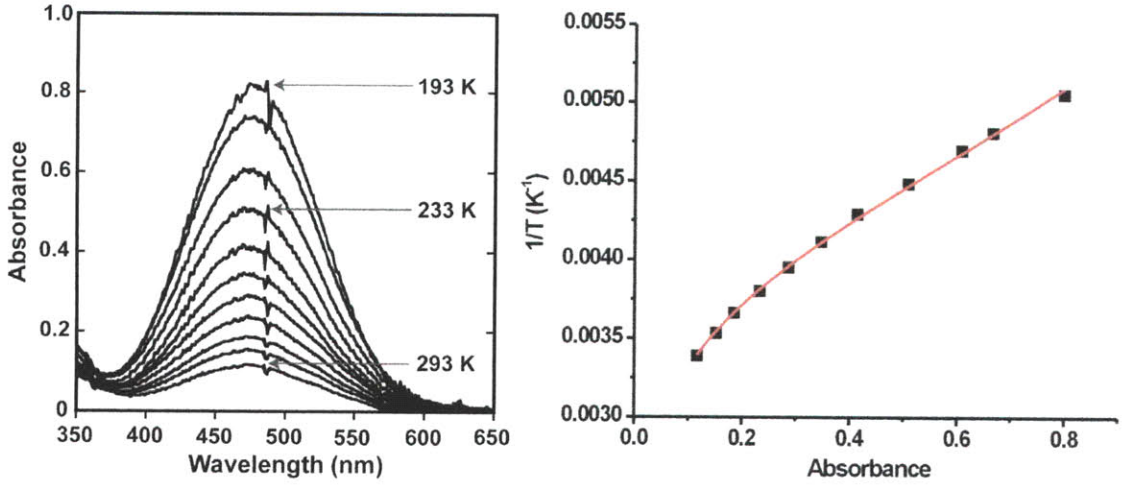

Figure 2.4. Temperature-dependent UV-vis spectra of $[Fe_2(\mu\text{-}O_2CTrp)_4(4\text{-}CNPy)_2]$ (**11**) in THF solution (Left). The absorbance change at 475 nm fit to eq 1 (Right). The solid line represents a least-squares fit to the data points and the estimated errors for the derived thermodynamic parameters are given in the text.

Dimetallic Core Disassembly to Form Mononuclear Fe(II) Complexes. Synthesis and Structural Characterization of 13 – 15. The crystal structure, bond lengths, and interbond angles for **13** – **15** are displayed in Figure 2.5 and Table 2.3. Compound **13** can be prepared from **1** by direct ligand substitution using TMEDA or by self-assembly from $Fe(OTf)_2{\cdot}2MeCN$, NaO_2CTrp, and TMEDA in a 1:2:1 ratio in anhydrous THF. Colorless crystals of $[Fe(O_2CTrp)_2(TMEDA)]$ (**13**), suitable for X-ray crystallography, were isolated in good yields (57%) by either method. Two carboxylates and one bidentate TMEDA molecule comprise the ligand sphere around the six-coordinate iron(II) atom. The carboxylate ligands each have a long and a short Fe–O bond ($\Delta_{Fe-O} \approx$ 0.18 Å), with the shorter bond being trans to the amine donors. The Mössbauer spectrum of **13**, displayed in Figure A1.16 (Appendix 1), was acquired at zero

field and 4.2 K. It shows a sharp quadrupole doublet with a linewidth of Γ = 0.31 mm/s, from which an isomer shift of δ = 1.13(2) mm/s and a quadrupole splitting parameter ΔE_Q = 3.01(2) mm/s could be derived. These values are characteristic for a high-spin (S = 2) Fe(II) center.[29,44] Reaction of **1** with four equivalents of tetrabutylammonium thiocyanate led to instant disassembly of the dinuclear starting material to afford colorless blocks of $(^nBu_4N)_2[Fe(O_2CTrp)_2(SCN)_2]$ (**14**) in good yield (55%). The compound has a crystallographically required C_2-axis bisecting the molecule. Two symmetry-related bidentate carboxylates and two isothiocyanate ligands support a distorted octahedral coordination environment around the Fe(II) atom. The carboxylates bind in an asymmetric fashion, which is reflected by the two distinct Fe–O distances with $\Delta_{Fe-O} \approx 0.21$ Å. The longer Fe–O bond is situated anti to the isothiocyanate ligand that binds through its nitrogen (N1) atom at a distance of 2.045(4) Å. The thiocyanate anion is nearly linear, with an N(1)–C(1)–S(1) angle of 178.2(4)°. The angle of coordination, Fe(1)–N(1)–C(1), is 163.1(4)°.

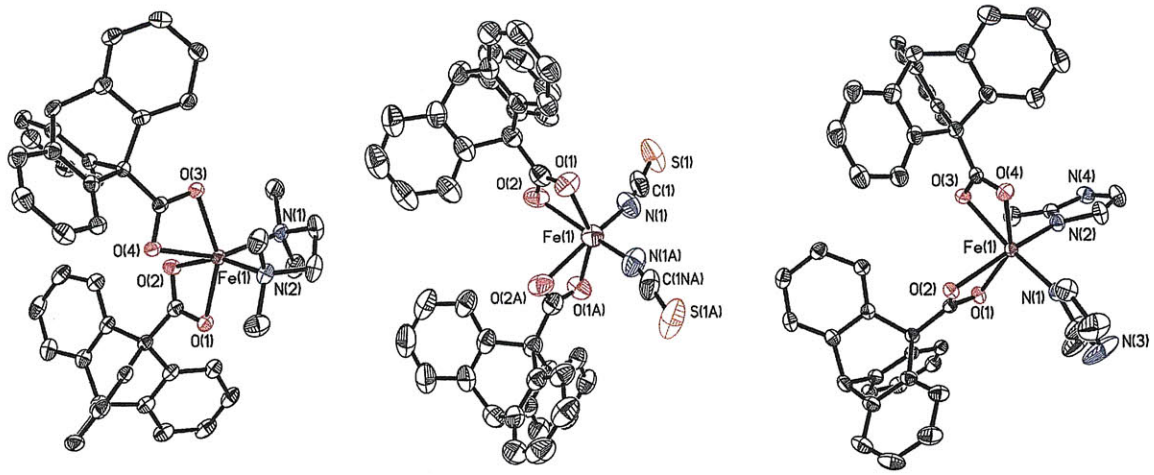

Figure 2.5. ORTEP diagram of $[Fe(O_2CTrp)_2(TMEDA)]$ (**13**), $[Fe(O_2CTrp)_2(SCN)_2]^{2-}$ (**14**) and $[Fe(O_2CTrp)_2(2\text{-MeIm})_2]$ (**15**) (illustrating 50% probability thermal ellipsoids for all non-hydrogen atoms).

Compound **15** was isolated from a mixture in which **1** was accidentally allowed to react with an excess (ca. 6.0 equiv) of 2-MeIm. Only a few colorless blocks of this compound, which were suitable for X-ray crystallography, formed, together with an amorphous precipitate, and no attempt was made to optimize the synthesis. The Fe(II) atom is coordinated by two bidentate carboxylates and two imidazole ligands. One of the carboxylate ligands binds asymmetrically with $\Delta_{Fe-O} \approx 0.198$ Å, whereas the other one coordinates in a more symmetric fashion. The distances between the iron and the imidazole N-atoms are nearly identical.

Addition of a stoichiometric amount of *N*-donor to **1** results in minimal perturbation of its diiron paddlewheel core to yield **2**–**12**. Reactions of **1** with the bidentate *N*-donor ligand TMEDA, an excessive amount of monodentate ligand 2-MeIm, or the thiocyanate anion, converted the dinuclear core to mononuclear complexes. Monoiron(II) complexes having two carboxylate and two *N*-donor ligands are relatively rare, and a CSD search[3] revealed that they all contain sterically hindered *m*-terphenylcarboxylate-ligands.[44,46] The complexes $[Fe(O_2CAr^{Tol})_2(TMEDA)]$ and $[Fe(O_2CAr^{Mes})_2(TMEDA)]$ have a stoichiometry analogous to that of **13**, but differ in the carboxylate-binding mode. In particular, only one carboxylate is bidentate and the second is monodentate, which results in five-coordinate species. A complex similar to **15**, $[Fe(O_2CAr^{Mes})_2(1\text{-MeIm})_2]$, has an unusual, nearly tetrahedral coordination environment. The *m*-terphenylcarboxylate compounds feature a low coordinate geometry because the steric bulk hinders bidentate coordination. In contrast, for **13**–**15**, which contain $^{-}O_2CTrp$, no bulky residues point toward the iron atoms, allowing the

carboxylates to bind in a bidentate manner while preventing higher oligomerization.

Table 2.3. Selected Bond Lengths (Å) and Angles (deg) for **13–15**.

13			
Fe(1)–O(1)	2.097(2)	O(2)–Fe(1)–O(4)	85.71(7)
Fe(1)–O(2)	2.281(2)	O(1)–Fe(1)–N(1)	109.60(9)
Fe(1)–O(3)	2.087(2)	O(1)–Fe(1)–N(2)	100.86(9)
Fe(1)–O(4)	2.257(2)	O(2)–Fe(1)–N(1)	105.27(9)
Fe(1)–N(1)	2.145(2)	O(2)–Fe(1)–N(2)	160.50(9)
Fe(1)–N(2)	2.202(2)	O(3)–Fe(1)–N(1)	93.20(9)
O(1)–Fe(1)–O(2)	59.87(7)	O(3)–Fe(1)–N(2)	99.88(9)
O(1)–Fe(1)–O(3)	150.71(8)	O(4)–Fe(1)–N(1)	152.99(8)
O(1)–Fe(1)–O(4)	97.30(7)	O(4)–Fe(1)–N(2)	94.53(8)
O(3)–Fe(1)–O(4)	60.56(7)		
14			
Fe(1)–O(1)	2.099(3)	O(1)–Fe(1)–O(2A)	95.3(1)
Fe(1)–O(2)	2.312(3)	O(1)–Fe(1)–O(1A)	146.5(2)
Fe(1)–N(1)	2.045(4)	O(2)–Fe(1)–O(2A)	84.2(2)
S(1)–C(1)	1.643(6)	N(1)–Fe(1)–O(1)	101.2(1)
C(1)–N(1)	1.139(6)	N(1)–Fe(1)–O(1A)	98.91(12)
C(1)–N(1)–Fe(1)	163.1(4)	N(1)–Fe(1)–O(2)	89.14(13)
N(1)–C(1)–S(1)	178.2(4)	N(1)–Fe(1)–N(1A)	105.8(2)
O(1)–Fe(1)–O(2)	58.7(1)		
15			
Fe(1)–O(1)	2.1178(2)	O(2)–Fe(1)–O(4)	97.33(7)
Fe(1)–O(2)	2.315(2)	O(1)–Fe(1)–N(1)	101.28(9)
Fe(1)–O(3)	2.222(2)	O(1)–Fe(1)–N(2)	104.11(8)
Fe(1)–O(4)	2.146(2)	O(2)–Fe(1)–N(1)	90.33(8)
Fe(1)–N(1)	2.095(2)	O(2)–Fe(1)–N(2)	162.77(8)
Fe(1)–N(2)	2.099(2)	O(3)–Fe(1)–N(1)	160.81(8)
O(1)–Fe(1)–O(2)	58.78(7)	O(3)–Fe(1)–N(2)	92.51(8)
O(1)–Fe(1)–O(3)	93.55(7)	O(4)–Fe(1)–N(1)	101.50(9)
O(1)–Fe(1)–O(4)	146.82(8)	O(4)–Fe(1)–N(2)	97.32(8)
O(3)–Fe(1)–O(4)	60.11(7)		

Numbers in parentheses are estimated standard deviations of the last significant figure.
Atoms are labeled as indicated in Figure 2.5.

Compound **14** was prepared in an attempt to synthesize an anionic tetracarboxylate-bridged diiron(II) complex with terminal thiocyanate ligands. No complex of this type has been reported in the literature. When thiocyanate was

added to the dinuclear complex **1** in a 2:1 ratio, however, the structure converted to mononuclear **14** with two isothiocyanate ligands per iron atom. Although many structures have two thiocyanates coordinated to Fe(II),[47,48] no compound with the carboxylate-coordination environment of **14** has been previously described.

Conclusions

A general strategy is described for synthesizing triptycenecarboxylate-bridged diiron(II) complexes. With increasing steric demand of the neutral donor axial ligand (L) in these $[Fe_2(\mu\text{-}O_2CTrp)_4(L)_2]$ compounds, a systematic increase in Fe–Fe distance occurs and, for the first time, a diiron(II) paddlewheel complex with an Fe–Fe distance greater than 3 Å was obtained. The reactivity of these complexes with excess water was tested and revealed neither disassembly of the dinuclear core nor a carboxylate shift, leading to the conclusion that the triptycene tetracarboxylate framework has unusual kinetic stability. The thermochromism of the colored compound **11** was used in variable UV-vis temperature studies to determine thermodynamic parameters for ligand substitution. Reactions of **1** with chelating or anionic ligands or with an excess of the *N*-donor converted the dinuclear core into mononuclear species, which all have an O_4N_2 coordination sphere, with a six-coordinate iron atom. Other mononuclear iron(II) complexes of bulky carboxylates have a lower coordination number of 4 or 5.

Acknowledgements. This work was supported by grant GM032134 from the National Institute of the General Medical Sciences. I thank Dr. Jeremy J. Kodanko for the initial synthesis of compounds **1**–**6**, Kyrstin L. Fornace for help with the synthesis of HO_2CTrp, and Dr. Peter Müller for assistance with X-ray crystallography.

Supporting Information. X-ray crystallographic information for **1a**, **2**–**15** (Table A1.1); selected bond distances and angles for **2**–**12** (Table A1.2); ORTEP diagrams of **2**–**12**; diagram of **1b**; zero-field Mössbauer spectra for **1**, **8**, **9** and **13** are reported in Appendix 1.

References

(1) Van Niekerk, J. N.; Schoening, F. R. L. *Acta Crystallogr.* **1953**, *6*, 227-232.

(2) Van Niekerk, J. N.; Schoening, F. R. L. *Nature* **1953**, *171*, 36-37.

(3) Cotton, F. A.; Murillo, C. A.; Walton, R. A.; Editors *Multiple Bonds Between Metal Atoms*; 3rd ed., 2005.

(4) *ConQuest*, version 1.8; Cambridge Crystallographic Data Center: Cambridge, U.K., 2007.

(5) Hilderbrand, S. A.; Lippard, S. J. *Inorg. Chem.* **2004**, *43*, 5294-5301.

(6) Randall, C. R.; Shu, L.; Chiou, Y.-M.; Hagen, K. S.; Ito, M.; Kitajima, N.; Lachicotte, R. J.; Zang, Y.; Que, L., Jr. *Inorg. Chem.* **1995**, *34*, 1036-1039.

(7) Reisner, E.; Telser, J.; Lippard, S. J. *Inorg. Chem.* **2007**, *46*, 10754-10770.

(8) Chavez, F. A.; Ho, R. Y. N.; Pink, M.; Young, V. G., Jr.; Kryatov, S. V.; Rybak-Akimova, E. V.; Andres, H.; Münck, E.; Que, L., Jr.; Tolman, W. B. *Angew. Chem., Int. Ed.* **2002**, *41*, 149-152.

(9) Rardin, R. L.; Tolman, W. B.; Lippard, S. J. *New J. Chem.* **1991**, *15*, 417-430.

(10) Lippard, S. J. *Angew. Chem., Int. Ed.* **1988**, *27*, 344-361.

(11) Holm, R. H.; Kennepohl, P.; Solomon, E. I. *Chem. Rev.* **1996**, *96*, 2239-2314.

(12) Solomon, E. I.; Brunold, T. C.; Davis, M. I.; Kemsley, J. N.; Lee, S.-K.; Lehnert, N.; Neese, F.; Skulan, A. J.; Yang, Y.-S.; Zhou, J. *Chem. Rev.* **2000**, *100*, 235-349.

(13) Du Bois, J.; Mizoguchi, T. J.; Lippard, S. J. *Coord. Chem. Rev.* **2000**, *200-202*, 443-485.

(14) Tshuva, E. Y.; Lippard, S. J. *Chem. Rev.* **2004**, *104*, 987-1011.

(15) Merkx, M.; Kopp, D. A.; Sazinsky, M. H.; Blazyk, J. L.; Müller, J.; Lippard, S. J. *Angew. Chem., Int. Ed.* **2001**, *40*, 2782-2807.

(16) Elango, N.; Radhakrishnan, R.; Froland, W. A.; Wallar, B. J.; Earhart, C. A.; Lipscomb, J. D.; Ohlendorf, D. H. *Protein Sci.* **1997**, *6*, 556-568.

(17) Bollinger, J. M., Jr.; Edmondson, D. E.; Huynh, B. H.; Filley, J.; Norton, J. R.; Stubbe, J. *Science* **1991**, *253*, 292-298.

(18) Logan, D. T.; Su, X. D.; Åberg, A.; Regnström, K.; Hajdu, J.; Eklund, H.; Nordlund, P. *Structure* **1996**, *4*, 1053-1064.

(19) Stubbe, J.; van der Donk, W. A. *Chem. Rev.* **1998**, *98*, 705-762.

(20) Broadwater, J. A.; Ai, J.; Loehr, T. M.; Sanders-Loehr, J.; Fox, B. G. *Biochemistry* **1998**, *37*, 14664-14671.

(21) Lindqvist, Y.; Huang, W.; Schneider, G.; Shanklin, J. *EMBO J.* **1996**, *15*, 4081-4092.

(22) Sazinsky, M. H.; Bard, J.; Di Donato, A.; Lippard, S. J. *J. Biol. Chem.* **2004**, *279*, 30600-30610.

(23) McCormick, M. S.; Sazinsky, M. H.; Condon, K. L.; Lippard, S. J. *J. Am. Chem. Soc.* **2006**, *128*, 15108-15110.

(24) Tolman, W. B.; Que, L., Jr. *J. Chem. Soc., Dalton Trans.* **2002**, *5*, 653-660.

(25) Lee, D.; Lippard, S. J. *Inorg. Chem.* **2002**, *41*, 2704-2719.

(26) Hagadorn, J. R.; Que, L., Jr.; Tolman, W. B. *J. Am. Chem. Soc.* **1998**, *120*, 13531-13532.

(27) Yoon, S.; Kelly, A. E.; Lippard, S. J. *Polyhedron* **2004**, *23*, 2805-2812.

(28) Yoon, S.; Lippard, S. J. *J. Am. Chem. Soc.* **2004**, *126*, 16692-16693.

(29) Yoon, S.; Lippard, S. J. *J. Am. Chem. Soc.* **2005**, *127*, 8386-8397.

(30) Reisner, E.; Abikoff, T. C.; Lippard, S. J. *Inorg. Chem.* **2007**, *46*, 10229-10240.

(31) Friedman, L.; Logullo, F. M. *J. Am. Chem. Soc.* **1963**, *85*, 1549.

(32) Kawada, Y.; Iwamura, H. *J. Org. Chem.* **1981**, *46*, 3357-3359.

(33) Hagen, K. S. *Inorg. Chem.* **2000**, *39*, 5867-5869.

(34) Loozen, H. J. J.; Drouen, J. J. M.; Piepers, O. *J. Org. Chem.* **1975**, *40*, 3279-3280.

(35) Kent, T. A. *WMOSS*, Minneapolis, 1998.

(36) *SMART, Software for the CCD Detector System*, version 5.6; Bruker AXS Madison, WI, 2000.

(37) Sheldrick, G. M. *SHELXTL-97*, University of Göttingen: Göttingen, Germany: 2000.

(38) Sheldrick, G. M. *Acta Crystallogr., Sect. A* **2008**, *A64*, 112-122.

(39) Sheldrick, G. M. *SADABS: Area-Detector Absorption Correction*, University of Göttingen: Göttingen, Germany, 2001.

(40) Spek, A. L. *PLATON, A Multipurpose Crystallographic Tool*, Utrecht University: Utrecht, The Netherlands, 2000.

(41) Herold, S.; Lippard, S. J. *Inorg. Chem.* **1997**, *36*, 50-58 and references therein.

(42) Zang, Y.; Jang, H. G.; Chiou, Y.-M.; Hendrich, M. P.; Que, L., Jr. *Inorg. Chim. Acta* **1993**, *213*, 41-48.

(43) Christoph, G. G.; Koh, Y. B. *J. Am. Chem. Soc.* **1979**, *101*, 1422-1434.

(44) Lee, D.; Lippard, S. J. *Inorg. Chim. Acta* **2002**, *341*, 1-11.

(45) Zhao, M.; Song, D.; Lippard, S. J. *Inorg. Chem.* **2006**, *45*, 6323-6330.

(46) Hagadorn, J. R.; Que, L., Jr.; Tolman, W. B. *Inorg. Chem.* **2000**, *39*, 6086-6090.

(47) Long, G. J.; Galeazzi, G.; Russo, U.; Valle, G.; Calogero, S. *Inorg. Chem.* **1983**, *22*, 507-510.

(48) Chen, K.; Zhang, Y. L.; Feng, M. Q.; Liu, C. H. *Act. Crystallogr., Sect. E* **2007**, *63*, m2033.

Chapter 3

Synthesis, Characterization, and Oxygenation Studies of Carboxylate-Bridged Diiron(II) Complexes with Aromatic Substrates Tethered to Pyridine Ligands and the Formation of a Unique Trinuclear Complex

Introduction

Bacterial multicomponent monooxygenases (BMMs) are a class of enzymes that catalyze the regio- and enantioselective oxidation of an array of hydrocarbons, including alkanes, alkenes and aromatics.[1,2] Enzymes belonging to this family include soluble methane monooxygenase (sMMO),[3] toluene/*o*-xylene monooxygenase (ToMO),[4,5] and phenol hydroxylase (PH).[6] The hydroxylase (H) components of these enzymes house a catalytic diiron center, coordinated by four carboxylates from glutamate and two histidine ligands, that differ only in the carboxylate binding modes and the ligation of water or hydroxide ion. The diiron active sites of sMMOH in its reduced form and of the manganese(II)-reconstituted ToMOH, an accurate model of its reduced form, are depicted in Chart 3.1.

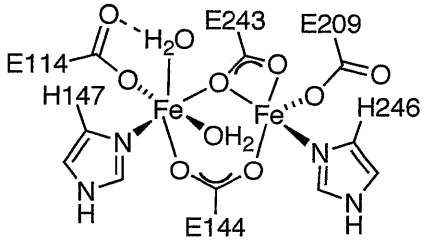

sMMOH

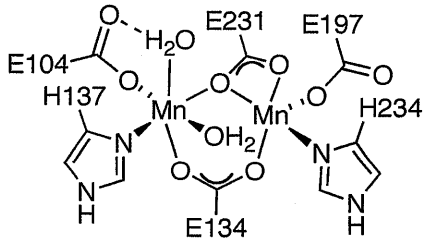

Mn_2ToMOH

Chart 3.1.

The dioxygen activation mechanism of sMMOH has been studied in detail.[3] The reduced state of this enzyme forms a peroxodiiron(III) intermediate ($MMOH_{peroxo}$) in a reaction with dioxygen, which converts to a high-valent diiron(IV) species (Q). The latter is capable of C–H bond activation to oxidize methane selectively to methanol. $MMOH_{peroxo}$ also functions as hydrocarbon

oxidant.[7,8] In addition to methane, sMMOH is a competent oxidant for alkynes, amines, and sulfides.[9-13] In ToMOH and PHH, peroxodiiron(III) intermediates are the catalytically relevant species. In contrast to $MMOH_{peroxo}$, these species have featureless UV-vis absorption spectra and significantly different Mössbauer spectroscopic parameters.[14]

Inspired by the versatile oxidation chemistry catalyzed by these non-heme diiron centers, we have been developing synthetic analogues to mimic enzyme function and to gain insight into the complexities of their dioxygen activation mechanisms. The introduction of sterically demanding *m*-terphenyl carboxylates, depicted in Chart 3.2, has facilitated the synthesis of the diiron complexes having the same ligand stoichiometry as that in non-heme diiron enzymes, namely, four carboxylates and two neutral *N*-donors.[15-17] The carboxylate ligands create a protective, hydrophobic sheath around the diiron centers, similar to that in the protein active sites, which prevents them from decomposition and offers excellent solubility in organic solvents. The dinuclear core structures can be tuned by the steric requirements of the carboxylate ligands, which results in doubly- triply-, and quadruply bridged diiron complexes.[18]

Attempts to oxidize external substrates by oxygenated diiron complexes bearing sterically hindered *m*-terphenyl carboxylates have thus been unsuccessful, presumably because the protective bulk around the diiron center blocks substrate access.[19-22] To circumvent this problem, the substrates were tethered to the ancillary neutral donor ligands. With the use of this approach, C–H activation of benzylic moieties in benzyl- and ethylpyridines,[23] oxidation of

sulfides and phosphines,[24-26] and oxidative *N*-dealkylation reactions were achieved.[27-29] The extent of oxidation reflected the proximity of the substrate to the diiron center, and little or no oxidation was observed when a substrate moiety was installed in the meta or para position of the pyridine ligand.

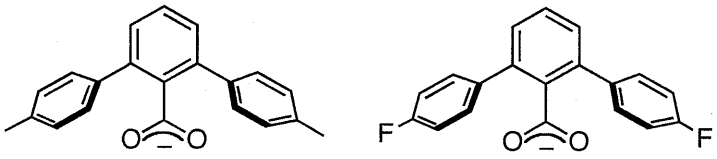

$Ar^{Tol}CO_2^-$ $Ar^{4\text{-}FPh}CO_2^-$

Chart 3.2

Models for ToMOH with polydentate, nitrogen-rich ligands have been reported previously.[30-32] In these studies, aromatic hydroxylation of the ligand was observed, and in one case a peroxodiiron(III) intermediate was characterized.[33] In the present work, we prepared synthetic model complexes for ToMOH and PHH with a carboxylate-rich ligand environment, with aryl groups tethered to the pyridine donor as potential substrates. The *N*-donor ligand 2-(pyridin-2-yloxy)phenol was incorporated to supply phenol, a substrate for PHH. Diiron complexes of this ligand displayed interesting coordination properties, forming dinuclear and trinuclear complexes that were characterized by structural and Mössbauer spectroscopic methods. All iron complexes were analyzed by single crystal structural X-ray methods. The dioxygen reactivity of these compounds was investigated by UV-vis spectroscopy and by product analysis.

Experimental

General Procedures and Methods. Tetrahydrofuran (THF), diethylether (Et_2O), pentane, and dichloromethane (CH_2Cl_2) were saturated with nitrogen and purified by passage through activated alumina columns under an argon atmosphere. Dry 1,2-dichloroethane (DCE) was purchased from Aldrich. Dioxygen (99.994%, BOC gases) was dried by passing the gas stream through a column of Drierite®. The synthesis and characterization of compounds $[Fe_2(\mu\text{-}O_2CAr^{4\text{-}FPh})_2(O_2CAr^{4\text{-}FPh})_2(THF)_2]$[18] and $[Fe_2(\mu\text{-}O_2CAr^{Tol})_2(O_2CAr^{Tol})_2(THF)_2]$[15] are reported elsewhere. The ligands 2-(3-methoxyphenoxy)pyridine [2-(*m*-MeOPhO)Py], 2-(4-methoxyphenoxy)pyridine [(2-(*p*-MeOPhO)Py], and 2-(pyridin-2-yloxy)phenol [2-(*o*-HOPhO)Py] were prepared using modified literature procedures.[34] All other reagents were obtained from commercial sources and used as received. Air sensitive manipulations were performed using Schlenk techniques or under nitrogen atmosphere in an MBraun glovebox.

Physical measurements. FT-IR spectra were recorded on a Thermo Nicolet Avatar 360 spectrometer with OMNIC software. Melting points were acquired on an electrothermal Mel-Temp melting point apparatus. All gas chromatographic studies were carried out on an Agilent 6890 gas chromatograph attached to an Agilent 5973N mass selective detector. An HP-5ms (5%-phenyl-substituted methylpolysiloxane) capillary column (30 m × 0.25 mm × 0.25 μm) was used.

$[Fe_2(\mu\text{-}O_2CAr^{4\text{-}FPh})_2(O_2CAr^{4\text{-}FPh})_2(2\text{-}PhOPy)_2]$ (1). A pale yellow solution of $[Fe_2(\mu\text{-}O_2CAr^{4\text{-}FPh})_2(O_2CAr^{4\text{-}FPh})_2(THF)_2]$ (90.0 mg, 60.3 μmol) in CH_2Cl_2 (3 mL)

was combined with 2-phenoxypyridine (2-PhOpy; 20.7 mg, 121 μmol) and allowed to react for 10 min. Vapor diffusion of Et_2O into the filtered solution resulted in the formation of pale yellow crystals of **1** suitable for X-ray crystallography. Yield: 43.0 mg (41%). FT-IR (KBr, cm^{-1}): 3106 (w), 3065 (w), 3035 (w), 2961 (w), 2846 (w), 1605 (s), 1569 (m), 1534 (m), 1511 (vs), 1489 (m), 1473 (s), 1454 (s), 1439 (s), 1410 (m), 1383 (m), 1281 (m), 1226 (s), 1204 (m),1159 (s), 1096 (m), 1014 (m), 892 (w), 859 (m), 845 (m), 839 (m), 807 (m), 789 (m), 774 (m), 752 (w), 733 (w), 712 (w). 691 (w), 579 (w), 555 (m), 528 (m), 478 (w), 460 (w). Anal. Calcd. for **1**, $Fe_2F_8O_{10}N_2C_{98}H_{62}$: C, 69.60; H, 3.70; N, 1.66. Found: C, 69.23; H, 3.83; N, 1.35. Mp: 163–165 °C (dec).

$[Fe_2(\mu\text{-}O_2CAr^{4\text{-}FPh})_2(O_2CAr^{4\text{-}FPh})_2(2\text{-}(m\text{-}MeOPhO)Py)_2]$ (2). A solution of 2-(*m*-MeOPhO)py (32.3 mg, 161 μmol) was added to a stirred suspension of $[Fe_2(\mu\text{-}O_2CAr^{4\text{-}FPh})_2(O_2CAr^{4\text{-}FPh})_2(THF)_2]$ (120 mg, 80.4 μmol) in 5 mL of CH_2Cl_2 and allowed to react for 10 min. After the yellow solution had been filtered, it was subjected to Et_2O vapor diffusion to yield pale yellow-green blocks of **2** suitable for X-ray crystallography. Yield: 94.5 mg (70.0%). FT-IR (KBr, cm^{-1}): 3057 (w), 2961 (w), 2921 (w), 2851 (w), 1605 (s), 1573 (m), 1455 (m), 1437 (m), 1411 (m), 1262 (m), 1160 (m), 1142 (m), 1040 (m), 1017 (m), 853 (w), 80 (m), 788 (w), 770 (w), 712 (m), 555 (w). Anal. Calcd. for **2**·0.25CH_2Cl_2, $Fe_2F_8O_{12}N_2C_{100.25}H_{66.5}Cl_{0.5}$: C, 67.93; H, 3.78; N, 1.58. Found: C, 67.90; H, 3.88; N, 1.13. Mp: 158–160 °C (dec).

$[Fe_2(\mu\text{-}O_2CAr^{4\text{-}FPh})_2(O_2CAr^{4\text{-}FPh})_2(2\text{-}(p\text{-}MeOPhO)Py)_2]$ (3). Pale yellow-green X-ray quality crystals of **3** formed by vapor diffusion of pentanes into a

reaction mixture of $[Fe_2(\mu\text{-}O_2CAr^{4\text{-}FPh})_2(O_2CAr^{4\text{-}FPh})_2(THF)_2]$ (120 mg, 80.4 μmol) and 2-(*p*-MeOPhO)py (32.3 mg, 161 μmol) in 5 mL of CH_2Cl_2. Yield: 118 mg (83%). FT-IR (KBr, cm^{-1}): 3065 (w), 2952 (w), 2837 (w), 1604 (s), 1547 (m), 1511 (s), 1473 (m), 1438 (m), 1277 (w), 1244 (m), 1222 (m), 1200 (m), 1160 (m), 1060 (w), 1016 (w), 846 (m), 809 (m), 793 (w), 775 (w), 735 (w), 713 (w), 550 (w). Anal. Calcd. for **3**, $Fe_2F_8O_{12}N_2C_{100}H_{66}$: C, 68.58; H, 3.80; N, 1.60. Found: C, 68.85; H, 3.95; N, 1.95. Mp: 165–167 °C (dec).

$[Fe_2(\mu\text{-}O_2CAr^{Tol})_2(O_2CAr^{Tol})_2(2\text{-}(o\text{-}HOPhO)Py)_2]$ (4). A pale yellow CH_2Cl_2 solution of $[Fe_2(\mu\text{-}O_2CAr^{Tol})_2(O_2CAr^{Tol})_2(THF)_2]$ (50 mg, 34 μmol) was combined with a solution of 2-(*o*-HOPhO)Py (13 mg, 70 μmol) and allowed to react for 10 min. Vapor diffusion of pentane into the lime-green filtered solution (total volume 2 mL) resulted in the formation of colorless crystals of **4** suitable for X-ray crystallography. Yield: 49 mg (86%). FT-IR (KBr, cm^{-1}): 3050 (w), 3019 (w), 2917 (w), 2857 (w), 1605 (s), 1590 (s), 1574 (s), 1563 (s), 1515 (m), 1492 (m), 1472 (s), 1455 (m), 1437 (s), 1411 (m), 1378 (m), 1277 (s), 1253 (w), 1185 (w), 1148 (w), 1108 (w), 1094 (w), 1016 (w), 897 (w), 861 (w), 817 (w), 800 (m), 767 (m), 734 (m), 712 (w), 702 (w), 584 (w), 545 (w), 519 (w), 452 (w). Anal. Calcd. for **4**, $Fe_2O_{12}N_2C_{106}H_{86}$: C, 75.27; H, 5.12; N, 1.66. Found: C, 74.75; H, 5.10; N, 1.93. Mp: 118–120 °C (dec).

$[Fe_3(\mu_2\text{-}O_2CAr^{Tol})_2(O_2CAr^{Tol})_2(2\text{-}(o\text{-}\mu_2\text{-}O\text{-}PhO)Py)_2]$ (5). In a procedure similar to that described above, a CH_2Cl_2 solution of $[Fe_2(\mu\text{-}O_2CAr^{Tol})_2(O_2CAr^{Tol})_2(THF)_2]$ (47 mg, 32 μmol) was combined with a solution of 2-(*o*-HOPhO)Py (8.0 mg, 43 μmol). The total volume of the resulting solution was ca.

2.5 mL. After filtration of the solution, ca. 2 mL of Et_2O was added and the lime-green solution was subjected to vapor diffusion of pentane. Lime-green blocks of **5**, suitable for X-ray crystallography, were harvested. Yield: 28 mg (80%). FT-IR (KBr, cm^{-1}): 3054 (w), 3021 (w), 2916 (w), 2854 (w), 1604 (m), 1597 (m), 1572 (m), 1545 (s), 1514 (s), 1490 (s), 1472 (s), 1436 (s), 1411 (m), 1387 (s), 1286 (s), 1257 (s), 1181 (w), 1156 (w), 1110 (w), 1098 (w), 1022 (w), 898 (w), 859 (w), 834 (w), 817 (m), 800 (m), 785 (m), 768 (m), 753 (m), 738 (m), 715 (m), 699 (w), 582 (m), 552 (w), 527 (m), 455 (w), 425 (w). Anal. Calcd. for **5**, $Fe_3O_{12}N_2C_{106}H_{84}$: C, 72.94; H, 4.85; N, 1.61. Found: C, 72.89; H, 4.98; N, 1.59. Mp: 215–217 °C (dec).

X-ray Crystallographic Studies. Single crystals were taken directly from the reaction vessel, coated with Paratone-N oil, and mounted at room temperature on the tips of quartz fibers or nylon loops (OXFORD magnetic mounting system), and cooled to 110 K under a stream of cold N_2 maintained by a KRYO-FLEX low-temperature apparatus. Intensity data were collected on a Bruker (formerly Siemens) APEX CCD diffractometer with graphite-monochromated Mo Kα radiation (λ = 0.71073 Å) controlled by a Pentium-based PC running the SMART software package.[35] The structures were solved by direct methods and refined on F^2 by using the SHELXTL-97 software.[36,37] Empirical absorption corrections were applied with SADABS[38] and the structures were checked for higher symmetry with PLATON.[39] All non-hydrogen atoms were refined anisotropically. Hydrogen atoms were generally assigned idealized positions and given thermal parameters equivalent to either 1.5 (methyl hydrogen atoms) or 1.2 (all other hydrogen atoms) times the thermal parameter of the

carbon to which they were attached. The hydrogen atom of the hydroxyl group (O5) of the 2-(pyridin-2-yloxy)phenol ligand in **4** was located on a difference electron density map. Complex **1** crystallizes without any solvent in the lattice. A pentane and a CH_2Cl_2 molecule share one position with a refined ratio of 73:27 in compound **2**. A molecule of CH_2Cl_2 was identified in the asymmetric unit of complex **3**. In the structure of **4**, a pentane molecule was disordered over two positions with 58% and 42% occupancy. Complex **5** contains two molecules of CH_2Cl_2 per triiron unit. Crystal data, data collection parameters, and structure refinement details for **1**–**5** are provided in Table 1.

Mössbauer Spectroscopy. Mössbauer spectra were obtained on an MS1 spectrometer (WEB Research Co.) with a ^{57}Co source in a Rh matrix maintained at room temperature. All samples were enriched with ^{57}Fe (40%) and prepared from $^{57}Fe(OTf)_2{\cdot}2MeCN$, which was synthesized following a published procedure.[40] Solid samples of **4** and **5** were prepared by suspending ca. 15 mg of pulverized compound in Apiezon N-grease and loading the suspension into a nylon sample holder. Solution samples of **4** and **5** were prepared in benzene and frozen. Data were acquired at temperatures ranging from 4.2 K to 200 K. The isomer shift (δ) values are reported with respect to natural iron foil that was used for velocity calibration at room temperature. The spectra were fit to Lorentzian lines by using the WMOSS plot and fit software.[41]

Oxidation Reactions. Solutions of **1**–**4** in CH_2Cl_2 prepared under anaerobic conditions in a glove box and dry dioxygen was bubbled through these solutions for at least 2–4 min at –78 °C. The reaction mixture was allowed to

warm up to 25 °C and stirred overnight. For the analysis of the products from the oxidation reaction, it was necessary to remove iron from the solutions. A chelating resin, CHELEX-100®, was employed for this purpose. The resulting pale-colored solutions were filtered and analyzed by GC-MS spectrometry by comparing their properties to those of authentic samples.

UV-vis Spectroscopy Studies. UV-vis spectra were recorded on a Hewlett-Packard 8453 diode array spectrophotometer. Solutions of [Fe_2] in CH_2Cl_2 or toluene under N_2-atmosphere were cooled to –78 °C (acetone/dry ice) in a custom-made quartz-cuvette, 1 cm pathlength, fused into a vacuum-jacketed dewar. Dry O_2 was bubbled through the solutions for 30 s, and UV-vis spectra were recorded at various time intervals.

EPR Spectroscopy. X-band EPR spectra were acquired on a Bruker EMX EPR spectrometer at the Department of Chemistry Instrumentation Facilities at MIT running Bruker Win-EPR software. An OXFORD instruments EPR 900 cryostat and an ITC503 controller were used to maintain the temperature at 4 K. Samples were prepared by transferring 300 μL aliquots of a 3.0 M solution of **3** in CH_2Cl_2 into EPR tubes under anaerobic conditions, which were then septum-sealed. Dry dioxygen was bubbled through these solutions for at least 20 s at –78 °C. The oxygenated solutions were frozen after 1, 2, 5, and 60 min reaction time at 77 K.

Table 3.1. Crystal Data and Details of Data Collection for **1**–**5**.

	1	**2**·1.5C_5H_{12}·0.5CH_2Cl_2	**3**·2CH_2Cl_2	**4**·C_5H_{12}	**5**·2CH_2Cl_2
Empirical formula	$Fe_2C_{98}H_{62}N_2O_{10}F_8$	$Fe_2C_{107.9}H_{84.7}N_2O_{12}F_8Cl_{1.1}$	$Fe_2C_{102}H_{70}N_2O_{12}F_8Cl_4$	$Fe_2C_{116}H_{108}O_{12}N_2$	$Fe_3C_{108}H_{88}O_{12}N_2Cl_4$
Formula weight	1691.20	1902.33	1921.10	1833.74	1915.15
Crystal System	Monoclinic	Monoclinic	Triclinic	Monoclinic	Orthorhombic
Space group	$P2_1/c$	$C2/c$	$P\bar{1}$	$P2_1/c$	$Pccn$
a (Å)	12.205(4)	23.578(5)	12.160(2)	16.035(3)	25.648(5)
b (Å)	24.088(7)	15.730(5)	13.918(3)	23.707(4)	14.847(3)
c (Å)	13.440(4)	25.052(6)	13.924(3)	13.007(2)	23.726(5)
α (deg)			105.674(3)		
β (deg)	97.980(6)	104.898(5)	92.481(3)	104.267(3)	
γ (deg)			106.665(3)		
V (Å^3)	3913(2)	8979(4)	2154.9(7)	4791.8(14)	9035(3)
Z	2	4	1	2	4
ρ_{calc} (g/cm^3)	1.435	1.407	1.480	1.272	1.408
Temperature (K)	110	110	110	110	110
μ (Mo Kα), (mm^{-1})	0.456	0.438	0.545	0.368	0.660
Θ limits (deg)	2.28 to 25.68	2.12 to 27.12	2.18 to 25.03	2.16 - 25.68	2.20 – 27.10
Crystal size (mm)	0.08 x 0.10 x 0.20	0.10 x 0.10 x 0.15	0.10 x 0.15 x 0.10	0.06 x 0.22 x 0.40	0.06 x 0.20 x 0.35
Completeness to Θ	99.9 %	99.9 %	99.7 %	99.9 %	99.9 %
max, min peaks (e/Å^3)	0.691 and -0.678	0.680 and -0.940	0.946 and -0.578	1.381 and -0.737	0.458 and -0.373
Total no. of data	57171	72313	29990	69173	140867
No. of unique data	7431	9902	7661	9072	9962
Goodness-of-fit on F^2	1.112	1.104	1.121	1.030	1.089
R_1 (%)[a]	6.34	6.17	6.43	6.57	4.77
wR_2 (%)[b]	11.91	14.31	14.98	15.25	9.90

[a] $R_1 = \Sigma||F_o|-|F_c||/\Sigma|F_o|$, [b] $wR_2 = \{\Sigma[w(F_o^2-F_c^2)]/\Sigma[w(F_o^2)^2]\}^{1/2}$

Results and Discussion

Synthesis and Structural Characterization of $[Fe_2(\mu\text{-}O_2CAr^{4\text{-}FPh})_2(O_2CAr^{4\text{-}FPh})_2(L)_2]$ with L = 2-PhOPy (1), 2-(*m*-OMePhO)Py (2), 2-(*p*-OMePhO)Py (3). Reaction of $[Fe_2(\mu\text{-}O_2CAr^{4\text{-}FPh})_2(O_2CAr^{4\text{-}FPh})_2(THF)_2]$ with two equivalents of *N*-donor ligand (L) led to the formation of the diiron(II) complexes **1**, **2**, and **3** having the general formula $[Fe_2(\mu\text{-}O_2CAr^{4\text{-}FPh})_2(O_2CAr^{4\text{-}FPh})_2(L)_2]$ in good yields (Scheme 3.1).

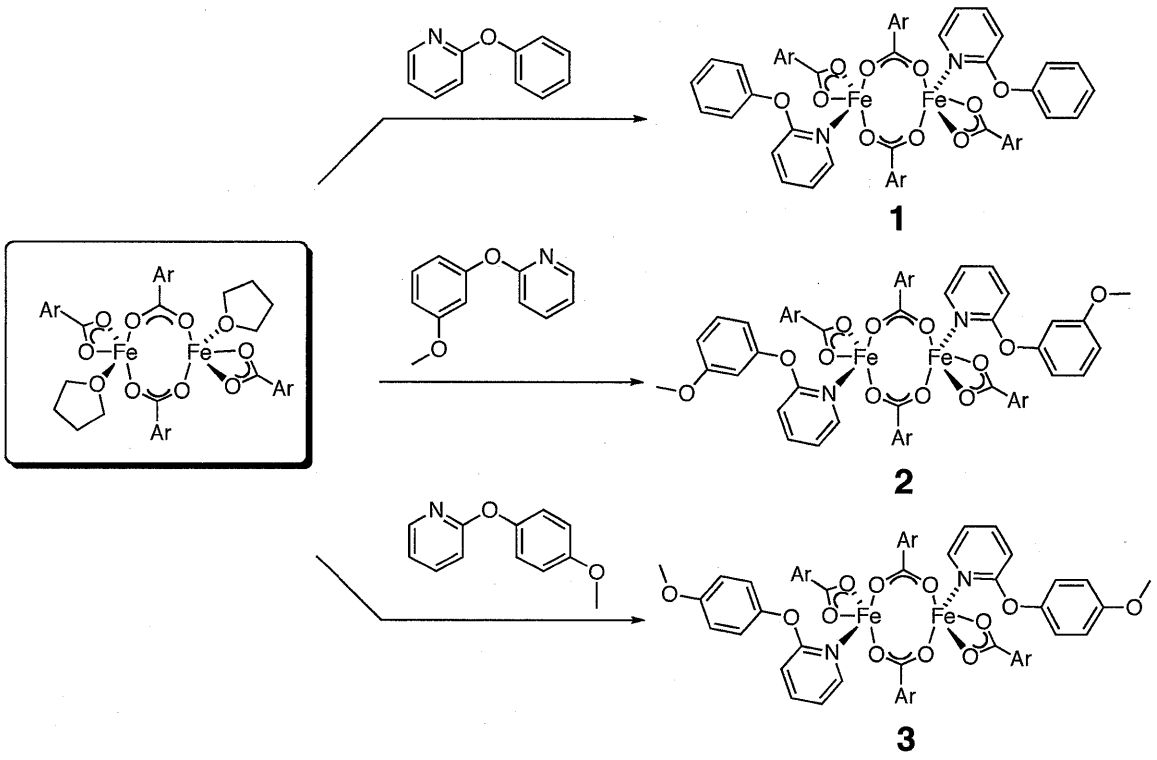

Scheme 3.1.

The structures of **1–3** are displayed in Figure 3.1 and pertinent bond lengths and angles are listed in Table 3.2. Each compound adopts a windmill geometry in which the iron atoms, related by a center of inversion, are

coordinated by two bridging carboxylates, a terminal carboxylate and a nitrogen atom from a pyridine ligand. The geometric parameters of **1**–**3** are very similar. The rather long Fe–Fe distances lie in a narrow range between 4.368 Å and 4.424 Å and are typical for doubly carboxylate-bridged diiron(II) complexes.[18]

Table 3.2. Selected Interatomic Bond Lengths (Å) and Angles (deg) for **1**–**4**.

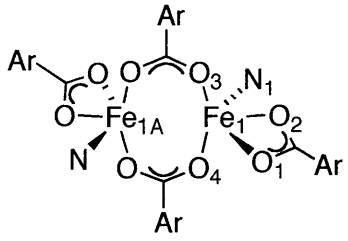

	1	**2**·1.5C_5H_{12} ·0.5CH_2Cl_2	**3**·2CH_2Cl_2	**4**·2C_5H_{12}
Fe(1)–Fe(1A)	4.3679(16)	4.4243(9)	4.4153(12)	4.2743(12)
Fe(1)–N(1)	2.133(3)	2.132(2)	2.137(3)	2.137(3)
Fe(1)–O(1)	2.237(2)	2.308(2)	2.344(3)	2.398(3)
Fe(1)–O(2)	2.089(2)	2.0590(19)	2.054(2)	2.054(3)
Fe(1)–O(3)	1.967(2)	1.946(2)	1.955(3)	1.927(3)
Fe(1)–O(4)	2.018(2)	2.0182(19)	2.026(2)	2.028(3)
O(1)–Fe(1)–O(2)	60.33(8)	60.13(7)	59.56(9)	58.43(9)
O(1)–Fe(1)–O(3)	93.09(9)	95.87(8)	96.37(9)	104.65(10)
O(1)–Fe(1)–O(4)	101.00(9)	97.13(7)	97.60(9)	88.28(10)
O(2)–Fe(1)–O(3)	133.53(9)	131.98(9)	135.09(10)	134.04(12)
O(2)–Fe(1)–O(4)	109.52(10)	112.63(8)	110.45(10)	109.22(11)
O(3)–Fe(1)–O(4)	112.81(10)	111.12(9)	109.89(9)	112.74(12)
O(1)–Fe(1)–N(1)	153.88(9)	149.56(8)	154.56(9)	147.91(10)
O(2)–Fe(1)–N(1)	94.81(9)	89.46(9)	95.49(10)	90.10(11)
O(3)–Fe(1)–N(1)	99.97(10)	105.01(9)	99.40(10)	102.12(12)
O(4)–Fe(1)–N(1)	94.67(10)	95.71(8)	95.5(1)	97.45(11)
O(2)–O(5)	–	–	–	2.686(4)

Numbers in parentheses are estimated standard deviations of the last significant figures.

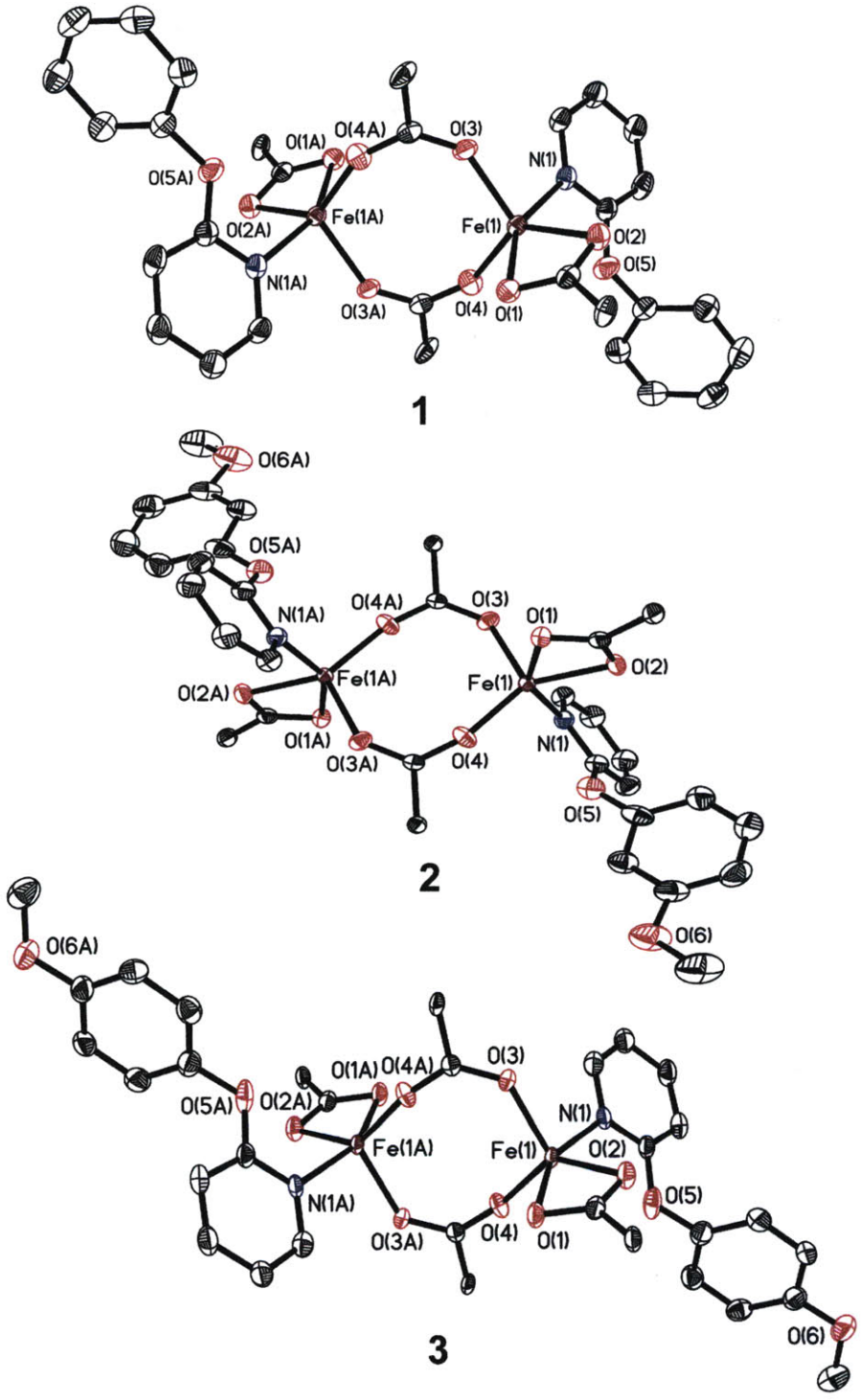

Figure 3.1. ORTEP diagrams of $[Fe_2(\mu\text{-}O_2CAr^{4\text{-}FPh})_2(O_2CAr^{4\text{-}FPh})_2(2\text{-}PhOPy)_2]$ (**1**), $[Fe_2(\mu\text{-}O_2CAr^{4\text{-}FPh})_2(O_2CAr^{4\text{-}FPh})_2(2\text{-}(m\text{-}MeOPhO)Py)_2]$ (**2**), and $[Fe_2(\mu\text{-}O_2C\text{-}Ar^{4\text{-}FPh})_2(O_2CAr^{4\text{-}FPh})_2(2\text{-}(p\text{-}MeOPhO)Py)_2]$ (**3**) showing 50% probability thermal ellipsoids for all non-hydrogen atoms. The 4-fluorophenyl groups of the $^{-}O_2CAr^{4\text{-}FPh}$ ligands are omitted for clarity.

Interestingly, a related diiron(II) compound with 2-phenylthiopyridine, the sulfur analog of 2-phenoxypyridine, adopts a rather different geometry and stoichiometry.[25] In this case, a triply bridged diiron(II) complex forms having a single pyridine donor bound to the diiron unit, the formula being $[Fe_2(\mu\text{-}O_2CAr^{Tol})_3(O_2CAr^{Tol})(L)]$. Chart 3.3 shows a comparison of this structure with that of **1**. The Fe–S distance in the thioether complex is 3.090 Å, which indicates a very weak interaction between the two atoms made possible by the larger size and more diffuse orbitals of sulfur.[26] In the case of the phenoxypyridine complex, however, no bonding interaction is feasible at an Fe–O distance larger than 3 Å and the complex therefore adopts the typical windmill structure. It is unlikely that the use of different carboxylates, $^{-}O_2CAr^{Tol}$ vs $^{-}O_2CAr^{4\text{-}FPh}$, would affect the coordination geometry.

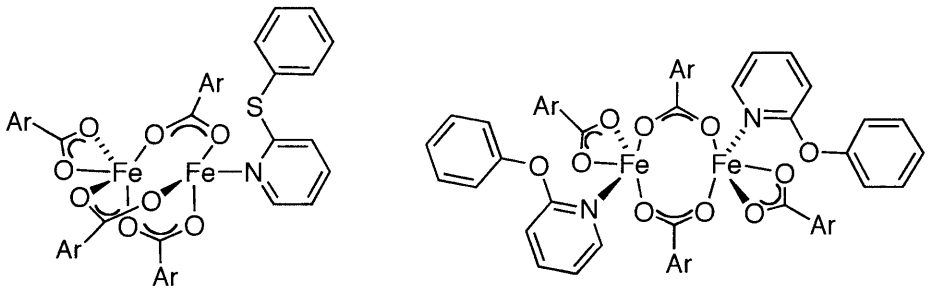

Chart 3.3. Comparison of the structure of $[Fe_2(\mu\text{-}O_2CAr^{Tol})_3(O_2CAr^{Tol})(2\text{-}PhSPy)]$[25] (left) with that of $[Fe_2(\mu\text{-}O_2CAr^{4\text{-}FPh})_2(O_2CAr^{4\text{-}FPh})_2(2\text{-}PhOPy)_2]$ (**1**; right).

Synthesis and Structural Characterization of Compounds 4 and 5 with 2-(Pyridin-2-yloxy)phenol. Treatment of $[Fe_2(\mu\text{-}O_2CAr^{Tol})_2(O_2CAr^{Tol})_2(THF)_2]$ with 2-(pyridin-2-yloxy)phenol in CH_2Cl_2 resulted in a lime-green solution,

which was initially subjected to vapor diffusion of pentane or Et_2O to isolate the product. We anticipated formation of a doubly bridged diiron complex having a structure analogous to those of compounds **1**–**3**. Colorless block-shaped crystals of the diiron(II) complex $[Fe_2(\mu\text{-}O_2CAr^{Tol})_2(O_2CAr^{Tol})_2(2\text{-}o\text{-}HOPhOPy)_2]$ (**4**) were isolated from the reaction mixture by pentane vapor diffusion in high yield (Scheme 3.2). Complex **4** has a windmill structure, as occurs in **1**–**3**, with each iron center being pentacoordinate and an Fe–Fe distance of 4.2743(12) Å. The structure is shown in Figure 3.2 and selected bond lengths and angles are compared to those of **1**–**3** in Table 3.2. The tethered phenol forms a strong hydrogen-bond to an oxygen atom of a terminal carboxylate, the O–O distance being 2.686(4) Å. This compound is rather air-sensitive and the colorless crystals readily turn black upon exposure to air. An attempt to incorporate meta- and para-(pyridin-2-yloxy)phenol ligands into the diiron(II) complex resulted in the formation of colorless crystals, which suffered from loss of solvent and rapid decomposition in air, which precluded their study by X-ray crystallography.

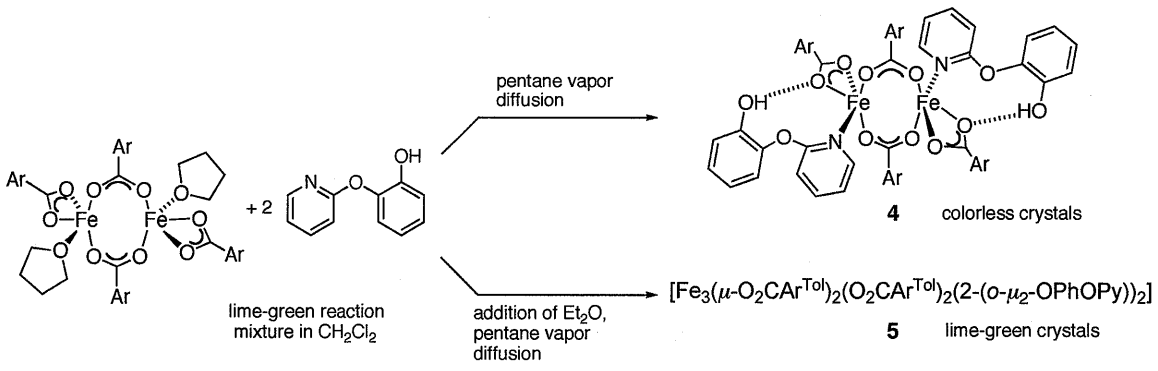

Scheme 3.2.

When the reaction mixture from the synthesis of **4**, which contained Et_2O, was further subjected to vapor diffusion of pentane, lime-green crystals of the triiron(II) compound $[Fe_3(\mu\text{-}O_2CAr^{Tol})_2(O_2CAr^{Tol})_2(2\text{-}(o\text{-}\mu\text{-}OPhO)Py)_2]$ (**5**) formed in significant quantity (Scheme 3.2). Knowing the exact composition of **5** from its crystal structure allowed us to adjust the stoichiometry of reagents to prevent formation of the dinuclear compound **4** as a side product and the complex could then be prepared in excellent yield (80%). Compound **5** has an unprecedented triiron(II) core, which is displayed in Figure 3.2. Selected bond lengths and angles are listed in Table 3.3. Three iron(II) atoms subtend an angle of 134° at the central atom, which resides on a two-fold symmetry axis. The two identical neighboring iron atoms contain a pentacoordinate ligand environment and are each connected to the central atom by a carboxylate and a phenoxide bridge. In contrast to **4**, the phenol is deprotonated, as deduced by charge considerations. The 2-(pyridin-2-yloxy)phenoxide ligand connects all three iron atoms, which gives rise to the bent Fe_3 unit. The central iron atom has a rare four-coordinate, pseudo-tetrahedral coordination environment with only *O*-atom donors, that has not been previously been reported for triiron complexes. Other examples of triiron(II) complexes with carboxylate-bridges have been reported previously, but they adopt a linear or nearly linear geometry for the iron atoms.[42-45] The formation of **5** may be driven by the tendency of the phenoxide ligand to bridge metal ions, as commonly encountered for polynuclear complexes containing phenolic units.[46]

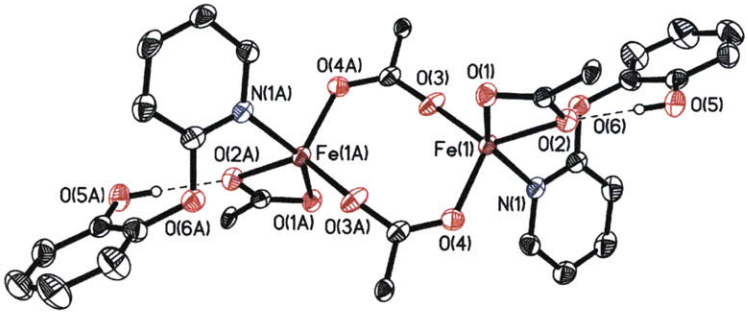

4

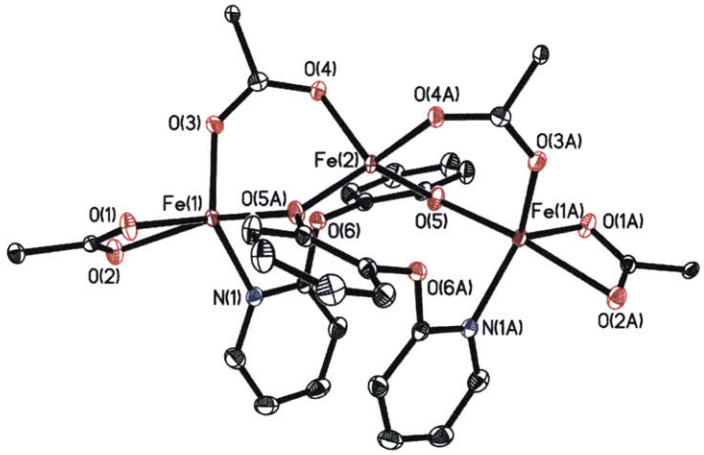

5

Figure 3.2. ORTEP diagrams of $[Fe_2(\mu\text{-}O_2CAr^{Tol})_2(O_2CAr^{Tol})_2(2\text{-}(o\text{-}HOPhO)Py)_2]$ (**4**) and $[Fe_3(\mu_2\text{-}O_2CAr^{Tol})_2(O_2CAr^{Tol})_2(2\text{-}(o\text{-}\mu_2\text{-}O\text{-}PhO)Py)_2]$ (**5**), showing 50% probability thermal ellipsoids for all non-hydrogen atoms. The tolyl groups of the $^{-}O_2CAr^{Tol}$ ligands are omitted for clarity.

Table 3.3. Selected Bond Distances and Angles for **5**.

	Bond Length (Å)		Bond Angle (deg)
Fe(1)–Fe(2)	3.4127(6)	Fe(1)–Fe(2)–Fe(1A)	133.98
Fe(1)–N(1)	2.1133(19)	Fe(1)–O(5)–Fe(2)	115.04(7)
Fe(1)–O(1)	2.0505(16)	O(4)–Fe(2)–O(4A)	104.85(9)
Fe(1)–O(2)	2.2931(17)	O(4)–Fe(2)–O(5)	113.00(6)
Fe(1)–O(3)	1.9715(16)	O(5A)–Fe(2)–O(4)	98.18(6)
Fe(1)–O(5A)	2.0596(16)	O(5)–Fe(2)–O(5A)	128.17(10)
Fe(2)–O(4)	2.0306(16)		
Fe(2)–O(5A)	1.9856(15)		

Numbers in parentheses are estimated standard deviations of the last significant figures.

Mössbauer Spectroscopy. Zero-field Mössbauer spectra of **4** and **5** were acquired at 4.2 K and are displayed in Figure 3.3. For both compounds the Mössbauer isomer shift and quadrupole splitting parameters fall in the ranges δ = 1.17 – 1.23 mm/s and ΔE_Q = 2.91 – 3.08 mm/s, values typical for high-spin diiron(II) complexes.[48-50] The spectra of powdered solid and benzene solution samples of **4** were acquired and fit to a single quadrupole doublet with essentially identical isomer shifts (δ = 1.23(2) and 1.22(2) mm/s) and quadrupole splitting parameters (ΔE_Q = 3.08(2) and 3.07(2) mm/s). The spectra of the solid displayed a somewhat broader linewidth of Γ = 0.38 mm/s (vs Γ = 0.30 mm/s for the solution sample). These values correspond to those generally observed in carboxylate-rich diiron compounds with an NO_4 coordination environment.[47] This experiment also confirms that the dinuclear complex **4** stays intact in solution and that there is no formation of the trinuclear species **5**. The Mössbauer spectrum of a powdered sample of **5** was fit to a single, rather broad quadrupole doublet with a linewidth of Γ = 0.45(2) mm/s, an isomer shift of δ = 1.18(2) mm/s and a quadrupole splitting parameter of ΔE_Q = 2.92(2) mm/s (Figure 3B). Despite the significantly different coordination environments of the two different iron sites in this complex - four-coordinate for the central atom and five-coordinate for the outer two iron atoms - their Mössbauer parameters were nearly identical and the two quadrupole doublets could not be resolved. This result is not surprising, considering that the isomer shifts and the quadrupole splitting parameters fall within a narrow range for high spin iron(II) sites.[47] An attempt to deconvolute the overlapping signals by increasing the temperature stepwise from 4.2 K to 200 K,

did not resolve the spectra. The temperature-dependent Mössbauer parameters of the samples are listed in Table 3.4. A frozen sample of **5** in a solution of benzene was also measured and, like the solid sample, it revealed only a single, broad quadrupole doublet (Γ = 0.49(2) mm/s) with Mössbauer parameters of δ = 1.24(2) mm/s and ΔE_Q = 2.80(2).

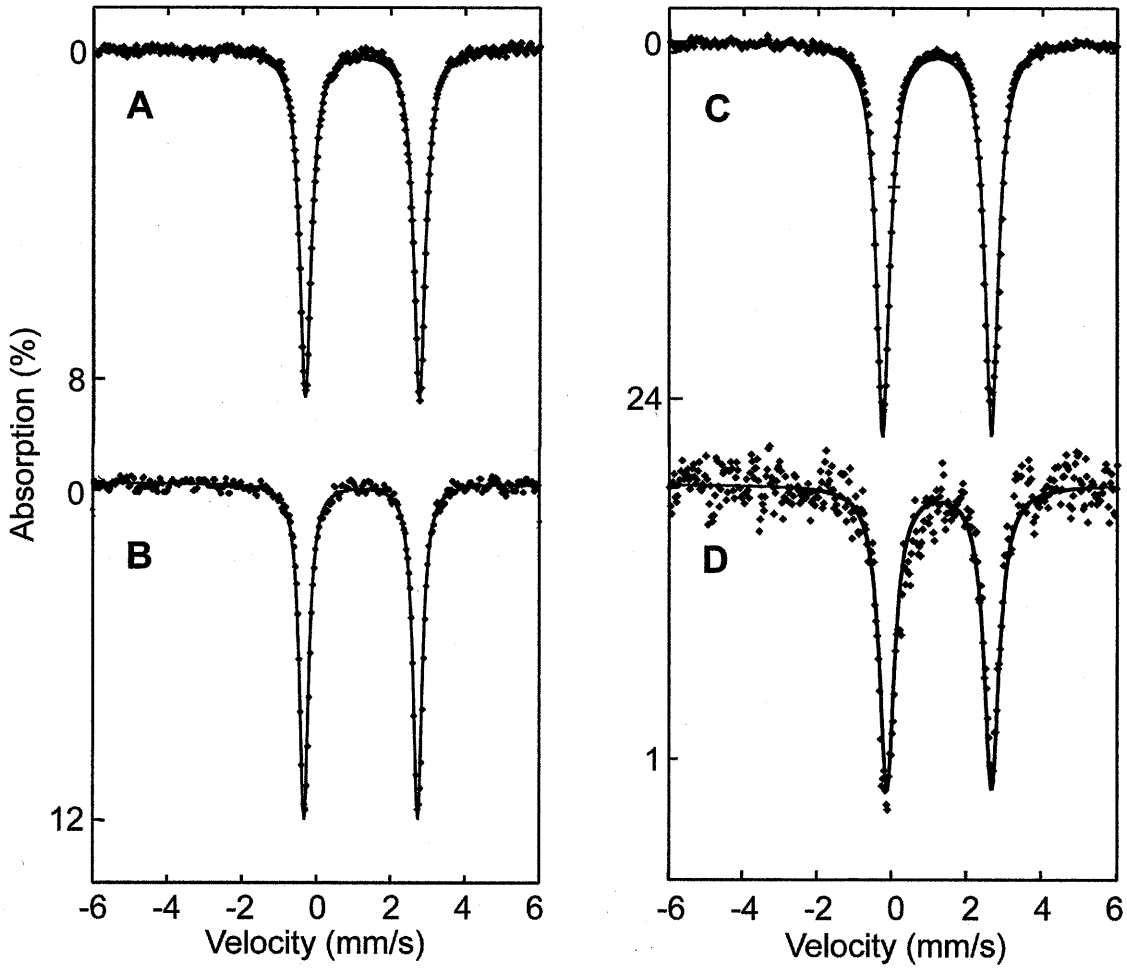

Figure 3.3. Zero-field Mössbauer spectra [experimental data (◆), calculated fit (–)] of solid samples of **4** (A) and **5** (C) and solution samples of **4** (B) and **5** (D) in benzene. All samples were recorded at 4.2 K, except sample D, which was acquired at 90 K.

Table 3.4. Mössbauer Parameters for a Solid Sample of **5**, Acquired at Different Temperatures.

Temperature (K)	δ (mm/s)	ΔE_Q (mm/s)	Γ (mm/s)
4.2	1.18(2)	2.92(2)	0.41
77	1.16(2)	2.88(2)	0.38
150	1.13(2)	2.76(2)	0.34
200	1.10(2)	2.67(2)	0.34

Dioxygen Reactivity Studies. Solutions of **1–3** in CH_2Cl_2 were exposed to dioxygen at –78 °C and examined by UV-vis spectroscopy. Broad visible absorption bands at λ_{max} = 700 and 710 nm ($\varepsilon \approx$ 500–600 M^{-1} cm^{-1}) for compounds **2** and **3**, respectively, grew in over 20 min. The spectra (Figure 3.4) have features nearly identical to those previously reported for oxygenated intermediates of related diiron complexes of *m*-terphenyl carboxylate ligands.[28,48-50] The optical transitions can be assigned to an intervalence charge transfer originating from a mixed-valent tetracarboxylate-bridged diiron(II,III) complex.[48,49]

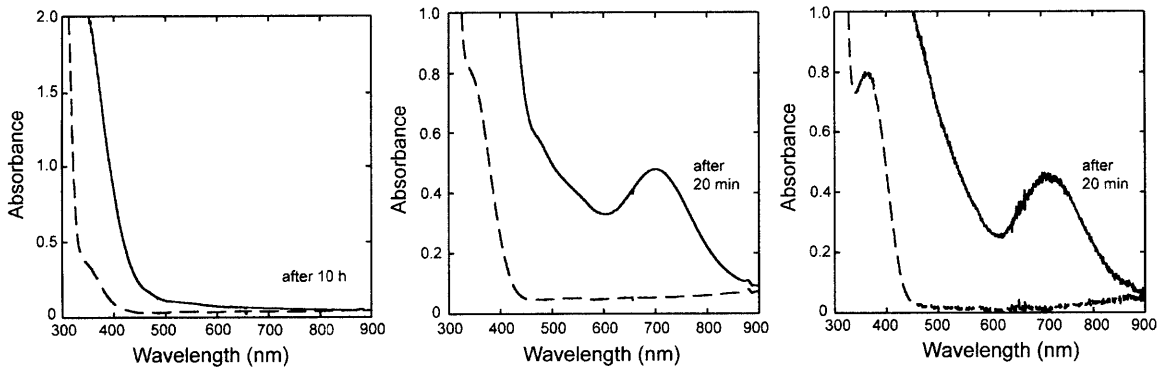

Figure 3.4. UV-vis spectra of O_2 reactions, recorded at –78 °C in CH_2Cl_2, of $[Fe_2(\mu\text{-}O_2CAr^{4\text{-}FPh})_2(O_2CAr^{4\text{-}FPh})_2(2\text{-}PhOPy)_2]$ (**1**, left), $[Fe_2(\mu\text{-}O_2CAr^{4\text{-}FPh})_2(O_2CAr^{4\text{-}FPh})_2(2\text{-}(m\text{-}OMePhO)Py)_2]$ (**2**, center), and $[Fe_2(\mu\text{-}O_2CAr^{4\text{-}FPh})_2(O_2CAr^{4\text{-}FPh})_2(2\text{-}(p\text{-}OMePhO)Py)_2]$ (**3**, right), displaying the spectra of the diiron(II) compound (---) and the intermediates (—).

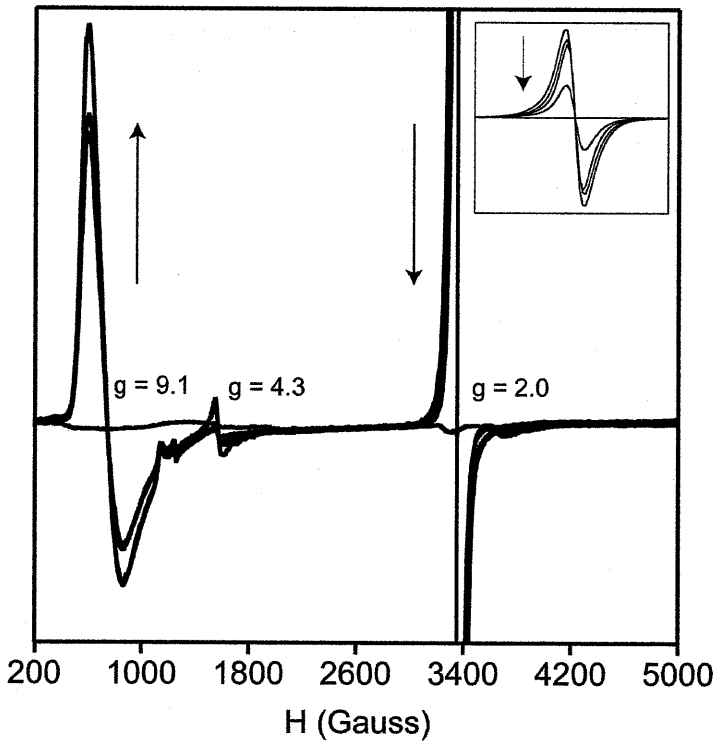

Figure 3.5. X-band EPR spectra of frozen solution samples of **2** and oxygenated **2** recorded at 4 K. The spectra represent 1, 2, 5, and 60 min reactions of **2** with dioxygen at –78 °C. The inset displays the decay of the signal at g = 2.0. The signal at g = 4.3 arises from a small amount of high-spin Fe(III) impurity.

The different electronic properties of the 2-PhOPy pyridine donor ligand vs those in **2** and **3**, which both contain methoxy-substituted phenoxypyridines, may account for the absence of an absorption band around 700 nm in the reaction of **1** with O_2 at low temperature. EPR spectra of oxygenated solutions of **2**, recorded at 4.2 K, revealed two signals g = 9.1 and g = 2.0, which correspond to a paramagnetic diiron(II,III) species with an S = 9/2 ground state and a diiron(III,IV) species with an S = 1/2 ground state, respectively (Figure 3.5). Both species are present in significant quantities after 1 min of reaction time, but the diiron(III,IV) species decays and while the amount of diiron(II,III) species increases over the time course of an hour. These two species form in a

previously established pathway of intermolecular electron transfer involving an oxygenated high-valent diiron species and the diiron(II) starting material.[51] This bimolecular reaction pathway is frequently observed for the oxygenation of diiron(II) complexes containing the $^{-}O_2CAr^{Tol}$ carboxylate ligand and has been thoroughly investigated by resonance Raman, Mössbauer, UV-vis, EPR spectroscopy, and X-ray crystallography.[22,50-52] The generation of the mixed-valent diiron species depends on temperature, solvent, and geometry of the diiron complex, but a detailed mechanism has not been established.

Solutions of **4** and **5** are remarkably air-sensitive and instantaneously turn deep purple upon exposure to air. When toluene solutions of these complexes were exposed to an excess of dioxygen at low temperature, the absorption spectra (Figure 3.6) revealed intense phenoxide-to-iron(III) charge-transfer bands at λ_{max} = 515 and 535 nm, respectively, which are characteristic for such compounds.[53,54] The UV-vis spectra of **4** and **5** are identical, displaying an absorption at 385 nm, which can be assigned to an Fe(II) → pyridine charge transfer (MLCT) band.[47] An X-band EPR spectrum of a freeze-quenched oxygenated solution of **4** did not display a characteristic signal for a phenoxy radical,[55] so this species can be excluded. In general, these radicals are only stable when the ortho and para positions of the phenol ring are blocked.

Phenoxy-substituents were appended to the pyridine ligands of the diiron compounds in order to incorporate an aryl group close as a potential substrate for oxygenation. The phenyl linker was chosen to provide additional flexibility and to avoid a benzylic position that is readily oxidized as previously established for

these types of compounds.[23] Methoxy- and hydroxy- substituents were included to activate the phenyl ring toward electrophilic substitution, because hydroxylation of aromatic substrates occurs by electrophilic attack on the π-system, as it is observed for peroxo intermediates in sMMOH[7] and ToMOH.[56]

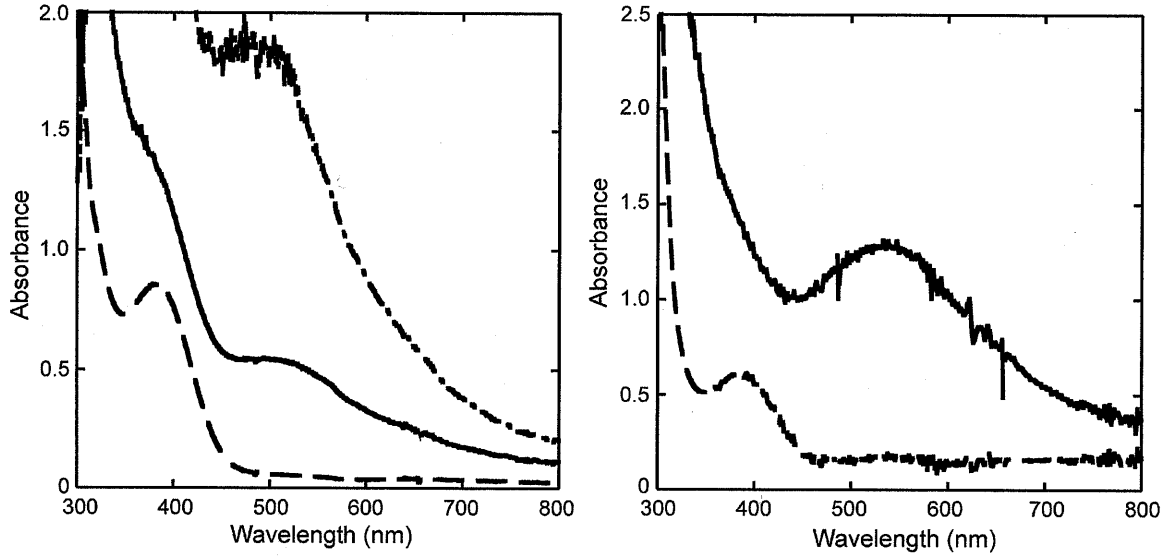

Figure 3.6. UV-vis spectra of O_2 reactions, recorded at –78 °C in toluene. Left: $[Fe_3(\mu_2\text{-}O_2CAr^{Tol})_2(O_2CAr^{Tol})_2(2\text{-}(o\text{-}\mu_2\text{-}O\text{-}PhO)Py)_2]$ (**5**) (---); the intermediate after 30 min (—) and after 7 h (–•–). Right: $[Fe_2(\mu\text{-}O_2CAr^{4\text{-}FPh})_2(O_2CAr^{4\text{-}FPh})_2(2\text{-}PhOPy)_2]$ (**4**) (---), the intermediate (—) after 3 h.

Analysis of the reaction mixture by GC–MS following oxygenation of the diiron(II) complexes **1**–**4**, however, did not reveal oxidation of the *N*-donor ligand. For the oxidation reaction of **3**, the pyridine ligand was recovered quantitatively. The reason for the failed oxidation may be explained by an inherent inability of the intermediate to hydroxylate aromatic substrates. Although benzylic oxidation was achieved in related diiron systems upon oxygenation,[23] the C–H homolytic bond dissociation energy is much larger in aromatic systems (85 kcal/mol vs ca.

110 kcal/mol, respectively).[57] Alternatively, the substrate moiety may be unfavorably positioned with respect to the peroxodiiron(III) unit. Unlike previous diiron compounds with tethered substrates, the phenyl ring is located farther away from the diiron center as found by X-ray crystallographic structural analysis and might be sterically unable to approach the oxygenated diiron center.[22-26] The oxidation of tethered phosphine and sulfide groups in analogous diiron systems revealed that the extent of oxidation diminishes when the substrate is systematically moved away from the diiron center.[24-26] In order to test this hypothesis, the tethered substrates would need to be redesigned to bring them closer to the diiron center. Alternatively, a diiron complex with less bulky carboxylates could be used to reduce steric crowding at the dimetal center.

Conclusions

The palette of carboxylate-rich diiron(II) compounds with tethered substrates was expanded in this work. Previously, oxidation of sulfide, phosphine, and benzyl-moieties and oxidative *N*-dealkylation were established with these systems. A series of doubly bridged diiron(II) complexes were prepared with methoxy- and hydroxy-substituted phenoxypyridine ligands to serve as substrates for aromatic hydroxylation following the introduction of dioxygen. In the reaction of these diiron(II) complexes with dioxygen no oxidation of the aryl substituent was observed, indicating the importance of substrate proximity to the diiron active site. Interesting coordination chemistry was observed with the 2-(pyridin-2-yloxy)phenol ligand that led to the formation of two

complexes of different nuclearity. In one case, the hydroxyl group on the phenoxypyridine is protonated and a diiron(II) complex is formed. Upon deprotonation, the phenoxide bridges two iron centers and an unprecedented triiron(II) core structure was obtained.

Acknowledgements. This work was supported by Grant GM032134 from the National Institute of General Medical Sciences. I thank Dr. Sebastian Stoian for assistance in acquiring the Mössbauer spectra and Dr. Erwin Reisner for helpful discussions.

References

(1) Sazinsky, M. H.; Lippard, S. J. *Acc. Chem. Res.* **2006**, *39*, 558-566.

(2) Murray, L. J.; Lippard, S. J. *Acc. Chem. Res.* **2007**, *40*, 466-474.

(3) Merkx, M.; Kopp, D. A.; Sazinsky, M. H.; Blazyk, J. L.; Müller, J.; Lippard, S. J. *Angew. Chem., Int. Ed.* **2001**, *40*, 2782-2807.

(4) Sazinsky, M. H.; Bard, J.; Di Donato, A.; Lippard, S. J. *J. Biol. Chem.* **2004**, *279*, 30600-30610.

(5) McCormick, M. S.; Sazinsky, M. H.; Condon, K. L.; Lippard, S. J. *J. Am. Chem. Soc.* **2006**, *128*, 15108-15110.

(6) Sazinsky, M. H.; Dunten, P. W.; McCormick, M. S.; Di Donato, A.; Lippard, S. J. *Biochemistry* **2006**, *45*, 15392-15404.

(7) Beauvais, L. G.; Lippard, S. J. *J. Am. Chem. Soc.* **2005**, *127*, 7370-7378.

(8) Valentine, A. M.; Stahl, S. S.; Lippard, S. J. *J. Am. Chem. Soc.* **1999**, *121*, 3876-3887.

(9) Colby, J.; Stirling, D. I.; Dalton, H. *Biochem. J.* **1977**, *165*, 395-402.

(10) Prior, S. D.; Dalton, H. *FEMS Microbiol. Lett.* **1985**, *29*, 105-109.

(11) Green, J.; Dalton, H. *J. Biol. Chem.* **1989**, *264*, 17698-17703.

(12) Fox, B. G.; Borneman, J. G.; Wackett, L. P.; Lipscomb, J. D. *Biochemistry* **1990**, *29*, 6419-6427.

(13) Fuse, H.; Ohta, M.; Takimura, O.; Murakami, K.; Inoue, J.; Yamaoka, Y.; Oclarit, J. M.; Omori, T. *Biosci. Biotech. Biochem.* **1998**, *62*, 1925-1931.

(14) Murray, L. J.; García-Serres, R.; Naik, S.; Huynh, B. H.; Lippard, S. J. *J. Am. Chem. Soc.* **2006**, *128*, 7458-7459.

(15) Lee, D. W.; Lippard, S. J. *J. Am. Chem. Soc.* **1998**, *120*, 12153-12154.

(16) Hagadorn, J. R.; Que, L., Jr.; Tolman, W. B. *J. Am. Chem. Soc.* **1998**, *120*, 13531-13532.

(17) Tolman, W. B.; Que, L., Jr. *J. Chem. Soc., Dalton Trans.* **2002**, *5*, 653-660.

(18) Lee, D.; Lippard, S. J. *Inorg. Chem.* **2002**, *41*, 2704-2719.

(19) Que, L.; Tolman, W. B. *Nature* **2008**, *455*, 333-340.

(20) Costas, M.; Chen, K.; Que, L. *Coord. Chem. Rev.* **2000**, *200-202*, 517-544.

(21) Feig, A. L.; Lippard, S. J. *Chem. Rev.* **1994**, *94*, 759-805.

(22) Carson, E. C.; Lippard, S. J. *J. Inorg. Biochem.* **2006**, *100*, 1109-1117.

(23) Carson, E. C.; Lippard, S. J. *Inorg. Chem.* **2006**, *45*, 828-836.

(24) Carson, E. C.; Lippard, S. J. *J. Am. Chem. Soc.* **2004**, *126*, 3412-3413.

(25) Carson, E. C.; Lippard, S. J. *Inorg. Chem.* **2006**, *45*, 837-848.

(26) Reisner, E.; Abikoff, T. C.; Lippard, S. J. *Inorg. Chem.* **2007**, *46*, 10229-10240.

(27) Lee, D.; Lippard, S. J. *J. Am. Chem. Soc.* **2001**, *123*, 4611-4612.

(28) Yoon, S. H.; Lippard, S. J. *Inorg. Chem.* **2003**, *42*, 8606-8608.

(29) Yoon, S.; Lippard, S. J. *Inorg. Chem.* **2006**, *45*, 5438-5446.

(30) Furutachi, H.; Murayama, M.; Shiohara, A.; Yamazaki, S.; Fujinami, S.; Uehara, A.; Suzuki, M.; Ogo, S.; Watanabe, Y.; Maeda, Y. *Chem. Commun.* **2003**, 1900-1901.

(31) Avenier, F.; Dubois, L.; Latour, J.-M. *New J. Chem.* **2004**, *28*, 782-784.

(32) Menage, S.; Galey, J.-B.; Dumats, J.; Hussler, G.; Seite, M.; Luneau, I. G.; Chottard, G.; Fontecave, M. *J. Am. Chem. Soc.* **1998**, *120*, 13370-13382.

(33) Yamashita, M.; Furutachi, H.; Tosha, T.; Fujinami, S.; Saito, W.; Maeda, Y.; Takahashi, K.; Tanaka, K.; Kitagawa, T.; Suzuki, M. *J. Am. Chem. Soc.* **2007**, *129*, 2-3.

(34) Hill, A. J.; McGraw, W. J. *J. Org. Chem.* **1949**, *14*, 783-788.

(35) *SMART, Software for the CCD Detector System*, version 5.6; Bruker AXS Madison, WI, 2000.

(36) Sheldrick, G. M. *Acta Crystallogr., Sect. A* **2008**, *A64*, 112-122.

(37) Sheldrick, G. M. *SHELXTL-97*, University of Göttingen: Göttingen, Germany, 2000.

(38) Sheldrick, G. M. *SADABS: Area-Detector Absorption Correction*, University of Göttingen: Göttingen, Germany, 2001.

(39) Spek, A. L. *PLATON, A Multipurpose Crystallographic Tool*, Utrecht University: Utrecht, The Netherlands, 2000.

(40) Hagen, K. S. *Inorg. Chem.* **2000**, *39*, 5867-5869.

(41) Kent, T. A. *WMOSS; Mössbauer Spectral Analysis Software*, versiòn 2.5; Minneapolis, 1998.

(42) Rardin, R. L.; Poganiuch, P.; Bino, A.; Goldberg, D. P.; Tolman, W. B.; Liu, S.; Lippard, S. J. *J. Am. Chem. Soc.* **1992**, *114*, 5240-5249.

(43) Rardin, R. L.; Bino, A.; Poganiuch, P.; Tolman, W. B.; Liu, S.; Lippard, S. J. *Angew. Chem.* **1990**, *102*, 842-4.

(44) Reynolds, R. A., III; Dunham, W. R.; Coucouvanis, D. *Inorg. Chem.* **1998**, *37*, 1232-1241.

(45) Reisner, E.; Telser, J.; Lippard, S. J. *Inorg. Chem.* **2007**, *46*, 10754-10770.

(46) Ambrosi, G.; Formica, M.; Fusi, V.; Giorgi, L.; Micheloni, M. *Coord. Chem. Rev.* **2008**, *252*, 1121-1152.

(47) Yoon, S.; Lippard, S. J. *J. Am. Chem. Soc.* **2005**, *127*, 8386-8397.

(48) Lee, D.; Krebs, C.; Huynh, B. H.; Hendrich, M. P.; Lippard, S. J. *J. Am. Chem. Soc.* **2000**, *122*, 5000-5001.

(49) Lee, D.; DuBois, J. L.; Pierce, B.; Hedman, B.; Hodgson, K. O.; Hendrich, M. P.; Lippard, S. J. *Inorg. Chem.* **2002**, *41*, 3172-3182.

(50) Carson, E. C. In *Doctoral Dissertation in Inorganic Chemistry* Massachusetts Institute of Technology: Cambridge, MA, 2005; Chapter 4.

(51) Lee, D.; Pierce, B.; Krebs, C.; Hendrich, M. P.; Huynh, B. H.; Lippard, S. J. *J. Am. Chem. Soc.* **2002**, *124*, 3993-4007.

(52) Lee, D.; Du Bois, J.; Petasis, D.; Hendrich, M. P.; Krebs, C.; Huynh, B. H.; Lippard, S. J. *J. Am. Chem. Soc.* **1999**, *121*, 9893-9894.

(53) Gaber, B. P.; Miskowski, V.; Spiro, T. G. *J. Am. Chem. Soc.* **1974**, *96*, 6868-6873.

(54) Koch, S. A.; Millar, M. *J. Am. Chem. Soc.* **1982**, *104*, 5255-5257.

(55) Altwicker, E. R. *Chem. Rev.* **1967**, *67*, 475-531.

(56) Murray, L. J.; Naik, S. G.; Ortillo, D. O.; García-Serres, R.; Lee, J. K.; Huynh, B. H.; Lippard, S. J. *J. Am. Chem. Soc.* **2007**, *129*, 14500-14510.

(57) Wade, L. G. *Organic Chemistry, 4th Edition*; Prentice Hall: Upper Saddle River, New Jersey, 1998.

Chapter 4

Modeling the Syn-Disposition of Nitrogen Donors in Non-Heme Diiron Enzymes. Synthesis, Characterization and Hydrogen Peroxide Reactivity of Diiron(III) Complexes with the Syn *N*-Donor Ligand H_2BPG_2DEV

Introduction

Carboxylate-bridged non-heme diiron centers occur in a variety of enzymes that activate dioxygen to catalyze key reactions in nature.[1-5] Members of this class include ribonucleotide reductase (RNR-R2),[6-8] Δ^9-desaturase (Δ^9D)[9,10] and the hydroxylase components of bacterial multicomponent monooxygenases (BMMs).[11,12] Soluble methane monooxygenase (sMMOH),[5] toluene/*o*-xylene monooxygenase (ToMOH),[13,14] and phenol hydroxylase (PHH)[15] belong to the family of BMMs and function as catalysts for the selective oxidation of hydrocarbons. Remarkably, despite their diverse roles in biology, the active sites in these enzymes all share common structural features, a carboxylate-rich environment with two histidine donors that are bound in a syn fashion with respect to the diiron vector.[16] Representations of the active sites of some of these enzymes in their reduced diiron(II) forms are provided in Chart 4.1.

In these enzymes, dioxygen activation occurs following 2-electron reduction of their diiron(III) resting states to generate an O_2-reactive diiron(II) species. Following reaction of this reduced form with dioxygen, peroxodiiron(III) intermediate species are generated that share common spectroscopic features.[5] Resonance Raman spectroscopic studies of peroxo intermediates in RNR-R2[17] and Δ^9D[10] suggest a μ-1,2-peroxo binding mode. Theoretical analysis of the peroxo intermediate in sMMOH, for which no vibrational spectroscopic data are yet available, find a μ-η^2:η^2-peroxo butterfly structure to be more stable,[18] and pH-dependent studies of the dioxygen activation chemistry indicate that proton transfer reactions,[19] most likely involving some kind of hydroperoxo intermediate,

are involved. Recently, novel peroxodiiron(III) transient intermediates were observed in the ToMOH and PHH systems, having no visible or near-IR optical bands, notably different Mössbauer parameters, and possibly a different coordination mode.[12,20] Peroxodiiron(III) intermediatess in these enzymes can in some cases undergo O–O bond cleavage to form high-valent species, such as the mixed-valent (μ-oxo)diiron(III,IV) intermediate X in RNR-R2[6] and the methane-oxidizing di(μ-oxo)diiron(IV) intermediate Q in sMMO.[21,22] Elucidating the structures of these oxygenated intermediates remains an important challenge.

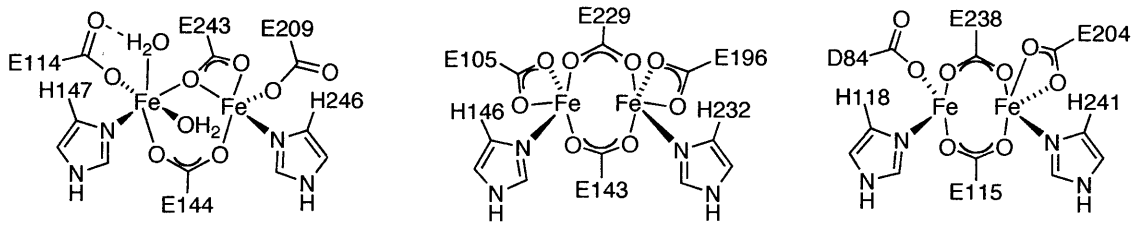

sMMOH Δ^9D RNR-R2

Chart 4.1.

Significant effort has been expended to construct model complexes that mimic the active site structures and functions of non-heme diiron enzymes.[23,24] These studies have predominantly been conducted to probe the mechanism of O_2 activation, the influence of structure on reactivity, and the requirements of iron-based catalysts for hydrocarbon oxidation. Two general ligand motifs have been extensively employed in the construction of these model complexes, namely, sterically encumbering 2,6-diarylbenzoate and tris(2-pyridylmethyl)amine (TPA)-based ligands (Chart 4.2).[23-26] Whereas the former group of ligands

facilitates formation of diiron(II) complexes with the same composition as the enzyme active sites, TPA-based constructs afford complexes that react with dioxygen to generate species more closely resembling intermediates observed spectroscopically in the reactions of BMMs with dioxygen. A structural feature that neither of these ligand motifs can rigidly enforce, however, is the syn orientation of the nitrogen donors with respect to the diiron vector. This feature may be important and it is likely that nature did not choose such a stereochemistry arbitrarily. The significance of the syn *N*-donor disposition of imidazoles from histidine residues with respect to the diiron vector is still unclear, although preliminary DFT calculations on intermediate Q of sMMOH suggest that a stereoelectronic effect derived from this configuration tunes its reactivity.[27] Apart from their inability to enforce syn *N*-donor character, terphenylcarboxylate- and TPA-based ligands are not pre-organized to stabilize a diiron core, which can lead to dissociation or aggregation to form monomeric or oligomeric species, respectively. To address these issues, we have been exploring N-donor ligands that are covalently tethered by a diethynylbenzene unit.[16,28-31] Selection of this moiety as the appropriate linker fixes the nitrogen donor atoms at a distance and orientation similar to that in the enzymes. Of particular interest is the 1,2-bis(pyridin-3-ylethynyl)benzene scaffold, because of convenience in functionalizing the pyridine moiety, as demonstrated in the synthesis of several ligands based on this platform.[29]

In the present chapter the synthesis of the syn *N*-donor ligand H_2BPG_2DEV (Chart 4.2) and three of its derivatives containing oxo-bridged

diiron(III) cores are reported. Two tripodal *N*,*N*'-bis(2-pyridylmethyl)-3-aminoacetate (BPG^-) units bridged by diethynylveratrole converge to incorporate diiron centers and provide carboxylate groups that more accurately represent the aspartate and glutamate residues of non-heme diiron enzymes than earlier constructs. We describe how this dinucleating ligand stabilizes the oxo-bridged diiron(III) cores and considerably influences the chemical and physical properties of a peroxodiiron(III) intermediate generated by addition of hydrogen peroxide.

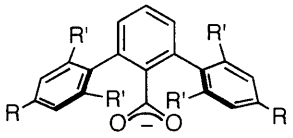

$Ar^{Tol}CO_2^-$, R = CH_3
$Ar^{4\text{-}FPh}CO_2^-$, R = F
$Ar^{Mes}CO_2^-$, R' = R = CH_3

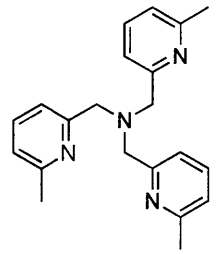

6-Me_3-TPA

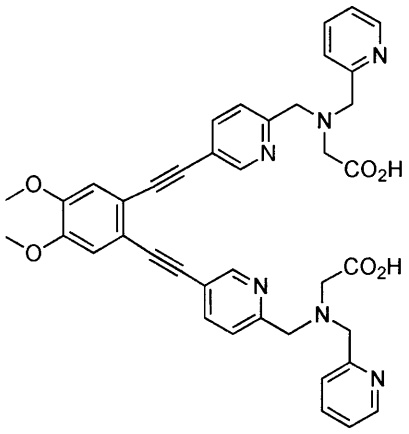

H_2BPG_2DEV

Chart 4.2.

Experimental Section

General Procedures and Methods. Reagents were purchased from commercial sources and used as received. Acetonitrile (CH_3CN), dichloromethane (CH_2Cl_2), and tetrahydrofuran (THF) were saturated with nitrogen and purified by passing though activated alumina columns under argon. Triethylamine (Et_3N) was distilled from CaH_2. The compounds (5-bromo-pyridin-

2-yl)methanol (**2b**),[32] [(pyridin-2-ylmethyl)amino]acetic acid ethyl ester (**3**),[33] 4,5-diethynylveratrole (DEV),[31] and $(Et_4N)_2[Fe_2(\mu\text{-}O)Cl_6]$[34,35] were prepared using methods described in the literature. The compound 2,6-diisopropoxybenzoic acid (HO_2CAr^{iPrO}) was synthesized by using a modified literature procedure.[36] ***Caution!*** *The perchlorate salts used in this study are potentially explosive and should be handled with care!*

Physical Measurements. NMR spectra were recorded on a Varian 300 spectrometer in the Massachusetts Institute of Technology Department of Chemistry Instrument Facility (MIT DCIF). All spectra were recorded at ambient probe temperature, 293 K. IR spectra were taken on a Thermo Nicolet Avatar 360 spectrometer with OMNIC software. Mass spectra were recorded in electrospray ionization mode. ESI-MS data were obtained with an Agilent 1100 series LC/MSD mass spectrometer. UV-vis experiments were performed on a Cary 50 spectrophotometer.

[(5-Bromo-pyridin-2-ylmethyl)-pyridin-2-ylmethyl-amino]acetic Acid Ethyl Ester (4). A solution of (5-bromo-pyridin-2-yl)methanol (**2b**) (4.69 g, 24.9 mmol) and Et_3N (4.53 mL, 32.4 mmol) in THF (95 mL) was cooled to 0 °C and treated dropwise with methanesulfonyl chloride (MsCl; 2.32 mL, 29.9 mmol). The mixture was warmed to room temperature, stirred for 2 h, and then combined with aqueous NH_4Cl (200 mL). The aqueous phase was extracted with CH_2Cl_2 (3 × 200 mL) and the organic layers were dried (Na_2SO_4), filtered, and concentrated to afford a solid (6.78 g, quant) that was used without further purification. This purple solid, K_2CO_3 (4.12 mg, 29.9 mmol), and [(pyridin-2-ylmethyl)-amino]-acetic

acid ethyl ester (**3**) (5.80 g, 29.9 mmol) were stirred overnight in CH_3CN (100 mL). During this period the color changed from purple-red to orange. The reaction mixture was combined with CH_2Cl_2 (300 mL) and the organics were washed with aq Na_2CO_3 (3 × 100 mL). The organic layer was dried (Na_2SO_4), filtered, and evaporated to dryness. The crude product was purified by column chromatography (alumina; EtOAc/hexanes, 1:3) to give **4** as a yellow oil, which was identical to the compound synthesized previously as judged by ^{1}H NMR spectroscopy and ESI-MS.[29] Yield: 7.92 g (87%). ^{1}H NMR (300 MHz, $CDCl_3$): δ = 8.56–8.50 (m, 2H), 7.67–7.61 (dt, J = 1.8, 7.5 Hz, 1H), 7.29 (d, J = 8.1 Hz, 1H), 7.17–7.12 (m, 2H), 4.19–4.11 (q, J = 7.2 Hz, 2H), 3.96 (s, 2H), 3.94 (s, 2H), 3.44 (s, 2H), 1.27–1.22 (t, J = 7.2 Hz, 3H). LRMS (ESI) calcd for $C_{16}H_{18}BrN_3O_2Na$ $[M+Na]^+$: 386, found: 386.

Et_2BPG_2DEV·2HCl (5·2HCl) (Diethyl 2,2'-(5,5'-(4,5-dimethoxy-1,2-phenylene)bis(ethyne-2,1-diyl)bis(pyridine-5,2-diyl))bis(methylene)bis((pyridin-2-ylmethyl)azane-diyl)diacetate) Hydrochloride. 4,5-Diethynylveratrole (0.474 g, 2.55 mmol), **4** (1.82 g, 5.03 mmol), $[Pd(PPh_3)_4]$ (0.250 g, 0.216 mmol), Et_3N (3.6 mL, 26 mmol), and THF (24 mL) were combined in a sealed tube under an inert atmosphere and stirred for 2.5 d at 60 °C. After the reaction mixture was cooled to room temperature, it was combined with EtOAc (50 mL) and washed three times with a solution of Na_2CO_3 (aq.), dried over Na_2SO_4, filtered, and evaporated to dryness. The crude material was purified by column chromatography (alumina; EtOAc/hexanes, 1:1–1:0) to give **5** as thick yellow oil. ^{1}H NMR spectroscopy confirmed complete conversion to the desired product, but

a phosphine oxide impurity was observed. To purify the material, the hydrochloride salt of the amine, **5**·2HCl, was synthesized. The oil was dissolved in ca. 100 mL of EtOAc and ca. 4 mL of a solution of HCl in Et_2O (2 M) was added dropwise with stirring until no further precipitation occurred. The yellow solid was filtered off and dried in vacuum. Yield: 1.20 g (57%). ^{1}H NMR (300 MHz, CD_3OD): δ = 8.92 (m, 2H); 8.89 (m, 2H); 8.54 (dt, J = 1.5; 7.8 Hz, 2H); 8.37 (dd, J = 2.1, 9.0 Hz, 2H); 8.07 (d, J = 7.8 Hz, 2H); 8.00-7.96 (m, 2H); 7.90 (d, J = 8.4 Hz, 2H); 7.25 (s, 2H); 4.58 (s, 4H); 4.56 (s, 4H); 4.18 (q, J = 7.2 Hz, 4H); 3.92 (s, 6H); 3.74 (s, 4H); 1.25 (t, J = 7.2 Hz, 6H). ^{13}C NMR (125 MHz, CD_3OD): δ = 171.27, 154.21, 153.90, 151.40, 147.44, 146.96, 145.77, 142.35, 127.61, 127.31, 126.77, 122.78, 117.88, 115.47, 94.90, 86.30, 61.68, 56.97, 56.48, 56.24, 54.90, 13.87. HRMS (ESI) calcd for $[M+H]^+$: 753.3397, found: 753.3397. IR (KBr, cm^{-1}): 2979 (m), 2914 (m), 2611 (m), 2214 (m, $\nu_{C\equiv C}$), 1731 (s), 1614 (m), 1593 (m), 1511 (s), 1464 (m), 1371 (m), 1251 (s), 1215 (s), 1155 (m), 1086 (m), 1024 (m), 987 (m), 858 (w), 772 (w). Mp: 103–105 ºC.

H_2BPG_2DEV (5a), 2,2'-(5,5'-(4,5-Dimethoxy-1,2-phenylene)bis(ethyne-2,1-diyl)bis(pyridine-5,2-diyl))bis(methylene)bis((pyridin-2-ylmethyl)azane-diyl)diacetic Acid. An aqueous solution of **5**·2HCl (0.55 g, 0.67 mmol) and KOH (1.4 g, 25 mmol) were combined to yield a total volume of 100 mL. The resulting suspension was heated to 60 °C under a nitrogen atmosphere for ca. 4 h. After cooling down to room temperature, the reaction mixture was acidified with dilute HCl to pH 5 and the product was extracted with CH_2Cl_2. The organic phase was dried over Na_2SO_4, filtered, and reduced to dryness to yield a yellow-brown solid.

Yield: 0.42 g (91%). ^{1}H NMR (300 MHz, $CDCl_3$): δ = 13.11 (s, 2H), 8.68 (m, 2H), 8.58 (m, 2H), 7.73 (m, 4H), 7.35 (m, 4H), 7.24 (m, 2H), 7.03 (s, 2H), 4.13 (s, 4H), 4.07 (s, 4H), 3.94 (s, 6H), 3.57 (s, 4H). ^{13}C NMR (125 MHz, d_6-DMSO): δ = 173.44, 160.29, 160.05, 151.76, 150.64, 149.93, 139.86, 137.83, 123.93, 123.65, 123.40, 118.94, 118.40, 115.49, 92.16, 90.19, 60.32, 60.22, 57.00, 55.46. HRMS (ESI) calcd for $[M+H]^+$: 697.2770, found: 697.2770. IR (KBr, cm^{-1}): 3054 (w), 3002 (w), 2912 (w), 2832 (w), 2206 (w, $\nu_{C\equiv C}$), 1714 (m), 1637 (w), 1593 (m), 1551 (w), 1511 (s), 1437 (m), 1401 (m), 1359 (m), 1248 (s), 1215 (s), 1149 (m), 1119 (m), 1085 (m), 1024 (m), 993 (m), 858 (w), 761 (m), 722 (m), 695 (m), 649 (w), 621 (w), 541 (m). Mp: 60–62 °C.

$[Fe_2(\mu\text{-}O)(H_2O)_2BPG_2DEV](ClO_4)_2$ (6). To a solution (2 mL; CH_3CN/H_2O, 10:1) of $Fe(ClO_4)_3{\cdot}9H_2O$ (77 mg, 150 μmol) was added a suspension of **5a** (50 mg, 72 μmol) in the same solvent mixture (2 mL). The color instantly changed to deep-red and the resulting solution was stirred for ca. 5 min. After filtration, the solution was subjected to vapor diffusion of Et_2O to yield crystalline red plates that were analyzed by X-ray crystallography. The yield of crystalline material was highly dependent on the H_2O content of the solution. Yield: 60 mg (78%). X-ray diffraction quality crystals were grown from vapor diffusion of Et_2O into a solution of **6** in CH_3OH and H_2O. LRMS (ESI) calcd for $[M-H]^+$: 857.1, found: 875.2. IR (KBr, cm^{-1}): 3430 (m), 3073(w), 2921 (w), 2854 (w), 2210 (w, $\nu_{C\equiv C}$), 1608 (s), 1590 (s), 1550 (m), 1512 (s), 1492 (m), 1462 (w), 1446 (m), 1402 (w), 1367 (m), 1348 (m), 1301 (w), 1286 (w), 1250 (s), 1212 (m), 1099 (vs), 1086 (vs), 1024 (m), 992 (w), 927 (w), 902 (w), 807 (m, $\nu_{Fe-O-Fe}$), 768 (m), 731 (w), 667 (w), 651 (w),

622 (m), 570 (w), 476 (w), 423 (w). Anal. Calcd. for **6**·2CH_3OH, $C_{42}H_{46}N_6O_{19}Cl_2Fe_2$: C, 44.98; H, 4.13; N, 7.49. Found: C, 45.18; H, 4.19; N, 7.12. UV–vis (CH_3CN:H_2O, 10:1) (λ_{max}, nm (ε, M^{-1} cm^{-1})): 480 (440). Mp: 175–180 °C (dec).

Synthesis of [$^{57}Fe_2$(μ-O)(H_2O)$_2$BPG_2DEV](ClO_4)$_2$ (^{57}Fe-6): A solution of $AgClO_4$ (38 mg, 181 μmol) in MeCN/H_2O (10:1, v/v) was added to a solution of ^{57}Fe-enriched $FeCl_3$·$6H_2O$ (16 mg, 60 μmol; 50% enriched) prepared by dissolution of metallic iron with aqueous HCl (37%) and subsequent evaporation of the solvent to yield an orange solid. After the voluminous precipitate was filtered off, a solution of **5a** (20 mg, 29 μmol) was added to the orange filtrate generating a deep-red reaction mixture, which was subjected to Et_2O vapor diffusion. Dark red crystals of **^{57}Fe-6** formed in one day, were washed with Et_2O, and dried at room temperature. Yield: ca. 15 mg (50%).

[Fe_2(μ-O)(μ-O_2CAr^{iPrO})BPG_2DEV](ClO_4) (7). Method A. A red CH_3OH/CH_2Cl_2 (1:1) solution of **6** (63 mg, 60 μmol) was allowed to react with HO_2CAr^{iPrO} (21 mg, 90 μmol) in the presence of NEt_3 (40 μL) to form an intense green solution. Clusters of green needles were isolated by vapor diffusion of Et_2O into this reaction mixture. Yield: 40 mg (57%). **Method B.** A CH_3OH/CH_2Cl_2 (1:1) solution of Fe(ClO_4)$_3$·$9H_2O$ (77 mg, 150 μmol) was combined with HO_2CAr^{iPrO} (19 mg, 79 μmol) and NEt_3 (60 μL). To this reaction mixture, a solution of **5a** (50 mg, 72 μmol) was instantly added and the resulting deep green solution was stirred for 10 min, filtered, and subjected to vapor diffusion of Et_2O. Deep green needle-shaped crystals, suitable for X-ray crystallographic analysis, were isolated. Yield:

38 mg (46%). LRMS (ESI) calcd for $[M–ClO_4]^+$: 1059.2, found: 1059.5. IR (KBr, cm^{-1}): 3076 (w), 2975 (w), 2930 (w), 2211 (w, $\nu_{C\equiv C}$), 1645 (s), 1608 (s), 1593 (s), 1530 (s), 1513 (s), 1459 (s), 1422 (s), 1372 (m), 1356 (m), 1332 (m), 1289 (m), 1249 (s), 1087 (vs), 1024 (m), 996 (w), 923 (w), 906 (w), 848 (w), 834 (w), 771 (m, $\nu_{Fe–O–Fe}$), 729 (w), 668 (w), 623 (m), 551 (w), 512 (w). Anal. Calcd for **7**·0.5CH_2Cl_2, $C_{53.5}H_{53}N_6O_{15}Cl_2Fe_2$: C, 53.43; H, 4.44; N, 6.99. Found: C, 53.84; H, 4.87; N, 7.08. UV–vis ($CHCl_3$:CH_3OH, 1:1) (λ_{max}, nm (ε, M^{-1} cm^{-1})): 642 (130); 522 (sh, 218); 490 (730); 475 (sh, 569); 436 (sh, 1171); 413 (1577). Mp: 195–200 °C (dec).

[Fe_2(μ-O)(μ-CO_3)BPG_2DEV] (8). A solution (6 mL, CH_2Cl_2/CH_3OH, 1:1) of **5a** (100 mg, 144 μmol) and Et_3N (40 mL, 290 μmol) was added dropwise to a solution (7 mL, CH_2Cl_2/CH_3OH, 1:1) of $(Et_4N)_2[Fe_2(\mu\text{-O})Cl_6]$ (87 mg, 144 μmol). Solid Ag_2CO_3 (159 mg, 576 μmol) was then added to the brown solution. The resulting suspension turned green and was allowed to react for ca. 45 min. The mixture was filtered and subjected to vapor diffusion of Et_2O. After 2–3 days, emerald-green needles of **8** were harvested that were suitable for X-ray crystallography. Yield: 93 mg (73%). LRMS (ESMS) calcd for $(M+H)^+$: 883.1, found: 883.0; calcd for $(M–CO_3+OH)^+$: 839.1, found: 839.2. IR (KBr, cm^{-1}): 3065 (w), 2956 (w), 2920 (w), 2846 (w), 2210 (w, $\nu_{C\equiv C}$), 1617 (s), 1610 (s), 1571 (w), 1533 (m), 1513 (s), 1495 (m), 1444 (m), 1403 (w), 1383 (w), 1358 (m), 1321 (m), 1304 (m), 1289 (m), 1272 (w), 1248 (m), 1214 (m), 1182 (m), 1158 (w), 1142 (w), 1123 (w), 1102 (w), 1087 (w), 1055 (w), 1040 (w), 1024 (w), 997 (w), 927 (w), 908 (w), 860 (w), 847 (w), 838 (w), 770 (m, $\nu_{Fe–O–Fe}$), 742 (w), 695 (w), 663 (w),

564 (w), 552 (w), 528 (w), 460 (w), 437 (w), 423 (w). UV–vis ($CHCl_3$:CH_3OH, 1:1) (λ_{max}, nm (ε, M^{-1} cm^{-1})): 638 (124); 517 (193); 487 (567); 473 (sh, 342); 411 (1576). Anal. Calcd for **8**·0.75CH_2Cl_2, $C_{41.75}H_{35.5}N_6O_{10}Cl_{1.5}Fe_2$: C, 53.00; H, 3.78; N, 8.88. Found: C, 52.99; H, 4.27; N, 9.10. Mp: 150–155 °C (dec).

X-ray Crystallographic Studies. Intensity data were collected on a Bruker SMART APEX CCD diffractometer with graphite-monochromated Mo Kα radiation (λ = 0.71073 Å), controlled by a Pentium-based PC running the SMART software package.[37] Single crystals were mounted on the tips of glass fibers, coated with Paratone-N oil, and cooled to 110 K under a stream of N_2 maintained by a KRYO-FLEX low-temperature apparatus. A total of 2800 frames were collected for each compound. The structures were solved by direct methods with the aid of successive difference Fourier maps and refined on F^2 by using the SHELXTL-97 software included in the SHELXTL software package.[38,39] Empirical absorption corrections were applied by using the SADABS program,[40] and the structures were checked for higher symmetry with the PLATON software.[41] All non-hydrogen atoms were located and their positions refined with anisotropic thermal parameters by least-squares cycles. All hydrogen atoms were assigned to idealized positions and given thermal parameters equivalent to either 1.5 (methyl hydrogen atoms) or 1.2 (all other hydrogen atoms) times the thermal parameter of the carbon atoms to which they were attached. The hydrogen atoms of O8 and O9 of the H_2O ligands in the diiron(III) complex **6** and of O1W were located from the difference map and their bond distances to the corresponding oxygen atoms restrained using a DFIX command. Crystal data,

data collection parameters, and structure refinement details for all compounds are provided in Table 4.4.

Compound **6** crystallizes with three molecules of H_2O and one molecule of CH_3OH as solvent. One of the solvent water molecules is hydrogen-bonded to methoxy groups located on the backbone of the BPG_2DEV^{2-} ligand and the other two water molecules were extensively disordered over several positions. These regions of diffuse solvent were modeled by applying a bulk solvent correction using the SWAT command in SHELXTL.[38] The water ligands on the diiron(III) complex **6** form strong hydrogen bonds to neighboring BPG_2DEV^{2-} ligands in the crystal. The hydrogen-bonding network is displayed in Figure 4.2. Two perchlorate anions (ClO_4^-) are also present in the unit cell. One of them is disordered over two positions with an occupancy ratio of 71:29. The other anion is disordered over two positions with an occupancy ratio of 59:41, sharing the location with a disordered CH_3OH molecule. In **7** there are two molecules in the asymmetric unit. One methyl group of a bridging carboxylate ($^-O_2CAr^{iPrO}$) is disordered over two positions in a ratio of 49:51. Three molecules of CH_3OH were located in the crystal structure of **7**, each hydrogen-bonded to an oxygen atom of a carboxylate group of the BPG_2DEV^{2-} ligand, respectively. Molecules of CH_2Cl_2 and water, the latter with 50% occupancy, were also located. A molecule of CH_2Cl_2 and CH_3OH share a common position with occupancies of 56% and 44%. In the crystal structure of **8**, five molecules of CH_3OH and one molecule of water were found. One of the former is disordered over two positions with a ratio of 53:47. Two of the CH_3OH molecules form hydrogen bonds to the carbonate

ligand on **8**. The water molecule is disordered over two positions with 64% and 36% occupancy, respectively.

Mössbauer Spectroscopy. Mössbauer spectra were recorded on an MSI spectrometer (WEB Research Company) with a ^{57}Co source in a Rh matrix maintained at room temperature. Solid samples of **6**, **7**, and **8** were prepared by suspension of 13 to 20 mg of the powdered solids in Apiezon M grease and placed in a nylon sample holder. Solution samples of reaction intermediates **8a** and **7a** were prepared by respectively treating suspensions (ca. 0.8 mL) of the oxo-bridged diiron complexes **8** (ca. 20 μmol, CH_3CN/H_2O, 1:1) and **7** (ca. 10 μmol, CH_3OH/H_2O, 4:1) with Et_3N (15 μL) followed by addition of aqueous solution of H_2O_2 (50 μL, 30%). After ca. 1 min, the red-brown reaction mixture was transferred to a sample holder and instantly frozen in liquid N_2. A sample of **6a** was prepared similarly, but using a more dilute solution (ca. 2 μmol, CH_3OH/H_2O, 20:1) of ^{57}Fe-enriched complex **6**, **^{57}Fe-6**, which was allowed to react with Et_3N (5 μL) and excess H_2O_2 (10 μL, 30%) for ca. 40-50 s and then frozen instantly. Data were acquired at 4.2 K and 90 K, and isomer shift (δ) values are reported relative to the room temperature Mössbauer spectrum of a metallic iron foil, which was used for calibration of the velocity scale. The spectra were fit to Lorentzian lines with the WMOSS plot and fit program.[42]

Resonance Raman Spectroscopy. Resonance Raman (RR) spectra were obtained on a custom built McPherson 2061/207 spectrometer equipped with a Princeton Instrument liquid-N_2 cooled CCD detector (LN-1100PB). Excitation at 647, 568, and 413 nm was provided by a Kr laser (Innova 302,

Coherent) and 514- and 488-nm excitations by an Ar laser (Innova 90, Coherent). The laser beam was kept at low power, between 40 and 10 mW, and was focused with a cylindrical lens onto frozen samples in NMR tubes. Long wave pass filters (RazorEdge filters, Semrock) or super-notch filters (Kaiser Inc.) were used to attenuate Rayleigh scattering. Sets of ~ 4 min accumulations were acquired at 4-cm^{-1} resolution. Frequency calibrations were performed using aspirin and are accurate to ±1 cm^{-1}. The samples were subjected to continuous spinning at 110 K to prevent adverse effects from laser illumination. Regular visual inspection of the sample colors during the course of the RR experiments and comparison of consecutive RR spectra provided a reliable means to evaluate photobleaching of species of interest.

EPR Spectroscopy. X-band EPR spectra were acquired on a Bruker EMX EPR spectrometer (9.37 GHz) with WinEPR software at the Department of Chemistry Instrumentation Facilities at MIT (DCIF). An OXFORD instruments liquid helium cryostat with an ITC503 controller was used to regulate the temperature. A 3.0 mM solution of **8** in MeCN/H_2O (2:1; v/v) was prepared. One aliquot was transferred to an EPR tube and frozen; another was allowed to react with 10 μL of NEt_3 and 175 μL of hydrogen peroxide (30%) until a maroon-colored solution formed, after which the reaction was freeze-quenched. Standard solutions of $Cu(OTf)_2$ in H_2O at concentrations of 2.0 mM and 5.0 mM were prepared for spin quantification.

Electrospray Ionization Mass Spectrometry of the Peroxo Intermediate. Products **6a**, **7a**, and **8a**, which result from reaction of H_2O_2 and

NEt_3 with **6**, **7**, or **8**, respectively, and the isotope-labeled species **7a,** were identified by ESI-MS using a Finnigan LTQ ion trap mass spectrometer maintained at the Department of Chemistry, Tufts University. High-resolution mass spectra of these intermediates were also acquired on a Bruker Daltonics APEXIV 4.7 Tesla Fourier Transform Ion Cyclotron Resonance Mass Spectrometer (FT-ICR-NS) at the MIT DCIF. The samples were prepared by addition of a 50-100 fold excess of a 2% aqueous H_2O_2 solution containing 5 equiv of NEt_3 to solutions of the diiron(III) complexes (ca. 1-2 mM) in solvent mixtures of CH_3CN/H_2O (ca. 4:1) or CH_3OH/CH_2Cl_2 (ca. 1:1). The peaks of interest were confirmed by comparison of the observed and calculated *m/z* values including isotope patterns.

Reaction of 6, 7, and 8 with H_2O_2 and Quantification of O_2 Evolution. In order to quantify the amount of dioxygen formed during hydrogen peroxide decomposition, 2 mL of a 0.4 mM solution of the diiron complex were placed in a 25-mL round-bottom flask equipped with a stir bar. The flask was then tightly sealed with a rubber septum and electrical tape. The solution was treated with ca. 5 μL of NEt_3 and cooled to 0 °C before H_2O_2 was added through the septum with a syringe. The concentration of diiron complex was kept constant by adjusting the final volume of the reaction mixture. The reaction flask was connected by a cannula to an inverted graduated cylinder, filled with H_2O, and the amount of O_2 generated was determined applying the ideal gas law. In the case of **6**, the solution was thoroughly purged with nitrogen to remove any traces

of CO_2 that can potentially react with **6** under basic conditions to form the carbonato-bridged complex **8**.

Substrate Oxidation Studies. Oxidation reactions were carried out under an inert atmosphere of N_2 (g). In each experiment, *cis*-cyclooctene (0.26 mL, 2.0 mmol) and NEt_3 (5 μL) were added to 2.0 mL of a 1.0 M solution of **6** or **7** in CH_3CN/H_2O (95:5) at 25 °C. To this mixture, H_2O_2 (97 μL, 10.3 M; diluted with CH_3CN to a total volume of 400 μL) was added by syringe pump over a period of one h. After stirring for an additional 2h, the products were determined by GC analysis. The structures of the products were confirmed by GC-MS spectrometry, and by comparison with authentic samples.

Results and Discussion

Synthesis of H_2BPG_2DEV (5a). Previously we reported an efficient route to a new family of diethynyltriptycene-linked dipyridyl ligands, including Et_2BPG_2DET (DET = 2,3-diethynyltriptycene), an analog of Et_2BPG_2DEV (**5**).[29] Our initial route started from commercially available 2,5-dibromopyridine (**1**). Following a known reaction, we synthesized 2-formyl-5-bromopyridine (**2a**) by treatment of **1** with *n*-BuLi, followed by quenching with DMF.[32] With aldehyde **2a** in hand, we prepared the pyridylbromide coupling partner **4** by reductive amination of **2a** with the *N*-pyridylmethylglycine ethyl ester **3**, which is available in one step from commercially available materials and can be isolated easily by distillation on a multi-gram scale.[33] Although the reaction sequence used to prepare **4** proceeded with moderate yields of less than a gram, we observed that

isolated yields of **2a** and **4** diminished by roughly 30% for each step upon scale up. We therefore devised an optimized route to the pyridylbromide **4** from **1**, which is compared to the previous method in Scheme 4.1. In this procedure we prepared alcohol **2b** by reduction of **2a** with $NaBH_4$ *in situ*.[32] Isolated yields for **2b** ranged between 54–60% starting with 10 g of **1**. In addition to the higher yield, **2b** could be readily purified by crystallization, in contrast to the aldehyde **2a**, which was difficult to separate from undesired byproducts. Mesylation of **2b** with MsCl and Et_3N afforded a mesylate that was allowed to react with **3** in the presence of K_2CO_3 to furnish **4** in 87% yield over two steps. Using this optimized route, we were able to prepare multi-gram quantities of **4** from **1** in a three step synthetic sequence that required only a single alumina column chromatography purification procedure.

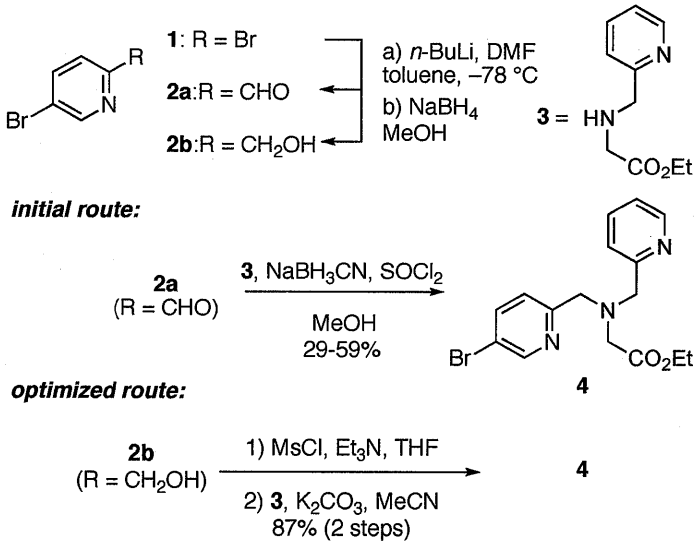

Scheme 4.1. Preparation of pyridylbromide **4**.

With sufficient amounts of the pyridylbromide **4** available, we were able to synthesize large quantities of Et_2BPG_2DEV (**5**) via a cross-coupling reaction

between **4** and 4,5-diethynylveratrole (DEV)[31] using 10 mol% of $[Pd(PPh_3)_4]$ catalyst in a mixture of Et_3N and THF at 60°C (Scheme 4.2). We chose the DEV over the DET backbone due to its greater solubility in organic solvents and more facile synthesis. The Sonogashira cross-coupling reaction worked remarkably well upon scale up and the conversion to the reaction product was greater than 90% as determined by ^1H NMR spectroscopy. In order to remove residual phosphine impurities that were present after purification of the crude product by alumina column chromatography, the HCl salt of the amine was isolated by treatment of an EtOAc solution of the purified material with an etheral hydrogen chloride solution. This purification sequence lowered the isolated yield of the corresponding dihydrochloride salt to 57%. Saponification of the esters with KOH in H_2O proceeded cleanly, affording H_2BPG_2DEV in nearly quantitative yield.

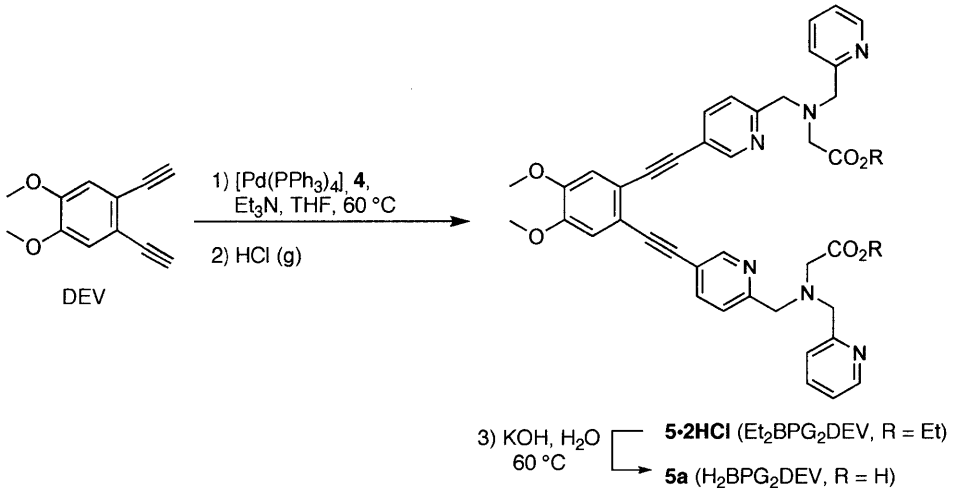

Scheme 4.2.

Although the salt of the ester is stable for months under ambient atmospheric conditions, the dicarboxylic acid decays to form a complex mixture of products

over time as evidenced by ^{1}H NMR spectroscopy. Therefore, we stored the ligand as the hydrochloride salt of the diester and prepared the acid freshly for the following metal complexation studies.

Synthesis of the Oxo-Bridged Diiron(III) Compounds [Fe_2(μ-O)(H_2O)$_2$BPG_2DEV](ClO_4)$_2$ (6), [Fe_2(μ-O)(μ-O_2CAr^{iPrO})BPG_2DEV](ClO_4) (7), [Fe_2(μ-O)(μ-CO_3)BPG_2DEV] (8). Compound **6** crystallizes in good yield as deep red-colored blocks by vapor diffusion of Et_2O into a reaction mixture containing H_2BPG_2DEV and two equiv of Fe(ClO_4)$_3$·9H_2O in CH_3CN/H_2O (10:1). The yields and the crystal quality depended strongly on the ratio of CH_3CN and H_2O. Only a few examples of oxo-bridged diiron(III) compounds with aqua ligands have been reported because H_2O is prone to substitution and tends to form oxo-bridged polyiron(III) complexes.[43] When excess base, such as NEt_3, was added under aerobic conditions in the synthesis of **6**, the color changed from deep red to intense green. The resulting complex **8** contained a carbonato- and oxo-bridged diiron(III) center that forms upon reaction with CO_2 from the air. This reaction was complete in less than a few seconds when CO_2 gas was introduced directly into the reaction mixture. With the aforementioned procedure, isolated yields of **8** varied widely. Therefore, an optimized protocol for the synthesis of **8** was developed. This procedure involved treating H_2BPG_2DEV with one equiv of the pre-formed (μ-oxo)diiron(III) complex (Et_4N)$_2$[Fe_2(μ-O)Cl$_6$] dissolved in CH_3OH/CH_2Cl_2, producing a yellow-brown solution. Addition of excess Ag_2CO_3 resulted in nearly instantaneous formation of a green suspension that was stirred for 45 min, filtered, and subjected to vapor diffusion of Et_2O. Emerald-green

needles were isolated in 73% yield after several days and analyzed by X-ray crystallography. Compound **8** belongs to a rather rare group of carbonato-bridged diiron complexes.[44-50]

As with the synthesis of the carbonate complex **8**, the carboxylato-bridged complex **7** could be prepared in a variety of ways in moderate yields, either in a reaction between the ligand H_2BPG_2DEV and two equivalents of $Fe(ClO_4)_3{\cdot}9H_2O$ in the presence of base and excess HO_2CAr^{iPrO}, or by addition of the carboxylic acid to a CH_3CN solution of **6** in the presence of base. Scheme 4.3 summarizes the pathways for the synthesis of compounds **6**, **7**, and **8**.

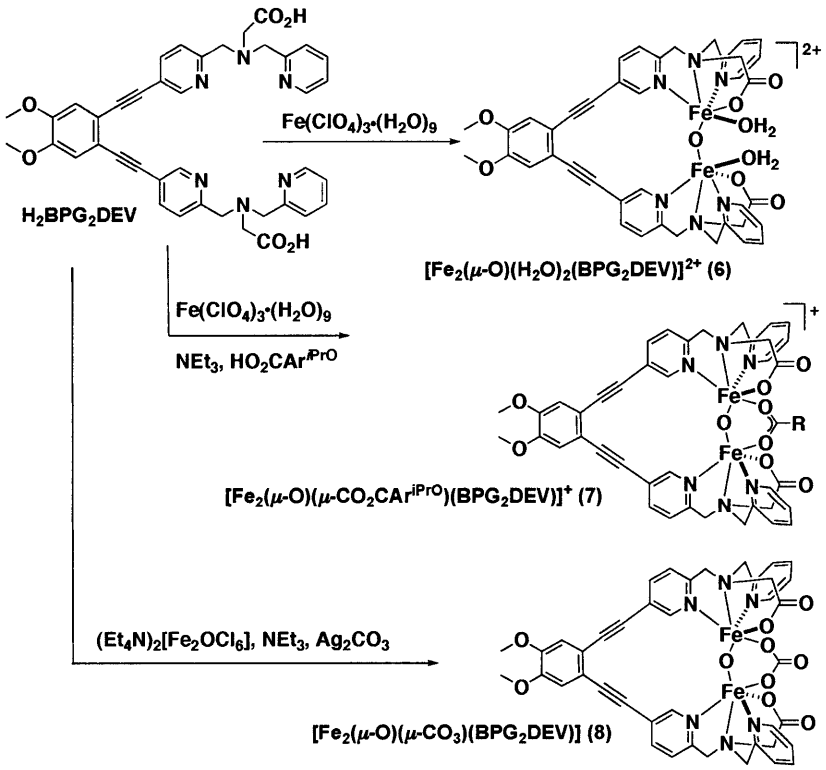

Scheme 4.3.

Structural Characterization. An ORTEP diagram of **6** is displayed in Figure 4.1 and selected bond lengths and angles are reported in Table 4.3.

Compound **6** is a dication and crystallizes with two perchlorate anions in the lattice. A packing diagram (Figure 4.2) reveals strong hydrogen-bonding interactions between the H_2O ligands and carboxylate groups of neighboring molecules (Table 4.2) as well as stacking of the diethynyl veratrole units. The two iron atoms are separated by 3.4837(9) Å with an Fe–O–Fe angle of 155.37(16)°. The two H_2O molecules bind in a syn fashion with respect to the diiron vector, similar to stoichiometrically analogous complexes that contain either two unlinked BPG^- or two BPP^- (bis(2-pyridylmethyl)aminopropionate) ligands.[51,52] In contrast to these two compounds, the pyridine nitrogen atoms of the BPG^- moieties in **6** are bound syn instead of anti to each other, which is a consequence of the linker. Furthermore, the values for the Fe–Fe distance and the Fe–O–Fe angle in **6** are significantly smaller in comparison to these two complexes (Table 4.1). In a similar complex with the ligand 6-HPA, where the two neutral TPA units are linked to one another by an ethylene bridge, the distances between the two iron atoms are even longer than 3.56 Å and the Fe–O–Fe angles close to linear.[51-53] The shorter distance and angle in **6** are most likely a consequence of more rigid DEV linker, which draws the iron atoms to be closer together.

Table 4.1. Comparison of Fe–Fe Distances (Å) and Fe–O–Fe Angles (deg) of Diiron Compounds with a $[Fe_2(\mu\text{-}O)(H_2O)_2]$ Core.

Compound	Fe–Fe (Å)	Fe–O–Fe (deg)	Ref.
6	3.4837(9)	155.37(16)	*a*
$[Fe_2(\mu\text{-}O)(H_2O)_2BPG_2]^{2+}$	3.56	169.8(2)	*51*
$[Fe_2(\mu\text{-}O)(H_2O)_2BPP_2]^{2+}$	3.564(2)	168.8(3)	*52*
$[Fe_2(\mu\text{-}O)(H_2O)_2(6\text{-}HPA)_2]^{4+}$	3.607(3)	179.2	*53*

a = This work. Abbreviations: BPP = bis(2-pyridylmethyl)aminopropionate; 6-HPA = 1,2-bis[2-{bis(2-pyridylmethyl)aminomethyl}-6-pyridyl]ethane.

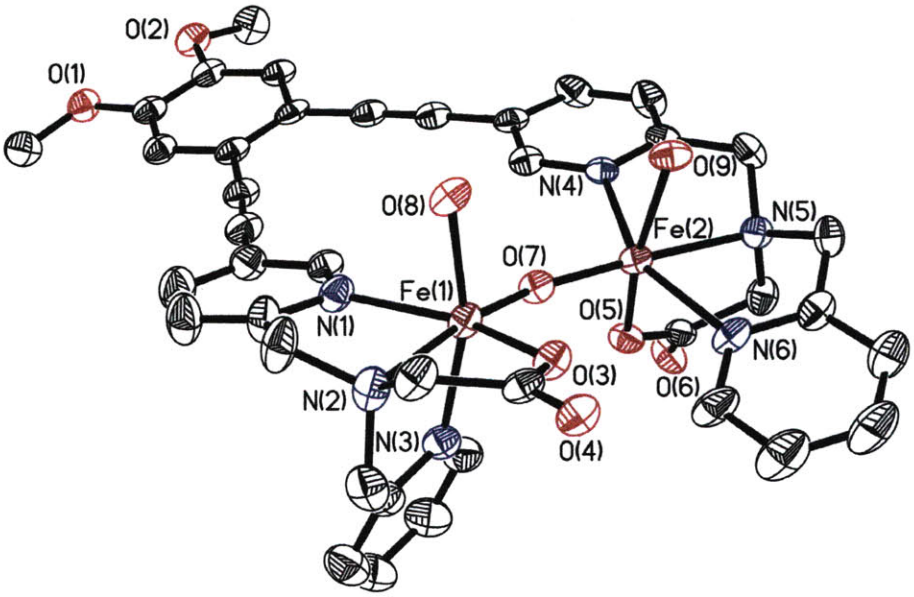

Figure 4.1. ORTEP diagram of **6** displaying thermal ellipsoids (40%). For clarity, the ClO_4^- anions are not shown.

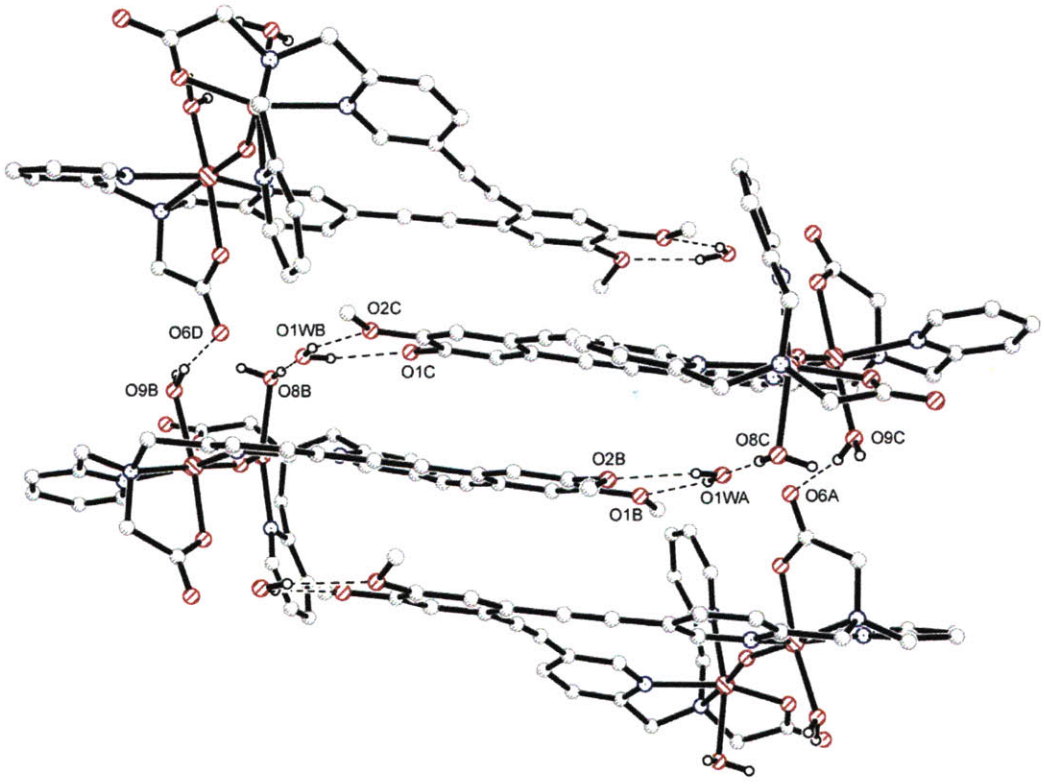

Figure 4.2. Ball and stick diagram of $[Fe_2(\mu\text{-}O)(H_2O)_2BPG_2DEV](ClO_4)_2$ (**6**) displaying intermolecular hydrogen bonds. For clarity, the ClO_4^- anions and solvent molecules not involved in hydrogen bonding are omitted and arbitrary isotropic thermal parameters are used.

Table 4.2. Summary of Distances (Å) between Hydrogen Bond Donor and Acceptor Atoms in the X-ray Crystal Structure of **6**.

Bond Lengths	Å
O1WA–H1WA...O1B	2.954(4)
O1WA–H1WB...O2B	2.820(4)
O8B–H8AB...O4C	2.664(4)
O8B–H8AB...O1W	2.675(4)
O9C–H9AC...O6A	2.576(3)
O9C–H9AC...O4C	2.652(4)

Compounds **7** and **8** have very similar structural parameters. They differ only in the presence of an additional bridging ligand, a carboxylate in the case of **7** and a carbonate ligand in **8**. Accordingly, compound **7** is positively charged and **8** is neutral. Both diiron cores are displayed in Figure 4.3 and selected bond distances and angles are summarized in Table 4.3. The BPG_2DEV^{2-} ligand stabilizes the dinuclear structures by bridging the diiron centers. The carbonato and carboxylato bridges in **7** and **8** lie approximately in the plane defined by the Fe–O–Fe unit, a feature generally observed in these types of compounds.[47,54] For compound **7** there are two crystallographically independent molecules in the unit cell and geometric comparisons are reported for averaged values. In **7**, the Fe–Fe distance is 3.218 Å and the Fe–O–Fe angle 128.5°. Compound **8** contains a (μ-oxo)(μ-carbonato)diiron(III) core in which the two iron atoms are separated by 3.1142(18) Å and related by a pseudo-C_2 axis. The Fe–O–Fe angle is 125.97(15)° and the distance to the bridging oxygen atom is 1.740(3) Å, which is consistent with values for other oxo-bridged diiron(III) complexes.[55,56]

Table 4.3. Selected Bond Lengths (Å) and Angles (deg) for **6**, **7** and **8**.

	6	**7**	**8**
Fe(1)–Fe(2)	3.4837(9)	3.2192(12)[b] 3.2171(12)[c]	3.1139(17)
Fe(1)–O(3)	2.007(3)	1.975(4)[b] 2.001(3)[c]	1.9515(13)
Fe(1)–O(7)	1.780(2)	1.787(3)[b] 1.787(3)[c]	1.7365(11)
Fe(1)–O(8)	2.092(3)	2.041(3)[b] 2.006(3)[c]	1.9281(12)
Fe(1)–N(1)	2.148(3)	2.156(4)[b] 2.142(4)[c]	2.1156(14)
Fe(1)–N(2)	2.265(3)	2.251(4)[b] 2.231(4)[c]	2.1922(14)
Fe(1)–N(3)	2.125(3)	2.140(4)[b] 2.178(4)[c]	2.0900(17)
Fe(2)–O(5)	2.012(3)	2.005(4)[b] 2.007(4)[c]	1.9654(13)
Fe(2)–O(7)	1.785(3)	1.787(3)[b] 1.785(3)[c]	1.7578(14)
Fe(2)–O(9)	2.047(3)	2.039(3)[b] 2.041(4)[c]	1.8915(13)
Fe(2)–N(4)	2.174(3)	2.152(5)[b] 2.150(4)[c]	2.0764(15)
Fe(2)–N(5)	2.239(3)	2.227(4)[b] 2.229(4)[c]	2.2224(17)
Fe(2)–N(6)	2.136(3)	2.152(5)[b] 2.165(4)[c]	2.1024(15)
O(8)–C(21)–O(9)	–	125.6(4)[b] 125.3(4)[c]	121.59(10)
Fe(1)–O(7)–Fe(2)	155.37(16)	128.51(18)[b] 128.49(18)[c]	126.03(5)

[a] Numbers in parentheses are estimated standard deviations of the last significant figures. [b] Molecule 1 in the asymmetric unit. [c] Molecule 2 in the asymmetric unit.

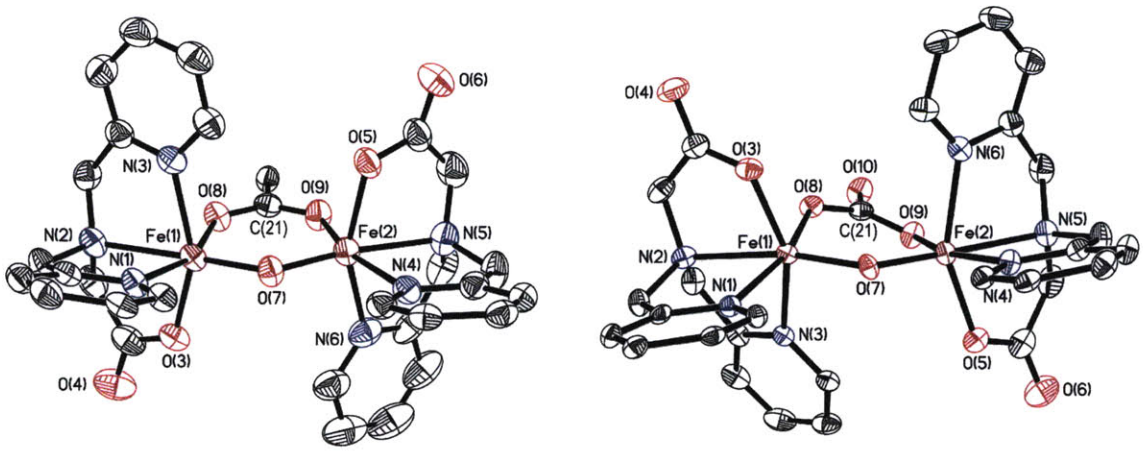

Figure 4.3. ORTEP diagram of **7** (left) and **8** (right) displaying thermal ellipsoids (50%). For clarity, the diethynylveratrole backbones, the Ar^{iPrO} group, and the ClO_4^- anion are not shown.

Table 4.4 Crystal Data and Details of Data Collection for **6**–**8**.

	6·CH_3OH·$3H_2O$	**7**·$1.7CH_3OH$·$0.3H_2O$·$0.8CH_2Cl_2$	**8**·$5CH_3OH$·H_2O
Empirical formula	$Fe_2Cl_2O_{21}N_6C_{41}H_{44}$	$Fe_2C_{55.5}H_{59.4}O_{17}N_6Cl_{2.6}$	$Fe_2O_{16}N_6C_{46}H_{54}$
Formula weight	1139.42	1270.84	1058.65
Crystal System	Monoclinic	Orthorhombic	Monoclinic
Space group	*C2/c*	*Pbca*	*C2/c*
a (Å)	37.310(7)	33.486(11)	29.39(2)
b (Å)	22.077(4)	17.521(6)	19.541(13)
c (Å)	13.469(3)	38.950(13)	16.328(11)
β (deg)	96.178(3)		103.023(12)
V (Å^3)	11030(4)	22825(13)	9137(11)
Z	8	16	8
ρ_{calc} (g/cm^3)	1.372	1.493	1.539
Temperature (K)	110	110	110
μ (Mo Kα), (mm^{-1})	0.699	0.704	0.716
θ range (deg)	2.31 – 24.41	2.04 – 25.03	2.08 – 27.10
Crystal size (mm)	0.10 x 0.22 x 0.28	0.25 x 0.28 x 0.40	0.06 x 0.10 x 0.40
Completeness to θ (%)	98.4	99.9	99.9
Max, min peaks (e/Å^3)	0.741 and -0.450	1.650 and -1.062	0.997 and -0.621
Goodness-of-fit on F^2	1.028	1.037	1.081
Total no. of data	66835	308521	58818
No. unique data	8949	20167	10082
R_1 (%)[a]	6.74	7.02	6.21
wR_2 (%)[b]	17.20	18.17	14.11

[a] $R_1 = \Sigma||F_o|-|F_c||/\Sigma|F_o|$, [b] $wR_2 = \{\Sigma[w(F_o^2-F_c^2)]/\Sigma[w(F_o^2)^2]\}^{1/2}$

Despite an extensive literature on diiron complexes having tripodal amine ligands, especially TPA derivatives, little has been reported for more carboxylate-rich systems.[24,25] In a CSD search, only three crystal structures with the simple BPG^- ligand bound to iron are listed.[57] The first has a structure similar to that of **7**, but with a bridging benzoate.[54] No reactivity studies of this compound were reported. The second is a hydroxo-bridged diiron compound[58] and the third structure contains two H_2O ligands bound to an oxo-bridged diiron core (vide infra).[51] Although we observed evidence for a hydroxo-bridged BPG_2DEV^{2-} diiron(III) complex by mass spectrometry (vide infra), we were not able to isolate such a species.

Spectroscopic Characterization of 6, 7, and 8. The UV-vis spectrum of **6**, which contains only oxo as a bridging ligand, differs dramatically from those of the oxo/carboxylato- and oxo/carbonato-bridged compounds **7** and **8**. Figure 4.4 reveals that **6** has a maximum in its optical absorption spectrum around 490 nm, whereas more bands appeared in the spectra of **7** and **8,** which are similar to one another. Despite this spectral similarity, the solubilities of the two latter complexes differ significantly. Compound **7** has excellent solubility in CH_3CN and other organic solvents, presumably owing to the lipophilic carboxylate ligand, but **8** is only significantly soluble in mixtures of CH_3OH/CH_2Cl_2 or CH_3CN/H_2O.

Zero-field Mössbauer spectra of solid samples of **6**, **7**, and **8** were acquired at 4.2 K and/or 90 K. Table 4.5 summarizes the derived Mössbauer parameters from these experiments and the spectra are displayed in Figure 4.5. The isomer shifts acquired at 90 K lie between δ = 0.45 and 0.47 mm/s and

quadrupole splitting parameters, between ΔE_Q = 1.35 and 1.59 mm/s for the three compounds. These values are characteristic of 6-coordinate high-spin (μ-oxo)diiron(III) complexes, which generally have quadrupole splitting values of > 1 mm/s.[55]

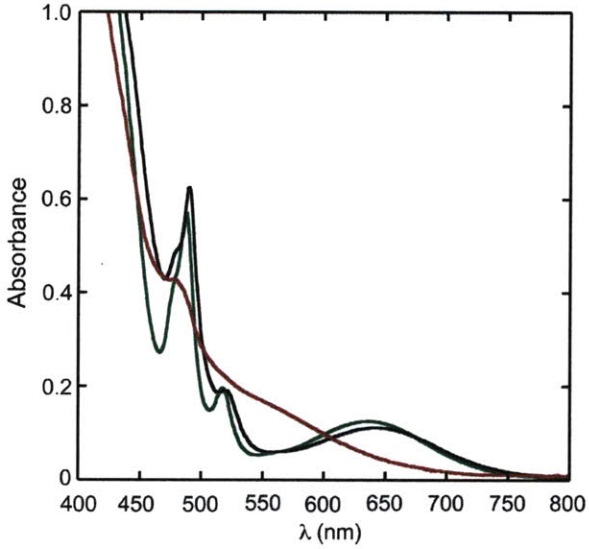

Figure 4.4. UV-vis absorption spectra of 1 mM solutions of **7** (black) and **8** (green) in $CH_3OH/CHCl_3$ (1:1) and of **6** (red) in CH_3CN/H_2O (10:1).

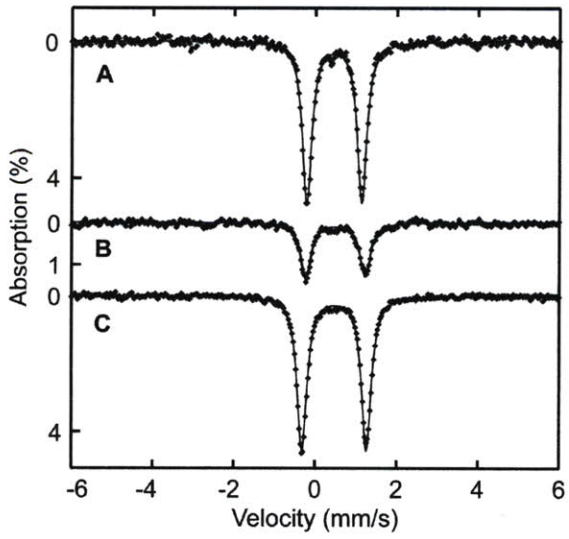

Figure 4.5. Zero-field Mössbauer spectrum of **8** (A), **7** (B), and **6** (C) acquired at 90 K [experimental data (◆) and calculated fits (—)].

Table 4.5. Zero-Field Mössbauer Parameters of Solid **6**, **7**, and **8**, Acquired at 90 K.

Compound	δ (mm/s)	ΔE_Q (mm/s)	Γ (mm/s)
6	0.47(2)	1.59(2)	0.29
7	0.46(2)	1.47(2)	0.31
8	0.47(2)[a]	1.35(2)[a]	0.28[a]
	0.45(2)	1.36(2)	0.31

[a] acquired at 4.2 K.

Fixation of CO_2 to Form the Carbonato-Bridged Complex 8. Complex **6** reacts with atmospheric CO_2 in organic solvents containing triethylamine to form the carbonato-bridged diiron(III) complex **8**. When this reaction was monitored by UV-vis spectroscopy, rapid and quantitative formation of a species having the spectral properties of **8** was apparent (Figure 4.6). Even at low temperatures (–78 °C), the reaction occurred in a few seconds following introduction of excess CO_2 (g). Fixation of CO_2 by hydroxo-bridged diiron(II) complexes has been observed previously,[59] but only three examples exist in which oxo-bridged diiron(III) complexes react with CO_2 to form carbonato-bridged species.[47,48,60]

We propose that **8** forms in stepwise manner via formation of a metal hydroxo species. An analogous mechanism was established for the enzyme carbonic anhydrase, which catalyzes the physiologically essential hydration of CO_2 to form bicarbonate.[61,62] Deprotonation of a water ligand in **6** could produce a bridging hydroxo ion, which is a reasonable supposition because a diiron species with this composition is observed in the electrospray mass spectrum of **6** under basic conditions (vide infra) and because base is required to promote the

reaction in organic solvents. In a second step, nucleophilic attack of the hydroxo ligand on the carbon atom of CO_2 would form bicarbonate. The latter is readily deprotonated to produce the observed carbonato-bridged diiron(III) complex.

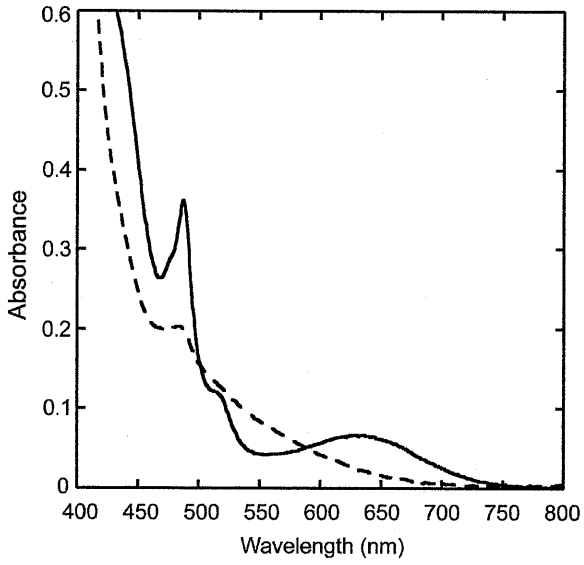

Figure 4.6. UV-vis spectra of **6** before (- - -) and after reaction with CO_2 (——) in a basic CH_3OH/CH_2Cl_2 (1:1) solution.

Mass Spectrometry – Stability of the Dinuclear Core. The coordination chemistry of complexes **6**, **7**, and **8** is also reflected in ESI mass spectrometry experiments. Mass spectra of the dinuclear complexes dissolved in neutral solution revealed the parent compounds, but in basic aqueous solutions, several new ion clusters are detected. Chart 4.3 displays the core structures of the resulting diiron species. Two new prominent peaks at *m/z* = 839 and 883 correspond to positively charged hydroxo- and carbonato-bridged complexes having the formula $[Fe_2(\mu\text{-}O)(\mu\text{-}OH)(BPG_2DEV)]^+$ and {$[Fe_2(\mu\text{-}O)(\mu$-

$CO_3)(BPG_2DEV)]+H\}^+$ (**8**), respectively. The hydroxo-bridged complex can form either by substitution of a bridging ligand by OH^- or by deprotonation of a ligated H_2O molecule in **6**. Although no crystal structure was obtained that revealed this particular unit, it is reasonable to propose that the core can readily form, by analogy to related diiron(III) complexes with a BPG^- ligand and derivatives thereof.[51,58] The carbonato-bridged species most likely derives from a reaction in basic solution of the diiron complex with atmospheric CO_2, as occurs during the synthesis of **8**. Since complex **6** contains weakly bound H_2O ligands, it is not surprising that a peak corresponding to the parent ion is not observed in the mass spectrum. When excess carboxylic or carbamic acid was added to solutions of **6**, **7**, and **8**, a dominant peak for the corresponding carboxylate- or carbamate-bridged species was observed. Interestingly, very bulky carboxylates could also be introduced this manner, suggesting that even sterically hindered bridging ligands are accommodated by the platform.[63] In contrast to the described systems, analogous Fe–O–Fe complexes containing non-covalently linked BPG^- units and derivatives thereof readily dissociate or oligomerize to give mononuclear or trinuclear complexes, respectively.[51,58]

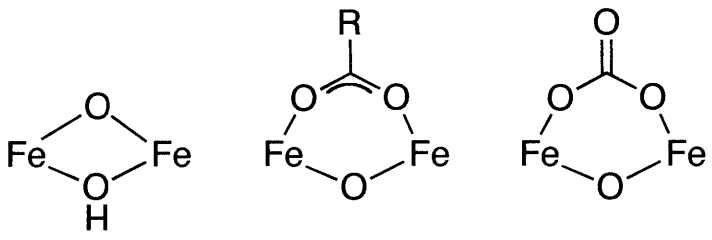

Chart 4.3.

Reaction of 6, 7, and 8 with H_2O_2 – Characterization of a Common Peroxo Intermediate. *(a) UV-vis Spectroscopy.* When **6**, **7**, and **8** were treated with excess H_2O_2 in the presence of a small amount of NEt_3, the solutions turned to a more intense, maroon color, concomitant with evolution of a gaseous product. A test with an alkaline pyrogallol-solution confirmed the formation of dioxygen.[64,65] The intermediate products from reactions with H_2O_2, **6a**, **7a**, and **8a**, in solutions of CH_3CN/H_2O were monitored by UV-vis spectroscopy. Buildup of a broad visible absorption band at 490 nm (ε = 1500 M^{-1} cm^{-1}) was observed in all three cases. The corresponding spectra are presented in Figure 4.7 and in Figures A2.4 and A2.5 (Appendix 2). When the reactions were repeated without the addition of NEt_3, the solutions turned yellow and no spectra analogous to those for **6a**, **7a**, or **8a** were observed. The formation rate of **6a**, **7a**, and **8a** was strongly dependent on the amount of H_2O_2 used. An excess of ca. 1000 equiv of H_2O_2 was required to achieve the maximum absorption intensity at 490 nm for the carbonato-bridged complex **8** over a period of more than an hour. With compound **7**, which has a bridging carboxylate ligand, the band maximized more rapidly (ca. 10-15 min) in the presence of a smaller amount of H_2O_2 (ca. 50-100 equiv). In contrast, only 5-10 equiv of H_2O_2 and less than a minute reaction time were required to form **6a**. These observations are consistent with loss of a H_2O ligand occurring more readily than a monoanionic carboxylate or more strongly coordinating dianionic carbonate ligand. Intermediates **6a**, **7a**, and **8a** were also observed in other solvent mixtures, including CH_3OH/H_2O (ca. 9:1) and CH_2Cl_2/CH_3OH (ca. 1:1). When **6a** was generated in a solution of aqueous

methanol, an absorbance with essentially the same features as found for **6a** in CH_3CN/H_2O was observed, but the peak maximum shifted from 490 nm to 470 nm (Figure A2.6 in Appendix).

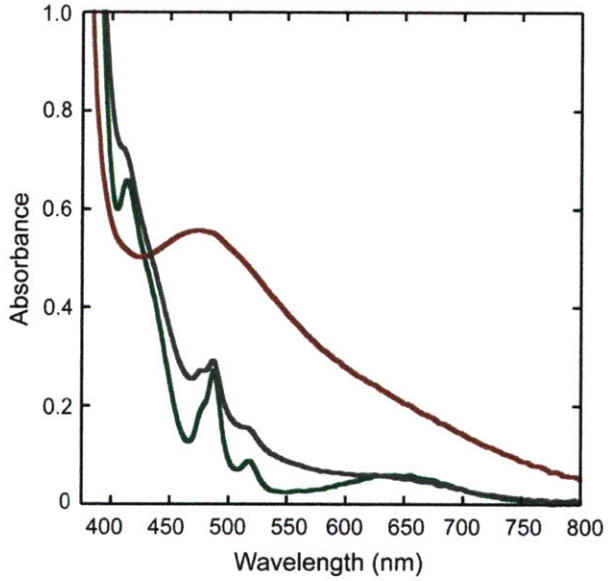

Figure 4.7. UV-vis spectra, recorded at 0 °C, of a reaction mixture of **8** (0.37 mM, green trace) in CH_3CN/H_2O (2:1), NEt_3, and H_2O_2 to form the peroxo intermediate **8a** (red trace). The grey trace corresponds to the product from the reaction.

Reaction of **8** with 1000-fold excess H_2O_2 and a catalytic amount of base, were monitored by UV-vis spectroscopy. Early in the time course of the reaction (ca. 90 min), the intermediate builds up but it subsequently decays to a species having a similar absorbance spectrum as the starting material. Upon addition of a second equivalent of H_2O_2, the band at 490 nm reappears. These experiments, together with mass spectral evidence, reveal that the oxo-bridged diiron core remains largely intact and is most likely bridged by a carbonate ligand because of the similarity of the final spectrum to that of the starting material.

(b) Mössbauer Spectroscopy. Zero-field Mössbauer spectra of frozen solution samples of **6a**, **7a**, and **8a** were acquired at 90 K. The spectrum of **6a** is shown in Figure 4.8, and those for **7a** and **8a** are displayed in Figures A2.7 and A2.8 (Appendix 2). Mössbauer parameters for the three compounds are listed in Table 4.6. A sample of **8a** (in CH_3CN/H_2O) was measured at 4.2 K and fit to two quadrupole doublets with an area ratio of 78/22. Because of limited solubility, the sample contains nearly 80% of starting material **8**, which can be assigned to one of the doublets. The second doublet, however, belongs to the reaction intermediate **8a** with an isomer shift of δ = 0.63(6) mm/s and quadrupole splitting parameter of ΔE_Q = 0.64(6) mm/s. Similarly, in the 90 K spectrum of **7a** (in CH_3OH/H_2O), there is evidence for a population of the starting material **7** in the spectrum, together with another quadrupole doublet assigned to a species having δ = 0.58(2) mm/s and ΔE_Q = 0.56(2) mm/s. The best conversion to the intermediate was achieved in a reaction of a dilute (ca. 2 mM) solution of ^{57}Fe-enriched **6** with H_2O_2 and base. Here, 66% of **6a** was generated with Mössbauer parameters of δ = 0.58(2) mm/s and ΔE_Q = 0.58(2) mm/s, identical within error limits to those for **7a**. Taking into account that the spectrum of **8a** was acquired at temperatures and from solvents different than those of **6a** and **7a**, the data strongly suggest that **6a**, **7a**, and **8a** are the same species.

Table 4.6. Zero-Field Mössbauer Parameters of Intermediates **6a**, **7a**, and **8a**, Acquired at 90 K.

	δ (mm/s)	ΔE_Q (mm/s)	Γ (mm/s)
6a	0.58(2)	0.58(2)	0.35
7a	0.58(2)	0.56(2)	0.29
8a	0.63(6)	0.64(6)	0.32

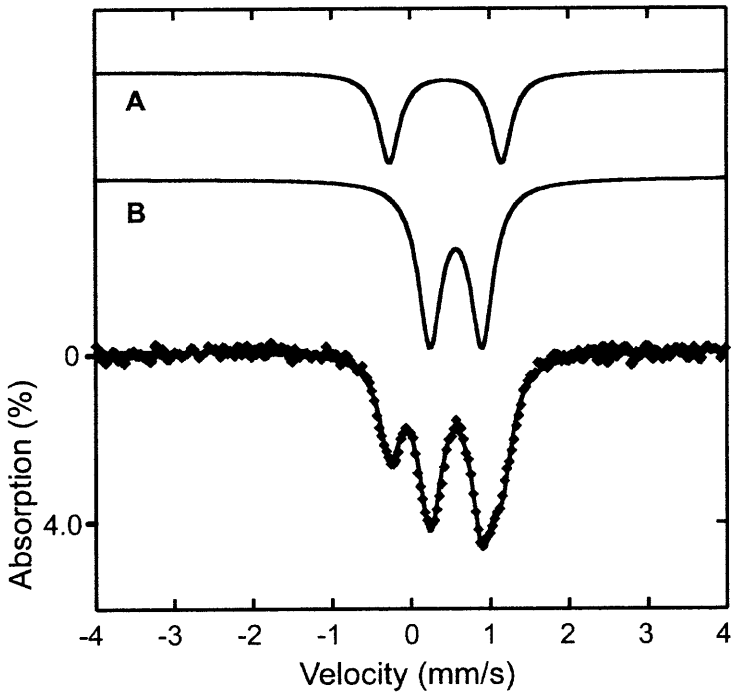

Figure 4.8. Zero-field Mössbauer spectrum [experimental data (◆) and calculated fits (—)] recorded at 90 K for a frozen solution sample of the product of the reaction of **6** with excess H_2O_2 and a trace of NEt_3. The sample contained 66% of **6a** (B) and 34% of a diiron(III) species (A; δ = 0.45 mm/s and ΔE_Q = 1.41 mm/s) with Mössbauer parameters similar to those of the starting material.

We were interested to learn whether the starting diiron complex reforms upon completion of reactions with H_2O_2, as implied by the UV-vis spectroscopic experiments. We therefore measured a frozen solution sample [CH_3OH/H_2O (20:1)] of the decomposition product from a reaction of **6** with ca. 50 equiv of H_2O_2 and a trace of NEt_3. The Mössbauer parameters of δ = 0.46(3) mm/s and ΔE_Q = 1.39(3) mm/s were very similar to those for the starting material **6** (δ = 0.45(3) mm/s; ΔE_Q = 1.51(3) mm/s) in the same basic solution mixture. We conclude that this species is most likely a (μ-oxo)(μ-hydroxo)diiron(III) complex and that no decomposition occurred (vide supra and Chart 4.3).

The spectroscopic and mass spectrometric (vide infra) data determined for the common intermediate formed in the H_2O_2 reactions of **6**, **7**, and **8** are characteristic of a (μ-oxo)(μ-peroxo)diiron(III) complex. Table 4.7 lists some examples of transient peroxo species observed in pre-steady-state studies of non-heme diiron enzymes and of oxo-bridged diiron(III) model systems. Well-defined peroxodiiron(III) intermediates are observed in sMMOH, RNR-R2, and Δ^9D^5 and in the T201S variant of ToMOH[20] that display characteristic peroxo ligand-to-metal charge transfer (LMCT) bands between 650 to 750 nm and Mössbauer parameters of δ = 0.62–0.68 mm/s and ΔE_Q > 1.0 mm/s.[5] In contrast, recently characterized, putative peroxodiiron(III) intermediates of ToMOH and PHH have Mössbauer quadrupole splitting parameters significantly less than 1 mm/s (ΔE_Q = 0.66 mm/s and 0.63 mm/s, respectively) and lack an optical band in their absorption spectra.[66,67] These significant differences can be rationalized by a different peroxo coordination mode and/or protonation state. Synthetically prepared peroxodiiron(III) complexes have the peroxo ligand generally bound in a μ-1,2-fashion with spectroscopic properties very similar to those of peroxo intermediates in the former group of enzymes.[4] The UV-vis and Mössbauer spectroscopic properties of the peroxodiiron(III) intermediate reported here, however, differ significantly from these prior complexes. To our knowledge, of all the synthetic examples of (μ-oxo)(μ-peroxo)diiron(III) species, only the intermediates reported here, **6a**, **7a**, and **8a**, have a Mössbauer quadrupole splitting parameter that is nearly identical to the values for colorless peroxo intermediates in ToMOH and PHH. In addition to their unique Mössbauer

spectroscopic properties, intermediates **6a**, **7a**, and **8a** display a considerably blue-shifted LMCT band, assigned by RR spectroscopy (see below), in their UV-vis spectra compared to other peroxodiiron(III) species (Table 4.7). A comparison with two (μ-oxo)(μ-peroxo)diiron(III) complexes providing an N_4 (6-Me_3-TPA)[68] and a closely related N_3O (6-Me_2-BPP) coordination environment on each iron atom,[69] similar to that supplied by the BPG^- unit, display LMCT bands at 648 nm and 577 nm, respectively, consistent with the carboxylate being a stronger donor. This observation might explain the hypsochromic shift in intermediates containing the BPG_2DEV^{2-} ligand.

Table 4.7. Spectroscopic Parameters for Peroxo Intermediates in Non-Heme Diiron Enzymes and Synthetic Oxo-Bridged Diiron(III) Compounds.

	Optical		Mössbauer		
	λ_{max} (nm)	ε ($M^{-1}cm^{-1}$)	δ (mm/s)	ΔE_Q (mm/s)	*Ref.*
sMMOH (*M. caps.* (Bath))	700	1800	0.66	1.51	*a*
ToMOH (*Pseudomonas* sp. OX1)	–	–	0.54	0.66	*66*
ToMOH T201S (*Pseudomonas* sp. OX1)	675	1500	0.67	1.51	*20*
PHH (*Pseudomonas* sp. OX1)	–	–	0.59	0.63	*67*
RNR-R2 D84E	700	1500	0.63	1.58	*a*
Δ^9-desaturase	700	1200	0.68	1.90	*a*
$[Fe_2(\mu\text{-}O)(\mu\text{-}O_2)(6\text{-}Me_3\text{-}TPA)_2]^{2+}$	494; 648	1100; 1200	0.54	1.68	*68*
$[Fe_2(\mu\text{-}O)(\mu\text{-}O_2)(\mu\text{-}O_2CR)(hexpy)_2]^{+}$	510; 605	1300; 1310	0.53	1.67	*70*
$[Fe_2(\mu\text{-}O)(\mu\text{-}O_2)(6\text{-}Me_2\text{-}BPP)_2]$	577	1500	0.50	1.46	*69*
$[Fe_2(\mu\text{-}O)(\mu\text{-}O_2)BPG_2DEV]$	490	1500	0.58	0.58	*b*

a = Parameters were taken from ref. 1. *b* = This work.

(c) EPR Spectroscopy. EPR spectroscopic analysis of **8a** reveals an axial signal with g values of 2.062 and 2.004, which we attribute to a mixed-valent diiron(II,III) (S = ½) species. Spin quantitation indicated only 2.6% abundance, however. The bulk of the sample is EPR-silent, which we assign to two iron(III) centers antiferromagnetically coupled to one another. This result is consistent

with a peroxo-bridged diiron(III) complex.[4] The absence of an EPR signal centered at g = 4.3, characteristic of mononuclear high-spin iron(III) complexes, is also in agreement with these findings. The EPR spectrum is displayed as Figure A2.11 in Appendix 2.

(d) Resonance Raman Spectroscopy. RR spectra of intermediate **6a**, prepared with either $H_2{}^{16}O_2$ (or $H_2{}^{18}O_2$) and obtained with 568 nm excitation, revealed two features at 819 and 845 (772 and 797) cm^{-1}, respectively (Figure 4.9). These RR signals are not observed in samples that were allowed to proceed in time beyond decay of intermediate **6a** (Figure 4.9B). The intensities of the RR doublets also decrease after prolonged laser exposure and photobleaching of the samples from dark brown to light yellow. Relative to solvent bands, these intensities also vary with excitation wavelength, revealing a significant decrease at 647 nm and at 413 nm, where intra-pyridine vibrations enter into resonance (Figure 4.10). Because of the complexity of these RR signals and the photosensitivity of intermediate **6a**, extracting excitation profiles would be an overinterpretation of the data. Nevertheless, the excitation wavelength dependence of the isotope-sensitive signals qualitatively matches expectation based on the absorption spectra of intermediate **6a** (Figure A2.6 in Appendix 2).

The observed RR frequencies and ^{18}O-shifts (-47/-48 cm^{-1}) are consistent with metal-peroxo vibrations. The ν(O–O) frequencies in symmetrically bridged (μ-1,2-peroxo)diiron(III) complexes range from 830 to 908 cm^{-1} and low frequency O–O stretching bands are generally correlated with short Fe–Fe

distances.[71] The RR bands associated with ν(O–O) in intermediate **6a** are at the lower end of this range and a comparison to these systems indicates that the Fe–Fe distance in intermediate **6a** may be as short as 3.1–3.2 Å.[71-73] Short Fe–Fe distances require stabilization from bridging ligands in addition to the peroxo group, with a μ-oxo group providing the shortest such distance. Although Fe–O–Fe modes were not identified in the RR spectra of intermediate **6a**, it is reasonable to assume that the oxo bridge, present in the starting material, remains in intermediate **6a**. This assignment is strongly supported by mass spectrometric analysis (vide infra). The covalent linkage between the two iron sites supplied by the syn N-donor ligand BPG_2DEV^{2-} may also play an important role in promoting a short Fe–Fe distance. In a similar peroxodiiron(III) peroxo species, with a dinucleating ligand having two covalently linked tris(2-pyridyl)methane moieties, the O–O mode of the bound peroxide appears at very low value of 830 cm^{-1}, which is consistent with this hypothesis.[71,74]

From spectroscopic studies we can conclude that the peroxo ligand bridges the two iron centers in **6a**, but we cannot definitively assign its binding mode. Detailed experimental and theoretical studies on (μ-oxo)(μ-1,2-peroxo)diiron(III) intermediates having unlinked tetradentate capping ligands, related to those in BPG_2DEV^{2-}, confirmed the 1,2-peroxo bridging mode. Furthermore, a crystal structure of [Fe_2(μ-O)(μ-1,2-O_2)6-Me_2-BPP] (see Table 4.7), which has an identical ligand set to that of **6a**, reveals a 1,2-bridging peroxo ligand lying approximately in the plane defined by the Fe–O–Fe unit.[69] The spectroscopic properties and the O–O stretching frequencies of the

peroxodiiron(III) compound described here, however, differ significantly from those reported for these species and we cannot rule out an alternative peroxo binding mode. Because the mass spectra of **6a**–**8a** reveal the presence of an added proton as well as the peroxo ligand (vide infra), the structure might contain a μ-1,1-hydroperoxodiiron(III) unit in which the dangling O-atom is protonated, a unit that is consistent with all of the data.

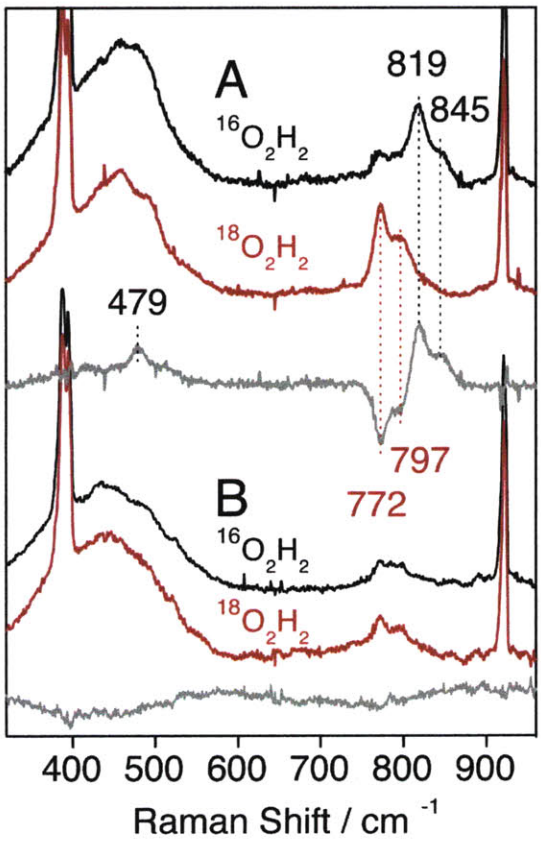

Figure 4.9: RR spectra of intermediate **6a** (A) and its decay product (B) obtained with 568 nm excitation at 110 K. Sharp Raman bands below 400 and above 900 cm^{-1} correspond to solvent vibrations.

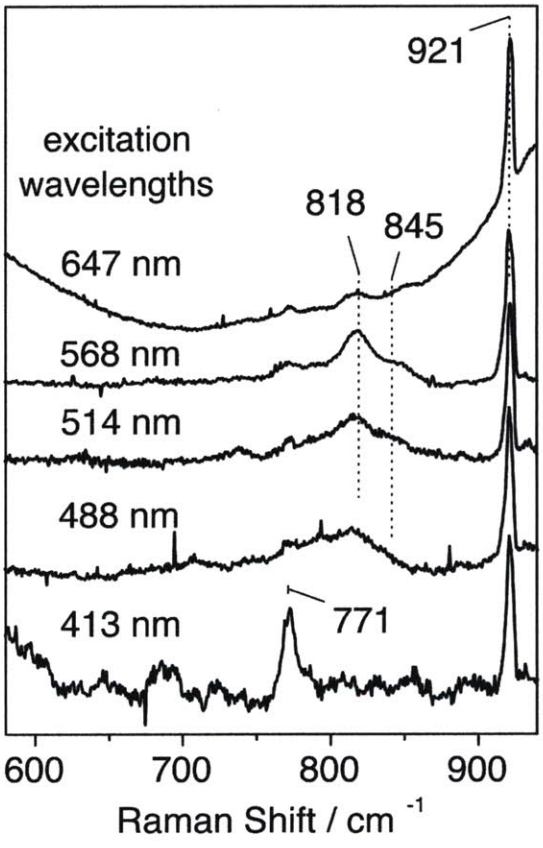

Figure 4.10: RR spectra of intermediate **6a** obtained with different laser excitations at 110 K. All traces are normalized on the 921 cm^{-1} solvent band.

The presence of a doublet rather than a single peak for the isotope-sensitive RR bands may result either from two different conformations of the peroxodiiron complex or Fermi splitting of a fundamental O–O stretch corresponding to the doublet average of 832 cm^{-1}. Fermi coupling of the ν(O–O) with underlying non-resonant vibrations has been invoked for several peroxodiiron complexes.[10,17,68,73] On the other hand, the possible occurrence of two distinct peroxodiiron species must also be taken into consideration, perhaps reflecting different protonation states. Optical spectroscopic and kinetic studies indicate the presence of two peroxo intermediates in the oxygenation chemistry of sMMOH[75,76] and ToMOH.[20] In the low-frequency region, the [^{16}O-intermediate–^{18}O-intermediate] RR difference spectrum isolates a positive feature at 479 cm^{-1} that may correspond to the expected ν(Fe–$^{16}O_2$) mode, even though its negative ^{18}O-counterpart does not emerge from the broad and nearly featureless background signal that occurs in this region (Figure 4.9).

(e) Mass Spectrometry. ESI-MS of **6a**, **7a**, and **8a** were acquired using solutions of CH_3CN/H_2O (3:1) or CH_2Cl_2/CH_3OH (1:1) in low and high resolution modes. In each high-resolution mass spectrum of **6a**, **7a**, and **8a** there was an ion cluster having a mass and isotope pattern identical to that calculated for the M+H (peroxo)diiron(III) species $\{[Fe_2(\mu\text{-}O)(\mu\text{-}O_2)BPG_2DEV]+H\}^+$ with a theoretical *m/z* = 855.1195. The recorded values were *m/z* = 855.1205, 855.1189, and 855.1161 for **6a**, **7a**, and **8a**, respectively. A comparison between the theoretical and observed spectra is presented in Figure A2.12 (Appendix 2). Isotope-labeling experiments carried out with $H_2{}^{18}O_2$ (2% in H_2O) revealed a peak shift of four

units from *m/z* = 855 to 859, demonstrating that the peroxide is bound to the diiron center. A comparison of the two mass spectra is shown in Figure 4.11.

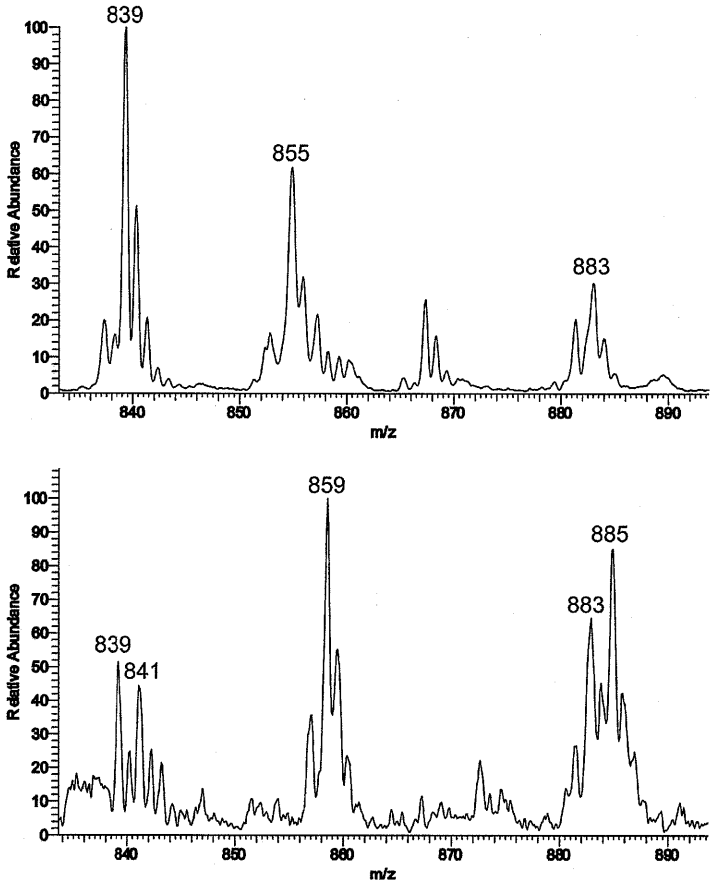

Figure 4.11. ESI mass spectrum of **7a** at 295 K in CH_3CN displaying the isotope patterns for ions at *m/z* 855 for {[Fe_2(μ-O)(μ-$^{16}O_2$)BPG_2DEV]+H^+} (top) and *m/z* 859 for for {[Fe_2(μ-O)(μ-$^{18}O_2$)BPG_2DEV]+H^+} (bottom). The peak *m/z* = 867 in the upper spectrum can be assigned to a formate-bridged diiron complex [Fe_2(μ-O)(μ-O_2CH)BPG_2DEV]$^+$, which is due to the presence of residual formic acid impurities.

Singly-charged ion clusters of [Fe_2(μ-O)(μ-OH)(BPG_2DEV)]$^+$ (*m/z* = 839) and {[Fe_2(μ-O)(μ-CO_3)(BPG_2DEV)]+H}$^+$ (*m/z* = 883) were also observed in these mass spectra, which derive from the reaction of the diiron complex with

hydroxide and CO_2 from the air (vide supra). Interestingly, two additional peaks at *m/z* = 841 and 885 were detected in the ^{18}O-labeled sample. These values are shifted by two mass units from the peaks for these two diiron complexes, indicating that an ^{18}O atom is incorporated into the hydroxo- and carbonato-bridged compounds, respectively. This result suggests that the O–O bond of the bound peroxide is indeed cleaved and, presumably, that H_2O is formed. An O–O bond scission is reasonable, because this reaction has been investigated extensively in related (μ-oxo)(μ-1,2-peroxo)diiron(III) complexes, which form high-valent diiron centers, and has been proposed for a similar compound in a dinucleating ligand system.[77] The intermediate could react with another equivalent of H_2O_2 to form H_2O and O_2. We propose that the newly formed H_2O molecule stays bound to the diiron center and can readily be deprotonated under basic conditions to form a bridging hydroxide ion. Such an intermediate could additionally react with CO_2 from air to form the carbonato-bridged species. By mass spectrometry, we were also able to establish that the peroxo species is regenerated upon additional treatment with H_2O_2 (data not shown).

Catalase Activity. When H_2O_2 was added to a basic solution of the diiron compounds **6**, **7**, or **8**, O_2 formation was observed, as confirmed by a test with an alkaline pyrogallol solution.[64,65] The catalase-like activity of the carbonato complex **8** was investigated in more detail and the O_2 formed in the reactions was quantified. To a fixed concentration of diiron(III) complex **8** and NEt_3 in a solution of CH_3CN/H_2O (2:1) at 0 °C were added various amounts of H_2O_2. The quantity of O_2 produced was measured volumetrically. The yield of O_2 depends

linearly on the amount of H_2O_2, with a slope of 0.53 (R^2 = 0.99), which corresponds to catalase-like reaction stoichiometry (Figure 4.12 and eq 1).

$$2H_2O_2 \rightarrow O_2 + 2H_2O \qquad (1)$$

The diiron catalyst is very efficient and achieves ~ 10,000 turnovers. Experiments with compounds **6** and **7** under the same conditions revealed them to be as efficient as **8** with respect to catalase function.

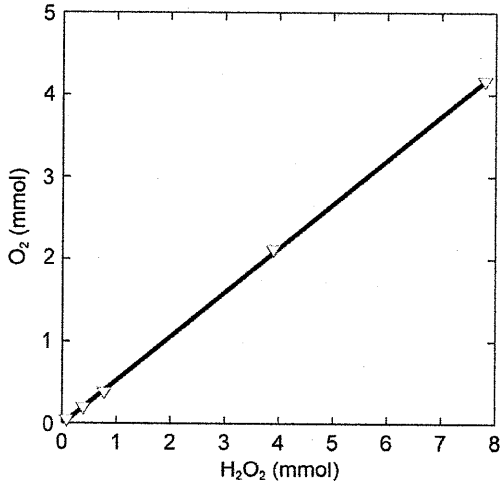

Figure 4.12. O_2 formation from 0.078 to 7.8 mmol H_2O_2 at 0 °C as catalyzed by **8** (2 mL of 0.4 mM solution in CH_3CN/H_2O, 2:1) and 10 µL of NEt_3.

Catalase activity has been reported in reactions of a relatively small number of oxo-bridged diiron(III) compounds with H_2O_2.[78-83] In all cases, intermediates with spectroscopic properties characteristic for peroxo-bridged diiron(III) complexes were observed. Some common features of these H_2O_2-disproportionation catalysts include complex decomposition, TON (turn-over number) dependence on the exchangeability of the bridging ligand, and

increasing O_2 formation rates at higher pH values. In contrast, to these previously reported systems, decomposition of the complexes **6**, **7**, and **8** upon treatment with H_2O_2 does not occur. The increased stability of the complexes is attributed to the BPG_2DEV^{2-} ligand. Remarkably, quantitative O_2 production is observed for all three complexes **6**–**8**, with TONs significantly higher than those reported for other systems (the ratio of $[Fe_2]$:H_2O_2 never exceeded 1:500) and only when base was added to the reaction mixture. In samples that were lacking additional base, quantitative O_2 production was not observed.

Catalase activity is important for protecting the cell from oxidative damage by excess H_2O_2. A ubiquitous family of metalloenzymes disproportionate H_2O_2 in an exothermic reaction to form H_2O and dioxygen. One of the two most abundant classes of catalases contains an iron protoporphyrin IX cofactor with an axial tyrosinate ligand.[84] The second most common catalase enzyme contains a dimanganese active site.[85] For non-heme diiron enzymes, catalase activity has been reported for ToMOH,[86] toluene-2-monooxygenase from *Burkholderia cepacia* G4,[87] and PHH.[76] By comparison with previous studies of diiron model compounds, the present findings are important for our general understanding of catalase activity in BMMs and the decomposition pathway of H_2O_2 catalyzed by diiron centers.

Substrate Oxidation. We also investigated whether the peroxo intermediates **6a**, **7a**, and **8a** might function as oxidases. The common intermediate quantitatively oxidizes PPh_3 to Ph_3O, a very easy conversion, but are poor catalysts for epoxidation of *cis*-cyclooctene, unlike some related

systems.[53,88,89] Quantitation of the epoxide revealed yields with < 1% and TONs of ca. 8 and 3, for **6a** and **7a**, respectively (Table 4.8). The production of O_2 was strongly diminished by addition of phosphine to the reaction, but was not significantly affected when cyclooctene was present, which is consistent with competitive catalase and substrate oxidation reactions.

Table 4.8. Studies of the Oxidation of *cis*-Cyclooctene to Cyclooctene Epoxide with **6** and **7**.

Complex	Yield (%)	TON
6	0.93	8.8[a]
7	0.35	3.5[a]

[a] Average values from two trials.

Summary and Perspective

This study describes the successful application of the dinucleating ligand H_2BPG_2DEV to specifically model the syn coordination of histidine residues in non-heme diiron enzymes. This scaffold is more biologically relevant than previous versions due to its greater carboxylate content. Three (μ-oxo)diiron(III) derivatives were characterized, one with a terminal water molecule on each iron atom and two with additional bridging ligands, either carbonate or carboxylate. Reactivity studies with H_2O_2 show that the dinucleating ligand conveys an inherent stability to all three oxo-bridged diiron complexes, which serve as catalases in multi-turnover reactions with large excesses of H_2O_2. These characteristics distinguish these complexes from the broader class of diiron(III) complexes that do not have covalently linked tripodal ligands. The present system belongs to a small group of non-heme diiron model complexes having

catalase activity that dominates over its oxygenating properties. Similar catalase activity has been observed in ToMOH and PHH, suggesting additional relevance of the present model complexes to biological counterparts. Spectroscopic analysis of a transient (μ-oxo)(μ-peroxo)diiron(III) species generated in this chemistry reveals properties that deviate from the characteristic parameters for peroxo-bridged intermediates in most model complexes and non-heme diiron enzymes. The Mössbauer spectroscopic properties closely resemble those for a peroxo intermediate in ToMOH, with ΔE_Q values less than 1 mm/s. Raman studies reveal an O–O stretching frequency that is atypically low, suggesting a short iron-iron distance in the peroxo intermediate, presumably facilitated by the dinucleating ligand and possibly reflecting a previously unknown μ-1,1 bridging mode. These physical properties of these complexes differentiate them from compounds with mononucleating ligands. Further studies of related complexes are warranted in pursuit of information to understand the origin of the spectroscopic properties and reactivity of non-heme diiron sites in biology.

Acknowledgements. This work was supported by Grant GM032134 from the National Institute of General Medical Sciences. I thank Dr. Jeremy J. Kodanko and Anna Morys who carried out initial studies on a related project with the H_2BPG_2DET ligand, Prof. Pierre Moënne-Loccoz and Takahiro Hayashi at Oregon Health and Science University for acquiring the resonance Raman spectra, Ms. Wanhua Ye at the Chemistry Department at Tufts University and Ms. Li Li at the DCIF at MIT for help with mass spectrometric measurements, Dr.

Sebastian Stoian for assistance in acquiring the EPR spectra, and Dr. Peter Müller for assistance with X-ray crystallography.

Supporting Information. ORTEP diagrams of the complete molecules **7** and **8**, space-filling diagrams of **6–8**, UV-vis spectra of **6a** and **7a**, solution Mössbauer spectra of **7a**, **8a**, **6**, and the decomposition product of **6a**; the EPR spectrum of **8a**, and high-resolution mass spectra of **6a–8a** are provided in Appendix 2.

References

(1) Feig, A. L.; Lippard, S. J. *Chem. Rev.* **1994**, *94*, 759-805.

(2) Wallar, B. J.; Lipscomb, J. D. *Chem. Rev.* **1996**, *96*, 2625-2657.

(3) Kurtz, D. M., Jr. *J. Biol. Inorg. Chem.* **1997**, *2*, 159-167.

(4) Solomon, E. I.; Brunold, T. C.; Davis, M. I.; Kemsley, J. N.; Lee, S.-K.; Lehnert, N.; Neese, F.; Skulan, A. J.; Yang, Y.-S.; Zhou, J. *Chem. Rev.* **2000**, *100*, 235-349.

(5) Merkx, M.; Kopp, D. A.; Sazinsky, M. H.; Blazyk, J. L.; Müller, J.; Lippard, S. J. *Angew. Chem., Int. Ed.* **2001**, *40*, 2782-2807.

(6) Sturgeon, B. E.; Burdi, D.; Chen, S.; Huynh, B.-H.; Edmondson, D. E.; Stubbe, J.; Hoffman, B. M. *J. Am. Chem. Soc.* **1996**, *118*, 7551-7557.

(7) Bollinger, J. M., Jr.; Edmondson, D. E.; Huynh, B. H.; Filley, J.; Norton, J. R.; Stubbe, J. *Science* **1991**, *253*, 292-298.

(8) Logan, D. T.; Su, X. D.; Åberg, A.; Regnström, K.; Hajdu, J.; Eklund, H.; Nordlund, P. *Structure* **1996**, *4*, 1053-1064.

(9) Lindqvist, Y.; Huang, W.; Schneider, G.; Shanklin, J. *EMBO J.* **1996**, *15*, 4081-4092.

(10) Broadwater, J. A.; Ai, J.; Loehr, T. M.; Sanders-Loehr, J.; Fox, B. G. *Biochemistry* **1998**, *37*, 14664-14671.

(11) Sazinsky, M. H.; Lippard, S. J. *Acc. Chem. Res.* **2006**, *39*, 558-566.

(12) Murray, L. J.; Lippard, S. J. *Acc. Chem. Res.* **2007**, *40*, 466-474.

(13) Cafaro, V.; Izzo, V.; Scognamiglio, R.; Notomista, E.; Capasso, P.; Casbarra, A.; Pucci, P.; Di Donato, A. *Appl. Environ. Microbiol.* **2004**, *70*, 2211-2219.

(14) Sazinsky, M. H.; Bard, J.; Di Donato, A.; Lippard, S. J. *J. Biol. Chem.* **2004**, *279*, 30600-30610.

(15) Sazinsky, M. H.; Dunten, P. W.; McCormick, M. S.; DiDonato, A.; Lippard, S. J. *Biochemistry* **2006**, *45*, 15392-15404.

(16) Kuzelka, J.; Farrell, J. R.; Lippard, S. J. *Inorg. Chem.* **2003**, *42*, 8652-8662.

(17) Moënne-Loccoz, P.; Baldwin, J.; Ley, B. A.; Loehr, T. M.; Bollinger, J. M. *Biochemistry* **1998**, *37*, 14659-14663.

(18) Rinaldo, D.; Philipp, D. M.; Lippard, S. J.; Friesner, R. A. *J. Am. Chem. Soc.* **2007**, *129*, 3135-3147.

(19) Lee, S.-K.; Lipscomb, J. D. *Biochemistry* **1999**, *38*, 4423-4432.

(20) Song, W. J.; Behan, R. K.; Naik, S. G.; Huynh, B. H.; Lippard, S. J. *J. Am. Chem. Soc.* **2009**, *131*, 6074-6075.

(21) Lee, S.-K.; Fox, B. G.; Froland, W. A.; Lipscomb, J. D.; Münck, E. *J. Am. Chem. Soc.* **1993**, *115*, 6450-6451.

(22) Liu, K. E.; Valentine, A. M.; Wang, D.; Huynh, B. H.; Edmondson, D. E.; Salifoglou, A.; Lippard, S. J. *J. Am Chem. Soc.* **1995**, *117*, 10174-10185.

(23) Du Bois, J.; Mizoguchi, T. J.; Lippard, S. J. *Coord. Chem. Rev.* **2000**, *200-202*, 443-485.

(24) Tshuva, E. Y.; Lippard, S. J. *Chem. Rev.* **2004**, *104*, 987-1012.

(25) Que, L., Jr.; Tolman, W. B. *Angew. Chem., Int. Ed.* **2002**, *41*, 1114-1137.

(26) Tolman, W. B.; Que, L., Jr. *J. Chem. Soc., Dalton Trans.* **2002**, *5*, 653-660.

(27) Baik, M.-H.; Gherman, B. F.; Friesner, R. A.; Lippard, S. J. *J. Am Chem. Soc.* **2002**, *124*, 14608-14615.

(28) Kodanko, J. J.; Xu, D.; Song, D. T.; Lippard, S. J. *J. Am. Chem. Soc.* **2005**, *127*, 16004-16005.

(29) Kodanko Jeremy, J.; Morys Anna, J.; Lippard Stephen, J. *Org. Lett.* **2005**, *7*, 4585-4588.

(30) Kodanko, J. J.; Lippard, S. J. *Inorg. Chim. Acta* **2008**, *361*, 894-900.

(31) Reisner, E.; Lippard, S. J. *Eur. J. Org. Chem.* **2008**, *2008*, 156-163.

(32) Wang, X.; Rabbat, P.; O'Shea, P.; Tillyer, R.; Grabowski, E. J. J.; Reider, P. J. *Tetrahedron Lett.* **2000**, *41*, 4335-4338.

(33) Policar, C.; Lambert, F.; Cesario, M.; Morgenstern-Badarau, I. *Eur. J. Inorg. Chem.* **1999**, 2201-2207.

(34) Armstrong, W. H.; Lippard, S. J. *Inorg. Chem.* **1985**, *24*, 981-982.

(35) Dunbar, K. R.; Longridge, J. J.; Rawson, J. M.; Sun, J.-S.; Hagen, K. S.; Do, B. *Inorg. Synth.* **2002**, *33*, 103-107.

(36) Gumanov, L. L.; Shteinman, A. A.; Nordlander, E.; Koldobskii, G. I. *Russ. J. Org. Chem.* **2002**, *38*, 606-608.

(37) *SMART, Software for the CCD Detector System*, version 5.6; Bruker AXS Madison, WI, 2000.

(38) Sheldrick, G. M. *SHELXTL-97*, University of Göttingen: Göttingen, Germany: 2000.

(39) Sheldrick, G. M. *Acta Crystallogr., Sect. A* **2008**, *A64*, 112-122.

(40) Sheldrick, G. M. *SADABS: Area-Detector Absorption Correction*, University of Göttingen: Göttingen, Germany, 2001.

(41) Spek, A. L. *PLATON, A Multipurpose Crystallographic Tool*, Utrecht University: Utrecht, The Netherlands, 2000.

(42) Kent, T. A. *WMOSS*, Minneapolis, 1998.

(43) Lippard, S. J. *Angew. Chem., Int. Ed.* **1988**, *27*, 344-361.

(44) Norman, R. E.; Holz, R. C.; Menage, S.; Que, L., Jr.; Zhang, J. H.; O'Connor, C. J. *Inorg. Chem.* **1990**, *29*, 4629-4637.

(45) Arulsamy, N.; Hodgson, D. J.; Glerup, J. *Inorg. Chim. Acta* **1993**, *209*, 61-69.

(46) Fujita, T.; Ohba, S.; Nishida, Y.; Goto, A.; Kokii, T. *Acta Crystallogr., Sect. C* **1994**, *C50*, 544-546.

(47) Hazell, R.; Jensen, K. B.; McKenzie, C. J.; Toftlund, H. *J. Chem. Soc., Dalton Trans.* **1995**, 707-717.

(48) Glaser, T.; Lügger, T.; Hoffmann, R.-D. *Eur. J. Inorg. Chem.* **2004**, 2356-2362.

(49) Schmitt, W.; Hill, J. P.; Malik, S.; Volkert, C. A.; Ichinose, I.; Anson, C. E.; Powell, A. K. *Angew. Chem., Int. Ed.* **2005**, *44*, 7048-7053.

(50) Schmitt, W.; Hill, J. P.; Juanico, M. P.; Caneschi, A.; Costantino, F.; Anson, C. E.; Powell, A. K. *Angew. Chem., Int. Ed.* **2005**, *44*, 4187-4192.

(51) Mortensen, M. N.; Jensen, B.; Hazell, A.; Bond, A. D.; McKenzie, C. J. *J. Chem. Soc., Dalton Trans.* **2004**, 3396-3402.

(52) Hazell, A.; Jensen, K. B.; McKenzie, C. J.; Toftlund, H. *J. Chem. Soc., Dalton Trans.* **1993**, 3249-3257.

(53) Kodera, M.; Itoh, M.; Kano, K.; Funabiki, T.; Reglier, M. *Angew. Chem., Int. Ed.* **2005**, *44*, 7104-7106.

(54) Menage, S.; Que, L., Jr. *New J. Chem.* **1991**, *15*, 431-438.

(55) Kurtz, D. M., Jr. *Chem. Rev.* **1990**, *90*, 585-606.

(56) Drüeke, S.; Wieghardt, K.; Nuber, B.; Weiss, J. *Inorg. Chem.* **1989**, *28*, 1414-1417.

(57) *ConQuest*, Cambridge Crystallographic Data Center: 2007.

(58) Furutachi, H.; Ohyama, Y.; Tsuchiya, Y.; Hashimoto, K.; Fujinami, S.; Uehara, A.; Suzuki, M.; Maeda, Y. *Chem. Lett.* **2000**, 1132-1133.

(59) Kitajima, N.; Hikichi, S.; Tanaka, M.; Morooka, Y. *J. Am. Chem. Soc.* **1993**, *115*, 5496-5508.

(60) Schmitt, W.; Anson, C. E.; Sessoli, R.; van Veen, M.; Powell, A. K. *J. Inorg. Biochem.* **2002**, *91*, 173-189.

(61) Silverman, D. N.; Lindskog, S. *Acc. Chem. Res.* **1988**, *21*, 30-36.

(62) Vahrenkamp, H. *Acc. Chem. Res.* **1999**, *32*, 589-596.

(63) Friedle, S.; Lippard, S. J. Unpublished results.

(64) Duncan, I. A.; Harriman, A.; Porter, G. *Anal. Chem.* **1979**, *51*, 2206-2208.

(65) Williams, D. D.; Blachly, C. H.; Miller, R. R. *Anal. Chem.* **1952**, *24*, 1819-1821.

(66) Murray, L. J.; García-Serres, R.; Naik, S.; Huynh, B. H.; Lippard, S. J. *J. Am. Chem. Soc.* **2006**, *128*, 7458-7459.

(67) Izzo, V.; Tinberg, C. E.; García-Serres, R.; Naik, S.; Huynh, B. H.; Lippard, S. J. Unpublished results.

(68) Dong, Y.; Zang, Y.; Shu, L.; Wilkinson, E. C.; Que, L., Jr.; Kauffmann, K.; Münck, E. *J. Am. Chem. Soc.* **1997**, *119*, 12683-12684.

(69) Zhang, X.; Furutachi, H.; Fujinami, S.; Nagatomo, S.; Maeda, Y.; Watanabe, Y.; Kitagawa, T.; Suzuki, M. *J. Am. Chem. Soc.* **2005**, *127*, 826-827.

(70) Kodera, M.; Taniike, Y.; Itoh, M.; Tanahashi, Y.; Shimakoshi, H.; Kano, K.; Hirota, S.; Iijima, S.; Ohba, M.; Okawa, H. *Inorg. Chem.* **2001**, *40*, 4821-4822.

(71) Fiedler, A. T.; Shan, X.; Mehn, M. P.; Kaizer, J.; Torelli, S.; Frisch, J. R.; Kodera, M.; Que, L., Jr. *J. Phys. Chem. A* **2008**, *112*, 13037-13044 and references therein.

(72) Brunold, T. C.; Tamura, N.; Kitajima, N.; Moro-oka, Y.; Solomon, E. I. *J. Am. Chem. Soc.* **1998**, *120*, 5674-5690.

(73) Moënne-Loccoz, P.; Krebs, C.; Herlihy, K.; Edmondson, D. E.; Theil, E. C.; Huynh, B. H.; Loehr, T. M. *Biochemistry* **1999**, *38*, 5290-5295.

(74) Kodera, M.; Itoh, M.; Kano, K.; Funabiki, T. *Bull. Chem. Soc. Jpn.* **2006**, *79*, 252-261.

(75) Brazeau, B. J.; Lipscomb, J. D. *Biochemistry* **2000**, *39*, 13503-13515.

(76) Tinberg, C. E.; Lippard, S. J. Unpublished results.

(77) Xue, G.; Fiedler, A. T.; Martinho, M.; Münck, E.; Que, L., Jr. *Proc. Natl. Acad. Sci. U.S.A.* **2008**, *105*, 20615-20620.

(78) Mauerer, B.; Crane, J.; Schuler, J.; Wieghardt, K.; Nuber, B. *Angew. Chem., Int. Ed.* **1993**, *32*, 289-291.

(79) Menage, S.; Vincent, J. M.; Lambeaux, C.; Fontecave, M. *J. Chem. Soc., Dalton Trans.* **1994**, 2081-2084.

(80) Ito, S.; Okuno, T.; Matsushima, H.; Tokii, T.; Nishida, Y. *J. Chem. Soc., Dalton Trans.* **1996**, 4479-4484.

(81) Okuno, T.; Ito, S.; Ohba, S.; Nishida, Y. *J. Chem. Soc., Dalton Trans.* **1997**, 3547-3551.

(82) Than, R.; Schrodt, A.; Westerheide, L.; Van Eldik, R.; Krebs, B. *Eur. J. Inorg. Chem.* **1999**, 1537-1543.

(83) Balogh-Hergovich, E.; Speier, G.; Reglier, M.; Giorgi, M.; Kuzmann, E.; Vertes, A. *Eur. J. Inorg. Chem.* **2003**, 1735-1740.

(84) Maté, M. J.; Murshudov, G.; Bravo, J.; Melik-Adamyan, W.; Loewen, P. C.; Fita, I. *Handb. Metalloproteins* **2001**, *1*, 486-502.

(85) Wu, A. J.; Penner-Hahn, J. E.; Pecoraro, V. L. *Chem. Rev.* **2004**, *104*, 903-938.

(86) Murray, L. J.; Naik, S. G.; Ortillo, D. O.; García-Serres, R.; Lee, J. K.; Huynh, B. H.; Lippard, S. J. *J. Am. Chem. Soc.* **2007**, *129*, 14500-14510.

(87) Newman, L. M.; Wackett, L. P. *Biochemistry* **1995**, *34*, 14066-14076.

(88) White, M. C.; Doyle, A. G.; Jacobsen, E. N. *J. Am. Chem. Soc.* **2001**, *123*, 7194-7195.

(89) Taktak, S.; Kryatov, S. V.; Haas, T. E.; Rybak-Akimova, E. V. *J. Mol. Catal. A: Chem.* **2006**, *259*, 24-34.

Appendix 1

Supporting Tables and Figures for Chapter 2. 9-Triptycenecarboxylate-Bridged Diiron(II) Complexes: Capture of the Paddlewheel Geometric Isomer

Table A1.1. Summary of X-ray Crystallographic Data.

	1a•7CH_2Cl_2	**2**•3.4DME•0.6Et_2O	**3**•4DME	**4**•5.2DME•0.8Et_2O
Empirical formula	$Fe_2C_{99}H_{82}O_{10}Cl_{14}$	$Fe_4C_{110}H_{102}N_2O_{15.34}$	$Fe_2C_{108}H_{104}N_4O_{16}$	$Fe_2C_{116}H_{121.92}N_4O_{19.25}$
Formula weight	2039.65	1809.08	1825.65	1991.80
Crystal System	Orthorhombic	Triclinic	Triclinic	Triclinic
Space group	$Pca2_1$	$P\bar{1}$	$P\bar{1}$	$P\bar{1}$
a (Å)	20.350(4)	10.4599(8)	10.4458(8)	12.856(2)
b (Å)	15.931(3)	14.8604(12)	14.8800(11)	14.640(2)
c (Å)	28.153(5)	15.6187(12)	15.6469(11)	16.029(3)
α (deg)		89.1410(10)	88.3290(10)	112.594(3)
β (deg)		73.3000(10)	71.9590(10)	107.033(3)
γ (deg)		79.0440(10)	78.8180(10)	101.096(3)
V (Å^3)	9127(3)	2280.9(3)	2267.3(3)	2499.1(7)
Z	4	1	1	1
ρ_{calc} (g/cm^3)	1.484	1.317	1.337	1.323
Temperature (K)	110	110	110	110
μ (Mo Kα), (mm^{-1})	0.788	0.388	0.392	0.364
θ range (deg)	2.13 – 25.02	1.91 – 25.03	1.37 – 25.03	2.34 – 25.03
Crystal size (mm)	0.09 x 0.25 x 0.25	0.10 x 0.20 x 0.30	0.20 x 0.15 x 0.10	0.08 x 0.08 x 0.20
Total no. of data	123186	17029	17036	35193
No. unique data	16102	8029	7974	8814
No. of parameters	1127	660	588	772
Completeness to θ (%)	99.9	99.3	99.3	99.7
max, min peaks (e/ Å^3)	0.752 and -0.706	0.775 and -0.5466	0.977 and -0.430	0.795 and -0.337
Goodness-of-fit on F^2	1.039	1.053	1.052	1.037
R_1 (%)[a]	4.57	4.999	5.55	4.49
wR_2 (%)[b]	10.38	13.45	13.83	10.50
Absolute structure	0.031(13)			

[a] $R_1 = \Sigma||F_o|-|F_c||/\Sigma|F_o|$, [b] $wR_2 = \{\Sigma[w(F_o^2-F_c^2)]/\Sigma[w(F_o^2)^2]\}^{1/2}$

Table A1.1. Continued.

	5•3.2DME•1.8Et_2O	**6**•2.4DME•3.6Et_2O	**7**•4PhCl	**8**•4PhCl
Empirical formula	$Fe_2C_{116}H_{121.87}N_4O_{16.12}Br_{0.1}$	$Fe_2C_{126}H_{128}N_4O_{16.38}$	$Fe_2C_{124}H_{97.97}N_4O_8Cl_4Br_{0.03}$	$Fe_2C_{126}H_{103.92}N_4O_8Cl_4Br_{0.08}$
Formula weight	1952.05	2072.10	2027.93	2061.94
Crystal System	Triclinic	Monoclinic	Triclinic	Monoclinic
Space group	$P\bar{1}$	$P2_1/c$	$P\bar{1}$	$P2_1/n$
a (Å)	13.448(4)	15.005(10)	13.924(4)	13.841(5)
b (Å)	13.769(4)	14.506(9)	16.620(5)	16.648(6)
c (Å)	15.973(5)	25.767(18)	21.344(7)	21.474(7)
α (deg)	102.805(6)			
β (deg)	109.766(5)	106.588(11)	94.959(6)	94.563(5)
γ (deg)	104.810(6)			
V (Å^3)	2532.2(14)	5375(6)	4921(3)	4933(3)
Z	1	2	2	2
ρ_{calc} (g/cm^3)	1.280	1.280	1.369	1.388
Temperature (K)	110	110	110	110
μ (Mo Kα), (mm^{-1})	0.406	0.339	0.480	0.501
θ range (deg)	2.46 – 27.88	2.31 – 25.06	1.37 – 25.03	2.45 – 25.03
Crystal size (mm)	0.08 x 0.15 x 0.20	0.10 x 0.20 x 0.21	0.20 x 0.15 x 0.10	0.08 x 0.12 x 0.20
Total no. of data	43656	57176	75643	67239
No. of unique data	11966	9515	10064	8717
No. of parameters	713	825	660	669
Completeness to θ (%)	99.8	99.8	99.9	99.9
Max, min peaks (e/ Å^3)	0.839 and -0.529	1.062 and – 0.457	0.758 and -0.664	0.694 and -0.563
Goodness-of-fit on F^2	1.020	1.035	1.115	1.037
R_1 (%)[a]	6.80	5.38	6.08	4.43
wR_2 (%)[b]	14.26	12.26	12.59	10.81

[a] $R_1 = \Sigma||F_o|-|F_c||/\Sigma|F_o|$, [b] $wR_2 = \{\Sigma[w(F_o^2-F_c^2)]/\Sigma[w(F_o^2)^2]\}^{1/2}$, [c] Compounds **5**, **7**, and **8** contained an impurity of brominated $^-O_2CTrp$.

Table A1.1. Continued.

	9•$4C_2H_4Cl_2$	**10**•$4CH_2Cl_2$	**11**•$5CH_2Cl_2$	**12**•$3.3CH_2Cl_2$•$0.6C_5H_{12}$
Empirical formula	$Fe_2C_{116}H_{95.90}N_4O_8Cl_8Br_{0.10}$	$Fe_2C_{102}H_{70}N_2O_{10}Cl_8$	$Fe_2C_{101}H_{70}N_4O_8Cl_{10}$	$Fe_2C_{108.68}H_{79.87}N_4O_8Cl_{6.66}Br_{0.13}$
Formula weight	2077.17	1878.90	1933.81	1939.25
Crystal System	Triclinic	Monoclinic	Tetragonal	Triclinic
Space group	$P\bar{1}$	$P2_1/n$	$P4/n$	$P\bar{1}$
a (Å)	13.1689(16)	16.048(3)	26.708(12)	12.688(8)
b (Å)	13.4564(17)	12.553(3)	26.708(12)	14.013(9)
c (Å)	16.343(2)	22.553(5)	12.347(8)	14.136(9)
α (deg)	87.559(2)			97.679(11)
β (deg)	68.652(2)	101.82(3)		103.262(10)
γ (deg)	74.568(2)			108.932(10)
V (Å^3)	2595.4(6)	4446.9(15)	8807(8)	2254(2)
Z	1	2	4	1
ρ_{calc} (g/cm^3)	1.329	1.403	1.458	1.429
Temperature (K)	110	110	110	110
μ (Mo Kα), (mm^{-1})	0.583	0.629	0.695	0.642
θ range (deg)	2.54 – 25.03	2.08 – 25.02	2.16 – 25.68	2.32 – 25.03
Crystal size (mm)	0.06 x 0.12 x 0.20	0.06 x 0.16 x 0.21	0.11 x 0.20 x 0.37	0.08 x 0.10 x 0.12
Total no. of data	36262	56457	126391	30833
No. of unique data	9155	7684	8359	7942
No. of parameters	754	588	716	691
Completeness to θ (%)	99.8	99.9	99.9	99.8
Max, min peaks (e/ Å^3)	1.433 and -0.697	1.057 and -0.652	1.327 and -0.497	0.622 and -0.742
Goodness-of-fit on F^2	1.074	1.120	1.068	1.086
R_1 (%)[a]	7.09	7.62	6.69	7.18
wR_2 (%)[b]	17.53	18.15	17.24	16.04

[a] $R_1 = \Sigma||F_o|-|F_c||/\Sigma|F_o|$, [b] $wR_2 = \{\Sigma[w(F_o^2-F_c^2)]/\Sigma[w(F_o^2)^2]\}^{1/2}$, [c] Compounds **9** and **12** contained an impurity of brominated $^-O_2CTrp$.

Table A1.1. Continued.

	13•$2CH_2Cl_2$	**14**	**15**•Et_2O
Empirical formula	$FeC_{49}H_{43.92}N_2O_4Cl_2Br_{0.08}$	$FeC_{76}H_{97.88}N_4O_4S_2Br_{0.12}$	$FeC_{54}H_{47.98}N_4O_5Br_{0.02}$
Formula weight	857.73	1261.42	890.00
Crystal System	Monoclinic	Tetragonal	Triclinic
Space group	$P2_1/n$	$P4_12_12$	$P\bar{1}$
a (Å)	16.286(3)	15.397(2)	8.975(2)
b (Å)	8.6906(14)	15.397(2)	15.942(4)
c (Å)	30.177(5)	30.880(9)	17.159(5)
α (deg)			65.714(4)
β (deg)	104.079(3)		89.066(4)
γ (deg)			86.579(4)
V (Å^3)	4142.8(12)	7320(3)	2233.7(10)
Z	4	4	2
ρ_{calc} (g/cm^3)	1.375	1.145	1.323
Temperature (K)	183	110	110
μ (Mo Kα), (mm^{-1})	0.619	0.380	0.406
θ range (deg)	2.17 – 25.03	1.98 – 25.03	2.27 – 26.37
Crystal size (mm)	0.10 x 0.15 x 0.20	0.10 x 0.15 x 0.25	0.15 x 0.30 x 0.40
Total no. of data	55907	102976	34568
No. of unique data	7324	6457	9092
No. of parameters	543	403	596
Completeness to θ (%)	100.0	99.9	99.5
max, min peaks (e/ Å^3)	0.846 and -0.698	0.333 and -0.274	0.672 and -0.689
Goodness-of-fit on F^2	1.048	1.168	1.050
R_1 (%)[a]	5.04	6.90	5.33
wR_2 (%)[b]	12.86	13.84	13.22

[a] $R_1 = \Sigma||F_o|-|F_c||/\Sigma|F_o|$, [b] $wR_2 = \{\Sigma[w(F_o^2-F_c^2)]/\Sigma[w(F_o^2)^2]\}^{1/2}$, [c] Compounds **13**–**15** contained an impurity of brominated $^-O_2$CTrp.

Table A1.2. Selected Bond Lengths (Å) and Angles (deg) for **2–12**.

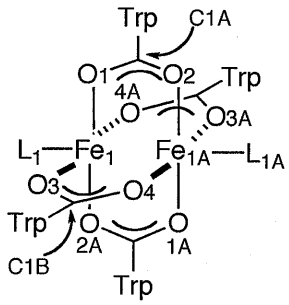

	2	3	4	5	6	7
Fe1–Fe1A	2.8460(6)	2.8604(8)	2.9033(7)	2.912(1)	3.007(2)	2.9215(10)
Fe1–L	2.1184(19)	2.080(3)	2.0837(19)	2.084(2)	2.133(2)	2.094(2)
Fe1–O1	2.0958(16)	2.059(2)	2.0573(16)	2.065(2)	2.072(2)	2.052(2)
Fe1A–O2	2.0597(17)	2.089(2)	2.0577(16)	2.151(2)	2.130(2)	2.131(2)
Fe1–O3	2.0889(16)	2.068(2)	2.0713(16)	2.062(2)	2.081(2)	2.046(2)
Fe1A–O4	2.0607(18)	2.091(2)	2.1133(16)	2.042(2)	2.071(2)	2.078(2)
Fe1–O1–C1A	137.66(16)	114.60(19)	130.71(16)	123.54(19)	127.67(18)	121.73(18)
Fe1A–O2–C1A	115.78(15)	140.0(2)	123.60(14)	129.9(2)	128.53(18)	131.43(18)
Fe1–O3–C1B	131.03(16)	121.6(2)	124.38(15)	131.00(19)	129.40(18)	121.88(18)
Fe1A–O4–C1B	121.72(17)	131.0(2)	129.04(15)	124.26(19)	127.53(17)	133.27(19)

	8	9	10	11	12
Fe1–Fe1A	2.906(1)	2.9639(11)	2.8692(15)	2.7716(14)	2.8214(17)
Fe1–L	2.087(2)	2.109(3)	2.126(4)	2.086(3)	2.083(3)
Fe1–O1	2.0567(18)	2.072(3)	2.087(4)	2.039(3)	2.091(3)
Fe1A–O2	2.1371(18)	2.035(3)	2.068(4)	2.043(3)	2.077(3)
Fe1–O3	2.0585(18)	2.069(3)	2.067(3)	2.062(3)	2.065(3)
Fe1A–O4	2.0928(18)	2.139(3)	2.046(3)	2.071(3)	2.076(3)
Fe1–O1–C1A	121.94(16)	133.8(3)	130.3(4)	118.6(3)	127.5(3)
Fe1A–O2–C1A	130.97(16)	122.9(3)	124.1(4)	131.9(6)	123.9(3)
Fe1–O3–C1B	121.97(16)	125.9(3)	130.4(3)	125.4(2)	115.9(4)
Fe1A–O4–C1B	132.56(17)	130.1(3)	121.9(3)	126.2(2)	137.9(3)

Numbers in parentheses are estimated standard deviations of the last significant figure.

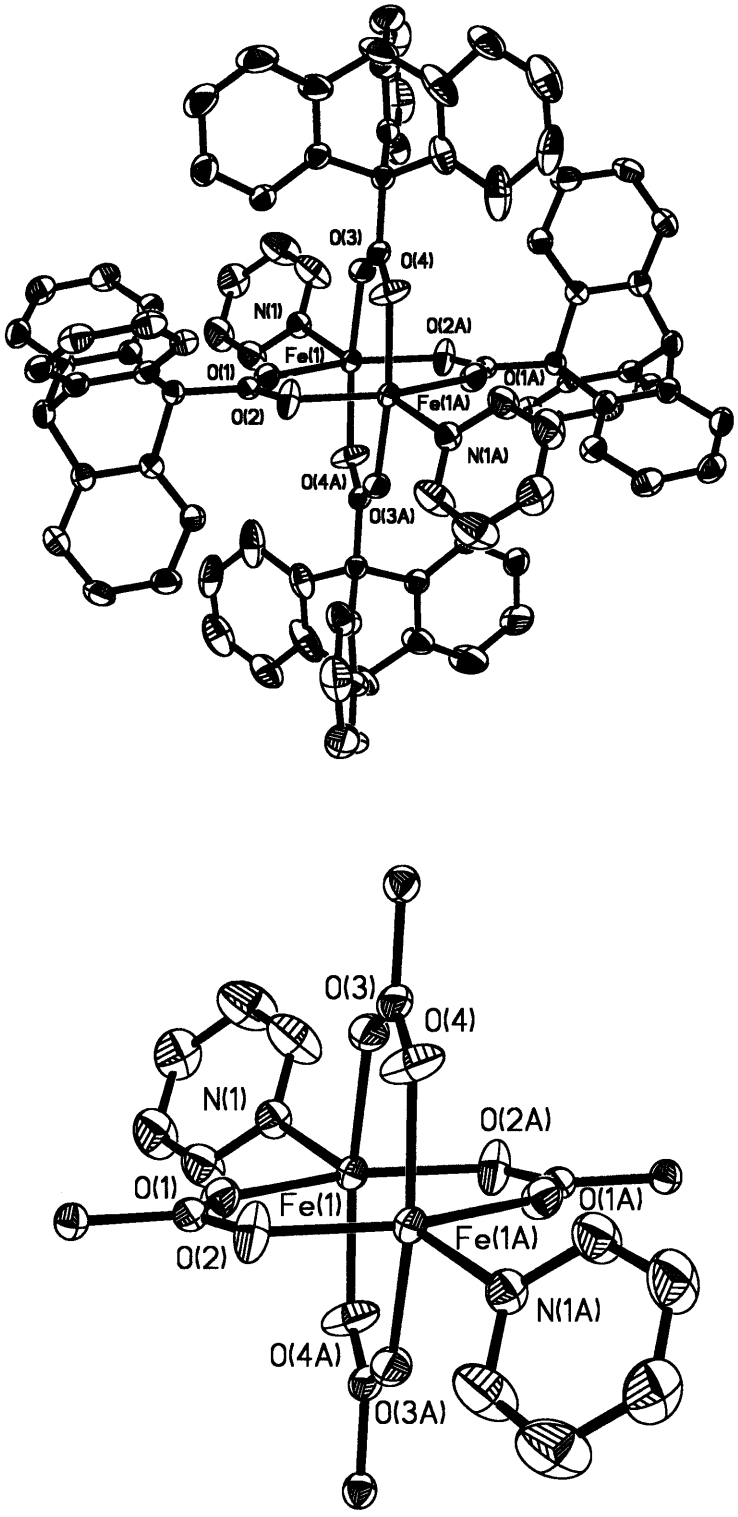

Figure A1.1. ORTEP diagrams of $[Fe_2(\mu\text{-}O_2CTrp)_4(py)_2]$ (**2**) showing 50% probability thermal ellipsoids for all non-hydrogen atoms. Bottom: Drawing in which the triptycene units are omitted for clarity.

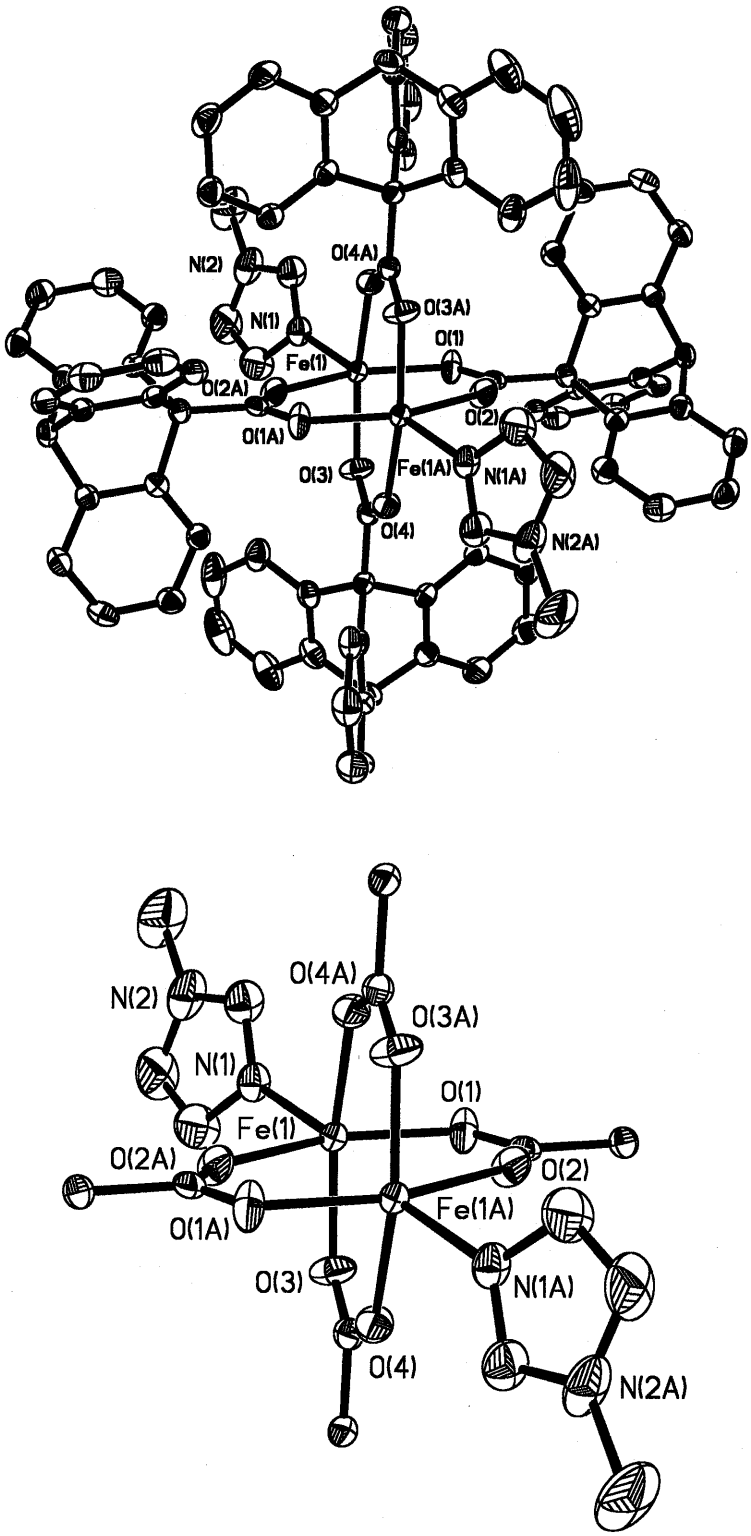

Figure A1.2. ORTEP diagrams of $[Fe_2(\mu\text{-}O_2CTrp)_4(1\text{-}MeIm)_2]$ (**3**) showing 50% probability thermal ellipsoids for all non-hydrogen atoms. Bottom: Drawing in which the triptycene units are omitted for clarity.

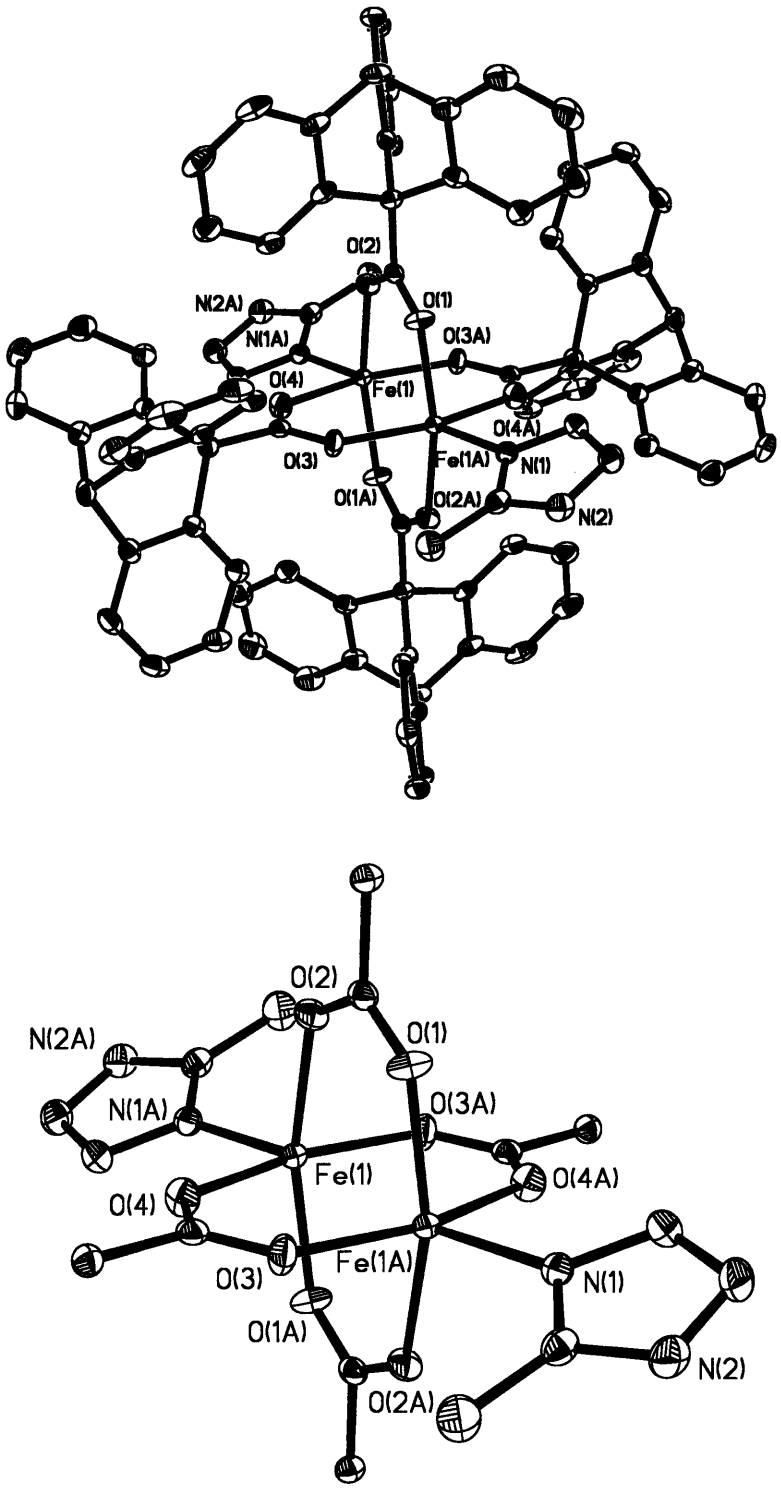

Figure A1.3. ORTEP diagrams of $[Fe_2(\mu\text{-}O_2CTrp)_4(2\text{-}MeIm)_2]$ (**4**) showing 50% probability thermal ellipsoids for all non-hydrogen atoms. Bottom: Drawing in which the triptycene units are omitted for clarity.

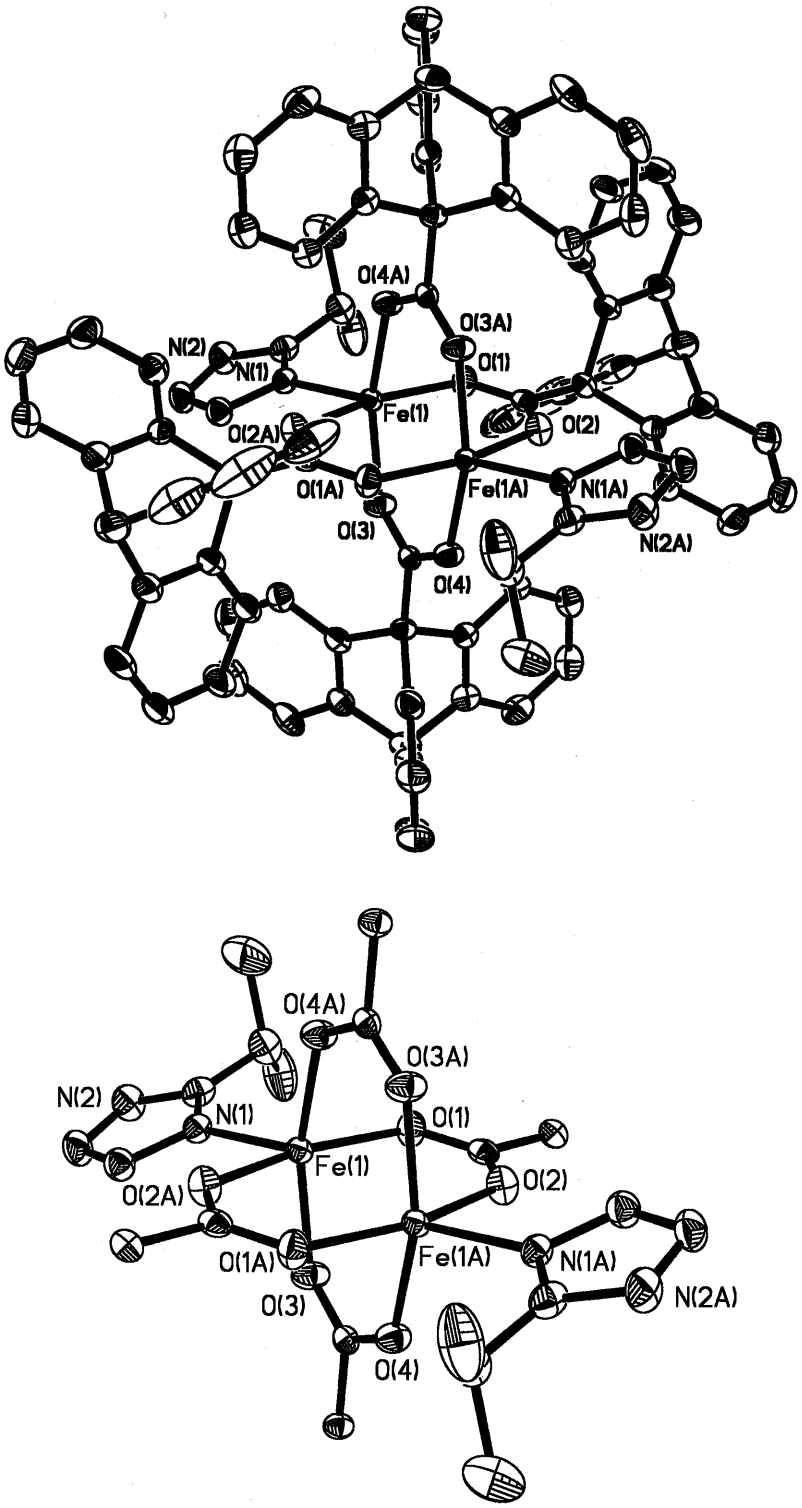

Figure A1.4. ORTEP diagrams of $[Fe_2(\mu\text{-}O_2CTrp)_4(2\text{-}^{i}PrIm)_2]$ (**5**) showing 50% probability thermal ellipsoids for all non-hydrogen atoms. Bottom: Drawing in which the triptycene units are omitted for clarity.

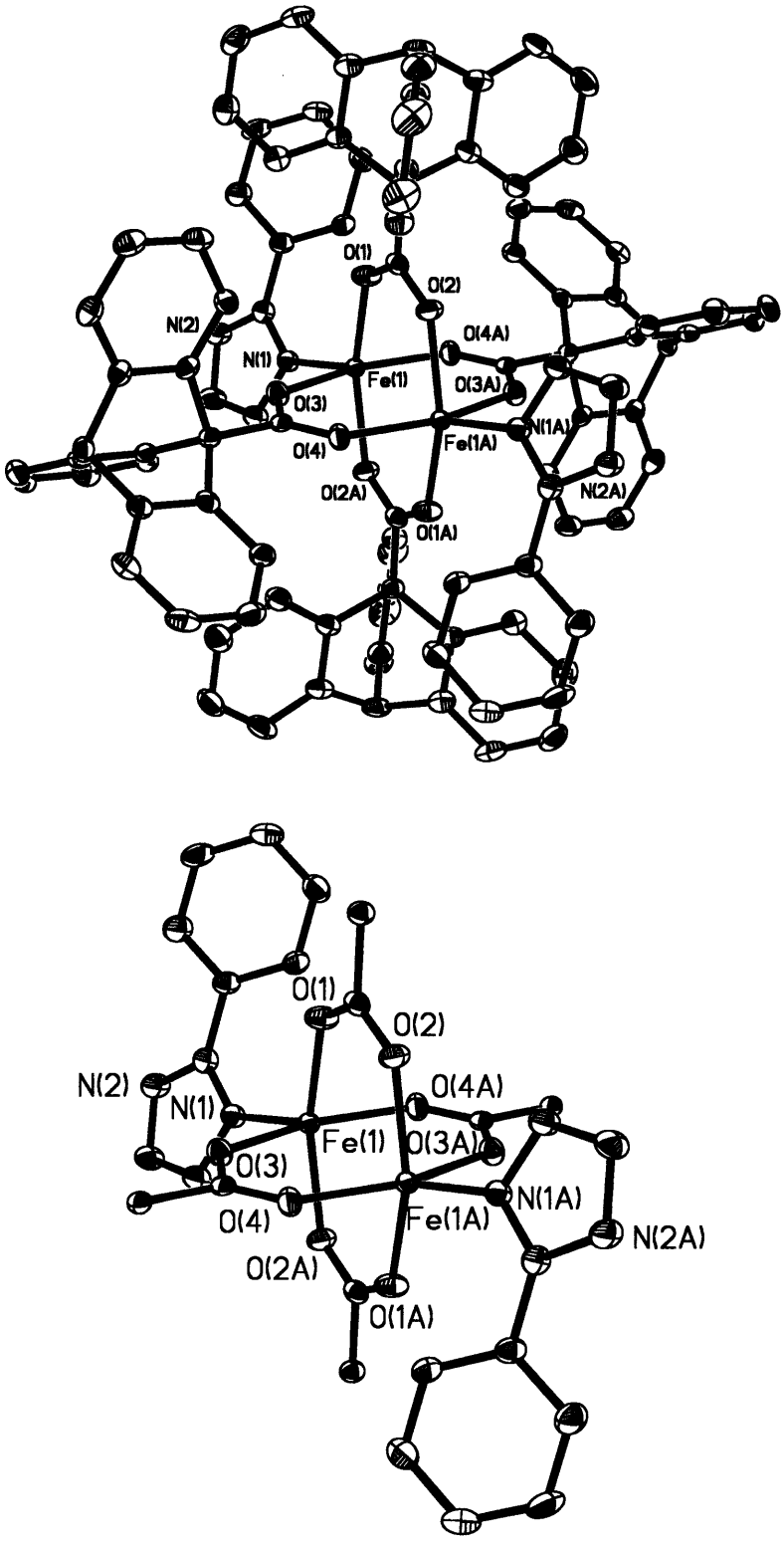

Figure A1.5. ORTEP diagrams of $[Fe_2(\mu\text{-}O_2CTrp)_4(2\text{-}PhIm)_2]$ (**6**) showing 50% probability thermal ellipsoids for all non-hydrogen atoms. Bottom: Drawing in which the triptycene units are omitted for clarity.

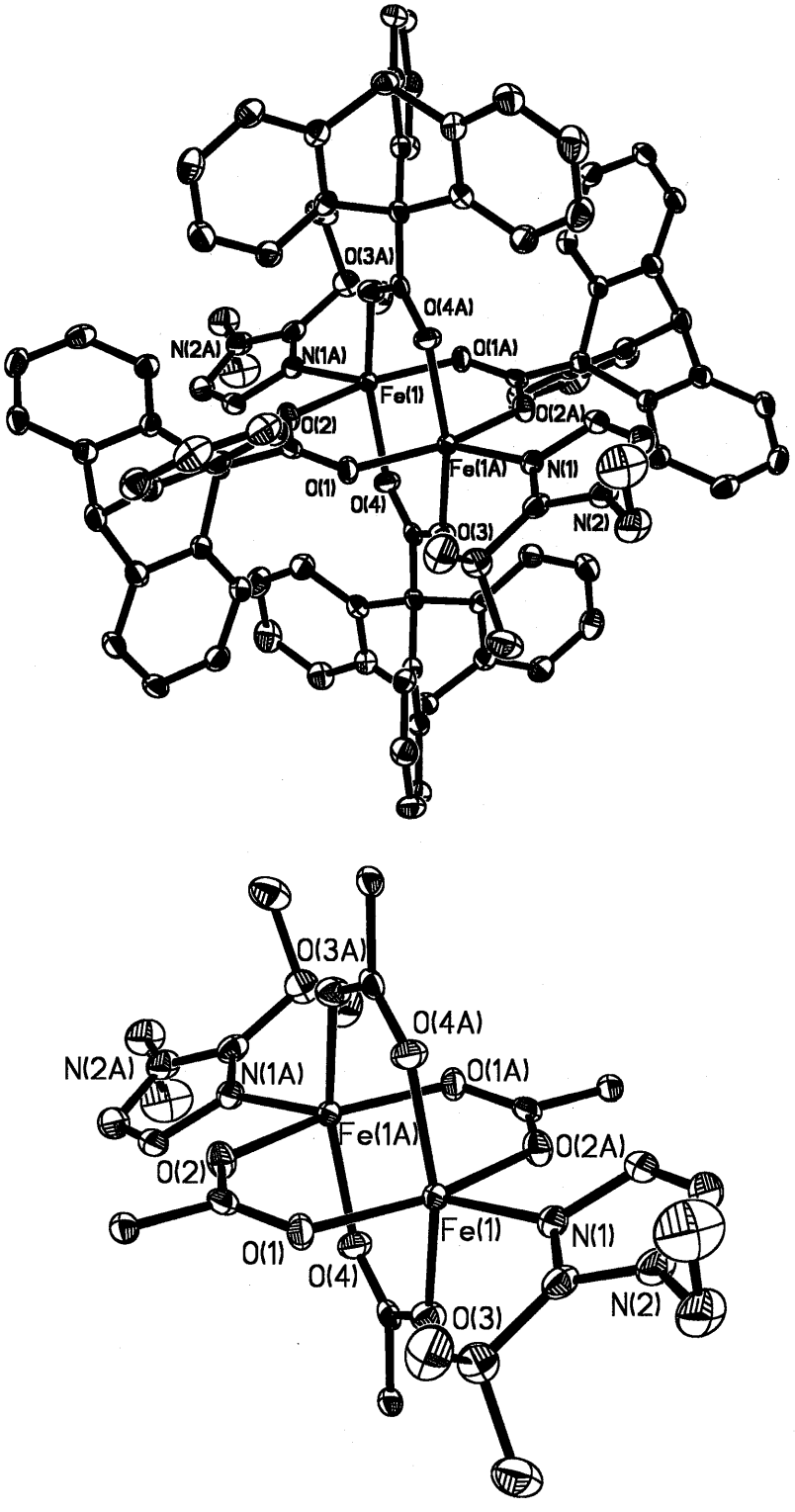

Figure A1.6. ORTEP diagrams of $[Fe_2(\mu\text{-}O_2CTrp)_4(1\text{-}Et\text{-}2\text{-}^{i}Prlm)_2]$ (**7**) showing 50% probability thermal ellipsoids for all non-hydrogen atoms. Bottom: Drawing in which the triptycene units are omitted for clarity.

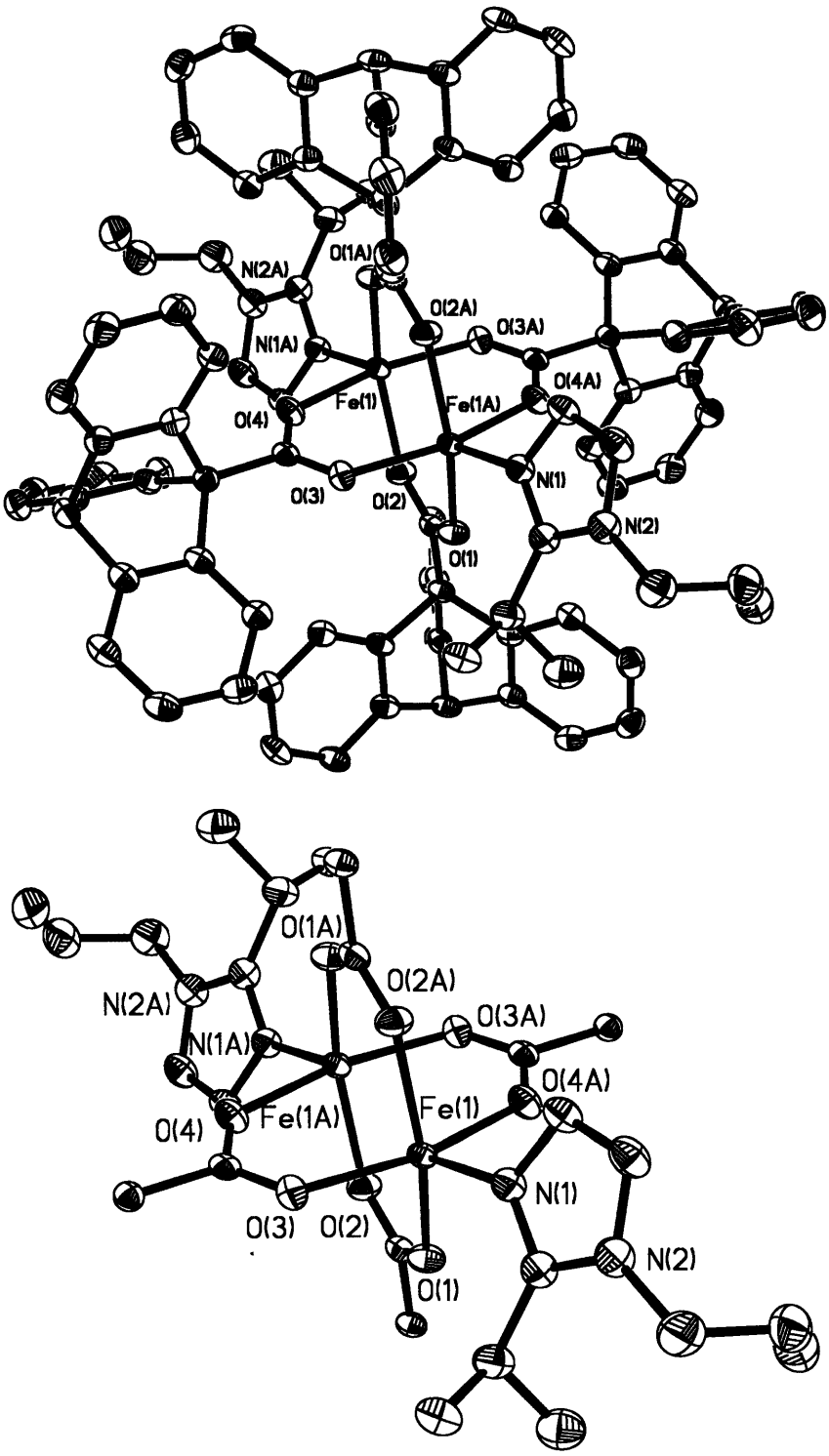

Figure A1.7. ORTEP diagrams of $[Fe_2(\mu\text{-}O_2CTrp)_4(1\text{-}Pr\text{-}2\text{-}^{i}PrIm)_2]$ (**8**) showing 50% probability thermal ellipsoids for all non-hydrogen atoms. Bottom: Drawing in which the triptycene units are omitted for clarity.

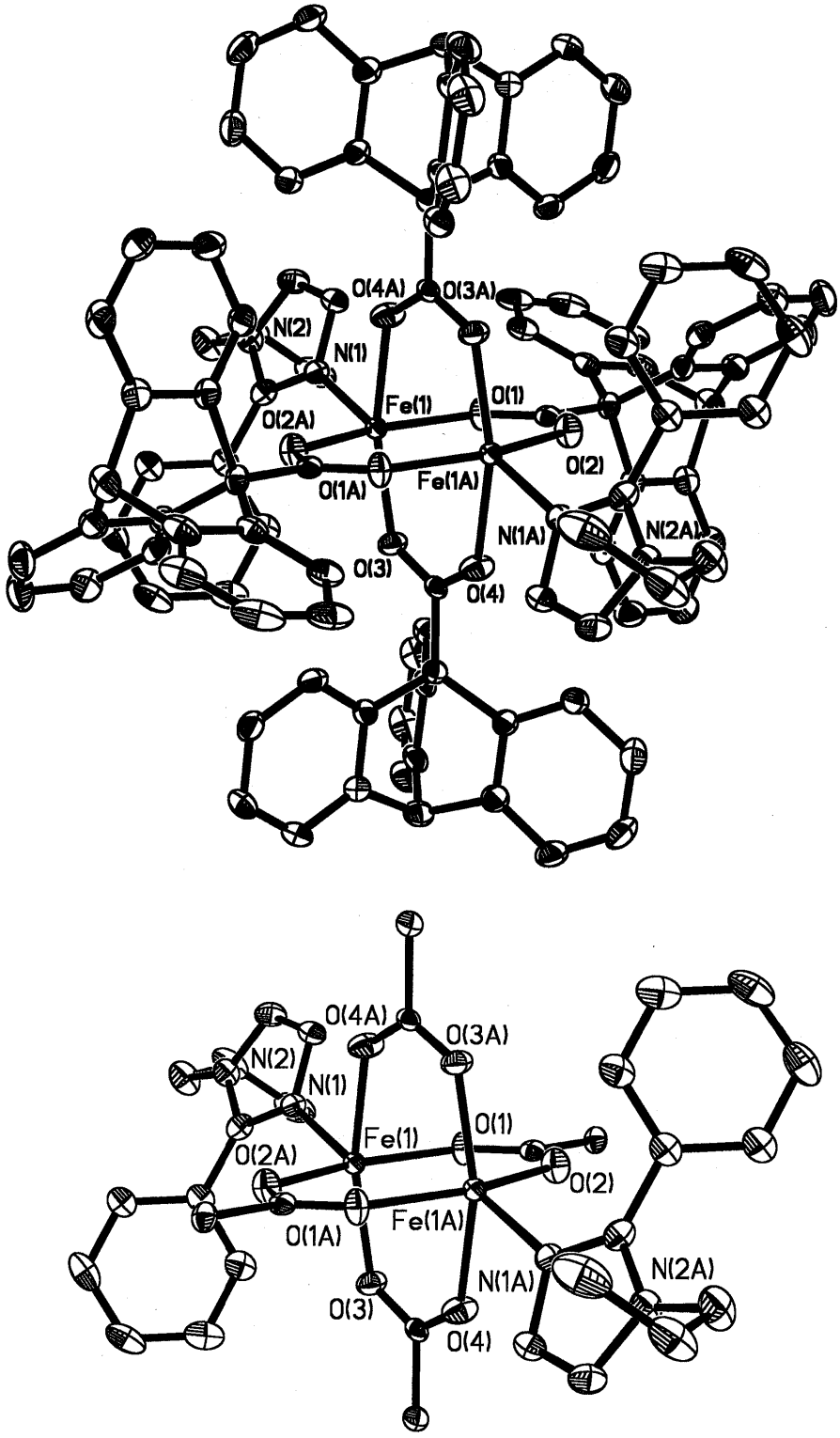

Figure A1.8. ORTEP diagrams of $[Fe_2(\mu\text{-}O_2CTrp)_4(1\text{-}Pr\text{-}2\text{-}PhIm)_2]$ (**9**) showing 50% probability thermal ellipsoids for all non-hydrogen atoms. Bottom: Drawing in which the triptycene units are omitted for clarity.

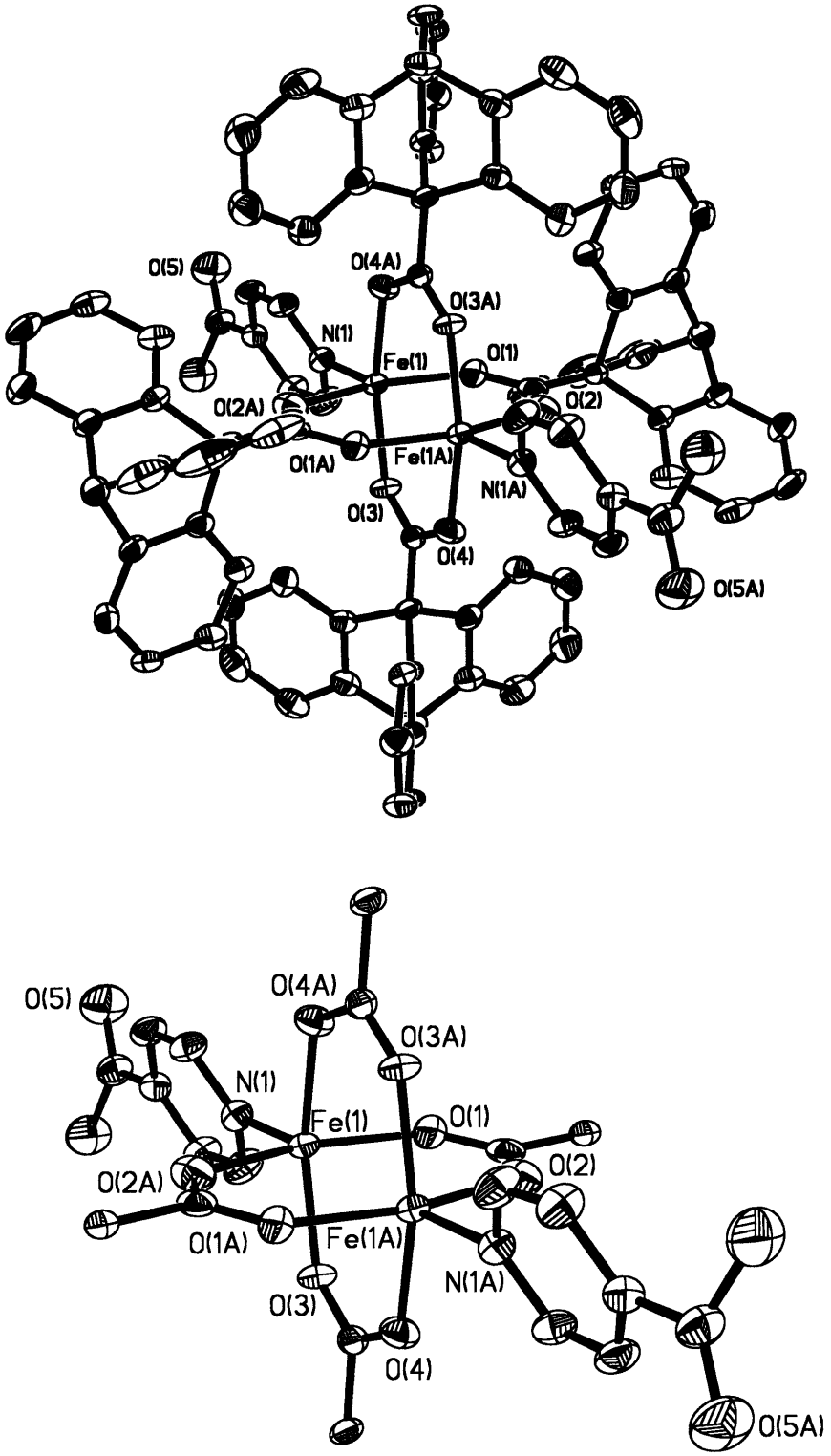

Figure A1.9. ORTEP-diagrams of $[Fe_2(\mu\text{-}O_2CTrp)_4(4\text{-}AcPy)_2]$ (**10**) showing 50% probability thermal ellipsoids for all non-hydrogen atoms. Bottom: Drawing in which the triptycene units are omitted for clarity.

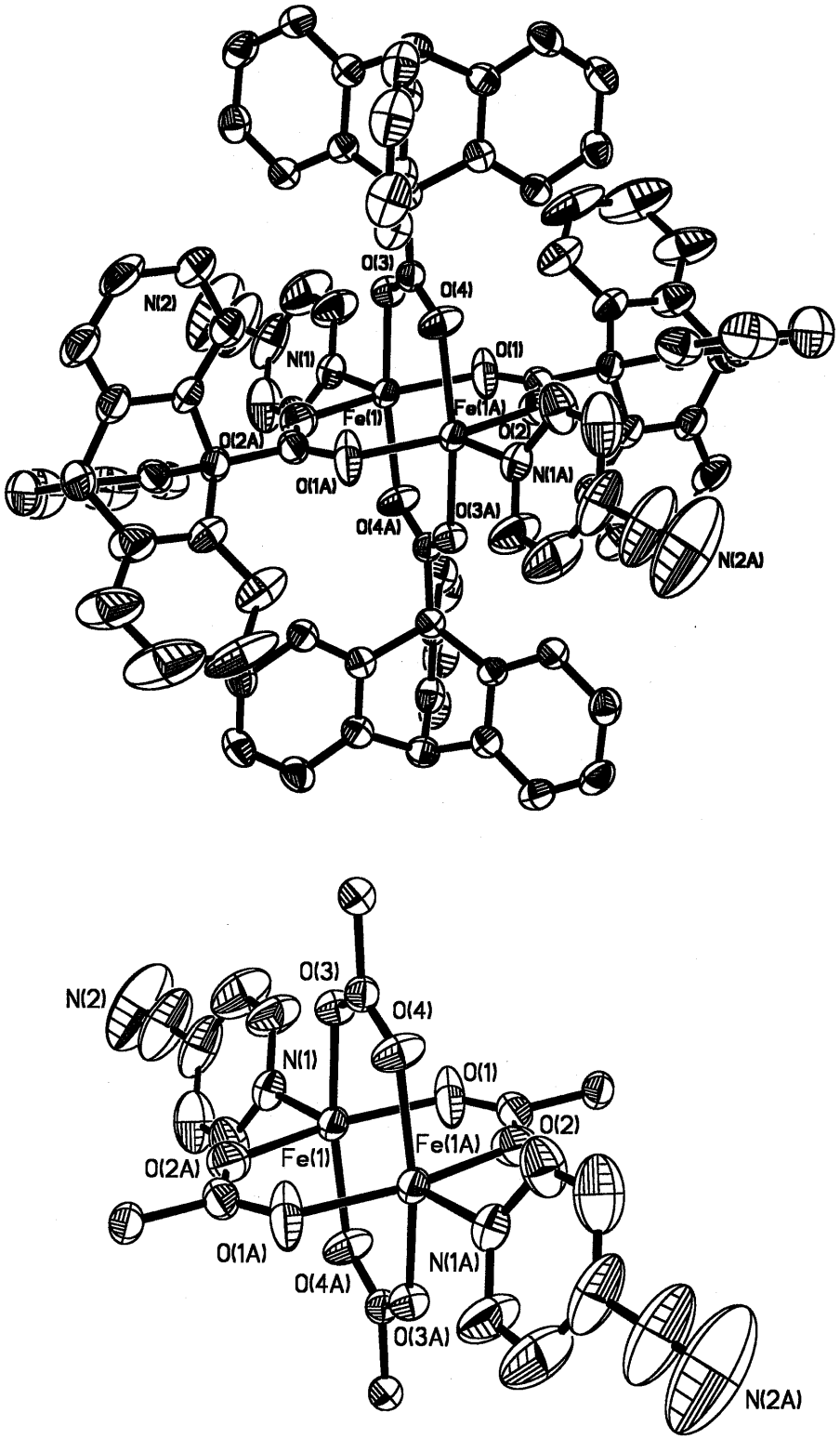

Figure A1.10. ORTEP-diagrams of $[Fe_2(\mu\text{-}O_2CTrp)_4(4\text{-}CNPy)_2]$ (**11**) showing 50% probability thermal ellipsoids for all non-hydrogen atoms. Bottom: Drawing in which the triptycene units are omitted for clarity.

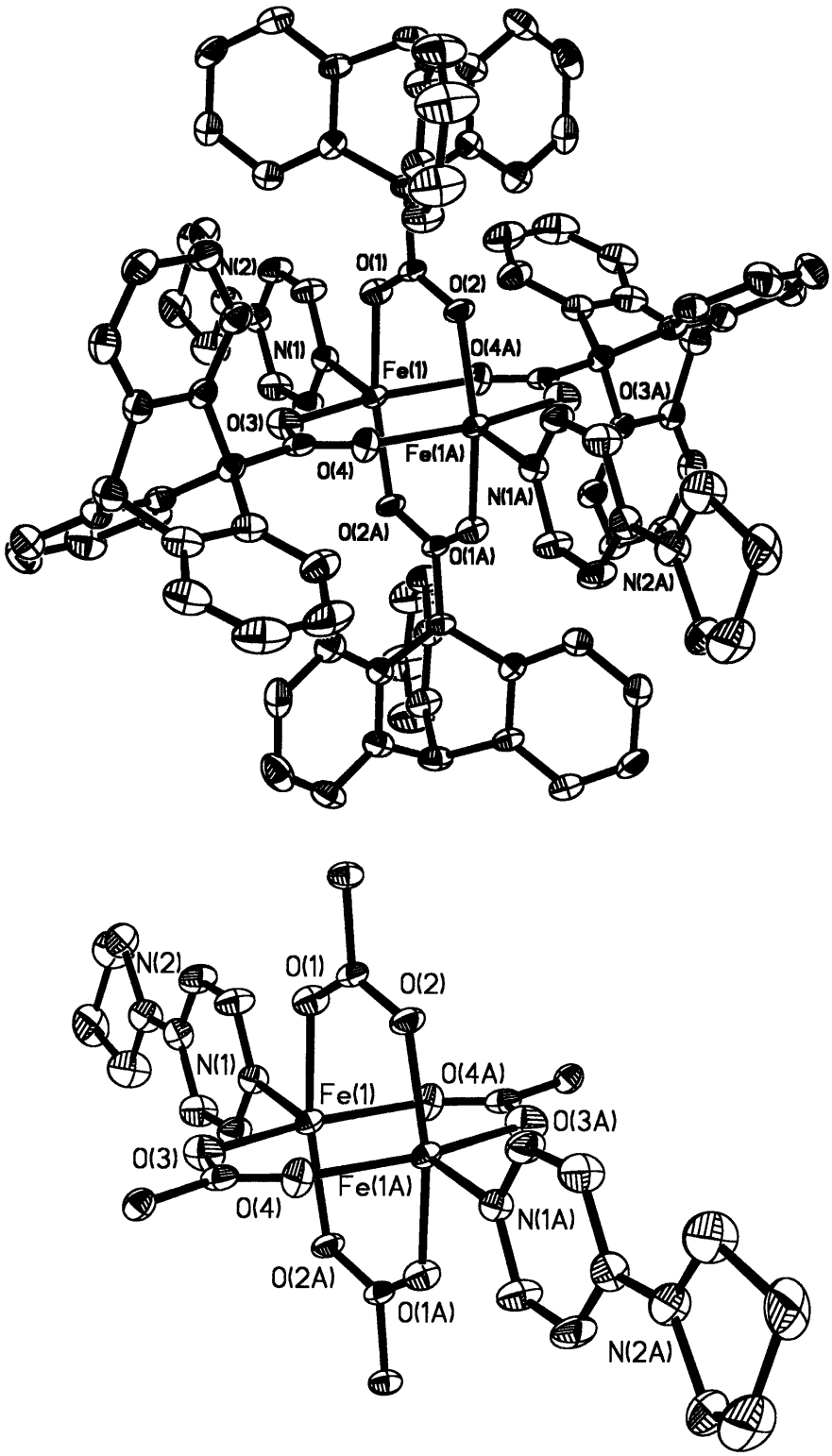

Figure A1.11. ORTEP-diagrams of $[Fe_2(\mu\text{-}O_2CTrp)_4(4\text{-}PPy)_2]$ (**12**) showing 50% probability thermal ellipsoids for all non-hydrogen atoms. Bottom: Drawing in which the triptycene units are omitted for clarity.

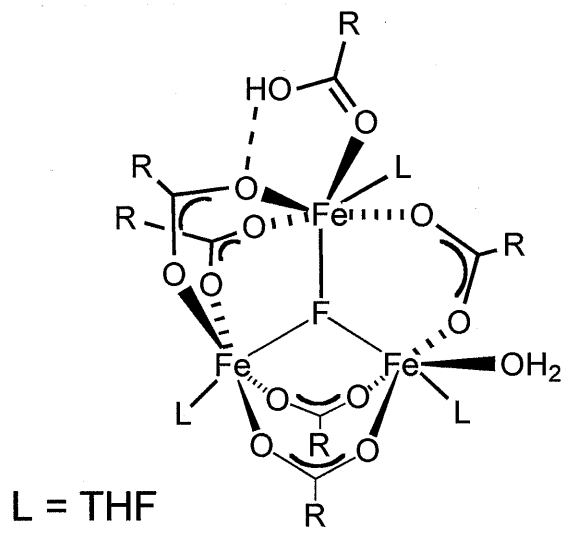

Figure A1.12. Diagram of the proposed structure of **1b**.
Unit cell parameters: monoclinic, $P2_1/n$; a = 16.279(12) Å, b = 27.48(2) Å, c = 26.564(19) Å, β = 103.129(13)°, V = 11571(15) Å^3, Z = 4, T = 110 K.

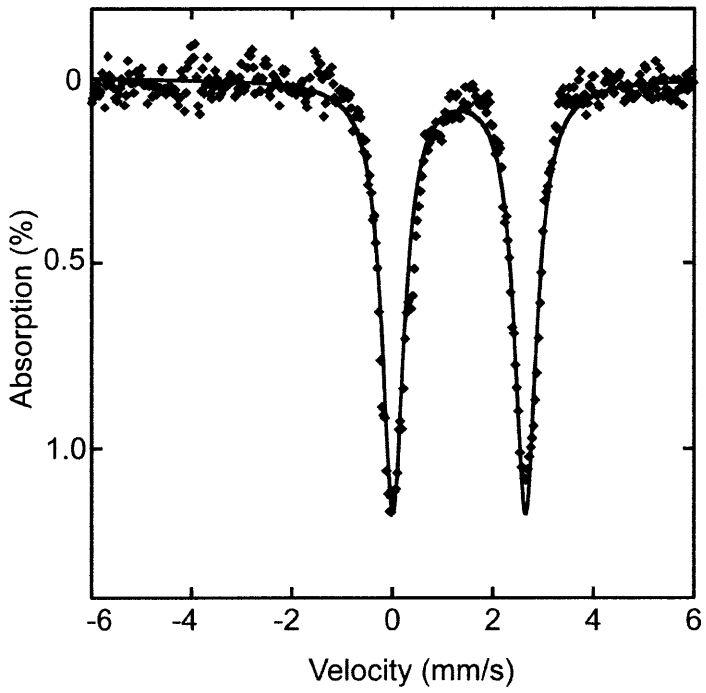

Figure A1.13. Zero-Field Mössbauer spectrum (experimental data (♦), calculated fit (—)) recorded at 4.2 K for **1** (mixture of **1a** and **1b**).

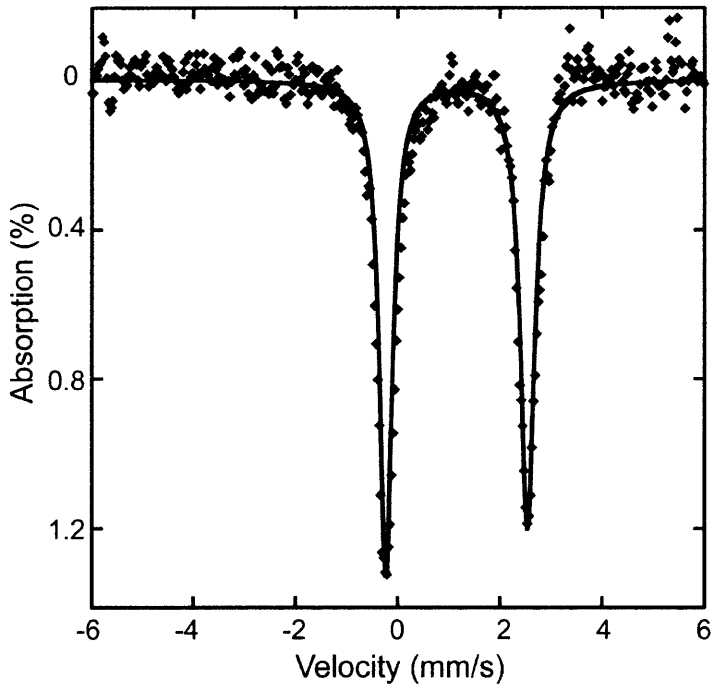

Figure A1.14. Zero-Field Mössbauer spectrum (experimental data (♦), calculated fit (—)) recorded at 4.2 K for $[Fe_2(\mu\text{-}O_2CTrp)_4(1\text{-}Pr\text{-}2\text{-}^{i}PrIm)_2]$ (**8**).

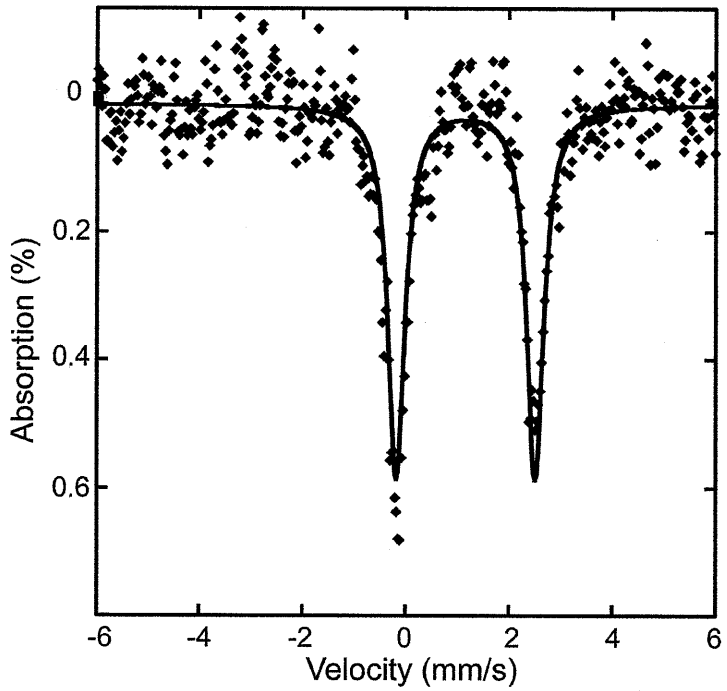

Figure A1.15. Zero-Field Mössbauer spectrum (experimental data (♦), calculated fit (—)) recorded at 4.2 K for $[Fe_2(\mu\text{-}O_2CTrp)_4(1\text{-}Pr\text{-}2\text{-}PhIm)_2]$ (**9**).

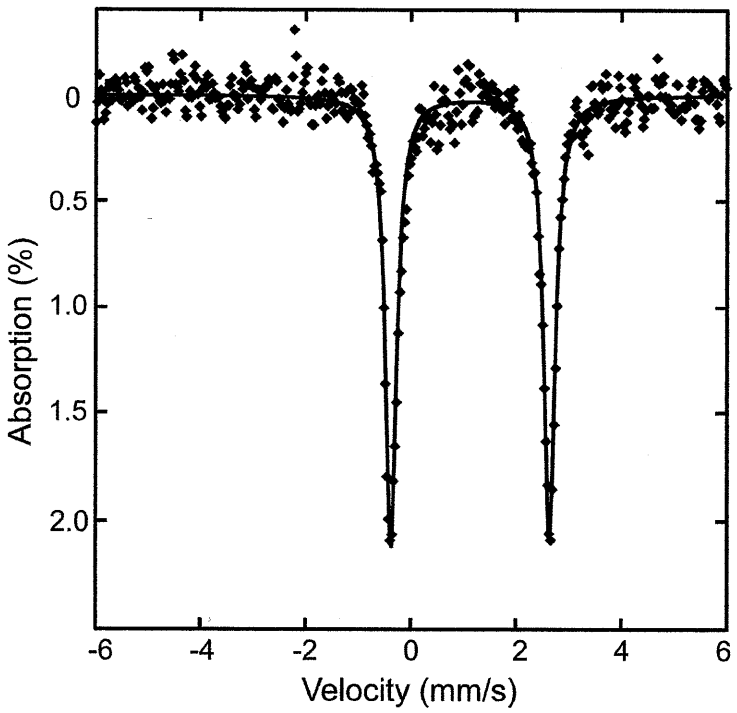

Figure A1.16. Zero-Field Mössbauer spectrum (experimental data (♦), calculated fit (—)) recorded at 4.2 K for $[Fe(O_2CTrp)_2(TMEDA)]$ (**13**).

Appendix 2

Supporting Information for Chapter 4. Modeling the Syn-Disposition of Nitrogen Donors in Non-Heme Diiron Enzymes. Synthesis, Characterization and Hydrogen Peroxide Reactivity of Diiron(III) Complexes with the Syn *N*-Donor Ligand H_2BPG_2DEV

1. X-ray Crystallography.

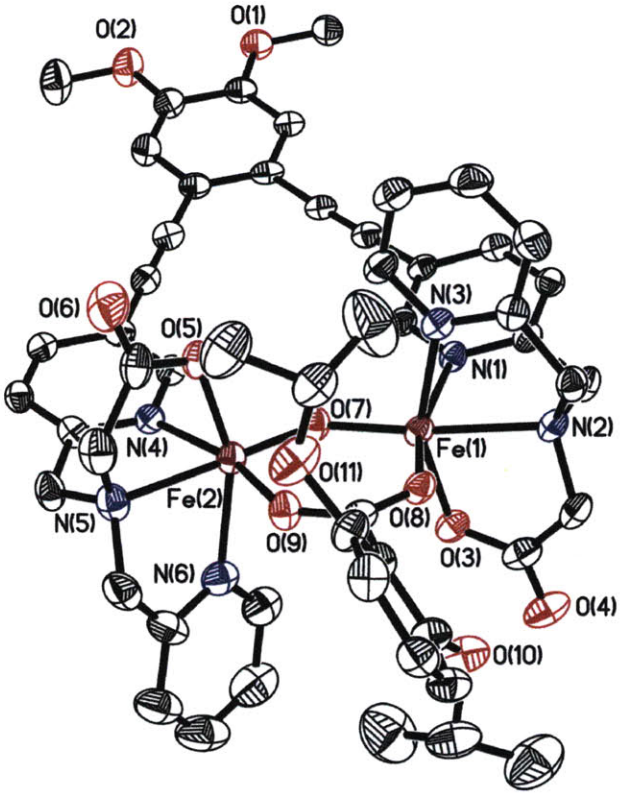

Figure A2.1. ORTEP diagram of $[Fe_2(\mu\text{-}O)(\mu\text{-}O_2CAr^{iPrO})BPG_2DEV](ClO_4)$ (**7**) displaying 40% thermal ellipsoids. For clarity, the ClO_4^- anions are not shown.

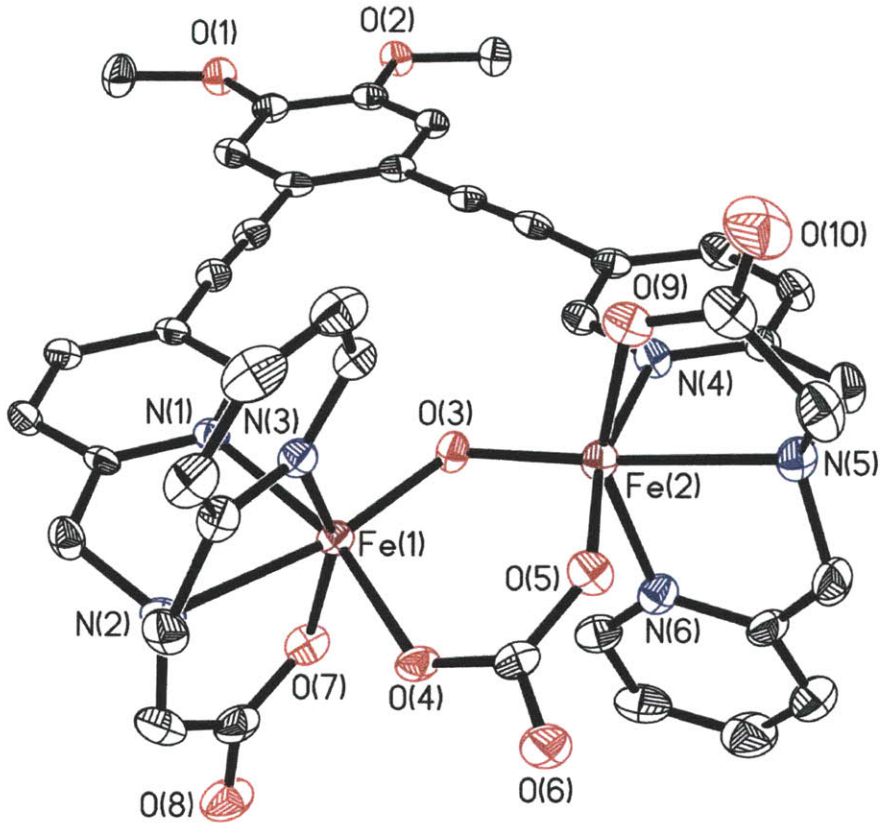

Figure A2.2. ORTEP diagram of [Fe_2(μ-O)(μ-CO_3)BPG_2DEV] (**8**) displaying 50% thermal ellipsoids.

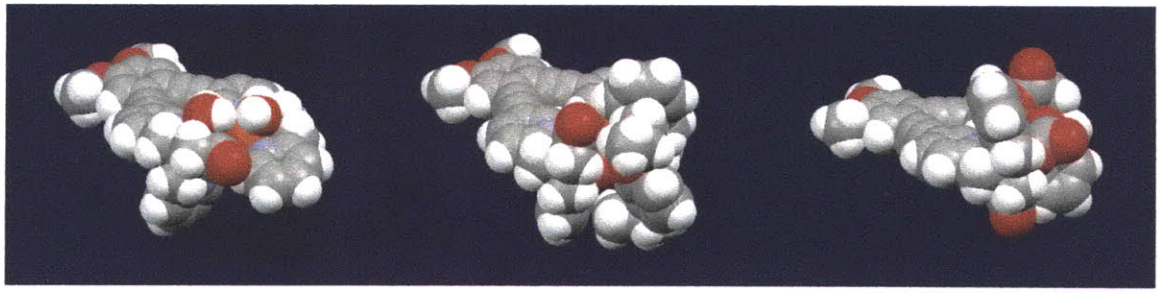

Figure A2.3. Space-filling diagrams of **6**, **7**, and **8** (from left to right). Solvent molecules and ClO_4^- anions are omitted for clarity.

2. UV-vis Spectra of 6a and 7a.

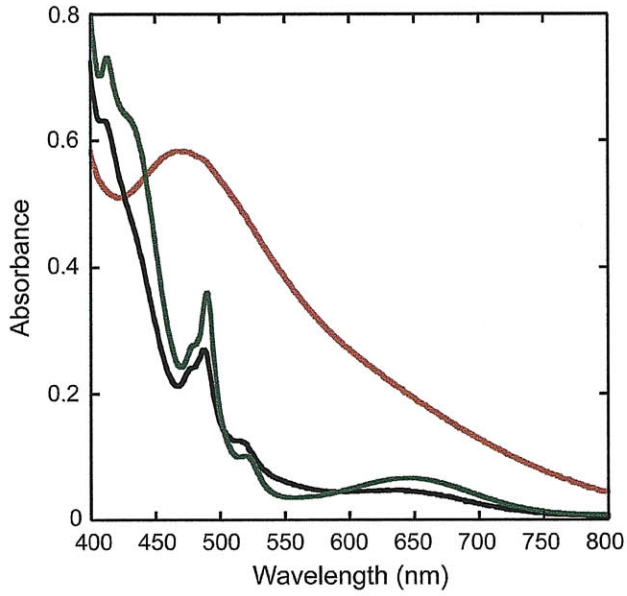

Figure A2.4. UV-vis spectra, recorded at 0 °C, of a reaction mixture of **7** (green trace) in MeCN/H_2O (4:1), NEt_3, and H_2O_2 to form peroxo intermediate **7a** (orange-red). The black trace corresponds to the reaction product.

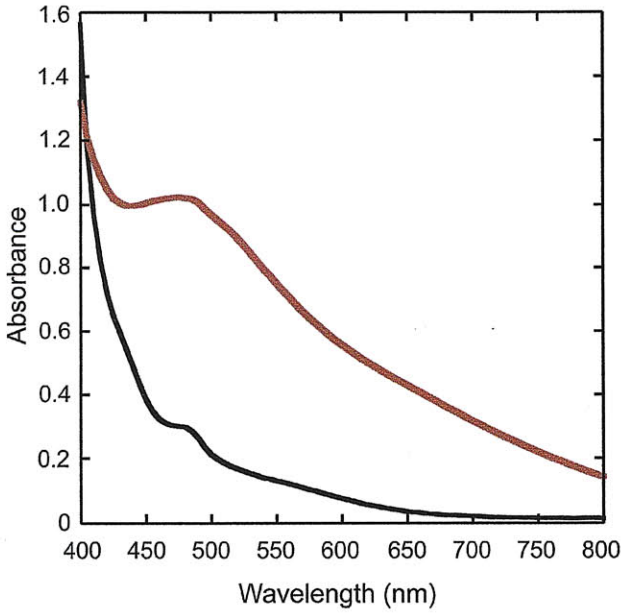

Figure A2.5. UV-vis spectra, recorded at 4 °C, of a reaction mixture of **6** (black trace) in MeCN/H_2O (4:1), NEt_3, and H_2O_2 to form peroxo intermediate **6a** (red trace). The solution of **6** was purged with N_2 (g) before addition of base to prevent formation of **8**.

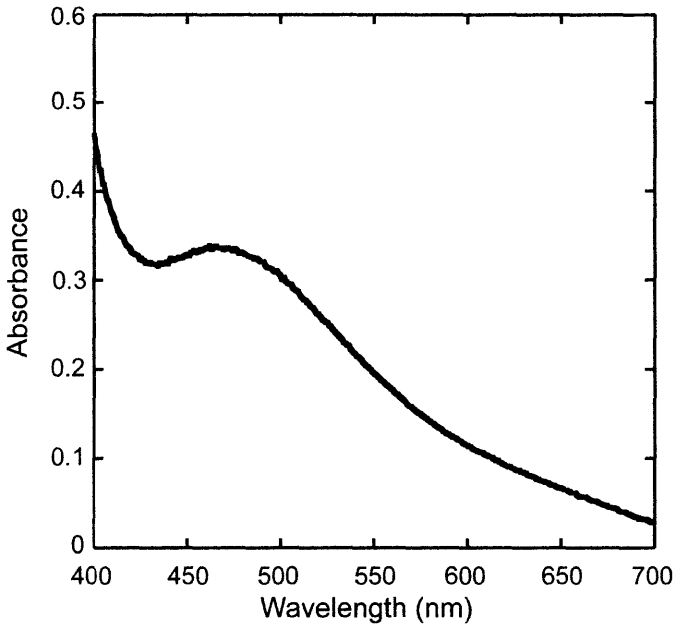

Figure A2.6. UV-vis spectrum of peroxo-intermediate **6a** in CH_3OH/H_2O.

3. Mössbauer Spectroscopy.

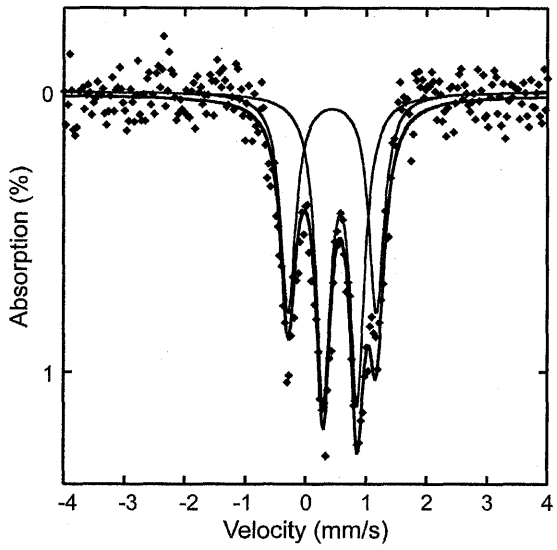

Figure A2.7. Zero-field Mössbauer spectrum [experimental data (◆), calculated fits (—)] recorded at 90 K for a frozen solution sample of the product from a reaction of **7** with excess hydrogen peroxide in the presence of NEt_3. The sample contained 56% of **7a** and 44% of a diiron(III) (δ = 0.45 mm/s and ΔE_Q = 1.46 mm/s) species with Mössbauer parameters similar to those of the starting material.

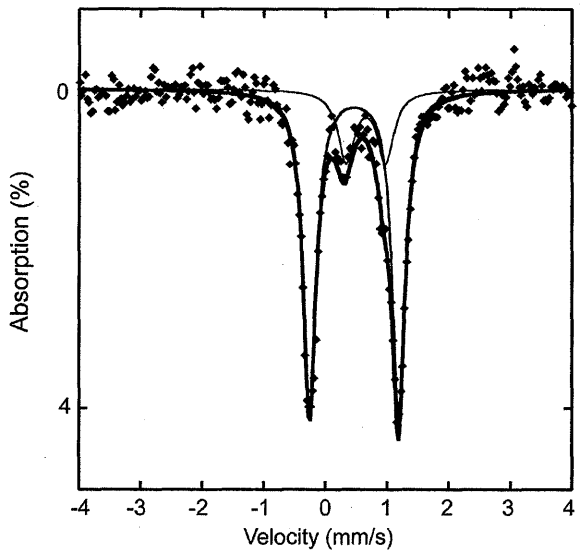

Figure A2.8. Zero-field Mössbauer spectrum [experimental data (◆), calculated fits (—)] recorded at 90 K for a frozen solution sample of the product from the reaction of **8** with excess hydrogen peroxide in the presence of NEt_3. The sample contained 22% of **8a** and 78% of a diiron(III) species (δ = 0.47 mm/s and ΔE_Q = 1.44 mm/s) with Mössbauer parameters similar to those of the starting material.

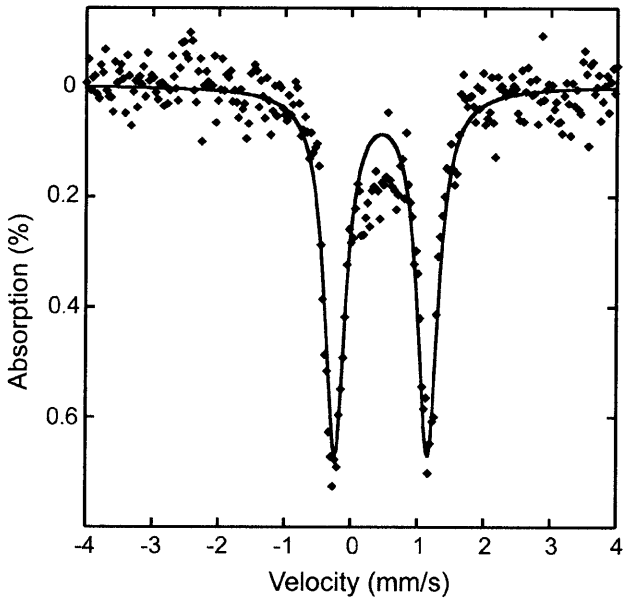

Figure A2.9. Zero-field Mössbauer spectrum [experimental data (◆), calculated fit (–)] recorded at 90 K for a frozen solution sample (CH_3OH/H_2O) of the decomposition product from a reaction of **6** with ca. 50 equiv of hydrogen peroxide in the presence of NEt_3. The sample contained a species with Mössbauer parameters (δ = 0.46(3) mm/s; ΔE_Q = 1.39(3) mm/s; Γ = 0.38 mm/s) similar to those of the starting material (**6**).

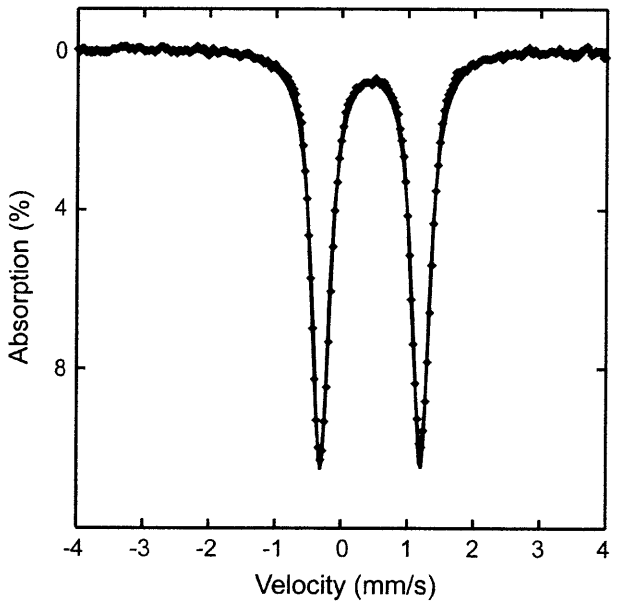

Figure A2.10. Zero-field Mössbauer spectrum [experimental data (◆), calculated fit (–)] recorded at 90 K for a frozen solution sample of **6** in a solution of CH_3OH/H_2O (ca. 15:1; v/v) with Mössbauer parameters δ = 0.45(2) mm/s; ΔE_Q = 1.51(2) mm/s; Γ = 0.45 mm/s.

4. EPR Spectroscopy.

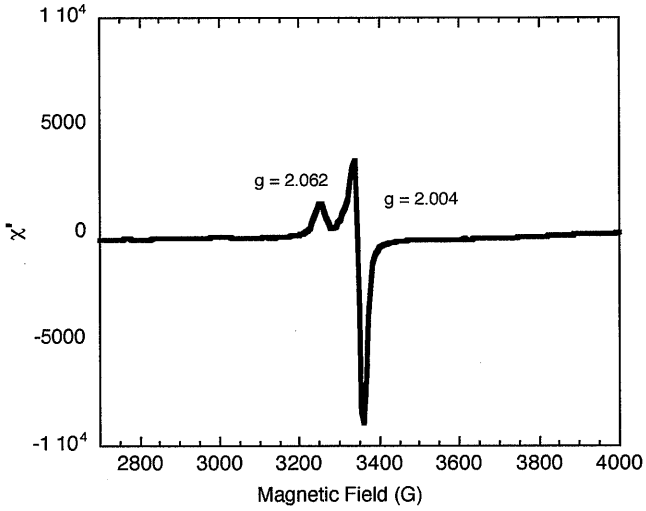

Figure A2.11. X-band EPR spectrum from a reaction of **8** with 10 equiv of Et_3N in $MeCN/H_2O$ (2:1) solution at 0 °C and 1000 equiv of H_2O_2, frozen in liquid N_2 after 3 min. Experimental conditions: temperature: 4 K, power: 0.2 mW at 9.3810 GHz; modulation amplitude: 10 G, receiver gain: 5000.

5. Mass Spectrometry.

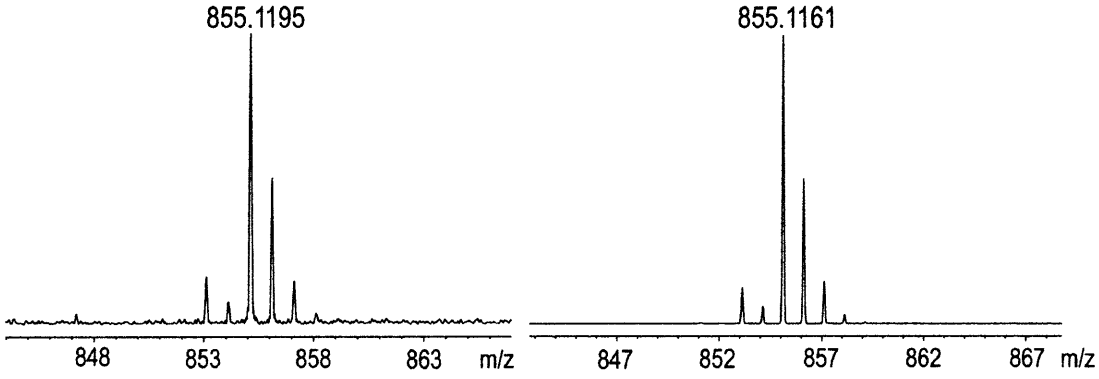

Figure A2.12. High-resolution ESI mass spectrum of **8a** - comparison between the observed (left) and theoretical (right) isotope pattern.

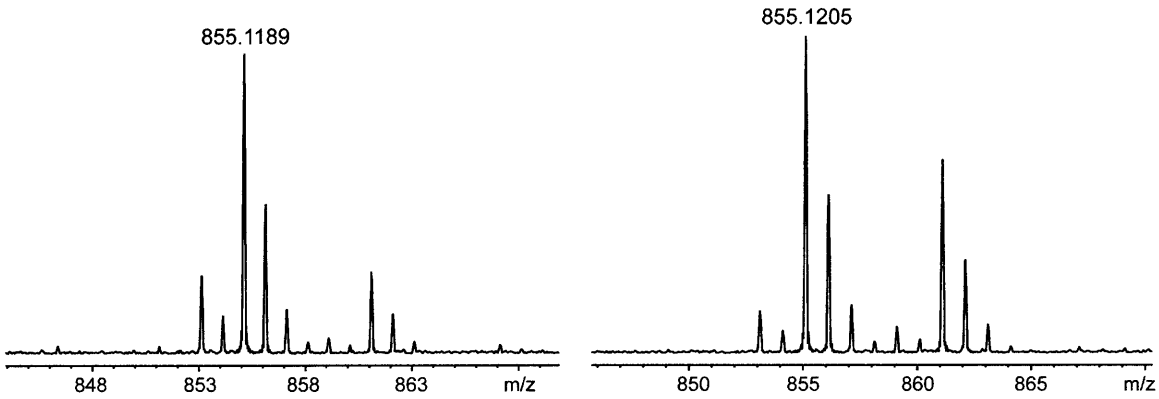

Figure A2.13 High-resolution ESI mass spectrum of **7a** (left) and **6a** (right). The species at *m/z* = 861 is due to an diiron(III) impurity.

Appendix 3

Synthesis of Triptycene Carboxylate-Bridged Dimetallic Complexes with First Row Transition Metals

Introduction

Since the structural characterization of the classic paddlewheel "copper acetate" core,[1,2] tetracarboxylate-bridged complexes have been synthesized with nearly every transition metal and a wide assortment of different carboxylates (RCO_2^-) and neutral ligands (L). Motivation for the synthesis of these complexes is to study structural, electronic, and magnetic properties of the two metal atoms constricted by the carboxylate bridges. Among late first row transition metals, over 500 dicopper paddlewheel structures alone have been published, owing to the interest sparked by the interesting magnetic properties of these complexes.[3] The first paddlewheel complexes containing divalent iron, cobalt, nickel, and zinc were reported relatively soon after the characterization of the cupric acetate structure.

In particular, carboxylate-bridged diiron(II) complexes have been synthesized as part of the study of small molecule models of the diiron active site of soluble methane monooxygenase (sMMOH).[4,5] Recent research has focused the coordination chemistry of triptycene carboxylate ($TrpCO_2^-$), which facilitates the formation of tetracarboxylate-bridged diiron(II) complexes with the general formula $[Fe_2(\mu\text{-}O_2CTrp)_4(L)_2]$.[6] These complexes have very stable paddlewheel cores and unusually long Fe–Fe distances, which are supported by "tongue in groove" binding of the four triptycene units. In this study, the coordination chemistry of this carboxylate with other divalent first-row transition metals was explored.

Experimental Section

General Procedures and Methods. Diethylether (Et_2O), pentane and dichloromethane (CH_2Cl_2) were saturated with nitrogen and purified by passage through activated alumina columns under an argon atmosphere. The syntheses of $TrpCO_2H$[7,8] and $TrpCO_2Na$ have been reported.[6] $Mn(OTf)_2{\cdot}2MeCN$ was prepared following a literature procedure.[9] All other reagents were obtained from commercial sources and used as received. Air sensitive manipulations were performed by using Schlenk techniques or under nitrogen atmosphere in an MBraun glovebox.

Physical measurements. FT-IR spectra were recorded on a Thermo Nicolet Avatar 360 spectrometer with OMNIC software.

$[Mn_2(\mu\text{-}O_2CTrp)_4(THF)_2]$ (1). To a solution of $Mn(OTf)_2{\cdot}2MeCN$ (47.6 mg, 110 μmol) in THF (4 mL) was added a solution of NaO_2CTrp (70 mg, 219 μmol) in THF (4 mL) and the colorless suspension was stirred overnight. The solvent was removed from the reaction mixture and the white residue was extracted with CH_2Cl_2 (3 mL). The mixture was filtered and the clear filtrate layered with THF (ca. 0.1 mL). Vapor diffusion of pentane afforded colorless blocks suitable for X-ray structural analysis. Yield: 15 mg (17%).

$[Co_2(\mu\text{-}O_2CTrp)_4(THF)_2]$ (2). To a solution of $CoCl_2$ (15.9 mg, 122 μmol) in THF (3 mL) was added AgOTf (70.4 mg, 274 μmol) and a solution of NaO_2CTrp (80 mg, 250 μmol) in THF (3 mL), and the light purple-gray solution was stirred overnight. The solvent was removed and CH_2Cl_2 (3 mL) added to the purple-gray residue. After stirring for 30 min, the mixture was filtered and the

filtrate layered with THF (ca. 0.1 mL). Vapor diffusion of pentane yielded **2** as blue-green dichroic blocks suitable for X-ray crystallography after two recrystallizations. Yield: 27.3 mg (31%). FTIR (KBr, cm^{-1}) 3058 (w), 2957 (w), 2902 (w), 1619 (s), 1459 (s), 1446 (s), 1408 (s), 1292 (m), 1265 (m), 1175 (m), 1031 (m), 870 (m), 789 (m), 748 (s), 721 (s), 687 (m), 648 (m), 625 (s), 482 (m), 463 (m).

$[Ni_2(\mu\text{-}O_2CTrp)_4(THF)_2]$ (3). To a solution of $NiBr_2$ (29.0 mg, 133 μmol) in THF (4 mL) was added AgOTf (70.4 mg, 274 μmol) and a solution of NaO_2CTrp (80 mg, 250 μmol) in THF (4 mL). The light yellow-green suspension was stirred overnight, during which time it turned to a dark gray suspension. The solvent was removed from the reaction mixture, and the gray residue was extracted with CH_2Cl_2 (2.5 mL). The mixture was filtered and the green filtrate layered with THF (ca. 0.1 mL). Vapor diffusion of pentane yielded **3** as green blocks suitable for X-ray crystallography after two recrystallizations. Yield: 12.1 mg (13%). FTIR (KBr, cm^{-1}): 3059 (w), 2957 (w), 2873 (w), 1624 (s), 1458 (m), 1447 (m), 1406 (m), 1311 (m), 1291 (m), 1217 (m), 1177 (m), 1031 (m), 872 (w), 751 (s), 721 (w), 635 (m), 625 (w), 483 (w).

$[Cu_2(\mu\text{-}O_2CTrp)_4(THF)_2]$ (4). To a solution of $Cu(OTf)_2$ (23 mg, 64 μmol) in THF (2 mL) was added a solution of NaO_2CTrp (40 mg, 125 μmol) THF (3 mL). The reaction mixture was stirred overnight, during which time a white precipitate formed. The solvent was removed from the mixture, and the turquoise residue was extracted with $CHCl_3$ (ca. 8 mL). Vapor diffusion of Et_2O into a solution mixture of $CH_2Cl_2/CHCl_3$ (1:4) afforded **4** as turquoise blocks suitable for X-ray

crystallography. Yield: 23.5 mg (52%). FTIR (KBr, cm^{-1}): 3060 (w), 2956 (w), 2923 (w), 2868 (w), 1620 (s), 1459 (m), 1447 (m), 1407 (s), 1292 (w), 1177 (w), 1036 (m), 1015 (w), 875 (m), 795 (m), 760 (m), 747 (m), 723 (m), 688 (w), 650 (w), 626 (s), 611 (w), 482 (w).

$[Zn_2(\mu\text{-}O_2CTrp)_4(THF)_2]$ (5). To a solution of $Zn(OTf)_2$ (85.5 mg, 236 μmol) in THF (5 mL) was added a solution of NaO_2CTrp (150 mg, 469 μmol) in THF (5 mL), and the pale yellow suspension was stirred overnight. The solvent was removed from the reaction mixture and the white residue was extracted with CH_2Cl_2 (7 mL). The mixture was filtered and the pale yellow filtrate was layered with THF (ca. 0.1 mL). Vapor diffusion of pentane yielded **5** as colorless blocks suitable for X-ray crystallography after two recrystallizations. Yield: 97.3 mg (56%). FTIR (KBr, cm^{-1}): 3059 (w), 2973 (w), 2955 (w), 2862 (w), 1638 (s), 1603 (m), 1459 (m), 1447 (s), 1410 (s), 1291 (m), 1188 (w), 1119 (w), 1031 (m), 875 (m), 789 (m), 763 (m), 746 (s), 722 (m), 686 (m), 648 (m), 626 (s), 606 (m), 480 (m), 451 (m).

X-ray Crystallographic Studies. Single crystals were coated with Paratone-N oil, mounted at room temperature on the tip of a glass fiber (Oxford magnetic mounting system), and cooled under a stream of cold N_2 maintained by a KRYO-FLEX low-temperature apparatus. Intensity data were collected on a Bruker (formerly Siemens) APEX CCD diffractometer with graphite-monochromated Mo Kα radiation (λ = 0.71073 Å) controlled by a Pentium-based PC running the SMART software package.[10] A total of 2800 frames were acquired for each measurement. The structures were solved by direct or

Patterson methods and refined on F^2 by using the SHELXTL software.[11,12] Empirical absorption corrections were applied with SADABS[13] and the structures were checked for higher symmetry with PLATON.[14] All non-hydrogen atoms were refined anisotropically. In general, hydrogen atoms were assigned idealized positions and given thermal parameters equivalent to either 1.5 (methyl hydrogen atoms) or 1.2 (all other hydrogen atoms) times the thermal parameter of the atom to which they were attached. Each structure contained 7 molecules of CH_2Cl_2; two of them were disordered in the crystal structures of **1**, **2**, **3**, and **5**.

Results and Discussion

The reaction of triptycene carboxylate and a divalent metal triflate (M = Mn, Co, Ni, Cu, Zn) in a 2:1 ratio afforded tetracarboxylate dimetallic complexes **1**–**5** in a self-assembly process. The yields varied from poor to moderate, due to the low solubility of the complexes, depending on the metal. The structures of **1**–**5** were determined by X-ray crystallographic analysis and all were isomorphous with the previously characterized diiron analog, $[Fe_2(\mu\text{-}O_2CTrp)_4(THF)_2]$ [Fe–Fe = 2.7307(8)].[6] The coordination sphere for each metal ion is square pyramidal and consists of an apical THF molecule and the four carboxylates, which form the base of the pyramid. The structures of the paddlewheel complexes are displayed in Figure A3.1, crystallographic information is given in Table A3.1, and selected bond distances and angles are listed in Table A3.2. The metal–metal distance decreases from the dimanganese(II) (2.998 Å) to the dicopper(II) (2.602 Å) system and increases again with the dizinc(II) complex (2.889 Å). This trend

corresponds to the Irving-Williams series, which predicts the order of stability of a high-spin M(II) compound: Mn < Fe < Co < Ni < Cu > Zn.[15] Tetracarboxylate complexes with Mn(II), Fe(II), Co(II), Ni(II), Cu(II), and Zn(II) have been reported previously and the separation between the metal atoms in **1**–**5** fall into the range of the corresponding compounds. Metal-metal distances in dizinc(II) compounds range between 2.9-3.0 Å,[16] in dicopper(II) between 2.5 to 2.9 Å,[17] in dinickel(II) compounds around 2.7 Å,[2] in dicobalt(II) compounds around 2.8 Å.[18] The first dimanganese(II) paddlewheel complex was reported only six years ago[19] and **1** belongs to the class of these rather rare complexes.

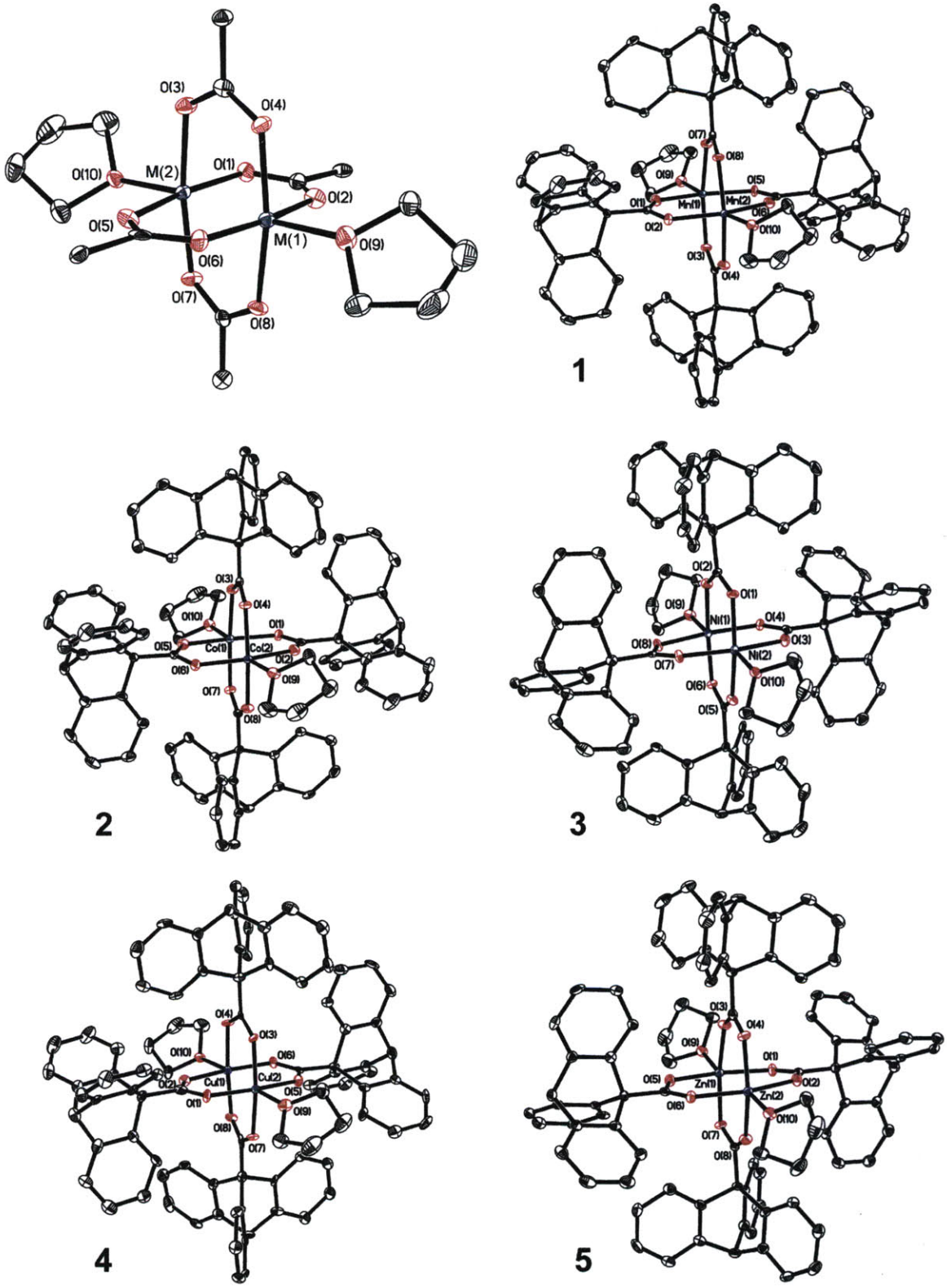

Figure A3.1. ORTEP diagram of **1–5** displaying thermal ellipsoids (50%). For clarity, the hydrogen atoms are not shown.

Table A3.1. Crystallographic information for compounds **1**–**5**.

	1·7CH_2Cl_2	**2**·7CH_2Cl_2	**3**·7CH_2Cl_2	**4**·7CH_2Cl_2	**5**·7CH_2Cl_2
Formula	$Mn_2C_{99}H_{82}O_{10}Cl_{14}$	$Co_2C_{99}H_{82}O_{10}Cl_{14}$	$Ni_2C_{99}H_{82}O_{10}Cl_{14}$	$Cu_2C_{99}H_{82}O_{10}Cl_{14}$	$Zn_2C_{99}H_{82}O_{10}Cl_{14}$
FW	2058.69	2045.81	2045.37	2055.05	2058.69
Crystal System	Orthorhombic	Orthorhombic	Orthorhombic	Orthorhombic	Orthorhombic
Space Group	$Pca2_1$	$Pca2_1$	$Pca2_1$	$Pca2_1$	$Pca2_1$
a (Å)	20.398(1)	20.3016(15)	20.285(5)	20.224(3)	20.256(19)
b (Å)	16.0062(11)	15.9860(12)	15.947(4)	16.042(2)	16.011(15)
c (Å)	28.085(2)	28.087(2)	27.944(7)	27.977(4)	28.06(3)
V (Å^3)	9169.6(11)	9115.6(12)	9040(4)	9077(2)	9101(15)
Z	4	4	4	4	4
ρ_{calc} (g/cm^3)	1.395	1.491	1.503	1.504	1.503
Temperature (K)	110	110	110	110	110
μ(Mo Kα) (mm^{-1})	0.626	0.835	0.891	0.942	0.999
Θ limits (deg)	2.12, 27.05	2.18, 27.88	2.14, 25.03	2.14, 27.12	2.14, 27.00
Completeness to Θ (%)	99.9	99.9	99.9	99.9	99.7
Total no. of data	124665	152100	98713	84414	111344
No. of unique data	15082	21703	15953	19872	18824
Goodness of fit on F^2	1.071	1.075	1.049	1.008	1.031
R_1 (%)[a]	4.97	5.64	4.93	7.23	4.09
wR_2 (%)[b]	12.19	12.52	11.15	13.76	9.37
Absolute struct. param.	0.407(14)	0.010(11)	0.014(12)	0.161(15)	0.056(7)
Max, min peaks (e/Å^3)	0.935, -0.628	0.866, -0.697	0.505, -0.714	0.586, -0.717	0.915, -0.684

[a] $R_1 = \Sigma||F_o|-|F_c||/\Sigma|F_o|$, [b] $wR_2 = \{\Sigma[w(F_o^2-F_c^2)]/\Sigma[w(F_o^2)^2]\}^{1/2}$

Table A3.2. Selected Bond Lengths (Å) and Bond Angles (deg) for Compounds **1**–**5**.

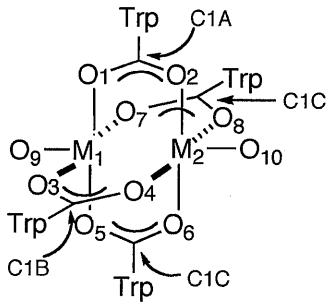

	1	2	3	4	5
M(1)–M(2)	2.9986(7)	2.7405(6)	2.6015(8)	2.6016(10)	2.889(2)
M(1)–O(1)	2.106(3)	2.021(3)	2.005(3)	1.961(5)	2.069(3)
M(1)–O(3)	2.116(3)	2.043(2)	2.004(3)	1.966(4)	2.030(3)
M(1)–O(5)	2.122(3)	2.043(3)	2.011(3)	1.970(5)	2.033(3)
M(1)–O(7)	2.127(3)	2.030(2)	2.009(3)	1.967(5)	2.031(3)
M(1)–O(9)	2.099(3)	2.026(3)	1.988(3)	2.167(5)	2.013(3)
M(2)–O(2)	2.111(3)	2.062(3)	1.993(3)	1.968(5)	2.037(3)
M(2)–O(4)	2.109(3)	2.016(2)	2.008(3)	1.973(4)	2.039(3)
M(2)–O(6)	2.125(3)	2.017(3)	1.996(3)	1.962(5)	2.050(3)
M(2)–O(8)	2.105(3)	2.028(2)	2.012(3)	1.990(4)	2.036(3)
M(2)–O(10)	2.101(3)	2.036(3)	1.988(3)	2.155(5)	2.006(3)
M(1)–O(1)–C(1A)	136.9(3))	134.3(3)	131.6(3)	127.7(5)	136.1(2)
M(1)–O(3)–C(1B)	133.2(3)	126.5(2)	124.9(3)	121.5(4)	127.7(2)
M(1)–O(5)–C(1C)	116.5(3)	117.1(2)	115.5(3)	119.1(5)	118.8(2)
M(1)–O(7)–C(1D)	125.9(3)	123.3(2)	122.3(3)	123.8(4)	123.8(2)
M(2)–O(2)–C(1A)	119.5(3)	115.8(3)	115.9(3)	118.1(5)	117.4(2)
M(2)–O(4)–C(1B)	122.9(2)	123.1(2)	121.7(3)	123.6(4)	125.2(2)
M(2)–O(6)–C(1C)	140.2(3)	133.6(3)	131.4(3)	127.5(5)	134.7(2)
M(2)–O(8)–C(1D)	130.3(3)	127.0(2)	124.2(3)	121.8(5)	129.6(2)

Numbers in parentheses are estimated standard deviations of the last significant figures.
M = Mn (**1**), Co (**2**), Ni (**3**), Cu (**4**), Zn (**5**).

Acknowledgements. This work was supported by grant GM032134 from the National Institute of the General Medical Sciences. I thank Kyrstin L. Fornace for help with synthesis and X-ray crystallographic measurements.

References

(1) Van Niekerk, J. N.; Schoening, F. R. L. *Nature* **1953**, *171*, 36-37.

(2) Cotton, F. A.; Murillo, C. A.; Walton, R. A.; Editors *Multiple Bonds Between Metal Atoms, Third Edition*, 2005.

(3) *ConQuest*, version 1.8; Cambridge Crystallographic Data Center: Cambridge, U.K., 2006.

(4) Tolman, W. B.; Que, L., Jr. *J. Chem. Soc., Dalton Trans.* **2002**, *5*, 653-660.

(5) Tshuva, E. Y.; Lippard, S. J. *Chem. Rev.* **2004**, *104*, 987-1011.

(6) Friedle, S.; Kodanko, J. J.; Fornace, K. L.; Lippard, S. J. *J. Mol. Struct.* **2008**, *890*, 317-327.

(7) Kawada, Y.; Iwamura, H. *J. Org. Chem.* **1981**, *46*, 3357-3359.

(8) Friedman, L.; Logullo, F. M. *J. Org. Chem.* **1963**, *28*, 1549.

(9) Bryan, P. S.; Dabrowiak, J. C. *Inorg. Chem.* **1975**, *14*, 296-299.

(10) *SMART, Software for the CCD Detector System*, version 5.6; Bruker AXS Madison, WI, 2000.

(11) Sheldrick, G. M. *SHELXTL-97*, University of Göttingen: Göttingen, Germany: 2000.

(12) Sheldrick, G. M. *Acta Crystallogr., Sect. A* **2008**, *A64*, 112-122.

(13) Sheldrick, G. M. *SADABS: Area-Detector Absorption Correction*, University of Göttingen: Göttingen, Germany, 2001.

(14) Spek, A. L. *PLATON, A Multipurpose Crystallographic Tool*, Utrecht University: Utrecht, The Netherlands, 2000.

(15) Huheey, J. E. *Inorganic Chemistry. 3rd Ed*; Harper & Row: New York, 1983.

(16) Clegg, W.; Little, I. R.; Straughan, B. P. *J. Chem. Soc., Dalton Trans.* **1986**, 1283-1288.

(17) Rodríguez-Fortea, A.; Alemany, P.; Alvarez, S.; Ruiz, E. *Chem. Eur. J.* **2001**, *7*, 627-637 and references therein.

(18) Benbellat, N.; Gavrilenko, K. S.; Le Gal, Y.; Cador, O.; Golhen, S.; Gouasmia, A.; Fabre, J.-M.; Ouahab, L. *Inorg. Chem.* **2006**, *45*, 10440-10442 and references therein.

(19) Grirrane, A.; Pastor, A.; Galindo, A.; Ienco, A.; Mealli, C.; Rosa, P. *Chem. Commun.* **2003**, 512-513.

Appendix 4

Synthesis and Structure of a Molecular Ferrous Wheel, $[Fe(O_2CH)(O_2CAr^{iPrO})(1,4\text{-dioxane})]_6$

Introduction

Sterically hindered benzoates, such as *m*-terphenyl carboxylates allow the assembly of discrete diiron species, which serve as model complexes for carboxylate-bridged non-heme diiron enzymes.[1,2] From these studies it was established that the geometry of the carboxylate influences the nuclearity of the diiron cluster and its reactivity. Here, we report the coordination chemistry of the carboxylate $Ar^{iPrO}CO_2^-$ with ferrous iron (Scheme A4.1).

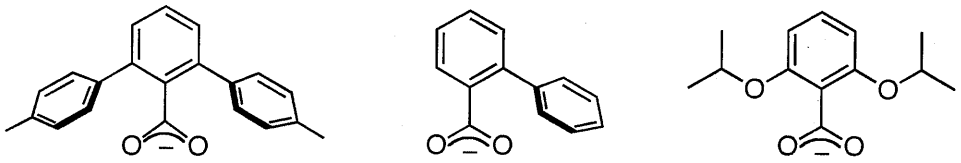

$Ar^{Tol}CO_2^-$ $\quad$ $biphCO_2^-$ $\quad$ $Ar^{iPrO}CO_2^-$

Chart A4.1.

Experimental

General Procedures and Methods. Pentanes, diethylether (Et_2O), tetrahydrofuran (THF) and dichloromethane (CH_2Cl_2) were saturated with nitrogen and purified by passage through activated alumina columns under an argon atmosphere. Dry 1,4-dioxane was purchased from Aldrich. The synthesis and characterization of NaO_2CAr^{PhO} and $Fe(OTf)_2{\cdot}2MeCN$ have been reported.[3,4] All other reagents were obtained from commercial sources and used as received. Air sensitive manipulations were performed by using Schlenk techniques or under a nitrogen atmosphere in an MBraun glovebox.

2,6-Diisopropoxybenzoic Acid (HO_2CAr^{iPrO}). A solution of dry pentane (15 mL) containing 1,3-diisopropoxybenzene (1.03 mL, 5.15 mmol) and *N,N,N',N'*-tetramethylethylenediamine (TMEDA, 1.01 mL, 6.70 mmol) in a Schlenk flask was cooled to –5 °C. To this solution, *n*–butyllithium (1.6 M in hexanes, 4.85 mL, 7.73 mmol) was added dropwise over a period of 15 min. The resulting white suspension was stirred at ambient temperature for 30 min and then allowed to react with gaseous, dry carbon dioxide for another 30 min. The precipitate was filtered off, washed with hexanes (1 x 10 mL), and subsequently dissolved in CH_2Cl_2 (30 mL) and aqueous HCl (5%, 30 mL). The aqueous phase was extracted with CH_2Cl_2 (3 x 15 mL) and the organic phase washed with water (3 x 15 mL). The organic phases were combined and dried with Na_2SO_4 to yield a white solid of HO_2CAr^{iPrO}. Yield: 764 mg (62%). ^{1}H-NMR (300 MHz, $CDCl_3$) δ: 7.25 (m, 1H), 6.56 (d, 2H), 4.57 (m, 2H), 1.34 (d, 12H).

Sodium 2,6-Diisopropoxybenzoate (NaO_2CAr^{iPrO}). To a solution of HO_2CAr^{iPrO} (0.744 g, 2.50 mmol) in MeOH (15 mL) was added NaOH (0.105 g, 2.62 mmol) and stirred for 2 h at 55 °C. The solvent was removed and the white residue thoroughly dried in vaccum at 100 °C overnight before being brought into the glove box. Yield: Quantitative.

[$Fe_6(\mu\text{-}O_2CH)_6(\mu\text{-}O_2CAr^{iPrO})_6$(1,4-dioxane)$_6$] (1). To a THF (2 mL) solution of $Fe(OTf)_2{\cdot}2MeCN$ (43.1 mg, 0.100 mmol) was added NaO_2CAr^{iPrO} (52.1 mg, 0.200 mmol) and the resulting suspension was stirred overnight. The next day, the solvent was removed and the residue extracted with CH_2Cl_2. The yellow extract was dissolved in 1,4-dioxane (1 mL). Vapor diffusion of pentanes into the

yellow solution yielded a small amount of colorless needles of **1** after ca. two weeks, suitable for X-ray crystallography.

X-ray Crystallographic Studies. A single crystal of **1** was coated with Paratone-N oil, mounted at room temperature on the tips of quartz fibers or nylon loops (OXFORD magnetic mounting system), and cooled to 110 K under a stream of cold dinitrogen maintained by a KRYO-FLEX low-temperature apparatus. Intensity data were collected on a Bruker (formerly Siemens) APEX CCD diffractometer with graphite-monochromated Mo Kα radiation (λ = 0.71073 Å) controlled by a Pentium-based PC running the SMART software package.[5] Data collection and reduction protocols are described elsewhere. The structures were solved by direct methods and refined on F^2 by using the SHELXTL-97 software.[6,7] Empirical absorption corrections were applied with SADABS[8] and the structures were checked for higher symmetry with PLATON.[9] All non-hydrogen atoms were refined anisotropically. In general, hydrogen atoms were assigned idealized positions and given thermal parameters equivalent to either 1.5 (methyl hydrogen atoms) or 1.2 (all other hydrogen atoms) times the thermal parameter of the carbon to which they were attached. One molecule of 1,4-dioxane was located in the structure of **1**, which is positioned on a 3-fold improper axis and is disordered over two positions in a ratio of 76:34.

Results and Discussion

The reaction between $^{-}O_2CAr^{iPrO}$ and iron(II) triflate in a 2:1 ratio did not lead to the desired dinuclear species. Instead, the hexanuclear complex **1**

crystallized from this reaction mixture as colorless blocks in small yields. The crystal structure reveals a Fe_6 wheel with S_6 symmetry. The structure of **1** is displayed in Figure A4.1; selected bond distances and angles for **1** are listed in Table A4.1 and crystallographic information provided in Table A4.2. Six $^{-}O_2CAr^{iPrO}$ carboxylates bridge a pair of Fe atoms, respectively, and six formate ligands each connect three neighboring iron atoms. The latter ligand has an unusual binding mode – one oxygen atom bridges two iron atoms in a syn,anti-μ_2-fashion whereas the "dangling" oxygen atom binds syn to a third iron atom.[10,11] Six 1,4-dioxane molecules complete the coordination sphere around the ferrous iron atoms. The μ_3-1,1,3-bridging of a carboxylate in multinuclear iron compounds has been reported in a few cases previously.[12-14] The origin of the formate ligand is unknown, but it is suggested that it forms from in a decomposition reaction of the $^{-}O_2CAr^{iPrO}$ carboxylate.

Table A4.1. Selected Bond Lengths (Å) and Bond Angles (deg) for Compound **1**.

Fe(1)–Fe(1A)	3.543	Fe(1)–O(8)	2.1934(15)
Fe(1)–O(1)	2.0324(15)	Fe(1)–O(4)–C(14)	121.60(13)
Fe(1)–O(2A)	2.0926(15)	Fe(1)–O(3)–C(14)	153.35(14)
Fe(1)–O(3)	2.1680(15)	Fe(1)–O(4)–Fe(1C)	113.40(6)
Fe(1)–O(4)	2.1055(14)	Fe(1)–O(2)–C(1)	136.05(14)
Fe(1)–O(4A)	2.1330(14)	Fe(1)–O(1)–C(1A)	130.90(14)

Numbers in parentheses are estimated standard deviations of the last significant figure.

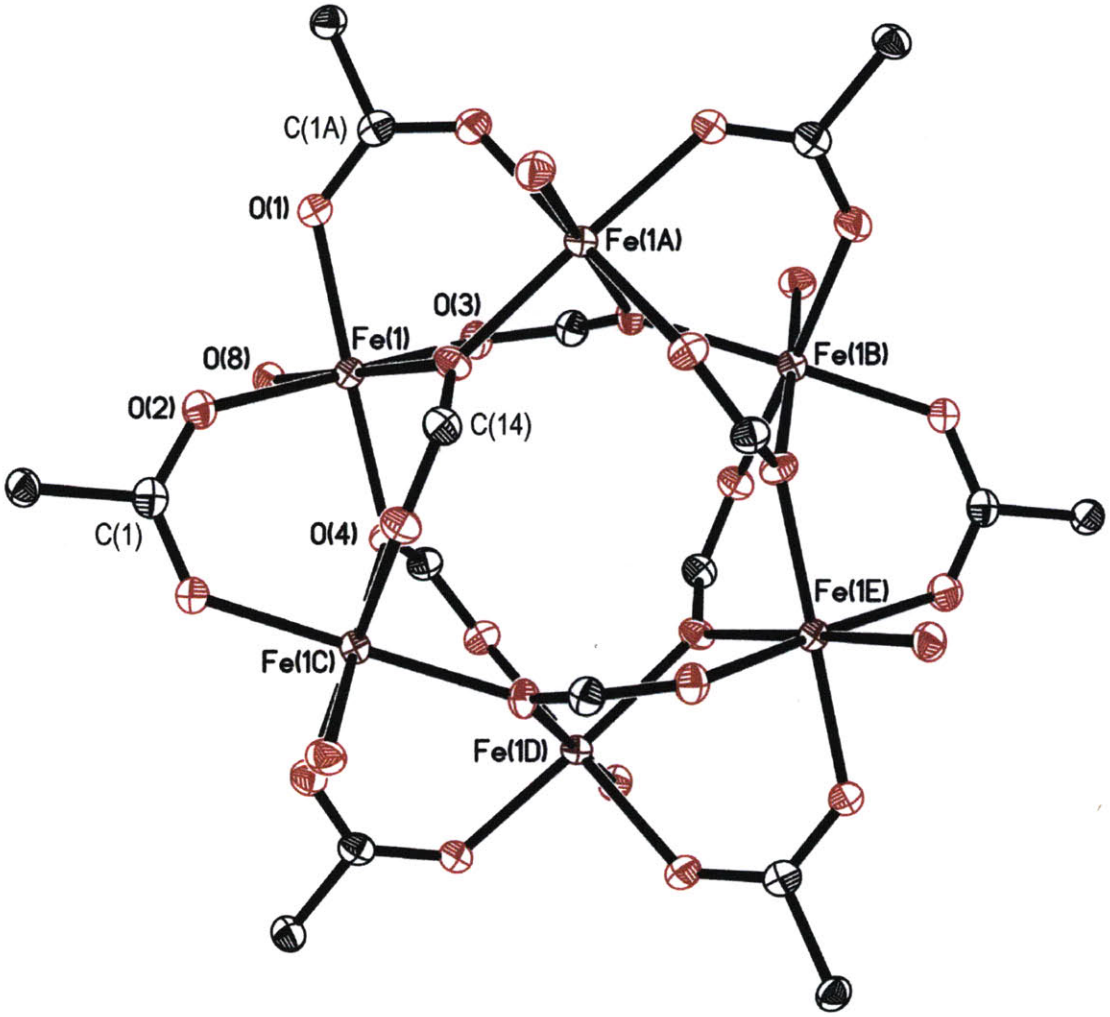

Figure A4.1. ORTEP diagram of $[Fe_6(\mu\text{-}O_2CH)_6(\mu\text{-}O_2CAr^{iPrO})_6(1,4\text{-dioxane})_6]$ (**1**) illustrating 50% probability thermal ellipsoids for all non-hydrogen atoms. The hydrogen atoms and the Ar^{iPrO} unit of the $^{-}O_2CAr^{iPrO}$ ligands are omitted for clarity.

Table A4.2. Summary of X-ray Crystallographic Data for **1**.

	1·1,4-dioxane
Empirical formula	$Fe_6O_{50}C_{112}H_{164}$
Formula weight	2645.53
Crystal System	Trigonal (Rhombohedral)
Space group	$R\bar{3}$
a (Å)	30.0684(17)
c (Å)	12.3469(14)
V (Å^3)	9667.4(13)
Z	3
ρ_{calc} (g/cm^3)	1.363
Temperature (K)	110
μ Mo Kα (mm^{-1})	0.743
θ range (deg)	2.27 – 27.88
Crystal size (mm)	0.08 x 0.10 x 0.15
Completeness to θ (%)	100.0
Max, min peaks (e/Å^3)	0.326 and -0.361
Goodness-of-fit on F^2	1.071
Total no. of data	55549
No. unique data	5136
R_1 (%)[a]	4.44
wR_2 (%)[b]	8.32

[a] $R_1 = \Sigma||F_o|-|F_c||/\Sigma|F_o|$, [b] $wR_2 = \{\Sigma[w(F_o^2-F_c^2)]/\Sigma[w(F_o^2)^2]\}^{1/2}$

References

(1) Tolman, W. B.; Que, L., Jr. *J. Chem. Soc., Dalton Trans.* **2002**, *5*, 653-660.

(2) Tshuva, E. Y.; Lippard, S. J. *Chem. Rev.* **2004**, *104*, 987-1012.

(3) Gumanov, L. L.; Shteinman, A. A.; Nordlander, E.; Koldobskii, G. I. *Russ. J. Org. Chem.* **2002**, *38*, 606-608.

(4) Hagen, K. S. *Inorg. Chem.* **2000**, *39*, 5867-5869.

(5) *SMART, Software for the CCD Detector System*, Bruker AXS: Madison, WI, 2000.

(6) Sheldrick, G. M. *SHELXTL-97*, University of Göttingen: Göttingen, Germany: 2000.

(7) Sheldrick, G. M. *Acta Crystallogr., Sect. A* **2008**, *A64*, 112-122.

(8) Sheldrick, G. M. *SADABS: Area-Detector Absorption Correction*, University of Göttingen Göttingen, Germany, 2001.

(9) Spek, A. L. *PLATON, A Multipurpose Crystallographic Tool*, Utrecht University: Utrecht, The Netherlands, 2000.

(10) Rardin, R. L.; Tolman, W. B.; Lippard, S. J. *New J. Chem.* **1991**, *15*, 417-430.

(11) Reisner, E.; Telser, J.; Lippard, S. J. *Inorg. Chem.* **2007**, *46*, 10754-10770.

(12) Viertelhaus, M.; Adler, P.; Clérac, R.; Anson, C. E.; Powell, A. K. *Eur. J. Inorg. Chem.* **2005**, *2005*, 692-703.

(13) Wang, Z.; Zhang, B.; Kurmoo, M.; Green, M. A.; Fujiwara, H.; Otsuka, T.; Kobayashi, H. *Inorg. Chem.* **2005**, *44*, 1230-1237.

(14) Wang, Z.-M.; Zhang, Y.-J.; Liu, T.; Kurmoo, M.; Gao, S. *Adv. Funct. Mater.* **2007**, *17*, 1523-1536.

Biographical Note

The author was born on 20th of November 1976 in Karlsruhe, Germany. She received her Diploma Degree in Chemistry ("Dipl.–Chem.") from the University of Karlsruhe, Germany in 2004. As a graduate student she completed her doctoral work in the laboratory of Professor Stephen J. Lippard.

Simone Friedle

Education

09/04 – 07/09	**Massachusetts Institute of Technology**	Cambridge, MA
	Ph.D., Inorganic Chemistry Thesis: "Modeling the Active Sites of Non-Heme Diiron Metalloproteins with Sterically Hindered Carboxylates and Syn *N*-Donor Ligands." Advisor: Prof. Stephen J. Lippard	
09/98 – 06/04	**University of Karlsruhe (TH)**	Karlsruhe, Germany
	Diploma Degree (*Dipl.-Chem.*) in Chemistry Thesis: "Synthesis of Alkyl-Substituted *Bis*(dithiolene) Complexes of Iron, Cobalt and Nickel." Advisors: Prof. Richard H. Holm, Harvard University, Cambridge, MA and Prof. Hansgeorg Schnöckel, University of Karlsruhe, Germany.	

Research Experience

01/05 – 08/09	**Massachusetts Institute of Technology** Lippard research group. Ph.D. thesis research.	Cambridge, MA
08/03 – 05/04	**Harvard University** Holm research group. Diploma thesis research.	Cambridge, MA
09/01 – 05/02	**University of Massachusetts, Boston** Zompa research group. Inorganic synthesis, physical methods.	Boston, MA
02/00 – 12/00	**University of Karlsruhe (TH)** Schnöckel research group. Synthesis of low-valent aluminium(I)- and gallium(I)-subhalogenides.	Karlsruhe, Germany
02/99 – 04/99 07/99 – 08/99 01/01 – 07/01	**Forschungszentrum (Research Center) Karlsruhe** Höll research group (Institute of Technical Chemistry). Development of new methods for elimination of fluoride from drinking water. Collaboration on a European Research Project concerning elimination of heavy metals from drinking water.	Karlsruhe, Germany
09/93 – 07/96	**Forschungszentrum (Research Center) Karlsruhe** Chemical laboratory assistant apprenticeship.	Karlsruhe, Germany

Awards

2003	"*Stipendium für Abschlussarbeiten*" – Fellowship from DAAD (German Academic Exchange Service).
2001	*Baden-Württemberg Exchange Program* – Fellowship from the government of Baden-Württemberg, Germany.

Publications

Friedle, S.; Lippard, S. J. "Synthesis, Characterization, and Oxygenation Studies of Carboxylate-Bridged Diiron(II) Complexes with Aromatic Substrates Tethered to Pyridine Ligands." Manuscript submitted.

Ye W.; Organo V. G.; Friedle, S.; Ho, D. M.; Lippard, S. J.; Rybak-Akimova, E. V. "The Role of Fe(IV)-Oxo Intermediates in Stoichiometric and Catalytic Oxidations with Iron Pyridine-Azamacrocycles (PyMACs)." Manuscript in preparation.

Friedle, S.; Kodanko, J. J.; Morys, A. J.; Hayashi, T.; Moënne-Loccoz. P.; Lippard S. J. "Modeling the Syn-Disposition of Nitrogen Donors in Non-Heme Diiron Enzymes: Synthesis, Characterization and Hydrogen Peroxide Reactivity of Diiron(III) Complexes with the Syn *N*-Donor Ligand H_2BPG_2DEV." *J. Am. Chem. Soc.* **2009**, in press.

Wong, B.; Friedle, S.; Lippard, S. J. "Subtle Modification of 2,2'-Dipicolylamine Lowers the Affinity and Improves the Turn-On of Zn(II)-Selective Fluorescent Sensors." *Inorg. Chem.* **2009**, *48*, 7009–7011.

Wong, B.; Friedle, S.; Lippard, S. J. "Solution and Fluorescence Properties of Symmetric Dipicolylamine-Containing Dichlorofluorescein-Based Zn(II) Sensors." *J. Am. Chem. Soc.* **2009**, *131*, 7142–7152.

Zhang, X.-a.; Hayes, D.; Smith, S. J.; Friedle, S.; Lippard, S. J. "New Strategy for Quantifying Biological Zinc by a Modified Zinpyr Fluorescence Sensor." *J. Am. Chem. Soc.* **2008**, *130*, 15788– 15789.

Friedle, S.; Kodanko, J. J.; Fornace, K. L.; Lippard, S. J. "9-Triptycene-Carboxylate-Bridged Diiron(II) Complexes: Capture of the Paddlewheel Geometric Isomer." *J. Mol. Struct.* **2008**, *890*, 317–327. (Contribution to a special issue in honor of the late Prof. F. Albert Cotton.)

Zhao, M.; Helms, B.; Slonkina, E.; Friedle, S.; Lee, D.; DuBois J.; Hedman, B.; Hodgson, K. O.; Fréchet, J. M. J.; Lippard, S. J. "Iron Complexes of Dendrimer-Appended Carboxylates for Activating Dioxygen and Oxidizing Hydrocarbons." *J. Am. Chem. Soc.* **2008**, *130*, 4352–4363.

Friedle, S.; Partyka, D. V.; Bennett, M. V.; Holm, R. H. "Synthesis of Metal Dithiolene Complexes by Si–S Bond Cleavage of a Bis(silanylsulfanyl)-alkene." *Inorg. Chim. Acta* **2005**, *359*, 1427–1434.

Dussalt, D.; Friedle, S.; Zompa, L. J. "Studies of Copper(II) and Nickel(II) Complexation by Bis(1,4,7-Triazacyclononane) Ligands containing Alkene and Alkyne Bridging Groups." *Inorg. Chim. Acta* **2004**, *357*, 1478–1486.

Conference Presentations

Friedle, S.; Lippard, S. J. "9-Triptycene-Carboxylate-Bridged Diiron(II) Complexes: Capture of the Paddlewheel Geometric Isomer." 234th National ACS meeting (Boston, MA: August 2007).

Friedle, S.; Lippard, S. J. "Modeling the Syn-Disposition of Nitrogen Donors at the Active Sites of Non-Heme Diiron Enzymes." Bacterial Multicomponent Monoxygenase Symposium (M.I.T., Cambridge, MA: 2006).